Advanced oxidation processes for food industry wastewater valorization and treatment

Giuseppina Iervolino

Unione Europea

Ministero dell'Istruzione, dell'Università e della Ricerca

UNIVERSITÀ DEGLI STUDI DI SALERNO

FONDO SOCIALE EUROPEO

Programma Operativo Nazionale 2000/2006
"Ricerca Scientifica, Sviluppo Tecnologico, Alta Formazione"
Regioni dell'Obiettivo 1 – Misura III.4
"Formazione superiore ed universitaria"

Department of Industrial Engineering

Ph.D. Course in Chemical Engineering
(XV Cycle-New Series, XXIX Cycle)

ADVANCED OXIDATION PROCESSES FOR FOOD INDUSTRY WASTEWATER VALORIZATION AND TREATMENT

Supervisor
Prof. Diana Sannino

Ph.D. student
Giuseppina Iervolino

Scientific Referees
Ph.D Vincenzo Vaiano
Prof. Luigi Rizzo
Prof. Paolo Ciambelli
Prof. Panagiotis Lianos

Ph.D. Course Coordinator
Prof. Ernesto Reverchon

Quando ti metterai in viaggio per Itaca
devi augurarti che la strada sia lunga,
fertile in avventure e in esperienze.
I Lestrigoni e i Ciclopi
o la furia di Nettuno non temere,
non sarà questo il genere di incontri
se il pensiero resta alto e un sentimento
fermo guida il tuo spirito e il tuo corpo.
In Ciclopi e Lestrigoni, no certo,
nè nell'irato Nettuno incapperai
se non li porti dentro
se l'anima non te li mette contro.

Devi augurarti che la strada sia lunga.
Che i mattini d'estate siano tanti
quando nei porti - finalmente e con che gioia -
toccherai terra tu per la prima volta:
negli empori fenici indugia e acquista
madreperle coralli ebano e ambre
tutta merce fina, anche profumi
penetranti d'ogni sorta; più profumi inebrianti che puoi,
va in molte città egizie
impara una quantità di cose dai dotti.

Sempre devi avere in mente Itaca -
raggiungerla sia il pensiero costante.
Soprattutto, non affrettare il viaggio;
fa che duri a lungo, per anni, e che da vecchio
metta piede sull'isola, tu, ricco
dei tesori accumulati per strada
senza aspettarti ricchezze da Itaca.
Itaca ti ha dato il bel viaggio,
senza di lei mai ti saresti messo
sulla strada: che cos'altro ti aspetti?

E se la trovi povera, non per questo Itaca ti avrà deluso.
Fatto ormai savio, con tutta la tua esperienza addosso
già tu avrai capito ciò che Itaca vuole significare.

Constantino Kavafis
(poeta e giornalista greco)

“Sii meno curioso della gente e più curioso delle idee.”

Marie Curie

(premio Nobel per la Fisica 1903, premio Nobel per la Chimica 1911, per gli studi sulle radiazioni e per aver scoperto il radio e il polonio. Unica donna ad aver vinto più di un premio Nobel, unica ad averlo vinto in due aree distinte)

“La struttura alare del calabrone, in relazione al suo peso, non è adatta al volo, ma lui non lo sa e vola lo stesso.”

Albert Einstein

(premio Nobel per la Fisica 1931, “per i contributi alla fisica teorica, in particolare per la scoperta della legge dell'effetto fotoelettrico..”)

Acknowledgments

Giunta al termine di questo bellissimo periodo che è stato il mio dottorato di ricerca, non posso fare a meno di fermarmi e ripensare a tutto ciò che ho vissuto, imparato, sognato e desiderato, e alle soddisfazioni vissute, ai sacrifici fatti. Tutto questo è stato accompagnato dalla presenza continua e costante di alcune persone che hanno segnato non solo questi tre anni ma tutta la mia vita. Io ho avuto un privilegio, una fortuna: essere circondata da persone che, ogni giorno, mi hanno dimostrato la loro stima, il loro affetto e rispetto, e tutto questo io lo tengo stretto, e sempre lo porterò con me come il dono più grande che abbia mai potuto ricevere.

Detto ciò, vorrei dire a queste persone quanto sono grata per la loro presenza. Senza di loro, questi tre anni non sarebbero stati cosi intensi e belli.

Il primo grazie va alla mia famiglia. Questa volta è diverso, non è come per la laurea, perché con il dottorato ha vissuto con me il primo vero passo verso la mia crescita professionale. Sono felice che siate tutti orgogliosi di me! Grazie a mamma, papà e Diletta, per gli abbracci, i sorrisi, gli incoraggiamenti, e per il calore che si respira in casa mia che tra alti e bassi non manca mai!

Grazie, a Domenico, per aver compreso quanto importante fosse per me questo lavoro, per aver capito la mia passione, per la presenza anche quando ero in Grecia, e per avermi spronata ad essere forte e ad essere felice.

Per aver avuto la possibilità di fare il dottorato e per avermi proposto questa bellissima opportunità vorrei ringraziare la mia relatrice, la Prof. Diana Sannino. Grazie per i consigli dispensati durante questi anni. Inoltre, vorrei ringraziare ancora il Prof. Luigi Rizzo, che dopo la tesi di laurea magistrale ha seguito il mio lavoro di dottorato, attraverso le pubblicazioni fatte, e per i preziosi contatti procurati con il dipartimento di Farmacia, fonte di importanti sviluppi per la mia ricerca. Vorrei inoltre ringraziare il Prof. Paolo Ciambelli, in qualità di componente del comitato scientifico del mio dottorato, per suoi consigli e le sue critiche costruttive. Ringrazio il Prof. Panagiotis Lianos, per avermi ospitata per tre mesi nel suo laboratorio dell'Università di Patrasso, dandomi la possibilità di fare nuovi esperimenti e studiare nuove tecniche per la mia ricerca.

Come dicevo, questi tre anni sono stati segnati dalla presenza di persone che ho conosciuto proprio iniziando questo percorso, e che sono diventate amicizie importati che porterò per sempre con me. E innanzitutto voglio ringraziare la persona che in laboratorio è stata indispensabile per la mia crescita, e che, oltre un collega e un tutor, è diventato un vero amico, Vincenzo Vaiano. Grazie per avermi insegnato tutto in questi tre anni, grazie

per non esserti mai risparmiato quando ero in difficoltà ed avevo bisogno di aiuto per comprendere meglio il mio lavoro, grazie per aver creduto nelle mie capacità. Ti ringrazio per essere stato sempre presente, seguendo ogni passo della mia ricerca (della nostra ricerca) e per avermi insegnato con passione questo lavoro. Grazie per la pazienza, anche durante il mio periodo all'estero, per le risate, le chiacchierate, le discussioni, i pranzi e le cene insieme. Grazie per la nostra amicizia.

La fortuna che ho avuto, che auguro a tutti, è quella di aver lavorato in un ambiente sereno, dove i sorrisi non mancano mai, dove ci si aiuta a vicenda, dove c'è ambizione ma non competizione, dove ognuno gioisce dei successi degli altri. E questo, credo che sia per la maggior parte merito di una persona che voglio ringraziare immensamente, Vincenzo Palma. Professore ma, prima di tutto, un uomo che mette al primo posto il rispetto verso gli altri. Sempre entusiasta, appassionato del suo lavoro, coinvolgente, e mai presuntuoso. Voglio ringraziarlo per essere stato per me un punto di riferimento, per avermi insegnato che le difficoltà vanno affrontate senza timore, trasformando le mie paure in coraggio. Grazie per il buon umore che mi ha sempre trasmesso in laboratorio quando arrivava la mattina, per i "buongiorno" detti a voce alta, per i caffè, per i sorrisi e per i mille consigli! Grazie per la consapevolezza che mi ha dato, su tutto.

Grazie ai miei amici e colleghi di laboratorio Concetta, Daniela, Marco, Eugenio, Antonio, Marta e Livia per tutti i bellissimi momenti passati insieme, in lab T1 e durante i convegni, per le gioie condivise e per essere le persone che sono, gentili e con un grande cuore. Grazie ad Olga e Giuseppe, che hanno condiviso con me la maggior parte del tempo in lab T3, per la loro presenza, anche da lontano, e per il bellissimo rapporto che abbiamo creato.

Grazie ad una persona che è entrata in punta di piedi nel mio cuore e che si è dimostrata una grande donna: Mariantonietta. Fin da subito si è creato un bellissimo rapporto tra noi, fatto di stima e complicità. Sono felice di averti conosciuta e di essere tua amica.

Grazie ai tesisti che ho avuto il privilegio di seguire: Stefano, Rosalba, Marina e Antonio. Ragazzi volenterosi, con cui è stato un piacere lavorare!

E poi, grazie ancora alle mie amiche di sempre, in particolare Anna ed Emanuela, soprattutto per le coccole e i momenti di relax post lavoro!

Grazie a Rossella e Roberta, con le quali ho iniziato Ingegneria, e con le quali, nonostante i percorsi lavorativi diversi, posso condividere la gioia del mio titolo di dottore di ricerca.

Grazie immensamente a tutti voi.

Giusy

Publications list

1. Iervolino, G., Vaiano, V. , Sannino, D., Rizzo, L., Palma, V. Enhanced photocatalytic hydrogen production from glucose aqueous matrices on Ru-doped LaFeO3, Applied Catalysis B: Environmental Volume 207, 15 June 2017, Pages 182-194

2. Iervolino, G., Tantis, I., Sygellou, L., Vaiano, V. , Sannino, D., Lianos, P., Photocurrent increase by metal modification of Fe_2O_3 photoanodes and its effect on photoelectrocatalytic hydrogen production by degradation of organic substances, Applied Surface Science 400 (2017), Pages 176-183.

3. Vaiano, V., Iervolino, G., Sannino, D., Murcia, J.J., Hidalgo, M.C., Ciambelli, P., Navío, J.A., Photocatalytic removal of patent blue V dye on Au-TiO2 and Pt-TiO2 catalysts, Applied Catalysis B: Environmental 188, (2016), Pages 134-146.

4. G. Iervolino, V. Vaiano, J.J. Murcia, L. Rizzo, G. Ventre, G. Pepe, P. Campiglia, M.C. Hidalgo, J.A. Navío, D. Sannino, Photocatalytic hydrogen production from degradation of glucose over fluorinated and platinized TiO_2 catalysts, Journal of Catalysis 339 (2016) 47-56.

5. G. Iervolino, V. Vaiano, L. Rizzo, G. Sarno, A. Farina, D. Sannino, Removal of arsenic from drinking water by photo-catalytic oxidation on MoO_X/TiO2 and adsorption on γ-Al_2O_3, Journal of Chemical Technology and Biotechnology 91 (2016) 88-95.

6. G. Iervolino, V. Vaiano, D. Sannino, L. Rizzo, P. Ciambelli, Photocatalytic conversion of glucose to H2 over LaFeO3 perovskite nanoparticles, Chemical Engineering Transactions, 2016, pp. 283-288.

7. G. Iervolino, V. Vaiano, D. Sannino, L. Rizzo, P. Ciambelli, Production of hydrogen from glucose by $LaFeO_3$ based photocatalytic process during water treatment, International Journal of Hydrogen Energy 41 (2016) 959-966

8. G. Iervolino, V. Vaiano, D. Sannino, L. Rizzo, G. Sarno, P. Ciambelli, L.A. Isupova, Influence of operating conditions in the photo-fenton removal of tartrazine on structured catalysts, Chemical Engineering Transactions, 2015, pp. 979-984.

9. V. Vaiano, G. Iervolino, D. Sannino, J.J. Murcia, M.C. Hidalgo, P. Ciambelli, J.A. Navío, Photocatalytic removal of patent blue V dye on Au-TiO_2 and Pt-TiO_2 catalysts, Applied Catalysis B: Environmental 188 (2016) 134-146.

10. V. Vaiano, G. Iervolino, D. Sannino, L. Rizzo, G. Sarno, MoO_x/TiO_2 immobilized on quartz support as structured catalyst for the photocatalytic oxidation of As(III) to As(V) in aqueous solutions, Chemical Engineering Research and Design 109 (2016) 190-199.

11. V. Vaiano, G. Iervolino, D. Sannino, L. Rizzo, G. Sarno, P. Ciambelli, L.A. Isupova, Food Azo-Dyes Removal from Water by Heterogeneous Photo-Fenton with $LaFeO_3$ Supported on Honeycomb Corundum Monoliths, Journal of Environmental Engineering (United States) 141 (2015).

12. V. Vaiano, G. Iervolino, D. Sannino, L. Rizzo, G. Sarno, A. Farina, Enhanced photocatalytic oxidation of arsenite to arsenate in water solutions by a new catalyst based on MoO_x supported on TiO_2, Applied Catalysis B: Environmental 160-161 (2014) 247-253.

13. V. Vaiano, G. Iervolino, G. Sarno, D. Sannino, L. Rizzo, J.J. Murcia Mesa, M.C. Hidalgo, J.A. Navío, Simultaneous production of CH4 and H_2 from photocatalytic reforming of glucose aqueous solution on sulfated Pd-TiO_2 catalysts, Oil and Gas Science and Technology 70 (2015) 891-902.

14. V. Vaiano, O. Sacco, G. Iervolino, D. Sannino, P. Ciambelli, R. Liguori, E. Bezzeccheri, A. Rubino, Enhanced visible light photocatalytic activity by up-conversion phosphors modified N-doped TiO_2, Applied Catalysis B: Environmental 176-177 (2015) 594-600.

Contents

Abstract

The research of new eco-friendly technologies that enable the production of energy is nowadays one of the topics of greatest interest to the scientific community. The population has chosen to break free from the use of fossil fuels, and this leads to the study and development of processes for the production of clean energy starting from biomass. However, at the same time, the concern of the industry is also the disposal and treatment of wastewater.

Starting from these considerations, it is advisable to develop processes that, under mild conditions, allow to obtain interesting hydrogen or methane yields. This objective could be achieved through the use advanced oxidation processes (AOPs), such as heterogeneous photocatalysis, photo-Fenton like reaction and photoelectrocatalysis.

So, an interesting approach is to explore, in parallel to wastewater treatment, the possibility to produce also an energy source such as hydrogen and/or methane from the degradation of organic substance present in wastewater by AOPs.

Considering the characteristic of food industries wastewaters, it is interesting to evaluate the performances of advanced oxidation processes for their treatment aimed to the valorization, through the conversion of specific substances (sugars), in order to obtain compounds with high energetic value, but also for removing substances hardly biodegradable (such as food dyes) that could be present in these industry wastewaters.

In this PhD thesis it has been studied the performances of the photocatalytic process for the hydrogen production from food industries wastewaters. In particular, starting from synthetic solution containing glucose, it was evaluated the effect of the presence of noble metals on the semiconductor surface and the effect of the photoactive support (TiO_2).

Subsequently, providing for the application of heterogeneous photocatalysis to industrial level, the study has been directed to the formulation of a noble metal free photocatalyst with good performances in the production of hydrogen and in the degradation of the sugars present in the solutions. The final formulation was represented by $LaFeO_3$ (a perovskite with semiconducting properties) prepared by combustion flame method. To improve the performances under visible light, $LaFeO_3$ was modified with Ru (Ru-$LaFeO_3$), whose cost is much lower than those of Pd, Pt or Au.

Always perspective of the application of the process to industrial level, it was developed a structured photocatalyst for solving the problems related to the photocatalyst separation after the treatment. In particular it was studied the efficiency of magnetic Fe_2O_3 as support for Ru-$LaFeO_3$.
It was also investigated the photoelectrocatalytic process for the hydrogen production, considering the general aspects of the process, the advantages and in particular the attention has been focused on the electrodeposition process for the synthesis of Fe_2O_3 based photoanodes.
Finally, the aim has been the application of the photocatalytic process on a real wastewater coming from the washing process of the fruit (especially cherries).
It was not underestimated the presence of food dyes in these types of wastewater. For this reason it was evaluated the efficiency of photo-Fenton process in the removal of several food dyes (such as Red Allura and Tartrazine) using $LaFeO_3$ deposited on corundum monoliths.
In addition, it has been evaluated the possibility to couple the photocatalytic process (used for the valorization of the wastewater through the production of hydrogen) to the optimized photo-Fenton system to completely remove the not-biodegradable substances still present in the wastewaters recovered after the photocatalytic treatment using Ru-$LaFeO_3$ supported on magnetic Fe_2O_3 particles.

I Introduction

Nowadays, the limited availability of fossil fuels, the air and water pollution and the global warming arising from their own use, are a problem that affects more and more the world's population. In order to free himself from the use of fossil fuels and therefore from their negative consequences on the environment, the scientific community has moved its interest in the development of new technologies for the production of new energy carriers (such as hydrogen or methane) which are primarily derived from renewable sources (sunlight, water and biomass). This need is clearly delineated by the various international agreements established in the recent past, since the Kyoto Protocol drawn up in December 1997 up to the agreement dated 19/10/2006 (IP / 06/1434) in which the member countries EU undertake to achieve three major objectives by 2020:

- 20% reduction of greenhouse gas emissions;
- Achieving a 20% share of energy from renewable sources in total energy consumption;
- 20% improvement in energy efficiency.

The recent Paris Agreement of December 2015 aims to consolidate globally as enshrined in the earlier, aiming to limit the temperature rise in the coming decades than 2°C.

Considering these objectives, sunlight is one of the most interesting renewable energy sources for the near future. Moreover a growing interest concerns the hydrogen that is considered a clean carrier energy. In fact, the chemical energy stored in the H-H bond formation is released when it reacts with oxygen, yielding only innocuous water as a product, in a highly exothermic reaction (Chiarello and Selli, 2014):

$$H_2 + \frac{1}{2} O_2 \rightarrow H_2O \qquad \text{(I.1)}$$

$$\Delta Gr^{\circ} = 273kJ \cdot mol^{-1} \quad \text{(I.2)}$$

However, to date, hydrogen is mainly used for the synthesis of methanol, in refineries, or in the catalytic hydrogenation of some organic compounds, and in ammonia synthesis for the production of fertilizers.

The hydrogen production remains a major problem. Most hydrogen produced today is obtained through steam reforming of hydrocarbons, a mature production process in which high-temperature steam (700°C–1000°C) is used to produce hydrogen from a methane source, such as natural gas. In steam-methane reforming, methane reacts with steam under 10–40 bar pressure over nickel-based catalysts to produce hydrogen, carbon monoxide, and a relatively small amount of carbon dioxide. Steam reforming is endothermic and therefore heat must be supplied to the process for the reaction to proceed.

The steam-methane reforming reaction is:

$$CH_4 + H_2O = CO + 3H_2 \quad \text{(I.3)}$$

$$\Delta Hr^{\circ} = 205kJ \cdot mol^{-1} \quad \text{(I.4)}$$

Subsequently, through the "water-gas shift reaction", the carbon monoxide and steam are reacted using a catalyst to produce carbon dioxide and more hydrogen. In a final process step called "pressure-swing adsorption," carbon dioxide and other impurities are removed from the gas stream, leaving essentially pure hydrogen. Steam reforming can also be used to produce hydrogen from other fuels, such as ethanol (Palma et al., 2015), or propane (Matsuka et al., 2014).

The water-gas shift reaction is:

$$CO + H_2O = CO_2 + H_2 \quad \text{(I.5)}$$

$$\Delta Hr^{\circ} = -42kJ \cdot mol^{-1} \quad \text{(I.6)}$$

Because of the endothermic nature of the steam reforming reaction, heat must be supplied for the reaction to proceed and this is usually provided by the combustion of part of the feedstock, with a consequent decrease of the net yield of the process (Chiarello and Selli, 2014).

Another process utilized for the hydrogen production is partial oxidation. In the partial oxidation, the methane and other hydrocarbons in natural gas react with a limited amount of oxygen (typically from air) that is not enough to completely oxidize the hydrocarbons to carbon dioxide and water. With less than the stoichiometric amount of oxygen available, the reaction products contain primarily hydrogen and carbon monoxide (and nitrogen, if

the reaction is carried out with air rather than pure oxygen), and a relatively small amount of carbon dioxide and other compounds. Subsequently, through the water-gas shift reaction, the carbon monoxide reacts with water to form carbon dioxide and more hydrogen.

Partial oxidation of methane reaction is:

$$CH_4 + \frac{1}{2} O_2 \rightarrow CO + 2H_2 (+ \text{heat}) \quad \text{(I.7)}$$

Over these processes nowadays used industrially for the production of hydrogen, there are also other technologies always based on the use of biomass from which it is possible to obtain H_2. For example the hydrogen production from "wet waste" or from industrial wastewater of food processes through anaerobic bioreactors which exploit the phenomena of fermentation.

In particular the anaerobic digestion is a widely used technology for the sustainable management of bio-waste (Hartmann and Ahring, 2005);(Lema and Omil, 2001) allowing the recovery of energy through the production of fuel gas and reducing the negative environmental impact.

The main products of this process are biogas and a solid residue (biomass) rich in nutrients and soil improvers with good properties, suitable for the controlled re-use in agriculture, thanks to which it is possible to achieve the recovery of nutrients (Edelmann et al., 2000) and a volume reduction of any waste in the process, reducing the final disposal costs.

With regard to the specific treatment of wastewater, the anaerobic digestion is a treatment technology of organic wastewater with high COD (Chemical Oxygen Demand) based on fermentation under oxygen deficiency in an anaerobic digester.

Anaerobic microbiological decomposition is a process in which micro-organisms derive energy and grow by metabolizing organic material in an oxygen-free environment resulting in the production of methane. In particular for the wastewater treatment the anaerobic digestion process can be subdivided into the following four phases, each requiring its own characteristic group of micro-organisms:

• Hydrolysis: conversion of non-soluble biopolymers to soluble organic compounds;

• Acidogenesis: conversion of soluble organic compounds to volatile fatty acids (VFA) and CO_2;

• Acetogenesis: conversion of volatile fatty acids to acetate and H_2;

• Methanogenesis: conversion of acetate and CO_2 plus H_2 to methane gas.

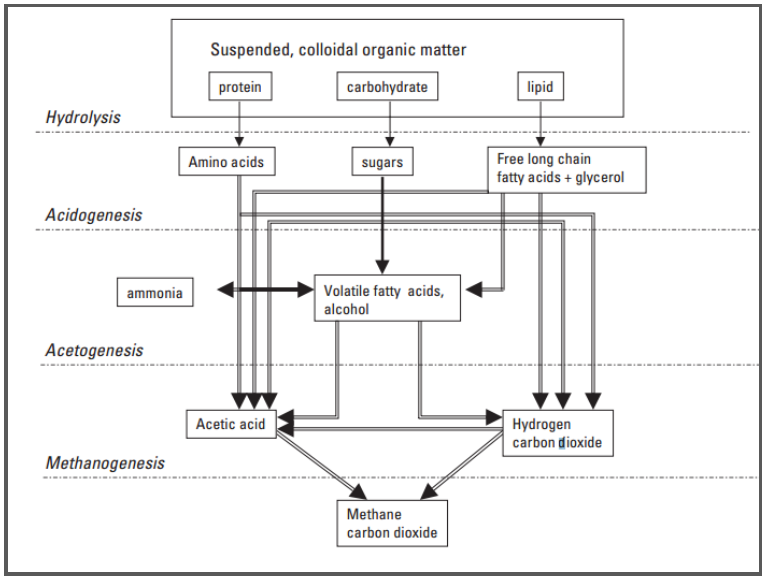

Figura I.1 *Simplified schematic representation of the anaerobic degradation process for wastewaters(Lettinga et al., 1999).*

This process is strongly influenced by environmental factors and in particular temperature, pH, alkalinity and toxicity are primary control factors. Depending on the temperature, the anaerobic digestion is divided into psychrophilic (10-20 ºC), mesophilic (20-40 ºC) or thermophilic (50-60 ºC) digestion. Psychrophilic digestion requires a long retention time, resulting in large reactor volumes, because bacterial growth and conversion processes are slow under low temperature conditions.

Thermophilic digestion is especially suited when the wastewater is discharged at a high temperature or when pathogen removal is an important issue. During thermophilic treatment high loading rates can be applied. It is important to note that with this process the rate of methane production increases with increasing temperature until a relative maximum is reached at 35 to 37° C (Lettinga, 1981). The temperature is further defined according to the value of the ratio between the energy requirements and the biogas yield. The maximum metabolizing activity occurs at higher temperatures and in particular the thermophilic bacteria replace the mesophilic bacteria and the maximum yield occurs at 55°C or higher. pH is another parameter that affects the process yield, in particular it is important for the methanogenesis step. In fact the methanogenesis only proceeds when the pH is neutral. For pH values outside the range 6.5 - 7.5, the rate of methane production is lower(Lettinga, 1981).

During this step it must be very alert to the presence of several compounds which can exhibit a toxic effect at excessive concentrations and, which adversely affect methanogenesis such as Volatile Fatty Acids (VFA), NH_3, cations such as Na^+, K^+ and Ca^{++}, heavy metals sulphide and xenobiotics.

Unlike aerobic wastewater treatment systems, the loading rate of anaerobic reactors is not limited by the supply of a reagent, but by the processing capacity of the microorganisms. Therefore, it is important that a sufficiently large bacterial mass is retained in the reactor. For low rate systems the latter is achieved by applying a sufficiently long retention time. For high rate systems the retention of biomass is increased in comparison with the retention of the liquid. There are essential operational conditions for high rate anaerobic reactors are, for example:

- A high concentration of anaerobic bacterial sludge must be retained under high organic (>10 $kg/m^3/day$) and high hydraulic (>10 $m^3/m^3/day$) loading conditions.
- Maximum contact must occur between the incoming feedstock and the bacterial mass.
- Also minimal transport problems should be experienced with respect to substrate compounds, intermediate and end products.

So, according to the technology, the anaerobic digestion systems is divided in “low rate” systems, in which long hydraulic retention times are applied, and “high rate” systems, in which hydraulic retention time is relatively short. Low rate systems are mainly used for waste streams such as slurries and solid waste, which require a long time for sufficient anaerobic degradation. High rate systems are mainly used for wastewater. In particular for wastewater treatment, the development of new treatment technologies which allow the valorization of wastewater and recovering materials and energy while keeping excellent depurative performance, is now of great interest. The aim is to contain the management costs obtaining “clean” energy from the depuration process, and restrict the disposal of final products of the treatment. In the context the valorization of wastewater (and in particular “food industries” wastewater) one of the most used processes is undoubtedly the anaerobic digestion with the high rate systems. In fact the High Rate Anaerobic Treatment systems like the UASB (Upflow Anaerobic Sludge Bed) reactor, Anaerobic Filter and the Contact Process, are unfit for the digestion of concentrated slurries but suitable for diluted and concentrated wastewater and can be part of a multi-stage system.

High rate systems are most suitable for waste streams with a low suspended solids content. Different types, used world-wide for the treatment of wastewater are (Lettinga et al., 1999) (Alexiou and Mara, 2003)

- Contact process; Biobulk-system by Biothane (Frankin, 2001);
- Upflow Anaerobic Sludge Bed (UASB);
- Anaerobic Fixed Film Reactor (AFFR);
- Fixed film Fluidised Bed system;
- Expanded Granular Sludge Bed (EGSB);
- Hybrid systems;
- Anaerobic Filter (AF).

In particular the Upflow Anaerobic Sludge Bed (UASB) configuration is frequently used in the treatment of wastewater with high organic content. This technology was developed in the late 1960's at Wageningen University in The Netherlands. The Dutch beet sugar firm, CSM, developed the basic technology for wastewater treatment in several sugar factories. The advantages of the UASB technology are:

- low energy and plant costs compared to conventional biological systems (no need to give oxygen);
- ability to break down extremely high organic loads (higher initial COD of 100-150,000 ppm);
- Almost complete transformation of sludge into biogas which can be used as biofuel. It is estimated usually a sludge production of 0.03 kg TSS/kg COD input.

Industrial wastewater is heterogeneous, both in composition and volume. Effluents from the Food & Beverage (F&B) industry contain the highest concentration of organic compounds which could be valorised (Lexmond and Zeeman, 1995). In particular the UASB system is widely used today for the treatment of wastewater from different food industries, such as breweries, distilleries, slaughterhouses, dairy production, yeast, fruit juices, fish-processing, sweets and sugar, flour, coffee processing, edible oil, chocolate and other products (Borzacconi et al., 1995). If the wastewater does not contain a large percentage of suspended solids, a high rate system is usually applied.

Generally, all stages of anaerobic digestion in the wastewater treatment can take place in a single volume. In this case the systems are called "*single*

stage". These anaerobic biological reactors are the most used for the degradation of the organic substrate and for the production of methane, convertible to thermal energy and electricity. An alternative to this technology is to conduct four metabolic steps in two different reactors. In this case it is called "*multi-stage"* systems: the hydrolytic and acidogenic stages take place separately from the methanogenic phase. In this way it is possible to exploit the potential of the acidogenic phase also to get a good production of H_2.

Hydrogen is a gas with excellent energy properties whose use does not cause adverse environmental impacts.

Batch test for the biohydrogen production in optimal operating conditions (pH, temperature, bacterial load) have been conducted to assess the productivity of biogas from biomass from farms in the Lombardy Region (Italy) in a "multi stage" system. In Table I.1 it is reported the hydrogen production from several kind of biomass (Manzini et al., 2015).

Table I.1 *Hydrogen production from biomass using "multi stage" system in anaerobic digestion (Manzini et al., 2015).*

SAMPLE	H_2 [L/Kg SS]
Corn silage	105.7
Blueberry extract	123
Beet pulp	69.9
Dried pomace	12.7
Rice flour	96.6
Olive pomace	48.7
Ryegrass	11
Glucose	240

For almost all the treated biomass, biogas yields obtained are higher than those obtained in the single-stage anaerobic process.

As regards the reuse of final waste and of intermediate products from the treatment of food wastewater, there are several applications for the valorization of the residue of anaerobic digestion (digestate) as fertilizer. Furthermore the digestate is a product that allows the closure of the carbon cycle and of nutrients, the process at the base of sustainable agriculture(Borken and Matzner, 2004).

Although anaerobic digestion represents one of the most common processes for the treatment and valorization of food industries wastewater, it has some disadvantages.

The disadvantages are summarized below(Lettinga et al., 1999); (Tafdrup, 1995):

- The high sensitivity of methanogenic bacteria to a large number of chemical compounds;
- The first start-up of an installation without the presence of proper seed sludge can be time consuming due to the low growth yield of anaerobic bacteria;
- When treating wastewater containing sulphurous compounds, the anaerobic treatment can be accompanied by odour due to the formation of sulphide. An effective solution to this problem is to employ a micro-aerophilic post-treatment step, to convert sulphide to elemental sulphur;
- The process is strongly temperature dependent, and it works efficiently only at pH close to neutrality;
- It requires a long period of acclimatization of the bacteria;
- It produces sludge for disposal;
- The reduction of pollutants is not to allow the direct discharge of water: the UASB usually takes a final stage of biological purification;
- Energy prices and access to energy markets;
- Poor data on economics;
- Low energy yield.

In order to study and implement a process that allows the valorization of food industry wastewater, in particular obtaining H_2 from organic substance present in wastewater, an interesting alternative to the conventional anaerobic digestion is represented by the Advanced Oxidation Processes (AOPs). Several excellent reviews were recently published, providing an exhaustive description of the fundamentals of photocatalysis and its application to hydrogen production (Bolton, 1996, Nakata and Fujishima, 2012, Matsuoka et al., 2007).

Typically, AOPs, such as heterogeneous photocatalysis, are studied with the aim of removing organic pollutants from wastewater through oxidation reactions which can finally result in the production of CO_2 and H_2O.

An interesting approach is to explore, in parallel to wastewater treatment, opportunities of mass recovery which can be sold as secondary raw material or used as energy resources, such as hydrogen and methane.

In particular some industry wastewaters from food processes contain high concentration of sugars, particularly glucose, which should be removed before effluent disposal or reuse, but if properly treated hydrogen could be produced. In fact, in the past two decades, photocatalytic processes have been investigated as possible method to obtain hydrogen from glucose aqueous solutions (Bellardita et al., 2016, Liang et al., 2016). The photocatalytic hydrogen production by decomposition of water containing glucose, or other sugars, seems to become very powerful method for the practical and low cost technologies in the hydrogen–based energy system.

So, considering the characteristic of food industries wastewaters, it is interesting to evaluate the performances of advanced oxidation processes (in particular photo Fenton, photocatalysis and photoelectrocatalysis) for the treatment of food industry wastewater, in particular for the valorization of the effluent, through the conversion of specific substances (sugars) contained in wastewater, in order to obtain compounds with high energetic value, such as hydrogen and methane, but also for remove completely substances hardly biodegradable (such as food dyes) that could be present in these industry wastewaters.

I.1 Advanced Oxidation Processes

All advanced oxidation processes (AOPs) are characterised by a common chemical feature: the capability of exploiting the high reactivity of OH· radicals in driving oxidation processes which are suitable for achieving the complete abatement and through mineralization of even less reactive pollutants (Andreozzi et al., 1999). OH radicals are extraordinarily reactive species and they attack the most part of organic molecules (Farhataziz and Ross, 1977). They are also characterised by a little selectivity of attack and they versatility is also strengthened by the fact that they offer several possible ways for the production of OH radicals thus allowing to better adapt to the requirements of the treatment. When AOPs are applied for wastewater treatment, these radicals, as a powerful oxidizing agent, are expected to sufficiently destruct wastewater pollutants, and transform them to less and even non-toxic products, thereby providing an ultimate solution for wastewater treatment (Huang et al., 1993). Hydroxyl radical is the most reactive oxidizing agent in water treatment, with an oxidation potential between 2.8 V (pH 0) and 1.95 V (pH 14) vs. SCE (saturated calomel electrode, the most commonly used reference electrode) (Iranpour et al.,

1999). Hydroxyl radicals attack organic pollutants through four basic pathways: radical addition, hydrogen abstraction, electron transfer, and radical combination. Their reactions with organic compounds produce carbon-centered radicals (R· or R·–OH). With O_2, these carbon-center radicals may be transformed to organic peroxyl radicals ($ROO^{\cdot}$). Among different available AOPs, those driven by light seem to be the most popular technologies for wastewater treatment as shown by the large amount of data available in the literature (Stasinakis, 2008). Solar AOPs are particularly attractive due to the abundance of solar light in regions where water scarcity is high and due to their relatively low costs and high efficiencies. It is possible to divide the different AOPs processes in two main categories: dark AOPs and light driven AOPs. They are listed in the following:

- Dark AOPs
    - Ozone (O_3)
    - Fenton ($Fe^{2+} + H_2O_2$)
    - Electrolysis (electrodes + current)
    - Sonolysis (Ultrasounds)

- Light driven AOPs
    - Photolysis ($UV + H_2O_2$)
    - Photocatalysis (light + catalyst)
    - Photo-Fenton (UV light + Fenton)

I.1.1 Photocatalysis: fundamental principles

Heterogeneous photocatalysis is based on the use of wide band-gap semiconductors. When these materials are illuminated with photons of energy "*hν"* higher than (or equal to) their band-gap EG ($h\nu \geq EG$), electrons and holes are generated as well as several subsequent reactions. An ideal catalyst should present chemical- and photo-stability, ability to adsorb reactants under efficient photonic activation, and preferentially should have a low cost and be easily available. TiO_2 has been the reference commercially available photocatalyst due to its relatively low toxicity, high photochemical stability, excellent activity, acceptable band gap energy and low cost.

(Hoffmann et al., 1995a). The first steps in this process are the absorption of the radiation and the photo-excitement of valence band electrons, resulting in electron–hole pairs eq. (8). Then, electrons and holes dissociate and migrate to the semiconductor surface. Holes generate reactive hydroxyl radicals eq. (9), or can also react directly with adsorbed species eq. (10), while electrons reduce dissolved oxygen leading to the production of superoxide radicals eq. (11) and later to hydroxyl radicals. All these radicals initiate multiple sequentially reactions.

$$TiO_2 + h\nu \rightarrow e^- + h^+ \quad \text{(I.8)}$$

$$TiO_2(h^+) + H_2O \rightarrow TiO_2 + HO\bullet + H^+ \quad \text{(I.9)}$$

$$TiO_2(h^+) + RXad \rightarrow TiO_2 + RXad\bullet^+ \quad \text{(I.10)}$$

$$TiO_2(e^-) + O_2 \rightarrow O_2\bullet^- \quad \text{(I.11)}$$

Some shortcomings of heterogeneous photocatalysis are the recombination of electron–hole pairs and that solar applications are frequently aimed but the overlapping between the absorption spectrum of TiO_2 and that of the solar irradiation reaching the Earth's surface only occurs in a small fraction of the UV range (Andreozzi et al., 1999). In fact, one of the main advantages of this process is the possibility to use the sunlight renewable energy to produce hydroxyl radicals (Gernjak et al., 2006). This approach has economic and sustainability advantages in comparison with processes involving ozone generation, lamps or electrodes, which require high energy costs (Martin et al., 1999). Another advantage is the possible disinfection of water contaminated with pathogenic microorganisms (McCullagh et al., 2007). Therefore, suppressing the recombination of photo-generated charge carriers, as well as the efficient utilization of visible light, are some of the main challenges to develop economically feasible photocatalytic processes. Various strategies have been developed to improve the photocatalytic performance of semiconductor materials, such as the addition of electron donors, metal ion or anion doping (Vaiano et al., 2015c), noble metal loading, dye sensitization and fabrication of composite semiconductors (Linsebigler et al., 1995).

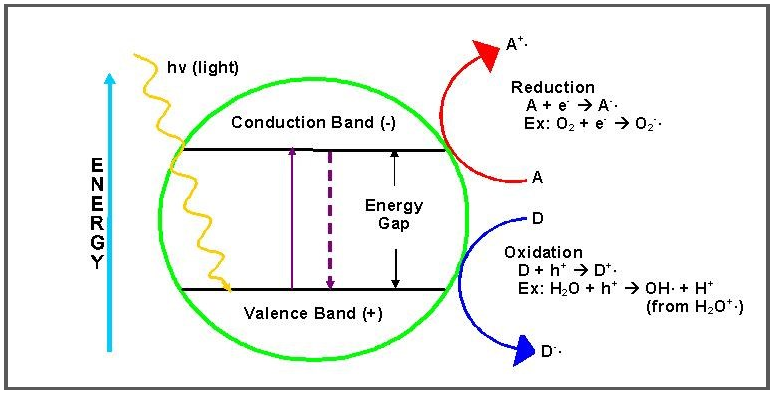

Figure I.2 *Mechanism of photocatalysis (Hoffmann et al., 1995a)*

The efficiency of a photocatalyst depends on the competition of different interface transfer processes involving electrons and holes and their deactivation by recombination (Fox and Dulay, 1993).The position of the flatband of a semiconductor in solution follows a Nernstian pH dependence, decreasing 59mV per pH unit (Ward et al., 1983), and consequently, the ability of electrons and holes to enact redox chemistry can be controlled by changes in the pH.

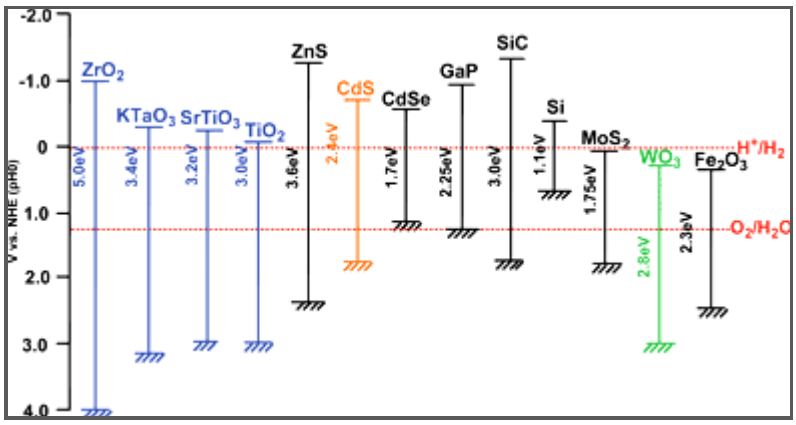

Figure I.3 *Relationship between band structure of semiconductor and redox potentials of water splitting* (Kudo and Miseki, 2009).

Fujishima and Honda described for the first time the photoelectrochemical decomposition of water under light radiation and without any applied electric current using TiO_2 (Fujishima and Honda, 1972a), but the particular interest of photocatalytic processes on

environmental applications only escalated when TiO_2 was used for oxidation of cyanide ion in aqueous solutions (Frank and Bard, 1977).

Since that time many scientists and researchers have employed their interest on the study of heterogeneous photocatalysis publishing a large number of works on photocatalytic water treatment and air and energy conversion.

Therefore, in general, the photocatalysis has been used with the aim to remove, from liquid or gaseous streams, the pollutants, and not-biodegradable compounds, which with the conventional processes are not removed. Through the photocatalysis, thanks to the presence of hydroxyl radicals, it is possible to obtain the complete mineralization of not biodegradable substances, managing to obtain as a final product the CO_2 and H_2O.

Beyond this objective that concerns the removal of pollutants, the photocatalysis was (and is till today) investigated as a process for the production of hydrogen. In fact, in recent years, there has been a growing interest in the development of new methods to generate H_2 from renewable and sustainable resources. Photocatalytic water splitting using solar energy for hydrogen production offers a promising option to produce hydrogen.

I.2 Hydrogen production by AOPs: photocatalysis and photoelectrocatalysis.

I.2.1 Photocatalytic hydrogen production: water splitting and photoreforming of organic substance.

Photocatalytic water splitting has been attracting significant interest in the recent literature because it uses two of the most abundant sources, clean, renewable and natural energy sources available to us. Photocatalytic hydrogen production, therefore, has been named as a potential solution to address excessive utilization, limited reserves and negative environmental impact issues related to fossil fuels (Jang et al., 2012). The prospective benefits of photocatalytic water splitting into hydrogen and oxygen can be listed as economic and environmental advantages because the process uses solar energy and produce hydrogen in a clean way with no GHG (Greenhouse Gas) emissions (Acar et al., 2016).

Photocatalytic reactions are usually classified into the following two categories: ‘‘down-hill’’ and ‘‘up-hill’’ reactions (Matsuoka et al., 2007).

In a down-hill reaction, the photon energy absorbed by a photocatalyst induces thermodynamically favoured reactions such as the complete oxidation of organic compounds into CO_2 and H_2O, accompanied by a large

negative change in the Gibbs free energy (ΔG<0). Such reactions have been practically applied for the degradation of toxic organic compounds in air or water with solid semiconducting photocatalysts such as TiO_2 (Fujishima and Zhang, 2006). On the other hand, one of the most significant ‘‘up-hill’’ reactions is the photosynthesis in plants. In this reaction, photon energy is converted into chemical energy and stored in the bonds of glucose, accompanied by a large positive change in the Gibbs free energy (ΔG > 0):

$$H_2O + CO_2 \rightarrow \tfrac{1}{6}(C_6H_{12}O_6) + O_2 \quad \Delta G=480 \text{ kJ/mol} \qquad (I.12)$$

One of the most promising of such ‘‘artificial photosynthesis’’ reaction is the photocatalytic splitting of water to produce H_2 and O_2 under solar light:

$$H_2O \rightarrow H_2 + \tfrac{1}{2}O_2 \qquad \Delta G= 237 \text{ kJ/mol} \qquad (I.13)$$

In particular, the electron acceptor species would be the H^+ ion, whereas water, or hydroxyl anions, would be the electron donor species, according to the following reactions:

$$TiO_2 + h\nu \rightarrow e_{CB}^- + h_{vb}^+ \qquad (I.14)$$

$$2H^+ + 2e_{CB}^- \rightarrow H_2 \qquad (I.15)$$

$$H_2O + 2h_{VB}^+ \rightarrow \tfrac{1}{2}O_2 + 2H^+ \qquad (I.16)$$

It is possible to observe that water splitting reaction proceeds on heterogeneous photocatalysts with semiconductor properties as shown in Figure I.4:

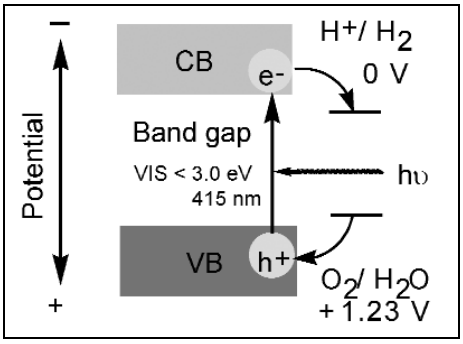

Figure I.4 *Principle of water splitting on semiconductor photocatalysts(Kudo and Miseki, 2009).*

The photogenerated electrons and holes cause redox reactions similarly to electrolysis. Water molecules are reduced by the electrons to form hydrogen and are oxidized by the holes to form oxygen for overall water splitting.

Water splitting using photocatalysts would seem to be simple and easy as shown in Figure. I.4.

However, it is a very tough reaction because of an up-hill reaction and the reactions easily carry back.

The band structure is merely a thermodynamic requirement, but not a sufficient condition. Some important factors are actually concerned with the photocatalytic properties such as bulk and surface properties, in particular: presence of co-catalysts (Pt, NiO, RuO_2), crystallinity, active site for chemical reaction, charge separation, photon, life time and mobility (Kudo and Miseki, 2009).

Titania (TiO_2) was the first material described as a photochemical water-splitting catalyst. It crystallizes in three structure types: Rutile, Anatase, and Brookite. All modifications contain TiO_6 octahedra that are interconnected via two (Rutile), three (Brookite), or four (Anatase) common edges and via shared corners, and as a result, the band gaps (3.0 eV for Rutile and 3.15 eV for Anatase) differ slightly (Rajeshwar et al., 2001).

Titanium dioxide has a good resistance to chemicals, corrosion and to reaction with water in the presence of light. This makes this semiconductor a good choice as a catalyst for the reactions aimed at the production of hydrogen. However, the photocatalytic H_2 production efficiency was affected by rapid recombination of photogenerated electrons and holes, fast backward reaction between hydrogen and oxygen, and large H_2 production over potential (Yu et al., 2011). Due to these reasons, low efficiency of hydrogen production occurs in bare TiO_2 (Gomathisankar et al., 2013b).

Various kinds of modifications, such as addition or deposition of metal ion and add of noble metals on catalyst surface, doping of cation or anion, dye sensitization, surface modification, and adding of sacrificial agents etc., enhance the photocatalytic activity (Gomathisankar et al., 2013b).

For example, in the case of metal deposition on the photocatalyst (TiO_2 or other) surface, the literature data reports an increase in the photocatalytic activity when a certain metal is deposited on the catalyst surface. It is generally due to the attraction of electrons to the metal particles on TiO_2, followed by a reduction in the recombination rate of electrons with holes (Ahmad et al., 2015). Many cases like this are reported in the literature.

In particular, among the noble metals, Ag-modified TiO_2 is studied for hydrogen production using low-energy UV lamps. Noble metal nanoparticles such as Pt, Au, Pd and Ag, deposited on the semiconductor surface can favor the separation of photoproduced electron-hole pairs (Kamat, 2002). The effectiveness in the photocatalytic performance of the noble metal co-catalysts can be related to their work function values ϕ, i.e. the energy required to promote an electron from the Fermi energy level into vacuum

(the higher is ϕ, the lower is the Fermi level energy). In fact, the greater is the difference between the metal work function and that of the TiO_2 support, the higher is the Schottky barrier (Kamat, 2002, Linsebigler et al., 1995), the electronic potential barrier generated by the band alignment at the metal semiconductor hetero-junction, with consequent increased efficiency of photogenerated electron transfer and trapping by the metal, ultimately leading to higher H_2 production rates (Chiarello and Selli, 2014).

Lalitha et al. (Lalitha et al., 2010) prepared Ag_2O/TiO_2 catalysts by impregnating Ag^+ ions on the surface layers of TiO_2. The authors concluded that the interacted Ag ions on the surface layers of TiO_2 play a vital role in maintaining hydrogen production activity under solar illumination. Wu and Lee (Wu and Lee, 2004) proved that the deposition of Pt-group metals, such as Ni, Pd and Pt, on TiO_2 has significantly improved the photocatalytic production of H_2 from either pure water or water with sacrificial reagent solutions. They also discovered that the deposition of Cu particles enhances the photocatalytic activity of TiO_2 in H_2 production from aqueous methanol solutions. Chiarello et al. (Chiarello et al., 2010) reported that the rate of hydrogen production on flame-made TiO_2 was higher than on unmodified TiO_2 P25 and that it was dramatically enhanced after noble metal deposition on the semiconductor oxide. Park et al. (Park et al., 2013a) reported that noble metals such as Au and Rh, and metal oxides such as Ni_2O_3 and CuO, can be utilized as photo-catalysts due to their unique plasmon absorption properties that can be used for visible light photo-catalysis.

To enhance the performance of the TiO_2 used in the water splitting reaction, over the use of noble metals, interesting results reported in the literature are relate to the surface modification of the TiO_2 particles with adsorbents (Ahmad et al., 2015).

This modification increases the efficiency of the photo-reduction process and to make the photoreduction of some metal ions possible. It is reported that non metallic inorganic anions, such as fluoride, phosphate and sulfate, might change the photocatalytic activity and mechanism by modifying the adsorption of substrates, surface acidity, surface charge, and surface functional groups (Park et al., 2013a). In particular, the surface-fluorinated TiO_2 (F-TiO_2) showed the great influences on the physicochemical and photocatalytic properties and increases the photo-generation of free hydroxyl radicals.

Other authors also suggested the use of some polymers as adsorbents such as polyaniline and polythiophene, which can enhance the absorption of visible light. Wang and Ku (Wang and Ku, 2007) reported that the surface charge of TiO_2 modified by Nafion layers greatly influences the electrostatic interaction between charged substrates and the photocatalyst surface.

Another interesting alternative is the use of organic dyes on the TiO_2 surface. This is a sensitization method for visible light-driven photo-electrochemical solar cells and water splitting. In fact, Le et al. (Le et al.,

2012) prepared Rh B (Rhodamine B) dye on the surface of Co/TiO_2 materials and observed a strong visible absorbance edge band in the range of 450–600 nm and a slightly lowered band gap of 2.58 eV compared to Co/TiO_2 (2.75 eV) and TiO_2 (3.21 eV), as well as better photocatalytic water splitting results.

In addition to TiO_2, other traditional metal oxides have also been widely studied considering their specific advantages. Among these are ZnO, α-Fe_2O_3 WO_3, and CuO. Copper oxide is one of the important p-type semiconductors with a narrow band gap of 1.4 eV. CuO is also used in solar cells due to its photoconductive and photochemical properties (Chang and Zeng, 2004) . However, it is reported that CuO was usually used only as a sensitizer of a composite photo-catalyst. This is because the photocatalytic activity achieved was not adequate when CuO alone was used as a photo-catalyst (Huang et al., 2006, Jin et al., 2007).

Another potential alternative is represented by metal sulfides, such as CdS, ZnS, normally considered potential candidates for visible-light-responsive photo-catalysis (Zhu and Zaech, 2009).

For example Ikeue et al.(Ikeue et al., 2012) reported that Pt-loaded CdS photo-catalyst has a high photocatalytic activity for H_2 generation. In their research they report that using Ag metal for the doping, acts as a co-catalyst and enhance the photocatalytic activity, achieving a higher rate of H_2 evolution. CdS is an interesting photocatalyst material, since it has a narrow band gap (2.4 eV) and a suitable conduction band potential to effectively reduce H^+ (Darwent and Porter, 1981, Sinha et al., 2001).

However, the photocatalytic properties of CdS are limited due to its photocorrosion under visible light irradiation (Meissner et al., 1988).

Although photocorrosion can be significantly reduced by adding sacrificial reagents, life cycle assessment studies associated with the processes of water splitting using Cd-based photocatalysts must be performed in order to evaluate the potential environmental impacts associated with Cd (Navarro et al., 2009).

Wu et al.(Wu et al., 2009) also reported that other metal sulfide photo-catalysts such as $CuInS_2$ and $AgInS_2$ can be used to produce H_2 and O_2 by water splitting under visible light irradiation from aqueous solutions.

It is important that a semiconductor that acts as a photocatalysts in the water splitting reaction should have a band gap close to 2 eV in order to account, in addition to the thermodynamic decomposition potential, for overpotential and Ohmic drop losses (Rajeshwar, 2007). The right semiconductor would not only have a suitable band gap, but also VB and CB energy levels matching the potentials of reactions (I.15) and (I.16), i.e. the CB edge energy should be more negative than the potential of the H^+/H_2 couple and the VB edge energy should be more positive than the O_2 evolution potential, on the electrochemical scale. For example, for TiO_2 in the anatase form, $\Delta_{EB} = 3.2$ eV, whereas for TiO_2 in the rutile form $\Delta_{EB} = 3.0$

eV, i.e. TiO_2 absorbs light only below 400 nm. This limits the photoactivity of such materials only to UV light irradiation, so that they are able to use only a small portion (ca. 4 %) of the solar spectrum. This represents one of the major limitations to the practical application of photocatalysis as a tool for solar light harvesting. Moreover, as mentioned before, other semiconductors, such as ZnO and CdS, are also possible candidates as photocatalysts for hydrogen production from water, in consideration of their narrower band gap compared to TiO_2. However, many of these materials have received less attention because, under illumination in contact with water, they can undergo photocorrosion (e.g. Zn^{2+} or Cd^{2+} dissolution) (Chiarello and Selli, 2014). On the other hand, more stable semiconductors, such as TiO_2, WO_3, Fe_2O_3 and MoS_2, have a conduction band potential ECB close or even slightly lower than that required to evolve H_2. This problem can be partially circumvented by applying a chemical or electrical bias in a two electrodes cell (such as the above mentioned PEC cell).

Interesting semiconductors used in the photocatalytic processes are also the perovskites.

Perovskite type photocatalysts are quite encouraging materials for water splitting owing to their stability in water. Their structures offer abundant scope in designing novel compounds based on A and B site occupancy, which gives rise to a wide range of materials systems with unique properties. Generally, in this crystal structure, the A site is occupied by the larger cation, while the B site is occupied by the smaller cation.

A large number of perovskite-based compounds have been studied for different photocatalytic application, in particular under visible light.

In fact, among these compounds, photocatalysts with pristine band gaps in the visible region such as $LaFeO_3$, $PrFeO_3$, $NaBiO_3$, and $AgBiO_3$ show promising photocatalytic performance under visible radiation (>400 nm).

Calcium titanate ($CaTiO_3$) is one of the common perovskite with a band gap of 3.6 eV. Cu doping in $CaTiO_3$ is widely studied and visible light-driven photocatalytic water decomposition has been reported (Zhang et al., 2010). Cu doping not only induces visible light absorption, but also enhances hydrogen evolution under UV radiation when NiOx co-catalyst is used (Kanhere and Chen, 2014).

$PrFeO_3$ was evaluated for hydrogen evolution reaction from ethanol-water mixture and showed a yield of 2847 $\mu mol \cdot g^{-1} \cdot h^{-1}$ under 200W tungsten lamp irradiation (Tijare et al., 2014). In literature it is reported the activity of the perovskite $GaFeO_3$ in the water splitting reaction without the use of cocatalysts, under visible light ($\lambda >$ 395 nm) (Dhanasekaran and Gupta, 2012). The authors also reported a yield of 0.10 and 0.04 $\mu mol \cdot h^{-1}$ under a 450 nm band pass filter. In this case, it is worth noting that the catalytic activity decreased due to deactivation of the catalyst.

$LaFeO_3$ (Eg 2.1 eV) has been explored for the hydrogen evolution under visible light. $LaFeO_3$ loaded with Pt co-catalyst showed high yield of

hydrogen evolution (3.315 μmol·h^{-1}·g^{-1}, in the presence of ethanol) under 400 W tungsten light source (Tijare et al., 2010). Another study on this phase demonstrates high yield of H_2 and O_2 (1290 μmol and 640 μmol after three hours, respectively), without any co-catalyst loading (Parida et al., 2010). It is worth quoting in Table I.2 a list of perovskites reported in the literature (with or without the presence of co-catalysts) used for the photocatalytic production of hydrogen. The table includes the chemical composition of the perovskite, the light source used and the possible presence of organic substances in solution used as sacrificial agents (s.a.).

Table I.2 *Collection of bibliographic data on the photocatalytic hydrogen production: different operating condiction (Kanhere and Chen, 2014).*

Material System	Irradiation (nm)	Performance	Experimental Details
1% Rh doped $SrTiO_3$ (0.5% Pt)	480-800	H_2 at 48 μmol·h^{-1} (s.a)	20% methanol, 50 mg in 50 mL of solution
Rh: $SrTiO_3$: $BiVO_4$	>420	H_2 at 128 μmol·h^{-1}	4.2% Efficiency, 50 mg 120 mL ($FeCl_3$ shuttle)
Cr-Sb co-doped $SrTiO_3$,(0.3% Pt)	>420	H_2 at 78 0.9 μmol·h^{-1} with sacrificial agents	in aqueous methanol and $AgNO_3$ solution
$MCo_{1/3}Nb_{2/3}O_3$ (0.2% Pt)	>420	H_2 at 1.4 μmol·h^{-1} (s.a)	500 mg catalyst in 50 mL methanol, 220 mL water,
Sr1-xNbO_3 (1% Pt)	>420	H_2 at 44.8 μmol·h−1 (s.a)	0.025M oxalic acid, 0.1g catalyst in 200 mL
$LaFeO_3$ (Pt co catalyst)	400-700	H_2 at 3315 μmol·h^{-1} (s.a)	1 mg in 20 mL of ethanol
$CaTi_{1\_x}Cu_xO_3$ (x = 0.02), NiO_x co-catalyst	>400	H_2 at 22.7 μmol·h^{-1} (s.a)	100 mg catalyst in 420 mL methanol solution
$PrFeO_3$, (Pt co-catalyst)	200W (Tungsten)	H_2 at 2847 μmol·h^{-1} (s.a)	1 mg in 20 mL ethanol solution
Bi doped $NaTaO_3$	>400	H_2 at 59.48 μmol·h^{-1} (s.a)	100 mg catalyst in 210 mL of methanol solution
$GdCrO_3$-$Gd_2Ti_2O_7$ composite	>420	H_2 at 246.3 μmol·h^{-1} (s.a)	4.1% apparent quantum efficiency, methanol solution

As it is possible to observe in Table I.2, to enhance the hydrogen production, often in the water splitting reaction is provided the use of a sacrificial agent (organic substance).

Several organic compounds, such as methanol, can act as sacrificial agents in the photocatalytic hydrogen production. In fact, these substances are able to combine with the valence band holes more effectively than water (Yamakata et al., 2003). In this way the electrons which are located in the conduction band become more available to reduce electron-acceptor species, e.g. H^+, to produce hydrogen (Chiarello and Selli, 2014).

In this case, the overall reaction turns into the photo-reforming of the organic compounds, obtaining a H_2 and CO_2 mixture. For example, in the case of ethanol photo-reforming the reaction is:

$$CH_3CH_2OH + 3H_2O = 6H_2 + 2CO_2 \qquad \text{(I.17)}$$

The addition of sacrificial agents such as methanol, can improve the efficiency of hydrogen production but this improvement is at the cost of non-renewable sacrificial reagents (Galinska and Walendziewski, 2005).

Alternatively the biomass, which represents a very versatile renewable resource, can also be utilized for the sustainable production of hydrogen(Fu et al., 2008a).

Photocatalytic reforming or organic compounds may be a good approach since the process can be carried out under ambient conditions and driven by sunlight. The pioneer study was conducted in 1980 by Kawai and Sakata (Kawai and Sakata, 1980). They reported that hydrogen could be generated from the carbohydrate on RuO_2/TiO_2/Pt photocatalyst under 500 W Xe lamp irradiation. Subsequently, they indicated that hydrogen could also be acquired from some other biomasses, such as cellulose, starch, dead insects, and waste materials using the same process, demonstrating the feasibility of producing hydrogen from biomass by the photocatalytic process (Kawai and Sakata, 1981, Sakata and Kawai, 1981).

In literature it is reported the use of different noble-metal-loaded TiO_2 photocatalysts to reform biomass, such as glucose, sucrose, and starch to hydrogen (Fu et al., 2008a). It was demonstrated that the rate of hydrogen evolution is decreased with increasing molecular weights of carbohydrates (i.e., in the soluble order starch<sucrose<glucose) (Fu et al., 2008a). Most recently Li et al. reported photocatalytic reforming of glucose under visible light over $Cd_xZn_{1-x}S$ and $ZnIn_2S_4$ (Li et al., 2010) and the hydrogen production under visible light by photocatalytic reforming of glucose over an oxide solid solution photocatalyst $Bi_xY_{1-x}VO_4$ (BYV) was demonstrated by Jing et al. (Jing et al., 2010a). In particular, from the photocatalytic degradation of glucose solution, they can observe also trace amount of methane in the gas product. So, not only presence of H_2 was observed by the photocatalytic reforming of biomass, but methane and carbon dioxide were

detected. For example, it was reported by Sakata that during photocatalytic hydrogen production from ethanol–water mixture, methane was detected as a by-product (Sakata and Kawai, 1981).

Therefore, the literature data show that the photocatalytic hydrogen production using light (solar) energy has received much attention in recent years for its potential to provide hydrogen as a clean and renewable energy resource even on a large scale (Bard and Fox, 1995) and it is important to underline that this can be attained mainly by two processes, i.e. either by the direct splitting of water into hydrogen and oxygen, or by the photoreforming of organic compounds (Patsoura et al., 2007).

The latter process that occurs in the absence of oxygen, is very attractive especially when the wastewater are used as the initial matrix for the treatment. In fact, in this way it is possible to pursue two goals simultaneously: one is the abatement of organic pollutants in the wastewater, the other is the production of hydrogen as energy carrier, made from photocatalytic reforming of organic substances.

Renewable hydrogen can be produced by the anaerobic photocatalytic reforming of biomass including glucose, sucrose and starch at ambient temperature. It is easier to evolve hydrogen with a small molecular weight carbohydrate than with a larger one and it was reported that the effect of the glucose initial concentration on the reaction rate is consistent with the Langmuir–Hinshelwood kinetic model(Fu et al., 2008a).

I.2.2 Photoelettrocatalytic hydrogen production: Basic principles.

Photocatalytic water splitting in a photo-electrochemical cell (PEC) was first demonstrated by Fujishima and Honda in 1972 (Fujishima and Honda, 1972a). The mechanism basically involves four main steps, which are the generation of electron–hole pairs from light irradiation on the photo-anode, the oxidation of water by photo-generated holes on the photo-anode surface to produce O_2 and H^+, the transfer of photo-generated electrons through an external circuit to the cathode and the reduction of H^+ by photo-generated electrons on the cathode surface to produce H_2.

The main components of a PEC cell are:

- The anode electrode which carries the photocatalyst and it is usually named “photoanode”. Generally the photoanode is a catalyst of type "n" ("n-type") therefore it is the negative electrode on which oxidation reaction occurs.
- The cathode electrode, which is made from the electrocatalyst. It is made with a material that facilitates the transfer of electrons from the cathode to the liquid phase.
- The electrolyte, which is added in order to increase to conductivity.

In Figure I.5 it is shown a schematic representation of a PEC cell with a TiO_2 anode and a Pt cathode, divided into two compartments by an ion-transport membrane.

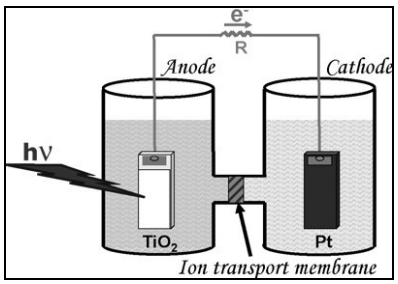

Figura I.5 *Schematic representation of a PEC cell (Lianos, 2011).*

In many cases, the base of the photoanode consists of a transparent conductive oxide (TCO) electrode in glass on which is present a thin transparent layer of indium-tin-oxide (ITO) or Fluorine-doped tin oxide (FTO).

The photoanode is constituted by an electrode on which a semiconductor film is deposited, typically titania. In many cases, the titania has been preferred for its properties as a semiconductor, and the reason is the stability in chemical environment, the easy synthesis and easy deposition as thin films (Lianos, 2011). However, other oxides and other n-type semiconductors have been reported in literature. For example, ZnO is an interesting semiconductor that has been studied for photoelectrocatalytic purposes. ZnO, as titania in anatase form, absorbs light in the UVA, and has approximately the same band gap and the same CB and VB levels(Miyauchi et al., 2002). It is possible to synthesize the zinc oxide through the electrodeposition method. This makes possible the application of the ZnO also on plastic electrodes (Nonomura et al., 2007).

Material properties, electronic structure, optical properties, and structural properties (say- interfacial properties, defect disorder) are important for the electrochemical properties. It is necessary that the photoelectrode materials should exhibit suitable optical properties for the maximum absorption of the light energy radiation, and suitable catalytic properties for effective water decomposition.

It can be seen that certain semiconductors (TiO_2, ZnO, SiC) posses large band-gap, and these materials are well suited to absorb only UV-light photons and not visible light photons. In order to be able to absorb visible light, the semiconductors were doped using metals (cations) or non-metals (anions, for example, N,C,S, etc.) (Lianos, 2011). For example, in the case of titania, these replacements create energy states within the band gap, making it smaller than that of the non-doped titania. In this way, the semiconductor is able to also absorb visible light. Titania doping has been reported in different literature data (Ji et al., 2010).

Another category of semiconductors (GaP, CdSe, CdS) show low band gap as well as desired Ev and CB, but they are photo-corrosive and hence are not stable.

Another kind of semiconductor with interesting properties for the photoelectrochemical application is ferrite. In fact, ferrite photocatalysts exhibit excellent visible light absorption capability in addition to being very stable, non-toxic, cost effective and also abundantly available (Dom et al., 2013).

Ferrite composite photo-electrodes have been found to be very efficient in addition to the nanostructured films of $ZnFe_2O_4$. A coupled semiconductor system can improve the efficiency of light energy absorption, and augment the concentration of the photo-generated carriers, and thus greatly enhance the photocurrent. Yin et al. (Yin et al., 2007) demonstrated that the photocurrent is greatly enhanced by using double layered films composed of $ZnFe_2O_4$ and TiO_2 as a coupled photoanode. A coupled-effect existing between the energy bands of $ZnFe_2O_4$ and TiO_2 due to the differences in their band-gap positions result in a desirable migration of photo-generated electrons produced by $ZnFe_2O_4$ to TiO_2. Fe_2O_3/ $ZnFe_2O_4$ composite electrode has been studied by McDonald et al (McDonald and Choi, 2011) for its use in solar water oxidation. An enhancement in the photocurrent was reported from such composite electrode. The combination of the two materials can effectively enhance the separation of exciton generated in both Fe_2O_3 and $ZnFe_2O_4$ regions thereby allowing the movement of electrons and holes to the opposite direction (Dom et al., 2013).

If it were considered all the experimental results available in the literature, it is possible to note that the choice of the photoanode is among a large variety of semiconductors. Depending on the material, the type of synthesis used, the light source, is possible to choose different semiconductors that can be applied as a photoanode.

On the contrary, with regard to the cathode, the choice is much more limited. In particular, from the literature data, the optimal choice seems to be represented by platinized Pt foil or platinized stainless steel mesh (Lianos, 2011, Ueno et al., 2009) For the platinization a method is the electrolytic reduction in a solution containing H_2PtCl_6 and appropriate electrolytes (Chojnowski et al., 1981) or the corresponding salt K_2PtCl_6 (Ueno et al., 2009). However, in most cases it is preferable to cover platinum with is a fine black powder of platinum (Pt-Black) (Ueno et al., 2009), or better, as reported in literature, to use Pt-Black mixed with Carbon-Black, a carbon fine powder (Antoniadou et al., 2010, Karakitsou and Verykios, 1993, Bae et al., 2008)

In the PEC configuration, also the choise of electrolyte is very limited. NaOH and KOH are the most used electrolyte (Tode et al., 2010). With these compounds it is possible to obtain a high pH. This allows to obtain a high concentration of OH^-, hence an effective production of hydroxyl radicals.

This is important, particularly when using organic substance as sacrificial agents, which are degraded during the reaction inside the photoelectrochemical cell.

Also in the photoelectrocatalytic hydrogen production organic substances were used. In particular it was observe that water itself can be split into the PEC cell and produces H_2, but, as reported in the literature, the presence of organic substances in solution improves the production of hydrogen (Lianos, 2011). Several substance was studied in this configuration as model fuel, such as methanol, ethanol, glycerol, sugars, organic acids, aldehydes and ketones (Lianos, 2011). The reason is the same observed for the photocatalytic hydrogen production from biomas: highest yield and in particular they are products of biomass, therefore, available and renewable.

For example glycerol is a byproduct of bio-diesel (Lianos, 2011) and can be treated as a waste material.

The reaction scheme for photocatalytic reforming, of organic substance ($C_xH_yO_z$) is given by the following reaction (Lianos, 2011) :

$$C_xH_yO_Z + (2_{X-Z})H_2O = xCO_2 + (2_{X-Z+(y/2)})H_2 \qquad \text{(I.18)}$$

Typically, in presence of organic substance in the solution of a PEC cell, a number of electrons should be conducted through the external circuit to reduce hydrogen ions and produce molecular hydrogen. For example, in the case of alcohols it corresponds to 6 electrons per carbon atom (Lianos, 2011). In this configuration, the photodegradation of an organic substance and its mineralization depends on the balance between the number of electrons flowing through the external load and those available to photodegradation procedure ((Lianos, 2011, Galinska and Walendziewski, 2005) Lianos review, A. Galinska, J. Walendziewski, Photocatalytic water splitting over Pt-TiO2 in the presence of sacrificial reagents, Energy Fuels 19 (2005) 1143–1147).

Wastewater from the food industry therefore appears to be an attractive source of biomass from which it is possible to recover elements with high added value such as hydrogen and methane. In particular, the application of advanced oxidation processes (photocatalysis or photoelectrocatalysis) allows to obtain interesting yields in the H_2 production, exploiting the presence of organic substances such as sugars.

It is worth considering a further feature of the wastewater of the food industry, namely the possible presence of food dyes (Xu et al., 2016, Xie, 2016, Castro et al., 2016).

The presence of these substances is not to be underestimated, and it must be considered if the advanced oxidation processes wants to be applied for the treatment of these wastewaters.

The use of AOPs processes makes it possible to obtain two important objectives: degradation and complete mineralization of not readily biodegradable substances (such as dyes) and the energy recovery (H_2 or CH_4 production) through the photocatalytic reforming of the organic substances present in wastewater.

As has been reported above, the photocatalytic or photoelectrocatalytic process allows the production of H_2 (or CH_4) with yields that depend on a number of factors such as the characteristics of the catalyst, the light source or the type of organic matter present in the wastewater.

As regards the degradation of dyes in food industries wastewater, the main advanced oxidation processes actually used, or that are currently studied, are reported below.

I.3 AOPs processes for food dyes removal from wastewater.

Organic dyes are used in a wide range of industrial applications such as textiles, cosmetics, pharmaceuticals or paper printing but also in food products (Fernández et al., 2010). Synthetic dyes are the largest groups of additives used in the food industry and as reported in literature, these food dyes and their by-products, such as phenolic compounds and aromatic amines, are toxic for the aquatic environment and, because of their carcinogenic and mutagenic nature (Greenlee et al., 1985, Gregory, 1986). Synthetic food dyes generally contain organic and inorganic groups that are recalcitrant. The conventional treatment for the removal of dye is rapresented by adsorption and biological oxidation.

In particular the adsorption is the most used method for the treatment of coloured effluents (Benkli et al., 2005) because of high efficiency in terms of colour removal, simply design, easy condition operation and insensitivity to toxic substances (Uzun and Güzel, 2004). But the adsorption also presents a series of disadvantages, among which the progressive decrease of the adsorbent capacity with the increase of the number of treatment cycles, and the need to adjust the pH before treatment. However, the conventional biological oxidation, typically used in wastewater treatment plants, is ineffective in treating food dye contaminated water (Robinson et al., 2001) due to the presence of aromatic rings present in some of food dye molecules.

AOPs have been widely and successfully investigated in the removal of several contaminants occurring in water and wastewater (Rizzo, 2011).

In particular heterogeneous photocatalysis, ozonation and photo-Fenton have been investigated for the treatment of waters contaminated with organic dyes (El Haddad et al., 2014, Da Silva et al., 2009, Soares et al., 2006).

I.3.1 Ozonation for the degradation of food dyes.

Ozone (O_3) is a strong oxidant effective in many applications, such as colour removal, disinfection, smell and taste removal, iron and manganese oxidation and organic contaminants removal (Kansal et al., 2011). In standard conditions of temperature and pressure, ozone has a low solubility in water, it is unstable (Whitby, 1989) and it has an average life of a few minutes. Ozone has a high oxidizing power, second only to that of fluorine and HO•.

In water solution, ozone can react with organic compounds via: direct 1,3-dipolar cycloaddition to double bonds (C=C, C=N, N=N) and in situ generation of HO• (Dalmázio et al., 2007).

In the case of dyes degradation, ozone selectively attacks the chromophoric functional group of a dye molecule resulting in a rapid colour removal (Soares et al., 2006). The degradation of the food dye Brilliant Blue by ozone in aqueous solution has been recently studied (Da Silva et al., 2009). Experimental results showed the high efficiency of ozonation in the decolourization of aqueous solutions containing the Brilliant Blue, whereas total organic carbon (TOC) measurements revealed that the mineralization of the intermediates generated by an initial attack of HO• (generated via the decomposition of ozone), occurred in a limited extent (Da Silva et al., 2012). The use of ozonation as a decolourization step was also applied to aqueous solutions of the commonly used food colorants 2-naphthalenesulfonic acid (Red 40), tartrazine (Yellow 5) and erioglaucine (Blue 1) (Zhu et al., 2013), identifying a number of carbonyl compounds as major by-products. The results suggested ring-opening reactions during colorant decomposition, typical of the interaction between ozone and aromatic compounds (Ghodbane and Hamdaoui, 2009, Wu et al., 2008). Experiments of degradation of Ponceau 4R azo dye in pure water were carried out by applying the ozonation process (Beninca et al., 2013). Almost complete apparent colour removal was obtained. However, a partial mineralization of the investigated azo dye and its intermediates, as well as negligible chemical oxygen demand (COD) removal from wastewater was observed (Beninca et al., 2013).

I.3.2 Photo-Fenton oxidation.

Ferrous ion (as homogeneous catalyst) combined with hydrogen peroxide (Fenton's reagent) reacts stoichiometrically to give HO• (Fenton, 1894). The oxidizing power of the Fenton reaction can be greatly enhanced by irradiation with UV light. The positive effect of irradiation on the degradation rate is due to the photo-reduction of Fe^{3+} to Fe^{2+} ions, which produce new HO• radicals with H_2O_2 (Ruppert et al., 1993, Pignatello and Sun, 1993). In literature there are some results on the degradation of food dyes through homogeneous photo-

Fenton process. For example, the photo-Fenton process has been applied for the removal of tartrazine. Tartrazine is a synthetic lemon yellow azo dye used in food colorants industry and it seems to cause most of the allergic and intolerance reactions of all the food azo dyes, particularly among asthmatics patients and those with aspirin intolerance. Photo-Fenton process has led to the total dye disappearance with a TOC removal of 80%.

In the photo Fenton process, the degradation mechanism of food dyes occurs thanks to the presence of HO• formed according to the following equations(Oancea and Meltzer, 2013b):

$$Fe^{2+}+H_2O_2= Fe^{3+}+HO\cdot + OH^- \quad (I.19)$$

$$Fe^{3+}+H_2O= Fe(HO)^{2+} + H^+ \quad (I.20)$$

$$Fe(HO)^{2+} +h\nu = Fe^{2+}+ HO\cdot \quad (I.21)$$

Hydroxyl radicals initiate the first step of the degradation:

$$R1\text{-}N{=}N\text{-}R2+ HO^{\bullet} = \text{oxidation intermediates} \quad (I.22)$$

$$HO^{\bullet} + \text{oxidation intermediates} = CO_2+ H_2O+\text{other inorganic products} \quad (I.23)$$

The dye removal rate increased as H_2O_2 concentration increased up to an optimum value. Beyond this value, the photo-Fenton activity decreased due to H_2O_2 scavenging effect on generated HO• radicals (Oancea and Meltzer, 2013b). The photo-Fenton reaction with the ferrous gluconate as homogeneous catalyst showed best results in the degradation of food dye Acid Green 25 when compared to the Fenton reaction (Silva et al.). Photo-Fenton reaction carried out with Fe^{2+} ions was also effective in the degradation of Carmoisine dye, a food dye having low level of beta naphthylamine that is a well known carcinogen (Sohrabi et al.). In this case, the comparison between dye removal efficiency of Fenton and photo-Fenton processes showed that the latter is a little more efficient but more expensive; accordingly, the authors concluded that the Fenton method is more appropriate than the photo Fenton for Carmoisine removal (Sohrabi et al.).

Drawbacks of homogeneous photo-Fenton process, such as low pH (≅3), production of Fe containing sludge, and deactivation can be overcome by heterogeneous photo-Fenton process (Sannino et al., 2013a, Sannino et al., 2011a, Vaiano et al., 2014c). In heterogeneous photo-Fenton process, catalysts have been used as suspended particles in the aqueous solution (Bossmann et al., 1998b). Nevertheless, the suspended catalysts should be removed before effluent disposal, making necessary a subsequent separation process which increases investment and operating costs. The use of structured catalysts could

be the solution to avoid an expensive separation process, thus saving money for wastewater treatment (Sannino et al., 2012b).

I.3.3 Heterogeneous photocatalysis

Heterogeneous photocatalysis can be seen as a "green" technology because it is able to work at ambient temperature and atmospheric pressure.

This process has been also investigated in the degradation of food dyes. Bukallah et al. report the photocatalytic degradation of Coomassie Brilliant Blue with a commercial TiO_2 (Degussa P25) irradiated with a UV lamp. Unfortunately, they only focused on dye decolourization, showing that the photocatalytic performances decreased with the increase of initial Coomassie Brilliant Blue concentration, probably because of light transfer limitation phenomena occurring in the used photoreactor (Ciambelli et al., 2011a). Nanostructured photocatalytic sol–gel TiO_2 films were used in degradation of Lissamine Green B dye as a model pollutant with the predominant irradiation wavelength of 365 nm, showing that decolourization was almost completed in 2 h while the total mineralization of the target dye was not achieved(Ćurković et al., 2014). Interestingly, TiO_2 was studied as catalyst in the photo-bleaching of many organic dyes in aqueous dispersions using visible light. In addition to the classic "photocatalytic oxidation'' mechanism, ''photosensitizing oxidation'' mechanism has been considered (Epling and Lin, 2002). This mechanism suggests that the electron from the excited dye molecule is injected into the conduction band of the TiO_2, and the cation radical formed at the surface quickly undergoes degradation to yield products:

$$Dye + h\nu = Dye^* \quad \text{(I.24)}$$

$$Dye^* + TiO_2 = Dye^{\cdot +} + TiO_2\,(e^-) \quad \text{(I.25)}$$

$$TiO_2\,(e^-) + O_2 = TiO_2 + O_2^{\cdot -} \quad \text{(I.26)}$$

The authors concluded that the used food dyes (Food Red 12, Food Yellow 13, Food Blue 1, Food Green 3, Food Red 9 and Food Red 17) were, in general, relatively easier to be bleached than the other dyes (Epling and Lin, 2002).

In a very recent paper, the photocatalytic activity of TiO_2 at different morphologies (nanosheets, nanotubes or spherical TiO_2) was tested for the degradation of three food dyes (yellow sunset, red allura and red carmoisine) underlining that the morphology strongly affects photocatalyst selectivity. The optimum degradation of sunset yellow was achieved by TiO_2

nanosheets, by spherical TiO_2 for red allura and by TiO2 nanotubes for carmoisine. The authors suggested that their results present the potential for tuning the morphology of TiO_2 based on the dye to be removed (Farghali et al., 2016). Despite the very interesting results presented in the cited literature, it must consider that photocatalysts suffer for the layout of photocatalytic plants, where the main limitation regards the low activity of photocatalysts samples and the effective transferring of the light towards the overall amount of photocatalyst. Therefore a key parameter for a successful implementation of photocatalytic processes at large scale is the reduction of reaction time. In order to improve the photoactivity of the semiconductor, many strategies, such as noble metal addition, have been employed (Sannino et al., 2012a, Chiarello et al., 2011, Antoniadou et al., 2013, Miranda et al., 2016) In fact, the presence of noble metals decreased the electron-hole recombination, thus improving the TiO_2 efficiency in the photocatalytic reactions, also for the degradation of food dyes (Hajaghazadeh et al., 2014, Muhd Julkapli et al., 2014).

It is noteworthy that the most of the photocatalysts formulations proposed are only active under ultraviolet (UV) radiation, which is only a little fraction (5%) of solar light. Therefore, to improve process efficiency, the absorption of the semiconductors should be within the visible light (43%) of the electromagnetic radiation reaching the planet's surface. Accordingly, a suitable photocatalyst should work in the visible-light region with a band gap of less than 3 eV . Interesting visible photocatalytic activity results were found using N-doped TiO_2, both under visible irradiation and under solar simulated radiation, in the removal of different pollutants such as emerging contaminants(Vaiano et al., 2015e) and bacteria (Rizzo et al., 2013). To increase the photocatalytic performances, N-doped TiO_2 photocatalyst was coupled with light carriers, such as light emitting phosphorescent particles (phosphors), and UVA-LEDs was used as light source to improve radiation emission and to decrease the optical path of irradiation towards the photocatalyst (Epling and Lin, 2002). A further enhancement of photocatalytic activity was achieved by combining the N-doped TiO_2 with up-conversion phosphors (OP), able to convert low-energy into high-energy photons. In this context, the photoactivity of visible active N-doped TiO_2 in the photocatalytic mineralization of spiramycin was found to be significantly enhanced in the presence of OP in the catalyst formulation (Vaiano et al., 2015e).

For the heterogeneous photocatalysts it is possible to note that the key parameter for process upscale in the removal of food dyes is the optimization of the photocatalyst formulation to enhance photons transfer inside the reactor.

I.4 Aim of the thesis

As mentioned in the previous paragraphs, the research of new eco-friendly technologies that enable the production of energy is nowadays one of the topics of greatest interest to the scientific community. However, at the same time, the concern of the industry is also the disposal and treatment of wastewater.

Starting from these considerations, an interesting approach is to explore, in parallel to wastewater treatment, the possibility to produce also an energy source such as hydrogen and/or methane from the degradation of organic substances present in wastewaters under mild operating conditions. This feature can be realized by using advanced oxidation processes.

So, it is interesting to evaluate the performances of advanced oxidation processes (in particular photo-Fenton, photocatalysis and photoelectrocatalysis) for the treatment of food industry wastewaters through the conversion of specific substances (sugars) to compounds with high energetic value, coupled with the removal of substances hardly biodegradable (such as food dyes).

In particular, the aim of this work is the study of the photocatalytic hydrogen or methane production from food industry wastewater, using specific semiconductors. The optimal design of the process needs, firstly, the formulation of a photocatalyst able to work under UV but also under visible light irradiation. Recently, many efforts have been made to modify titanium dioxide with noble metals (such as Pd, Pt, Au). Providing for the photocatalytic application to industrial level, a good solution for a final scale-up is the choice of a noble metal free photocatalyst able to work also under visible light.

So, starting from this consideration, the synthesis of perovskite ($LaFeO_3$), was developed through a simple solution combustion method.

The synthesis conditions have been studied in order to maximize the photocatalytic activity under visible light. The effectiveness of the formulated $LaFeO_3$ has been tested in the valorization of aqueous solutions containing sugars. To increase the photoactivity, the $LaFeO_3$ was doped with transition metals (not noble metals), such as ruthenium. The $LaFeO_3$ photocatalyst performances were compared with those ones of catalysts based on titania modified with noble metals

The optimized photocatlyst was afterwards deposited on nanoparticles with magnetic properties to avoid the drawback related to the separation of a catalyst in powder form after the reaction.

Finally, the application of the photocatalytic process in the treatment of a real wastewater from the washing process of the fruit (especially cherries) has been evaluated.

It was also investigated the photoelectrocatalytic process for the hydrogen production, considering the general aspects of the process and in particular

the attention has been focused on the electrodeposition process for the synthesis of photoanodes to be used in photoelectrocatalytic reactors .

Finally, it has been evaluated the possibility to couple the photocatalytic reactor (used primarily for the valorization of the wastewater through the production of hydrogen and /or methane) with a photo-Fenton system able to mineralize the unconverted organics coming from the photoreactor and for the removal of not-biodegradable substances still present in the wastewaters.

II Experimental

This chapter contains all the characterization techniques used for the study of the synthesized catalysts used for this work.

It has also been reported the analytical techniques required to assess the production of H_2, CH_4 and CO_2 and to determine the amount of organic matter present in the liquid phase.

In addition, the reactor configurations employed for photocatalytic, photoelectrocatalytic and photo Fenton experiments have been described.

II.1 Characterizations techniques

All the investigated photocatalysts, whose performance will be reported in subsequent chapters, have been characterized by the following experimental techniques:

- UV-vis Diffuse Reflectance Spectroscopy
- XRD powder diffraction
- The Raman spectroscopy
- Surface area and pore structure evaluation by gas adsorption
- Electron microscopy
- X-ray fluorescence (XRF)
- XPS
- Magnetization measurements
- Photoelectrochemical characterization

In particular the crystallite size and crystalline phase of photocatalysts were studied with an X-ray diffractometer (Assing), using Cu-Kα radiation. Total metal content used for the photocatalysts doping were determined by X-ray fluorescence spectrometry (XRF) in a thermoFischer ARL QUANT'X EDXRF spectrometer. The specific surface area analysis was performed by BET method using N_2 adsorption with a Costech Sorptometer 1042 after a pretreatment at 150°C for 30 minutes in He flow (99.9990 %). The Raman spectra of the samples were recorded with a Dispersive MicroRaman system (Invia, Renishaw), equipped with 785 nm diode-laser, in the range 100-1000

cm^{-1} Raman shift. UV–vis reflectance spectra (UV-vis DRS) of powder catalysts were recorded by a Perkin Elmer spectrometer Lambda 35 using a RSA-PE-20 reflectance spectroscopy accessory (Labsphere Inc., North Sutton, NH). All spectra were obtained using an 8° sample positioning holder, giving total reflectance relative to a calibrated standard SRS-010-99 (Labsphere Inc., North Sut-ton, NH). Band-gap energy determinations of the photocatalysts were obtained from Kubelka–Munk function $F(R_\infty)$ by plotting $[F(R_\infty) \times h\nu]^2$ *vs.* $h\nu$. Scanning electron microscopy (SEM) (Assing, mod. LEO 420) was used to characterize the morphology of the samples at an accelerating voltage of 20 kV. The M(T) measurements of Magnetization as function of the Temperature were performed using the Zero Field Cooling (ZFC)-Field Cooling (FC) procedure. More precisely, the samples were first cooled down to 5 K in presence of a zero magnetic field, then the field was turned on at 0.1 Tesla and the data were acquired for increasing temperature (ZFC) up to 300 K. After that, the samples were cooled down again while acquiring FC magnetizations.

II.2 Reactors configuration

II.2.1 Photocatalytic reactor

Photocatalytic reactor design must address important parameters, such as uniform light distribution, providing high illuminated catalyst surface area, and mixing inside the reactor. Photocatalytic reactions are promoted by solid photocatalyst particles that usually constitute the discrete phase distributed within a continuous fluid phase in the reactor. Therefore, at least two phases, that is, liquid and solid, are present in the reactor. The solid phase could be dispersed (SPD) or stationary (SPS) within the reactor (Ray, 2009). SPD photoreactors may be operated with the catalyst particles and the fluid phase(s) agitated by mechanical or other means. Slurry reactors have been the object of fundamental studies (e.g.(Li Puma and Brucato, 2007)= with the aim of either getting true kinetic data or allowing large reactors to be designed. Several designs have been studied or suggested. Suspended catalyst has often been used as a flow in an annular space(Alfano et al., 2000, Martin et al., 1999) around a linear lamp but a thorough study has been dedicated to a falling film reactor(Li Puma and Yue, 1998), where a thin film runs freely on the outer wall within the annular space. If the reaction is fast enough, a radial concentration gradient in the reactants will take place, this can be reduced by creating a turbulent flow by the presence of baffles of various design. A completely different design is the fountain reactor (Li Puma and Yue, 2001) where a nearly planar horizontal film is exposed to artificial or solar irradiation. These reactors are meant for water treatment where conversion in the reactor is usually very low so that they are coupled with a tank with a continuous recirculation of the fluid.

Mass balance for the whole reactor has to take this situation into account although in the case of a low conversion and good stirring of the tank, the reactor is formally analogous to a batch reactor.

The central problem in a photocatalytic reactor is focused on a uniform distribution of light to a large surface area of catalyst. To achieve uniformity in photon flux distribution within the reactor, a correct position of light source is essential to ensure maximal and symmetrical light transmission and distribution.

In this work, the reactor configuration used to carry out the photocatalytic experiments for the production of hydrogen and/or methane is shown in Figure II.1.

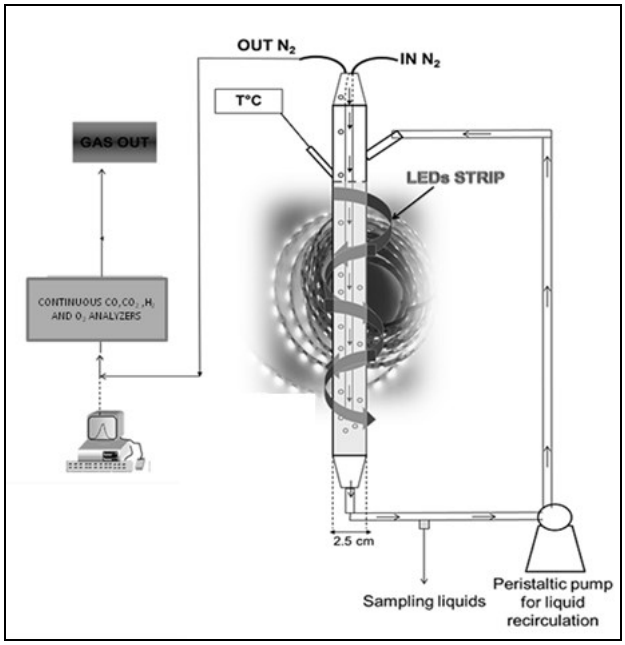

Figure II.1 *Photocatalytic reactor configuration for hydrogen production.*

It is a slurry pyrex cylindrical reactor (generally with an internal diameter (ID) equal to 2.5 cm) equipped with a N_2 distributor device (Q = 0.122 NL/min). In order to ensure a good catalyst distribution within the solution, the continuous mixing of the solution in the reactor was achieved by an external recirculation of water through a peristaltic pump. The photoreactor was irradiated by a strip of UV-LEDs (nominal power: 10 W) with wavelength emission in the range 375–380 nm, or with a strip of visible LEDs with the main wavelength emission at 440 nm (nominal power: 10 W).

The LED strip was positioned around the external surface of the reactor.

In this way the light source is able to uniformly irradiate the entire reaction volume.

II.2.2 Photo-Fenton reactor

For the degradation of the hardly biodegradable substances (such as dyes) downstream of the photocatalytic process, photo-Fenton process has been used. In particular, the photo-Fenton tests were carried out on 160 ml of solution in a properly designed sealed stainless-steel batch cylindrical photoreactor (Sannino et al., 2011b). Aqueous solutions containing an initial concentration of dye, at the spontaneous pH of the solution (pH=6.6) were used in the tests. An 8 W mercury vapors lamp emitting at 254 nm was used as light source. 13 g of the monolith catalysts were placed in the reactor. The reactor was maintained in the absence of irradiation at 25°C for t=180 min to reach the adsorption equilibrium of food dyes on catalysts surface. During the tests, a continuous dosage of H_2O_2 (0.038 mol h^{-1}) was carried out. The continuous mixing of the solution in the reactor was realized by bubbling N_2 (Q=140 mL/min (STP–Standard Temperature and Pressure)). Moreover, the solution was cooled by a cold trap to keep the temperature constant at 25 °C. Nitrogen acts also as carrier for the gaseous species formed during the irradiation period. Reaction products in gas-phase were monitored by continuous analyzers, measuring CO, CO_2 (Uras 14, ABB) and O_2 (Magnos 106, ABB) gaseous concentrations at the reactor outlet.

II.2.3 Photoelectrocatalytic reactor

In the case of hydrogen production, a large pyrex glass H-shaped reactor was used, which could accommodate large photoanode and counter electrodes (3.5 cm x 5 cm active area) (Figure. II.2). The Pt/Elcocarb/FTO electrode was used as counter electrode. For the fabrication of the counter electrode, a commercial carbon paste (Elcocarb C/SP (Solaronix)) was applied on FTO by doctor blading and was annealed at 450 C for 30 min. Pt was then deposited on the top using a solution of Diamminedinitritoplatinum(II) (Aldrich) in ethanol and casted on warm film

lying on a hot plate at 40 °C. The film was subsequently annealed again at 450 °C. The final quantity of Pt on the film was calculated to be 0.1 mg/cm^2.

The active area of the prepared electrocatalyst film was 3 cm x 5 cm.

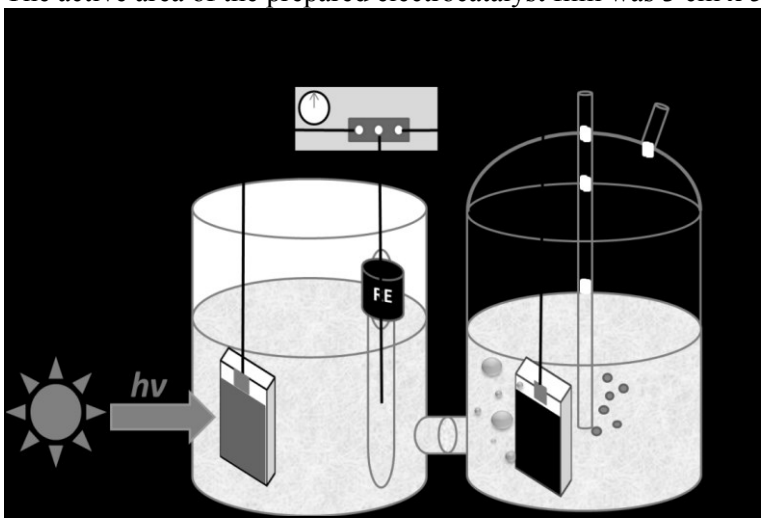

Figure II.2. *Illustration of a H-shape reactor producing hydrogen by employing a semiconductor covered FTO anode and a Pt-enriched carbon paste covered FTO cathode.*

Combination of carbon paste with Pt has been previously successfully tested as electrocatalyst for hydrogen production (Kalamaras et al., 2016). 1M aqueous NaOH without or with the organic substance (glucose, sorbitol, glycerol and ethanol) was used as electrolyte. The organic substance was added only in the anode compartment. The quantity of the electrolyte was 250 ml in each compartment of the cell. The two compartments were separated by a silica frit (porosity SGQ 5, diameter 25 mm, thickness 2 mm). The reactor was equipped with fittings in a manner to allow Ar gas flow through the electrolyte. The latter was deoxygenated for 20 min by a vigorous flow of Ar and then the flow continued at a controlled flow rate of 20 cc min^{-1}.

Hydrogen was monitored on line by using Ar as carrier inert gas and by applying bias measured vs Ag/AgCl. Illumination was made in all cases using a Xe lamp providing an intensity of 100 mW/ cm^2 at the position of the photoanode.

II.3 Chemical analysis

The chemical analyses made during the experiments have involved both the analysis of the compounds both in gas phase and in the liquid phase.

The analysis of the gaseous phase from the photocatalytic reactor was performed by continuous analyzers (ABB Advance Optima). In particular:

- CO, CO_2 and CH_4 analysis through module URAS (IR type)
- H_2 analysis through module CALDOS
- O_2 analysis through module MAGNOS.

For the liquid phase, the analysis of sugar it was made by a colorimetric method using a spectrophotometer, and by high-performance liquid chromatography (HPLC).

In the case of colorimetric method, 2 mL of a carbohydrate solution was mixed with 1 mL of 5 wt% aqueous solution of phenol (Sigma-Aldrich) in a test tube. Subsequently, 5 mL of concentrated sulfuric acid (Sigma-Aldrich) was added rapidly to the mixture. The concentration of the glucose was measured at 490 nm using the UV-vis spectrophotometer (Lambda 35, Perkin Elmer) (Dubois et al., 1956).

The other sugars were measured by HPLC using a Shimadzu Nexera LC-30A system (Shimadzu, Kyoto, Japan), consisting of a controller CBM-20A, two dual-plunger parallel-flow pumps LC-30AD, a degasser DGU-20 A5R, an autosampler SIL-30 AC, a column oven CTO-20AC and a evaporative light scattering (ELSD) detector. Mobile phase used was composed by H_2O (A) and CH_3CN (B), the following binary gradient was applied: 0.01-4.50 min, 74-80% B; 4.50-4.51 min, 80-74% B; 4.51-8.00 min, isocratic at 74% B. Flow rate was set to 0.80 mL/min. The oven temperature was set at 25 °C. The injection volume of the sample analyzed was 5 μL. The chromatogram was monitored by ELSD with the following parameters (Gain 5, T = 70 °C, N_2 = 270KPa). For the separation, an Supelcosil LC-NH2 150 mm × 3 mm × 3 μm (L × ID × particle size, 120 Å) was employed (Supelco, Belle-fonte, PA, USA). The data were processed by the LabSolutions® software (Version 3.50.346, Shimadzu).

The gluconic acid formed during the irradiation time was analyzed by the UV absorption of liquid samples at 264 nm (Li et al., 2010) using UV-Vis spectrophotometer (Lambda 35, Perkin Elmer).

In the case of wastewaters containing dyes, the concentration of color in aqueous samples was determined with a Perkin Elmer UV-Vis spectrophotometer. In particular, for tartrazine dye the concentration was determined at λ_{max} = 426 nm, for red allura dye at λ_{max} = 506 nm and for patent blue V dye at λ_{max} = 635 nm. For comparison, organic dyes different from food ones, have been also used in photocatalytic tests. In particular, rhodamine b, methylene blue and eriochrome black concentration was measured at λ_{max} = 553 nm, λ_{max} = 663 nm, and λ_{max} = 528 nm respectively.

For the analysis of dyes, over the concentration of color, it is important also to evaluate the mineralization of the organic substance. In this case the

Total Organic Carbon (TOC) measurement was made. The TOC was measured by the high temperature combustion method on a catalyst (Pt-Al_2O_3) in a tubular flow microreactor operated at 680 °C, with a stream of hydrocarbon free air to oxidize the organic carbon. Laboratory apparatus consisted of mass flow controllers (Brooks) operating on each gas; an injection system; a NDIR continuous analyzer (Hartmann & Braun Uras 10E) for measurements of CO and CO_2 concentrations at the combustion reactor outlet and a paramagnetic analyzer (Hartmann & Braun Magnos 6G) for continuous monitoring of O_2.

III Experimental results: Hydrogen and methane production from photocatalytic degradation of glucose on noble metals based photocatalysts.

The effect of noble metals doped photocatalyst in the simultaneous production of CH_4 and H_2 from photocatalytic reforming of glucose under UV light irradiation by light-emitting diodes (LEDs) with low energy consumption (10W) were evaluated. TiO_2 was prepared via a sol–gel technique, while noble metals addition was carried out by photodeposition. In addition, it was evaluated the effect of the surface modification of TiO_2, in particular modified with fluorine ($F–TiO_2$) that can inhibits the recombination rate of holes and free electrons, enhancing the photocatalytic activity in the removal of pollutants from aqueous samples (Yang et al., 2007). All the samples were characterized and the influence of some parameters was evaluated.

III.1 Pd-TiO_2 photocatalysts.

Different catalysts containing noble metals on the surface (Au, Pt, Pd) have been investigated for the photocatalytic hydrogen production (Gomathisankar et al., 2013a, Kondarides et al., 2008a) because the presence of noble metals on the surface of the semiconductor improves photocatalytic performances. Linsebigler et al. (1995) observed that by adding a small amount of noble metals, it is possible to suppress to some extent the charge recombination by forming a Schottky barrier (Linsebigler et al., 1995). Rh or Pt, Pd, Cu or Ni supported on TiO_2 has been investigated in the conversion of glucose into H_2 (Chong et al., 2014b).. Moreover, a few results are reported in the scientific literature about the production of methane through photocatalytic reforming of wastewater. Following the results about the

performances to the production of H_2 or CH_4 of Pd deposition onto the sulfated TiO_2 surface throughout the photodeposition method were reported.

It was found that the experimental conditions during photodeposition, such as deposition time, have a strong influence on the final properties of the materials, and consequently on their photocatalytic activity in glucose reforming.

III.1.1 Sol-gel synthesis and photodeposition of Pd on sulfated TiO_2

TiO_2 was prepared by hydrolysis of titanium tetraisopropoxide (Aldrich, 97%) in isopropanol solution (1.6 M) by the slow addition of distilled water (volume ratio isopropanol/water 1:1). The TiO_2 powder was recovered by filtration, dried at 110 ºC for 24 h and pre-treated by immersion in a 1M sulfuric acid solution under continuous stirring for 1 h. After pre-treatment, the solution was filtered, dried and calcinated at 650 ºC for 2 h; the resulting photocatalyst was used as starting material (S-TiO_2). The fresh TiO_2 powder was submitted to a sulfate treatment, taking into account that previous results have shown that sulfate pre-treatment stabilizes the anatase phase up to high temperatures and protects the surface area against sintering (Colon et al., 2003).

Photodeposition of palladium was performed over the sulfated TiO_2 powders using palladium chloride (II) ($PdCl_2$, Aldrich 99%) as the metal precursor. Under an inert atmosphere (N_2), a suspension of the corresponding TiO_2 sample in distilled water containing isopropanol (Merck 99.8%), which acts as the sacrificial donor, was prepared. Then, the appropriate amount of $PdCl_2$ solution to obtain the desired nominal palladium loading was added; in order to dissolve the metal precursor, the pH of this solution was adjusted to 2 by using a HCl 0.1M solution. Photodeposition of palladium was then performed by illuminating the suspension for 120 min with an Osram Ultra-Vitalux lamp (300 W) which possesses a sun-like radiation spectrum with a main emission line in the UVA range at 365 nm. The light intensity on the suspensions was 60 W/m^2 determined by a PMA 2200 UVA photometer (Solar Light Co.). After photodeposition, the powders were recovered by filtration and dried at 110 ºC overnight. Series of Pd-TiO_2 catalysts were prepared by using different metal contents (0.5% or 2% weight total to TiO_2) and photodeposition times (15 or 120 min). The photocatalysts prepared by TiO_2 metallization will be denoted in this document as 0.5Pd15, 0.5Pd120, 2Pd15 and 2Pd120.

III.1.1.1 X-ray diffraction

Figure III.1.1 shows the XRD patterns of the Pd-TiO_2 photocatalysts; the only crystalline phase present in all the samples was anatase, identified by the main XRD peak located at 25.25º, thus indicating that the sulfation pre-treatment inhibited the formation of the rutile phase of TiO_2 during the calcination process, as has been reported by different authors (Hidalgo et al., 2011).

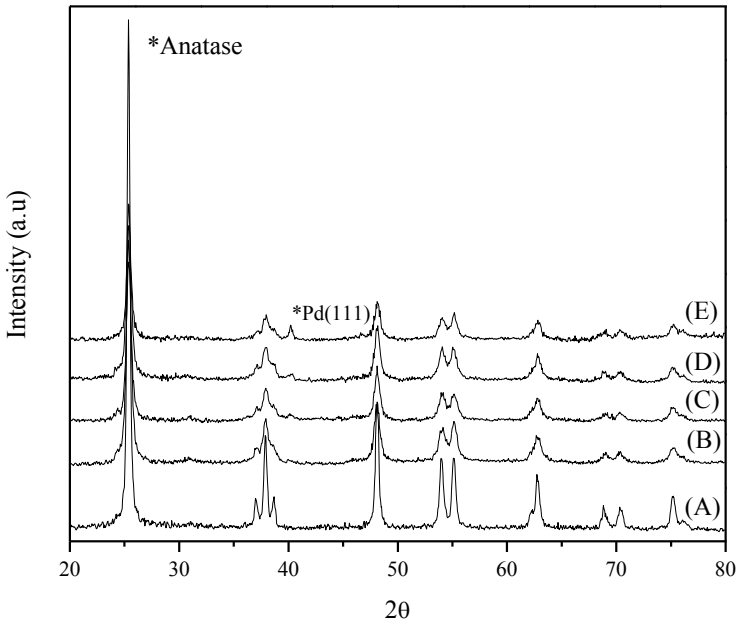

Figure III.1.1 *XRD patterns for TiO_2 and Pd-TiO_2 photocatalysts prepared with different Pd content and deposition time. (A) TiO_2; (B) 0.5 wt.% Pd-TiO_2, 15 min; (C) 0.5 wt.% Pd-TiO_2, 120 min; (D) 2 wt.% Pd-TiO_2, 15 min and (E) 2 wt.% Pd-TiO_2, 120 min.*

On the other hand, photodeposition of palladium did not affect the phase composition in any case. In the spectra of metallized samples, a diffraction peak for Pd was detected at 40º; this peak is assigned to Pd (111) (Navaladian et al., 2008). It was observed that the intensity of this peak increased with the Pd loading, being highest in the catalysts prepared with 2 wt.% of nominal content and 120 min of deposition time; this could be due to a higher metal particle size in these samples. The anatase crystallite sizes calculated by the Scherrer equation from the (101) peak of the XRD pattern are listed in Table 1. As can be seen, the TiO_2 presents a value of 20 nm; the Pd addition did not significantly modify crystallite sizes beyond this value.

Table III.1 *Characterization of the investigated photocatalysts*

Photocatalyst	Pd nominal loading (wt.%)	Photo-deposition time (min)	Real Pd content (wt.%)*	Sulfate amount (wt.%)	S_{BET} (m^2/g)	Band gap (eV)**
S-TiO_2	0	-	-	0.3	58	3.2
0.5Pd 15	0.5	15	0.18	0.28	46	3.2
0.5Pd 15	0.5	120	0.20	0.27	48	3.2
2 Pd 15	2	15	0.34	0.27	48	3.2
2Pd 120	2	120	0.80	0.28	49	3.3

III.1.1.2BET Surface Area

BET surface area values (SBET) for all the samples are shown in Table 1. As can be seen, Pd addition did not induce significant modifications in the SBET of the analyzed materials, and the observed slight decreases are probably due to pore blocking by metal deposits on the TiO2 surface.

III.1.1.3 X-ray fluorescence

The real palladium content in the metallized samples was measured by XRF and the values are listed in Table III.1. These values are less than the nominal metal content used to prepare these materials (0.5 or 2 wt.%), indicating an incomplete reduction of the metal precursor ($PdCl_2$) on the TiO_2 surface during the photodeposition process. However, the amount of deposited Pd was highest in the samples prepared with the highest deposition time (120 min).

In all the samples, XRF analysis revealed that a certain amount of S and Cl- species remained on the solid after preparation. The sulfur content was between 0.27 and 0.30%, and the chloride content was below 0.02%.

III.1.1.4 UV-Vis Diffuse Reflectance spectra

The absorption spectra of all the samples are shown in Figure III.2. The typical absorption band edge of the TiO_2 semiconductor was observed at around 400 nm for all the samples. As can be seen, metallization did not substantially alter the absorption properties of the samples; however, a slight increase in absorption throughout the visible range of the spectrum was observed due to the gray color of these materials; this increase is more evident in samples with the highest Pd loading.

From the UV-Vis DRS spectra, band-gap energies were calculated, being 3.20 eV for the TiO_2 corresponding to the anatase phase. Pd photodeposition

did not induce any significant change in this value; estimated band-gap energies are between 3.2 and 3.3 eV.

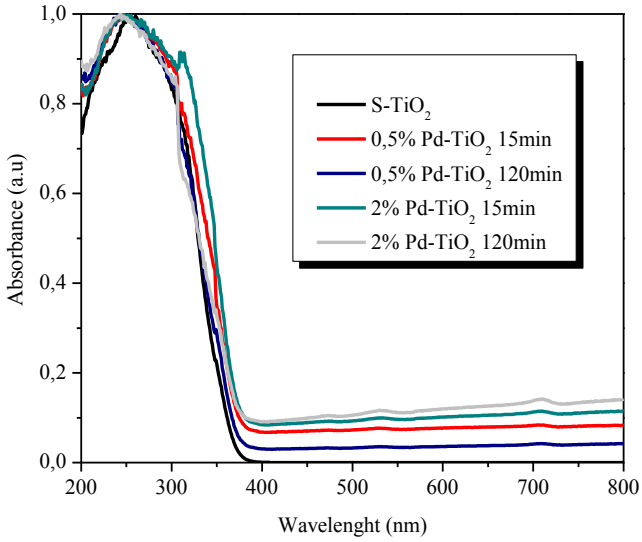

Figure III.1.2. *UV-Vis DRS spectra for the investigated photocatalysts.*

III.1.1.5 Microscopic analysis

The morphology and Pd particle size in the samples prepared was studied by TEM.

As was observed from the TEM images, in the samples prepared with 0.5 wt.% Pd loading, metal nanoparticles appear to be homogenously distributed all over the surface, with sizes around 2-4 nm (images are not shown).

Figure III.3 shows representative TEM images of TiO_2 after photodeposition of 2 wt % Pd with irradiation times of 15 and 120 min (Figures III.1.3A and III.1.3B, respectively). In both samples, palladium particles can be seen as dark spherical spots placed on the larger anatase particles; in these samples Pd nanoparticles are heterogeneously distributed on the TiO_2 surface and particle sizes higher than 6 nm were observed.

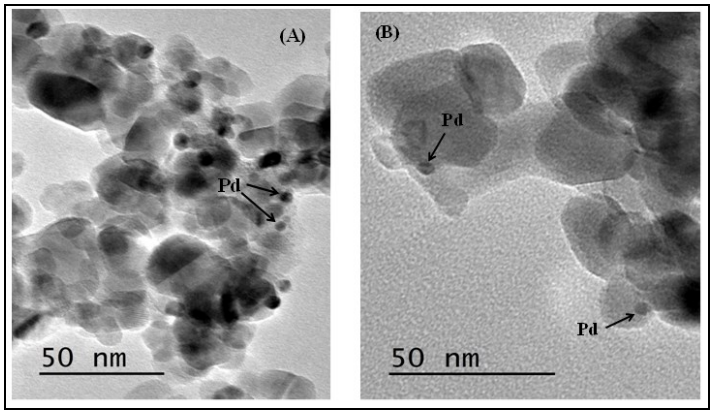

Figure III.1.3. *TEM images of 2wt.% Pd-TiO_2 samples. (A) Pd-TiO_2, 15 min and (B) Pd-TiO_2, 120 min*

III.1.1.5 XPS analyses

XPS measurements were performed and a summary of these results is reported in Table 1.

Figure III.4 shows spectra of Ti 2p and O1s for the different samples analyzed. The Ti 2p core peaks exhibit a main component at around 458.5 ± 0.1 eV (Ti $2p_{3/2}$) in all the samples, representative of theTi^{4+} ions in the TiO_2 lattice. The addition of Pd did not modify the oxidation state or the chemical environment of titanium atoms at the surface of the TiO_2. In the O 1s region, a peak located at 529.8 ± 0.2 eV can be observed for all the samples, assigned to oxygen atoms in the TiO_2 lattice. This peak is asymmetric, with a shoulder at higher binding energies assigned to surface OH groups. The shoulder is more prominent in the non-metallized TiO_2 sample, indicating a higher hydroxylation degree in this sample. The intensity of this shoulder is lower in Pd-TiO_2 samples; this is mainly due to the presence of metallic nanoparticles partially covering the TiO_2 surface, as was observed by TEM (Figure III.1.3).

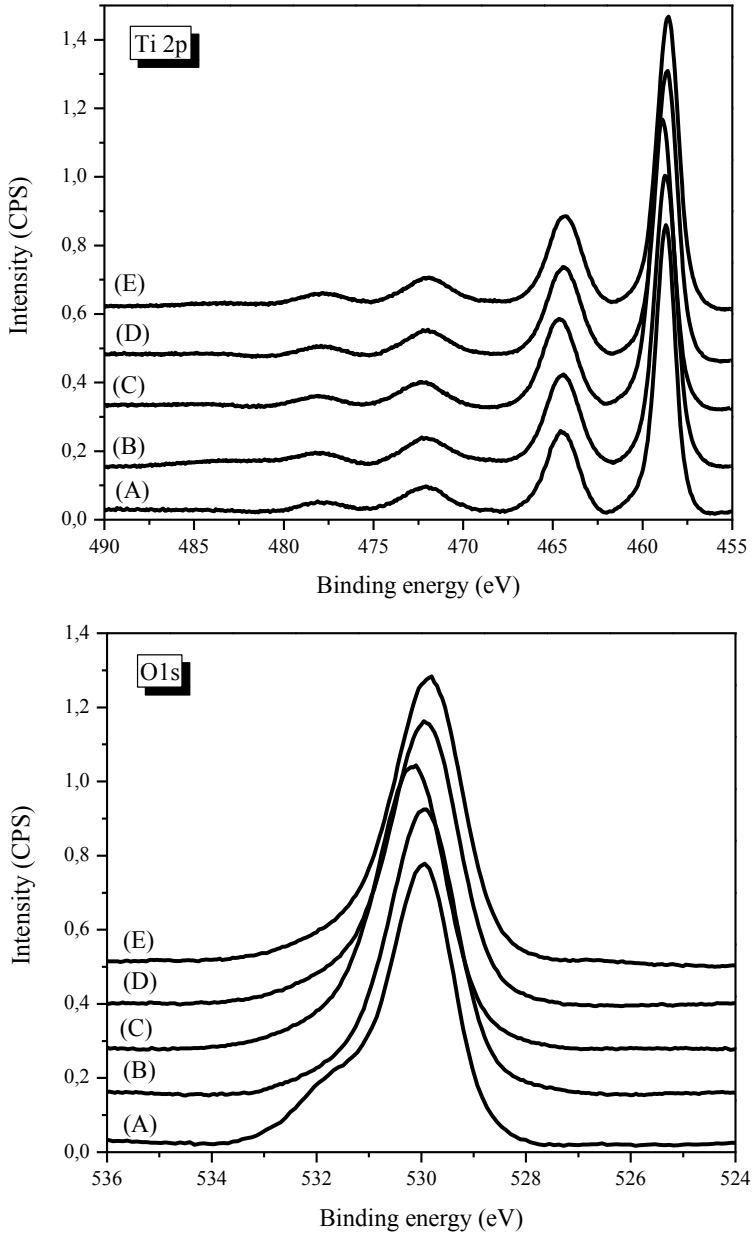

Figure III.1.4. *XPS core level spectra of Ti 2p and O 1s regions for the investigated photocatalysts. (A) S-TiO_2; (B) 0.5wt.% Pd-TiO2, 15 min; (C) 0.5wt.% Pd-TiO_2, 120 min; (D) 2wt.% Pd-TiO_2, 15 min and (E) 2 wt.% Pd-TiO2, 15 min.*

The study of XPS Pd 3d peak regions can provide information concerning the oxidation state of the Pd species adsorbed on the TiO_2 surface. A Pd 3d region is formed by a doublet corresponding to the signals for $3d_{7/2}$ and $3d_{5/2}$. The Pd $3d_{7/2}$ binding energy for metallic palladium (Pd0) appears near to 334 eV, while for partially oxidized forms (Pd^{2+}/Pd^{4+}) it appears at higher binding energies with values of ca. 336 and 338 eV, respectively (Brun et al., 1999). The XPS Pd 3d region for the Pd-TiO_2 samples prepared with 0.5 and 2 wt.% metal content and deposition times of 15 and 120 min is shown in Figure III.1.5. All the spectra were calibrated with the C1s peak at 284.6 eV attributed to "adventitious" surface carbon. Pd^0 and $Pd^{\sigma+}$ species were detected in all the analyzed samples, thus indicating an incomplete reduction of the metal precursor on the TiO_2 surface; these observations are in agreement with the results obtained by XRF analysis. However, the Pd^0 on TiO_2 increased with the deposition time and with the metal content. As can be seen qualitatively in Figure III.1.5, the highest intensity of the peaks assigned to Pd^0 species content was observed in the catalyst prepared with 120 min of deposition time and 2 wt.% of nominal Pd loading.

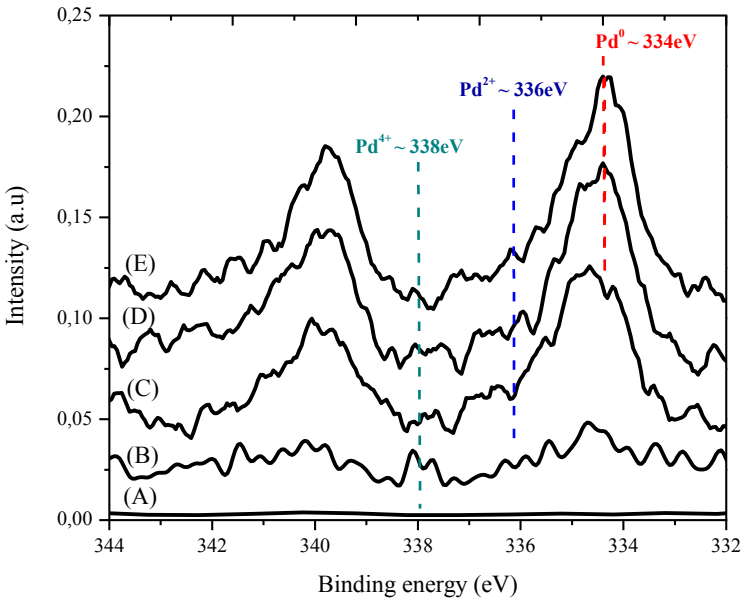

Figure III.1.5. *Comparative XPS spectra of Pd $3d_{7/2}$ and $3d_{7/2}$ core level of Pd-TiO_2 catalysts prepared with different Pd content and deposition time. (A) S-TiO_2 (B) 0.5 wt.% Pd-TiO_2, 15 min; (C) 0.5 wt.% Pd-TiO_2, 120 min; (D) 2 wt.% Pd-TiO_2, 15 min and (E) 2 wt.% Pd-TiO_2, 120 min.*

Pd $3d_{7/2}$ and $3d_{5/2}$ doublets were deconvoluted using the UNIFIT 2009 software assuming a doublet separation of 5.2 eV of the two components. The spectrum obtained for the 2wt.% Pd-TiO_2 catalysts prepared with 120

min of deposition time is shown in Figure III.1.6. A Shirley-type background was subtracted from each spectrum. By the deconvolution of the doublets it is possible to observe clearly the presence of $Pd^0/Pd^{\sigma+}$ species in the analyzed sample.

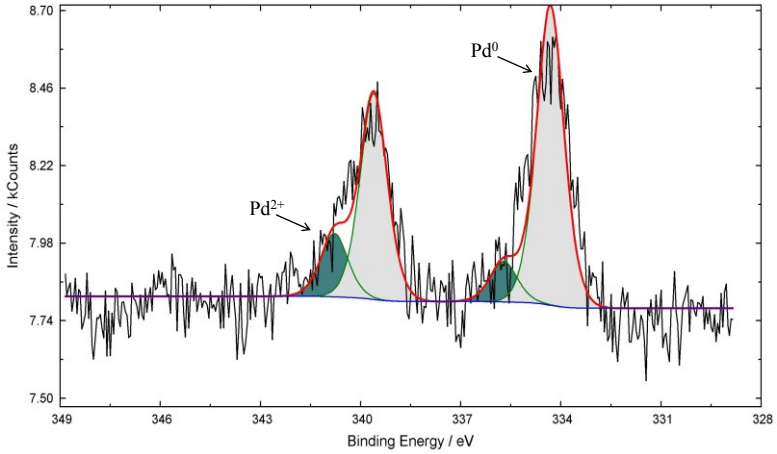

Figure III.1.6. *XPS Pd $3d_{7/2}$ and $3d_{7/2}$ regions for 2 wt.% Pd-TiO_2 catalyst prepared with 120 min of deposition time.*

III.1.2 Photocatalytic activity results

Typically, in the photocatalytic, tests 0.04 g of catalyst was suspended in an 80-mL aqueous solution containing 500 mg/L of glucose (D+ Glucose VWR, Sigma-Aldrich). The suspension was left in dark conditions for 2 hours to reach the adsorption-desorption equilibrium of glucose on the photocatalyst surface, and then a photocatalytic reaction was initiated under UV light for up to 3 hours. Hydrogen and methane yield during the irradiation time is evaluated according to the following relationship:

$$R_{H_2} = \frac{2 \cdot nH_2}{12 \cdot n^0 C_6H_{12}O_6} \cdot 100 \qquad \text{(III.1)}$$

$$R_{CH_4} = \frac{4 \cdot nCH_4}{12 \cdot n^0 C_6H_{12}O_6} \cdot 100 \qquad \text{(III.2)}$$

Where:

R=yield;

nH_2=moles of H_2 produced;

nCH_4=moles of CH_4 produced;

$n^0C_6H_{12}O_6$=moles of glucose after dark adsorption.

III.1.2.1 Influence of Pd presence

The preliminary test performed in dark conditions showed no reaction product in the gaseous phase. The final concentration of glucose after the dark period was 351 and 305 mg/L for S-TiO_2 and 0.5Pd120, respectively.

Control tests with UV as a standalone process and under photocatalytic conditions with UV/S-TiO_2 and UV/0.5Pd120 were carried out to evaluate the contribution of each process in the production of hydrogen and methane from glucose (Figure III.1.7). During the irradiation time, the production of H_2, CO_2 and CH_4 was observed, but no formation of CO and O_2 was observed. The presence of palladium photodeposited on the surface of the titania enhanced the production of hydrogen (Figure III.1.7a). In particular, a production of H_2 as high as 26 μmol (R_{H2}=3%) after 3 hours of irradiation with a 0.5Pd120 catalyst was observed. The hydrogen yield on 0.5Pd120 (3%) is significantly higher than that obtained on S-TiO_2 (0.9%).

However, a large fraction of glucose is not converted into hydrogen and methane under the present conditions.

These results are in agreement with those reported in the literature. In particular, loading noble metals such as Pt (Siemon et al., 2002) and Au (Bamwenda et al., 1995) onto the photocatalyst surface can separate photogenerated electrons and holes more effectively and thus improve hydrogen production. In a similar way, the coexistence of Pd with TiO_2 in the Pd-TiO_2 composite photocatalyst may lower the recombination rate between photogenerated electrons and holes, thus improving the efficiency of the photocatalysis process. It is well known that there are two forms of electron-hole recombination in TiO_2, surface recombination and bulk recombination, and both can lower the efficiency of photocatalysis . The Fermi energy level of Pd is lower than that of TiO_2, and since they are closer to each other, the electrons on the surface of TiO_2 can spontaneously transfer to the surface of Pd until their Fermi energy levels become equal. As a result, excessive negative charges accumulate on the surface of Pd and excessive positive charges accumulate on the surface of TiO_2. Therefore, the energy band of TiO_2 bends upwards, forming the Schottky barrier. Therefore, in the composite catalyst, Pd acts as an electron trap, which can effectively prevent the surface electron-hole recombination (Liu et al., 2006).

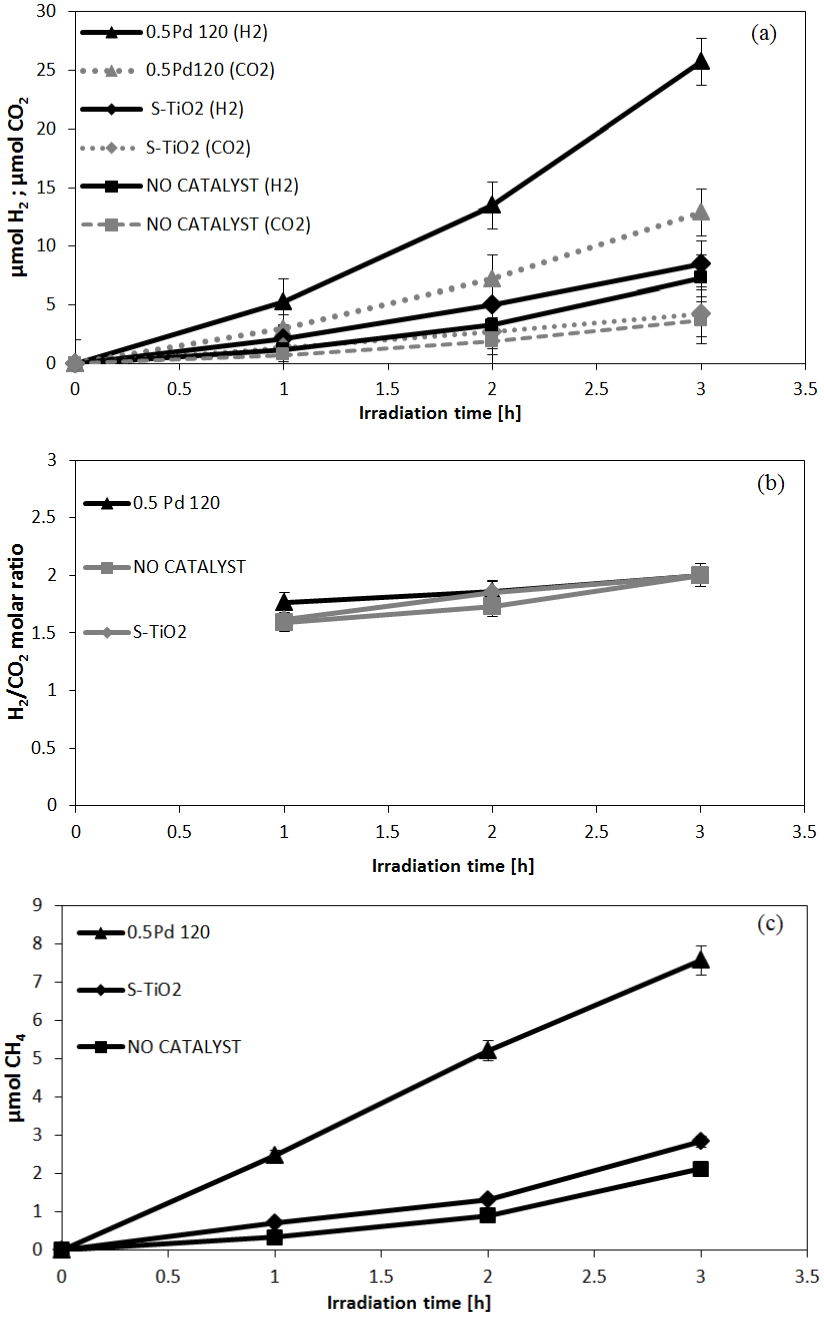

Figure III.1.7. *Control tests with UV as standalone process and under photocatalytic conditions with UV/S-TiO_2 and UV/0.5Pd120: H_2 and CH_4 production (a), H_2/CO_2 molar ratio (b) and CH_4 production (c).*

The value of the H_2/CO_2 molar ratio did not change significantly as irradiation time increased, tending to a value approximately equal to 2 after three hours of irradiation (Figure III.1.7b). CO_2 and H_2 are mainly produced from the photocatalytic wet reforming of glucose, according to the following reaction (1):

$$C_6H_{12}O_{6(l)} + 6H_2O_{(l)} = 6CO_{2(g)} + 12H_{2(g)} \quad \text{(III.3)}$$

The deposition of Pd (0.5Pd120) resulted in an increased methane production (7.58 μmol) and yield (2%) compared with the S-TiO_2 catalyst, for which CH_4 production and yield were about 2.8 μmol and 0.6%, respectively (figure III.1.7c).

In the absence of oxygen, methane could result from the degradation of glucose through the following reaction (2)(Kenney et al., 2002):

$$C_6H_{12}O_6(l) = 3CH_4(g) + 3CO_2(g) \quad \text{(III.4)}$$

Since CO_2 mainly comes from the photocatalytic wet reforming of glucose (1), as confirmed by the molar ratio H_2/CO_2 being equal to 2, CH_4 could be formed through the following reaction (3), similar to anaerobic digestion:

$$C_6H_{12}O_6\ (l) + 6\ H_2O\ (l) = 6CH_4\ (g) + 6O_2\ (g) \quad \text{(III.5)}$$

This result is confirmed by the analysis of the liquid phase after 3 hours of irradiation, which showed the presence of gluconic acid (Figure III.1.8), a typical product of glucose oxidation. Therefore, the oxygen produced according to Eq. 3 possibly reacts with glucose, leading to the formation of gluconic acid. The presence of the latter was detected by spectrophotometric analysis of the liquid sample whose result is reported in Figure III.1.8; gluconic acid is represented by a band with a peak at a wavelength of 264 nm. The presence of any intermediate compounds that have been produced by the oxidation of glucose, such as gluconic acid, is important because they may possibly be recovered and used for different purposes (food, pharmaceutical and hygienic products) (Ramachandran et al., 2006).

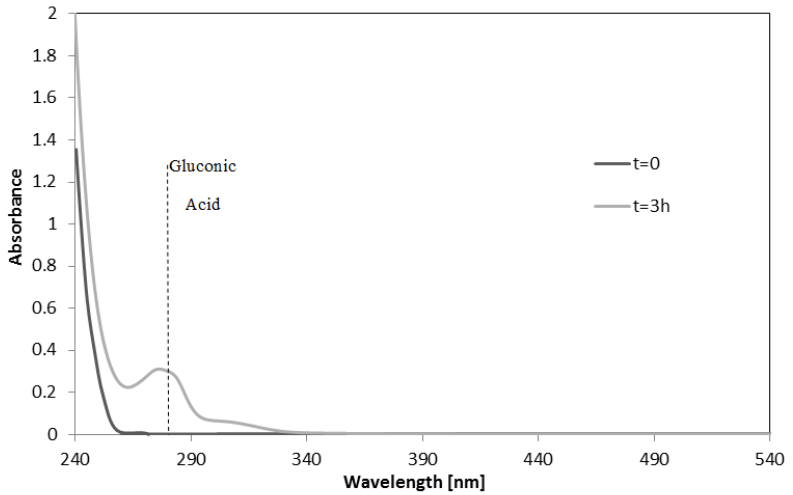

Figure III.1.8. *Spectrophotometric analysis of the aqueous solution before and after treatment with 0.5Pd120 catalyst.*

Glucose conversions observed during S-TiO_2 and Pd-TiO_2 photocatalytic treatment after 3 hours of irradiation are shown in Figure III.1.9. The photocatalytic activity of Pd-TiO_2 was influenced by the photodeposition time and by the content of palladium used in the synthesis of the photocatalysts. The increase in the photodeposition time up to 120 min had a positive effect on the TiO_2 photoactivity for 0.5 wt.% of Pd loading. Glucose conversion values obtained with the catalysts with 2wt.% of Pd content were lower than those obtained with the catalysts with 0.5 wt.% of Pd loading, for both deposition times investigated. In particular, the best catalyst for the conversion of glucose was 0.5Pd120, for which the glucose conversion was as high as 26%.

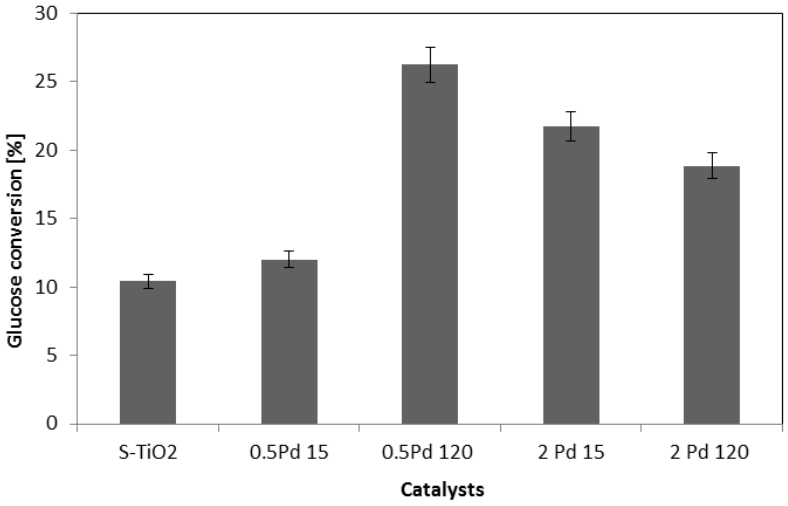

Figure III.1.9. *Glucose conversion after photocatalytic treatment by S-TiO_2 and Pd-TiO_2 catalysts (3h irradiation time).*

This result is in agreement with the production of hydrogen and methane (Figure III.1.10); the highest production of H_2 and CH_4 was observed for the catalyst 0.5Pd120. In particular, on this catalyst it is possible to obtain 0.65 mmol/g_{cat} of H_2 and 0.18 mmol/gcat of CH_4 .

It is very important to note that the hydrogen production is very similar to that obtained by using a UV lamp with a nominal power of 125 W (Colmenares et al., 2011).

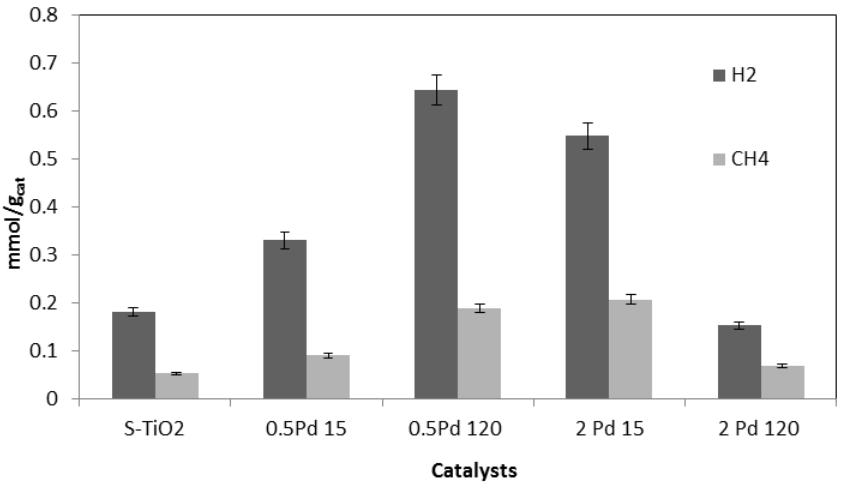

Figure III.1.10.*H_2 and CH_4 production after photocatalytic treatment by S-TiO_2 and Pd-TiO_2 catalysts (3 hours irradiation time).*

The behavior observed could be explained taking into account that in the analyzed photocatalysts partially oxidized Pd species and metallic Pd were detected. These species could be responsible for the differences observed in the glucose conversion and hydrogen production in the glucose reforming over Pd-TiO_2 photocatalysts. The catalyst prepared with 0.5 wt.% Pd loading and 120 min of photodeposition time resulted in the highest glucose conversion and H_2 production. The highest performances are possibly related to a homogeneous Pd nanoparticle distribution over the TiO_2 surface with sizes lower than 4 nm (as observed by TEM analysis) and Pd^0 oxidation state (according to XPS analysis, metal preferentially occurs in its metallic state (Pd^0)).

For the catalysts with a Pd content higher than 0.5 wt%, the presence of $Pd^{\delta+}$ species on the TiO_2 surface could induce a preferential Pd photodeposition on these species, not over TiO_2, leading to an increase in the Pd particle size. Moreover, the metal oxidation state can modify the adsorption of glucose on the photocatalyst surface, thus determining a different catalytic activity.

III.1.2.2 Optimization of catalyst dosage for photocatalytic tests

The optimization of the catalyst dosage was carried out under UV irradiation by testing different concentrations of 0.5Pd120 photocatalysts, in the range 0.125-1 g/L. Photocatalytic efficiency increased as catalyst loading was increased up to 0.25 g/L. As catalyst loading was further increased, the conversion of glucose and the simultaneous formation of H_2 and CH_4 decreased (Figure III.1.11).

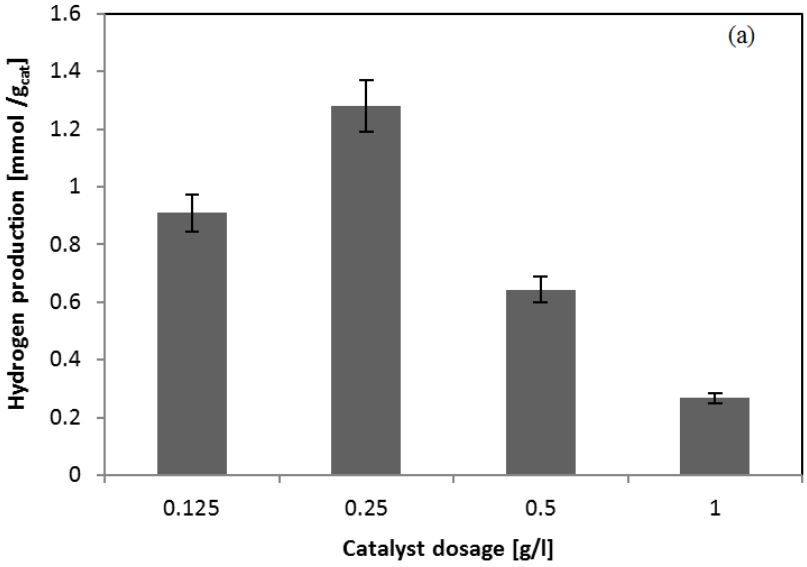
(a)
Hydrogen production [mmol /gcat]
1.6
1.4
1.2
1
0.8
0.6
0.4
0.2
0
0.125
0.25
0.5
1
Catalyst dosage [g/l]

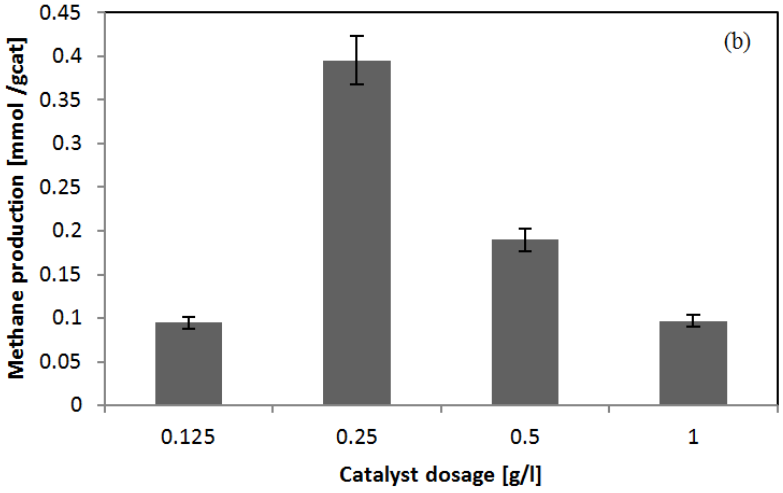
(b)
Methane production [mmol /gcat]
0.45
0.4
0.35
0.3
0.25
0.2
0.15
0.1
0.05
0
0.125
0.25
0.5
1
Catalyst dosage [g/l]

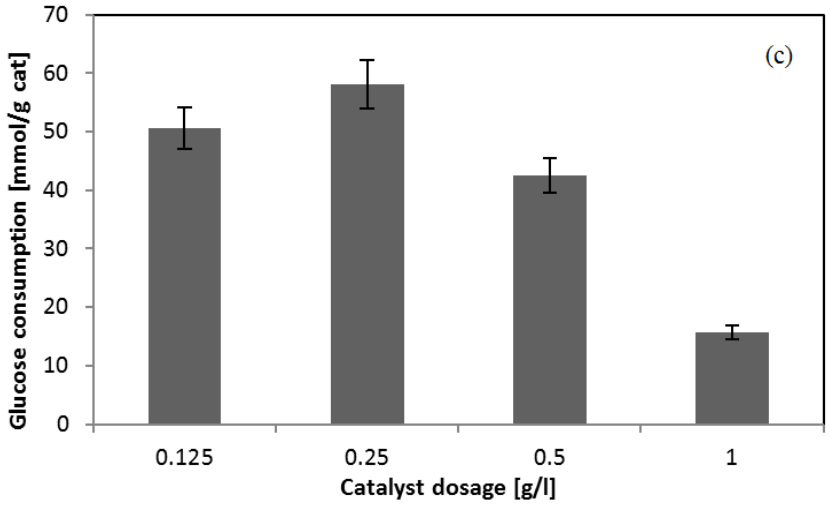

Figure III.1.11. *Optimization of catalyst loading according to hydrogen (a) and methane(b) production, and glucose conversion (c).*

Possibly, the increase in the catalyst dosage over the optimum value resulted in a decreased light penetration through the solution because of the increased opacity of the aqueous suspension (Sannino et al., 2012a).

III.1.2.3 Influence of initial pH of solution

The effect of the pH on the production of hydrogen (Figure III.1.12a) and methane (Figure III.1.12b) as well as on the conversion of glucose (Figure III.1.12c) was evaluated. The specific conversion of glucose increased as the solution pH was increased. The effects of pH on hydrogen generation are considered to be quite complex, involving the changes of the chemical state of glucose, redox potential of H^+/H_2 and relative position of the band edges of the semiconductor. At lower pH values (pH=3), the redox potential of H^+/H_2 would become more positive, which is advantageous for efficient hydrogen generation (Jing et al., 2010b). However, the most favorable condition for methane production is alkaline solution. Accordingly, the highest methane production was observed at pH 11 (about twice that at pH 3). Possibly, when the redox potential of $H+/H_2$ becomes more negative and the pH of the solution is similar to the p_{ka} of glucose, the methane production is enhanced.

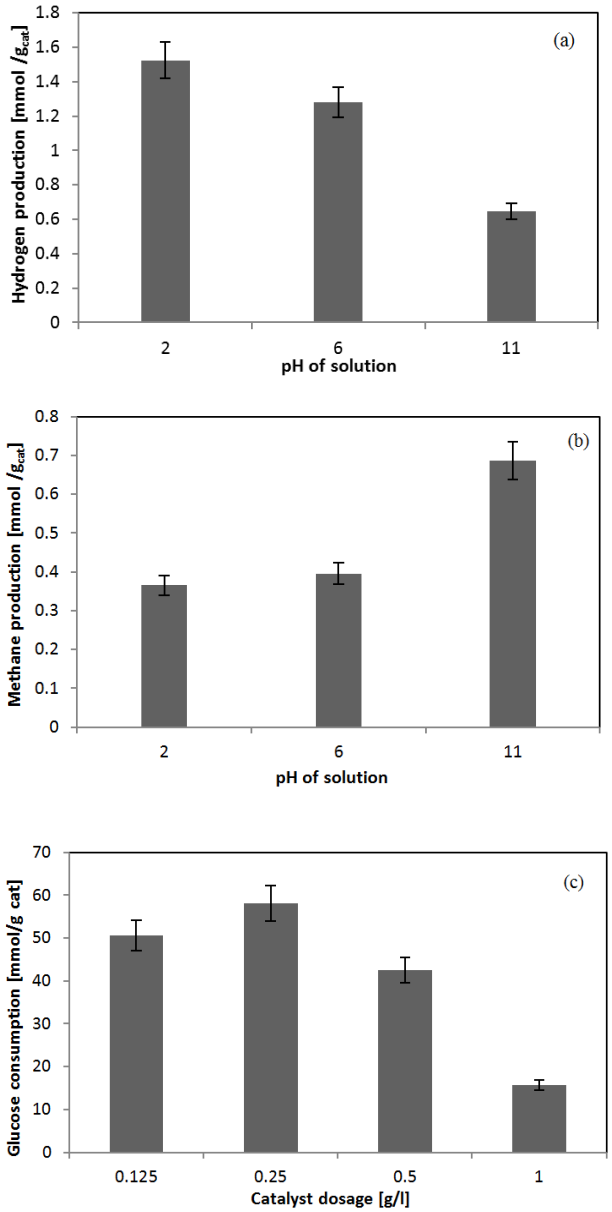

Figure III.1.12. *Effect of initial pH on hydrogen (a) and methane (b) production, and, glucose conversion (c).*

So, Pd deposition onto the sulfated TiO_2 surface throughout the photodeposition time was favorable to the production of H_2 or CH_4 by photocatalysis. The experimental conditions during photodeposition, such as deposition time, were found to have a strong influence on the final properties

of the materials, and consequently on their photocatalytic activity in glucose reforming. A short deposition time (15 min) led to a smaller average particle size and higher dispersion of the palladium on the sulfated TiO_2 surface, as well as a higher fraction of the metal in its metallic state. These features resulted in a good photocatalytic performance in terms of glucose conversion. The best photocatalytic behavior was observed in the sample prepared with 0.5 wt.% of palladium and 120 min of photodeposition time.

By changing the pH of the solution it is possible to modulate the performance of the photocatalytic reaction, producing more methane in alkaline conditions or more hydrogen in acidic conditions.

III.2 Fluorinated and platinized TiO_2 catalysts

The properties of TiO_2 such as surface area, surface charge, crystallinity, particle size and lattice defects affect photocatalytic activities in a complex way. The surface of TiO_2 is particularly important in determining the photocatalytic reaction kinetics, mechanisms, and efficiencies because the photocatalytic reactions mostly take place on the surface of the TiO_2[20]. Surface modifications of semiconductor photocatalysts may have a marked influence on the photocatalytic processes occurring at the water–semiconductor interface (Kim et al., 2008). With respect to commercial titania samples, TiO_2 modified with fluorine (F–TiO_2) inhibits the recombination rate of holes and free electrons, enhancing the photocatalytic activity in the removal of pollutants from aqueous samples (Yang et al., 2007). In particular, it has been reported that F–TiO_2 is an effective material in the photocatalytic removal of not biodegradable contaminants (such as phenol or methylene blue) (Yu et al., 2009, Yang et al., 2007).

Despite noble metals modified TiO_2 (in particular Pt/TiO_2) photocatalysts were studied for the hydrogen production by photocatalytic reforming of organic substance such as methanol (Murcia et al., 2015a), no article reports the use of F–TiO_2 as support for noble metals in the photocatalytic production of hydrogen from water polluted by organic compounds. For this reason, platinized F–TiO_2 photocatalysts were studied with the aim to producing hydrogen from the degradation of glucose. The effect of the TiO_2 source, the TiO_2 fluorination, the presence of Pt nanoparticles and the initial pH of the reaction solution over the hydrogen evolution and glucose degradation were investigated.

III.2.1 Photocatalyst preparation and characterization

TiO_2 was prepared by hydrolysis of titanium tetraisopropoxide in isopropanol solution by the slow addition of distilled water (volume ratio isopropanol/water 1:1). The powder was recovered by filtration and dried at 110 C overnight. A fraction of this material was calcined at 650 C for 2 h and the sample thus obtained was called home prepared TiO_2 (hp–TiO_2). Commercial TiO_2 Evonik P25 was used as received. Fluorinated samples were prepared by adding 10 mM NaF to an aqueous suspension of uncalcined hp–TiO_2 or P25, and these materials were named F–TiO_2 and F–P25, respectively. In order to maximize fluoride adsorption, the pH was adjusted to 3 using 1 M HCl solution (Yu et al., 2009). This suspension was stirred for 1 h in the dark. In order to compare the effect of the TiO_2 modification by fluorination or sulfation, hp–TiO_2 was immersed in a 1 M H_2SO_4 solution and stirred for 1 h. Precipitate of fluorinated or sulfated TiO_2 (S–TiO_2) was recovered by filtration, dried and calcined at 650 C for 2 h. Platinum was deposited on the surface of the fluorinated or sulfated samples by photodeposition method, using hexachloroplatinic acid (H_2PtCl6, Aldrich 99.9%) as metal precursor. The final amount of Pt was 0.5 wt.%. A suspension of the corresponding F–TiO_2, F–P25 or S–TiO_2 sample in distilled water containing isopropanol (Merck 99.8%) and the appropriate amount of H_2PtCl6 used as precursor for Pt nanoparticles was prepared. Pt photodeposition was then performed under an inert atmosphere (N_2), by illuminating the suspension for 120 min with an Osram Ultra-Vitalux lamp (300 W) which possesses a sun-like radiation spectrum with a main emission line in the UVA range at 365 nm. Light intensity on the suspensions, used for the photodeposition of platinum, was 60 W/m^2 (Nomikos et al., 2014).

After photodeposition, the powders were recovered by filtration and dried at 110 C overnight. All the prepared photocatalysts with characterization results are reported in Table III.2.

Table III.2 *Summary of the characterization results*

Photocatalyst	**$D_{Anatase}$ (nm)**	**S_{BET} (m^2/g)**	**Band gap (eV)**
S-TiO_2	0	-	-
0.5Pd 15	0.5	15	0.18
0.5Pd 15	0.5	120	0.20
2 Pd 15	2	15	0.34
2Pd 120	2	120	0.80

III.2.1.1. X-ray diffraction results

XRD analysis showed that hp-TiO_2 and P25 samples contain rutile and anatase phases (Figure III.2.1); the anatase to rutile ratio for these samples was 90:10 and 80:20, respectively. XRD analysis also showed that only anatase phase results from fluorination process in F-TiO_2 (home prepared sample) catalyst, according to previous works that had documented how fluorination inhibits the formation of rutile phase of TiO_2 during the

calcination process (Murcia et al., 2015b, Trapalis et al., 2008). In the case of P25, after fluorination and calcination, anatase: rutile ratio is almost the same. The anatase crystallite size ($D_{anatase}$) calculated by the Scherrer equation from the (1 0 1) peak of the XRD pattern are listed in Table III.2. As observed, hp-TiO_2 presents the lowest value and after fluorination this value notably increases. This result is in agreement with previous studies where it was observed that fluoride enhanced the crystallization of anatase phase and promoted the growth of crystallites (Yu et al., 2010, Yamabi and Imai, 2002)

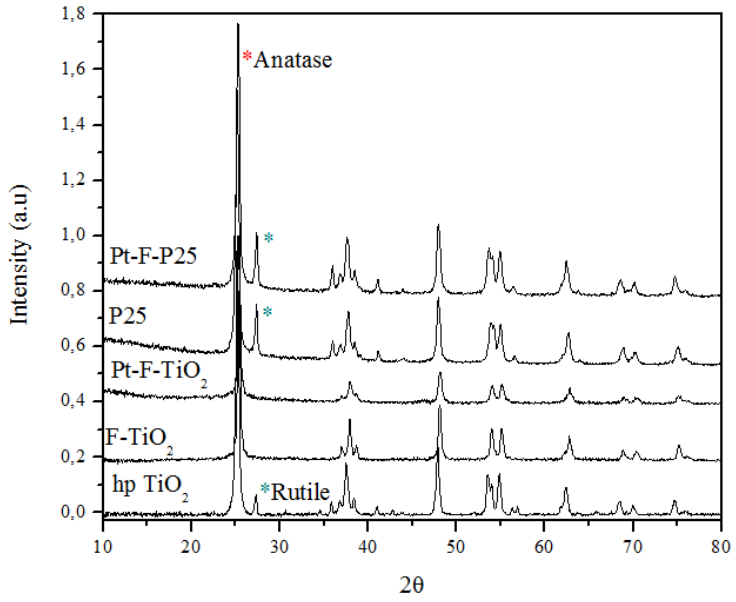

Figura III.2.1 *XRD patterns for home prepared and commercial TiO_2 modified by simultaneous fluorination and Pt photodeposition*

III.2.1.2 BET Surface Area

BET surface area values (SBET) for all samples are shown in Table 1. Hp-TiO_2 presents the lowest specific surface area (11 m^2/g); this can be due to the large degree of particles sintering during the calcination process(Murcia et al., 2015a). As it can be observed the SBET of hp-TiO_2 considerably increases after fluorination or sulfation; in fact these ions protect anatase phase against rutilization and sintering, preserving the surface area during the calcination process (Murcia et al., 2015a). The fluorination of P25 did not induce significant modification on this parameter. It was also observed that Pt addition induces a slight decrease in the SBET value; this is probably due to pore blocking by metal deposits on the modified TiO_2 surface.

III.2.1.3 UV-Vis Diffuse Reflectance spectra

The light absorption properties of the photocatalysts were evaluated by UV-Vis DRS analysis (Figure III.2.2) and it was observed a slight increase of the absorption throughout the visible range of the spectrum in the fluorinated and platinized samples; this is mainly due to the grey color of these materials. In the platinized catalysts (inset in Figure III.2.2), three small peaks located at ca. 450, 520 and 700 nm were observed; these peaks can be attributed to the Pt clusters and to the visible-light-induced electron transfer from the Pt nanoparticles to the TiO_2 particle (Maicu et al., 2011). Surface plasmon resonance of Pt nanoparticles excited by visible light facilitates the excitation of the surface electron and promotes interfacial electron transfer process, thus improving the TiO_2 photoactivity.

The band gap values calculated for the samples are presented in Table III.2, as it can be observed this parameter does not significantly modified by the different treatments applied to TiO_2.

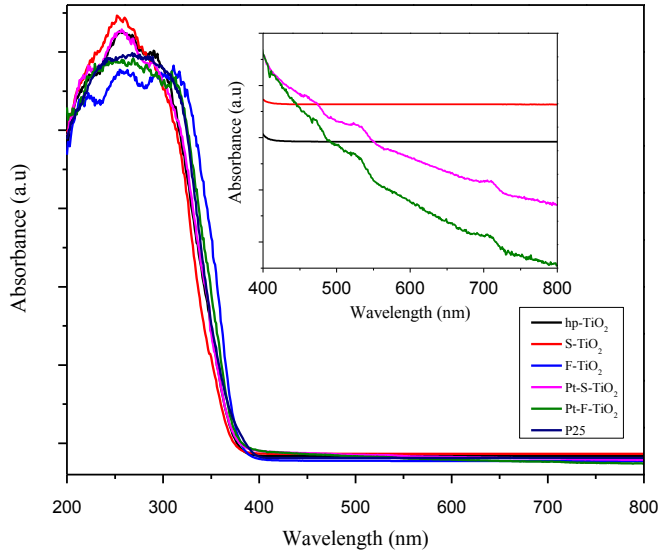

Figure III.2.2. *UV-Vis DR spectra for the photocatalysts analyzed.*

III.2.1.4 X-ray fluorescence

Chemical composition of the samples was evaluated by XRF and it was observed that the real platinum content was 0.36 and 0.39 % for Pt-F-P25 and Pt-F-TiO_2, respectively. These values are under the nominal metal content (0.5 wt%) thus indicating an incomplete reduction of the metal

precursor during the synthesis. A negligible amount of Cl^- species, remained on the platinized solids after preparation, was detected (i.e <0.02 wt %). F or Na species were not detected by XRF.

III.2.1.5 Microscopic analysis

Morphology of the samples was studied by SEM and selected images are presented in Figure III.2.3. As it can be observed the platinum particles in the Pt-S-TiO_2 sample are higher than the fluorinated and platinized photocatalyst. In order to achieve an accurate identification of the platinum particles in the samples, analyzes by EDX were also performed. In Figure III.2.3 c, it is evident that platinum particles are present in the Pt-S-TiO_2 sample, together with other elements such as titanium, oxygen and sulfur, coming from the sulfated titania. Other EDX spectra are not shown for the sake of brevity, but in all of them were also identified Pt, Ti, O or F species.

Platinum particles size was evaluated by TEM and selected micrographs for platinized samples are presented in Figure III.2.4. As it can be seen, in the platinized samples, the Pt nanoparticles can be identified as small black

dots. In the Pt-S-TiO_2 sample, platinum particles are homogeneously distributed on TiO_2 surface. It is worthwhile noting that Pt-F-TiO_2 sample is the only catalyst having Pt nanoparticles in the range 1-2 nm. Moreover, the aggregation of Pt particles heterogeneously distributed on titania surface was clearly observed in the Pt-F-P25 sample (Figure III.2.4c). The Pt particle size distribution (*fi*) is also presented in Figure III.4. The highest Pt particle size (i.e 9-10 nm) was obtained in the Pt-F-P25 sample; this result could be due to the presence of the rutile phase in this catalyst that makes difficult the homogeneous photodeposition of the metal particles on the titania surface. The best Pt particles dispersion was observed in the catalyst Pt-S-TiO_2 (Figure III.4a), in this sample the particles are more homogeneously distributed on surface with sizes between 4-5 nm.

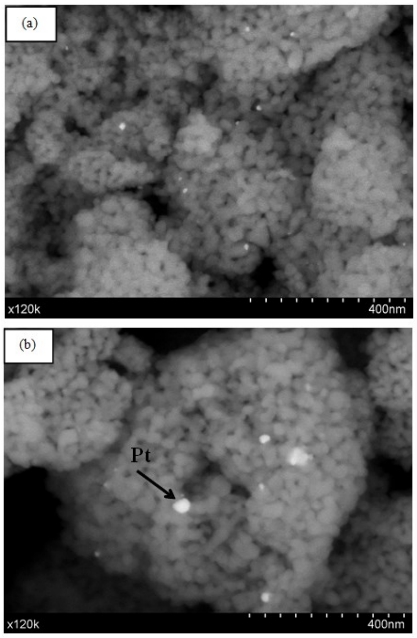

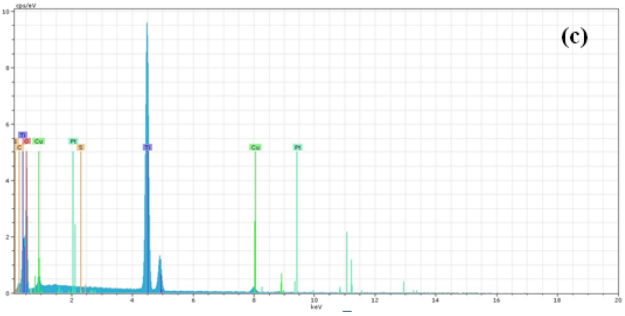

Figure III.2.3. *SEM images for analyzed samples. (a) Pt-S-TiO_2, (b) Pt-F-TiO_2 and (c) EDX identification of the Pt-S-TiO_2 sample.*

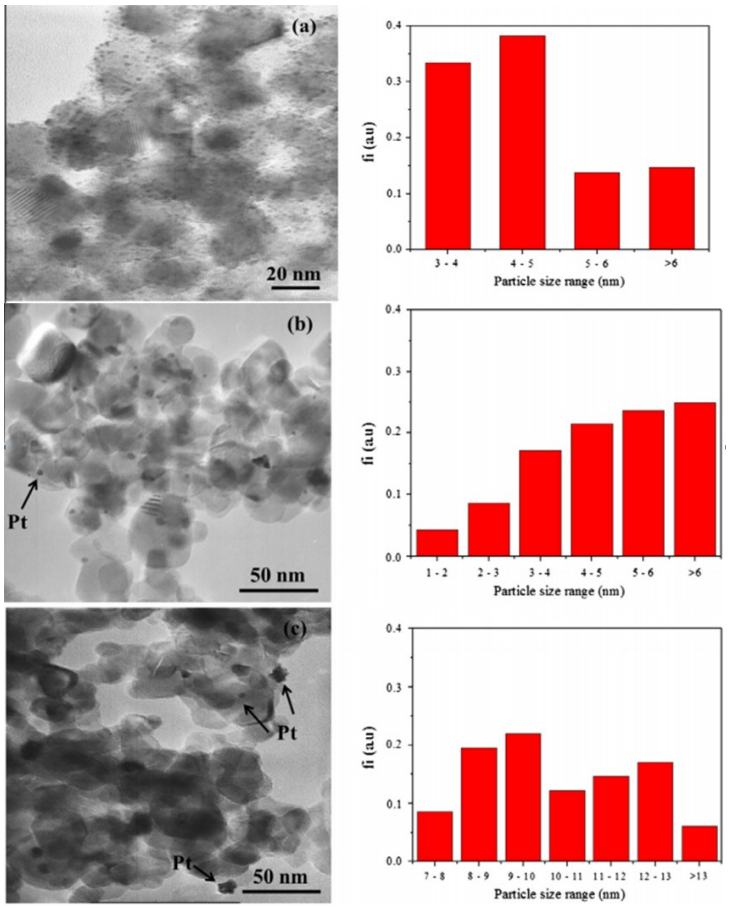

Figure III.2.4. *TEM images for analyzed samples. (a) Pt-S-TiO_2, (b) Pt-F-TiO_2 and (c) Pt-F-P25.*

III.2.1.6 X-ray photoelectron spectroscopy (XPS)

XPS measurements for all the samples were also performed and the obtained spectra are showed in Figure III.2.5. In the O 1s region, a peak located at binding energy of 529.6 ± 0.2 eV was detected for all the samples, corresponding to O_2- in the TiO_2 network. In addition, broad shoulder at higher binding energies (530.3 eV) ascribed to oxygen in surface hydroxyl groups were also observed. On the other hand, the Ti 2p core level spectra were similar for all the studied samples with peaks of binding energies located at 458 ± 0.5 eV, ascribed toTi4+ as the main component.

XPS analysis detected also the presence of Na and fluoride species on the surface fluorinated samples, indicating that ≡Ti-OH_2 species could be substituted by ≡Ti-F (Vohra et al., 2003, Yamabi and Imai, 2002, Trapalis et al., 2008, Yan et al., 2009).

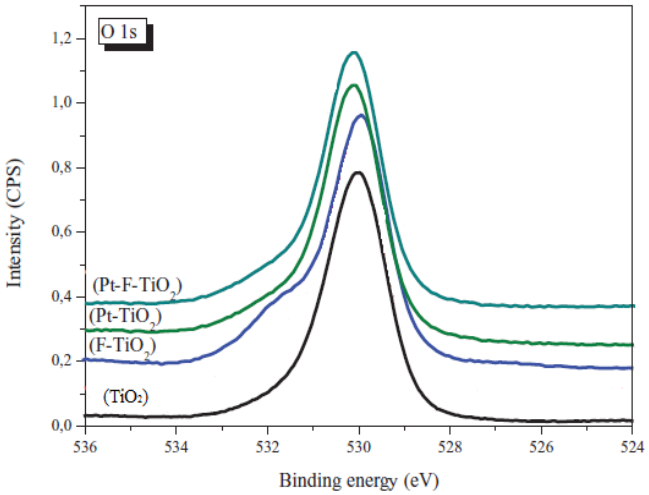

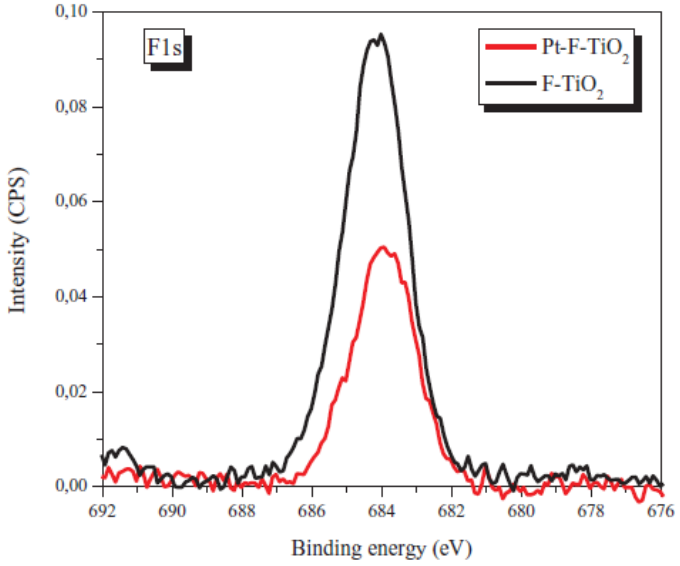

Figure III.2.5. *XPS core level spectra of O 1s and F 1s regions for selected samples.*

III.2.2 Photocatalytic activity

In a typical photocatalytic test, 0.12 g of catalyst was suspended in 80 ml aqueous solution containing 2000 mg/L of glucose (D + Glucose VWR, Sigma Aldrich). The suspension was left in dark condition for 2 h to reach the adsorption– desorption equilibrium of glucose on the photocatalyst surface, and then photocatalytic reaction was initiated under UV light up to 3 h. In order to evaluate the influence of the initial pH of the solution on the production of H_2 and CO_2, the pH of solution was adjusted by adding nitric acid (Baker Analyzed, 65%) or Ammonium Hydroxide (Baker Analyzed, 30%).

Hydrogen yield was evaluated according to the following relationship

(Vaiano et al., 2015a)

$$R_{H_2} = \frac{2 \cdot nH_2}{12 \cdot n^0 C_6 H_{12} O_6} \cdot 100 \quad \text{(III.6)}$$

Where:

RH_2=hydrogen yield;

nH_2=moles of H_2 produced during the irradiation;

$n^0C_6H_{12}O_6$ = moles of glucose after dark adsorption.

The quantum efficiency (QE) of photocatalysts was calculated according to the following equation (Yan et al., 2009):

$$QE[\%] = \frac{N_{H_2} \cdot 2}{N_{photons}} \cdot 100 \quad \text{(III.7)}$$

Where:

N_{H2}= number of evolved H_2 molecules per second;

$N_{photons}$= number of incident photons per second.

The number of incident photons on the external surface of the photoreactor was 2.014×10^{16} photons/s, measured by using a LMV UV-Meter,

III.2.2.1 Hydrogen production and glucose degradation for the different fluorinated photocatalysts

Figure III.2.6a and III.2.6b show respectively, the relative glucose concentration (C/C_0) and hydrogen production during the exposition to UV-LEDs irradiation at the spontaneous pH of solution (pH=6) for all the photocatalysts. As expected, no H_2 production was observed in the absence of Pt. On the contrary, the photocatalytic H_2 production from the glucose solution can be significantly enhanced in presence of Pt on TiO_2 surface. In particular, the highest glucose degradation and H_2 production was achieved on Pt-F-TiO_2 catalyst (about 100 µmol after 3 hours of irradiation). This can be due to the presence of the platinum and to its lower particle size

distribution and better dispersion of the metal nanoparticles over the anatase surface of F-TiO_2 photocatalyst with respect to F-P25 photocatalyst. Moreover, Pt-F-TiO_2 was also found to be the best photocatalyst for glucose degradation (74% removal after 3 hours of irradiation). For Pt-F-P25 and Pt-F-TiO2, the only detected byproduct was CO_2 (4.4 μmol).

In Table III.2, the H_2 evolution rate and QE values over Pt-F-TiO_2 and Pt-F-P25 catalysts are given. For Pt-F-P25 the H_2 formation rate is estimated to be 0.1 mmol h^{-1}, corresponding to a QE of 17%. Both values are remarkably increased for Pt-F-TiO_2, reaching values equal to 0.3 mmol h^{-1} and 56 % for H_2 evolution rate and QE, respectively.

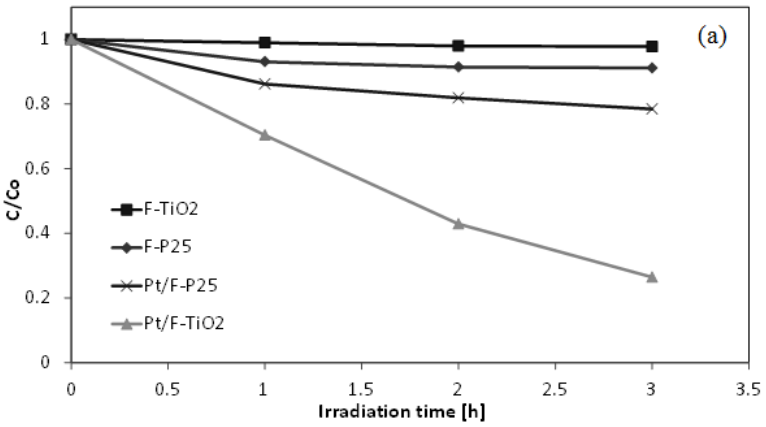

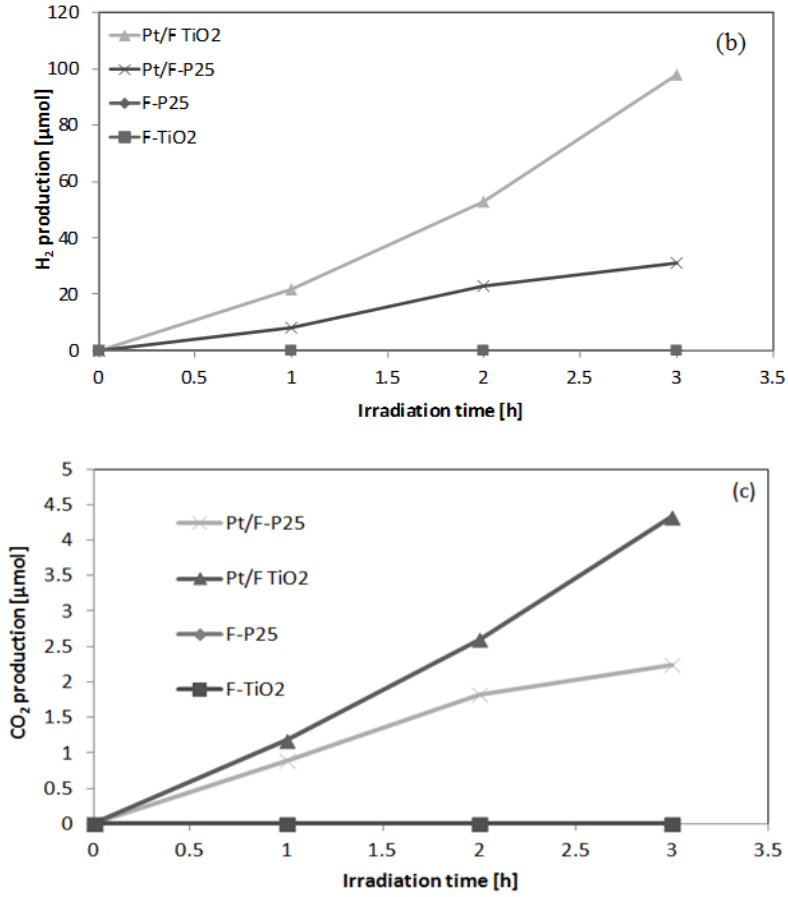

Figure III.2.6. *Behavior of glucose normalized concentration (a) H_2 (b) and CO_2 (c) production as a function of irradiation time; catalyst dose: 1.5 g/L; initial glucose concentration: 2000 mg/L; pH=6.*

III.2.2.2 Comparison between the photocatalytic activity of Fluorinated and Sulfated platinized TiO_2

Home prepared sulfated titania (Pt-S-TiO_2) performances in terms of glucose degradation (Figure III.2.7a) and H_2 production (Figure III.2.7b) containing the same nominal weight of platinum (0.5 wt %) were compared with home prepared Pt-F-TiO_2. After 3 hours of UV irradiation, the degradation of glucose on Pt-S-TiO_2 (Figure III.2.7a) is equal to 57 % and the H_2 production (Figure III.2.7b) is equal to 82 µmol (H_2 yield of 2%), lower than that obtained with fluorinated titania (glucose degradation and H_2 yield equal to 74% and 4%, respectively). These results are in agreement with scientific literature regarding photocatalytic activity of F-TiO_2 in both

the removal of pollutants from wastewater and hydrogen production (Kim et al., 2008).

The sulfation of TiO_2 surface was carried out for two reasons; firstly, sulfation pre-treatment leads to a stabilization of the TiO_2 anatase crystalline phase and surface area against sintering during the calcination process (as it can be seen in Table III.2, sulfation considerably increases the SBET value of hp-TiO_2); secondly, a dehydroxylation process of the excess of adsorbed protons takes place during calcination of sulfated titania, leading to the creation of surface oxygen vacancies and promoting the separation of photogenerated charges, thus, improving the TiO_2 photocatalytic efficiency (Maicu et al., 2011, Li et al., 2010, Tandon and Gupta, 1970). The oxygen vacancies also has been reported to be preferential sites for Pt photodeposition (Maicu et al., 2011); in fact, as it was observed by TEM (Figure III.2.4a), the Pt-S-TiO_2 sample presents the highest number of Pt nanoparticles homogeneously covering the hp-TiO_2 surface. Taking into account the previous assumptions, it could be expected that sulfated and platinized TiO_2 shows the better performance in glucose photodegradation and therefore the highest H_2 production, but, as it was observed in this work, this photocatalyst presents lower glucose degradation and H_2 yield compared with their counterpart Pt-F-TiO_2.

This behavior can be mainly due to the increase of photocatalytic activity of the fluorinated sample by the formation of unbounded •OH that are more reactive than •OH trapped on catalyst surface (Park et al., 2013b, Yu et al., 2009), thus leading to the better photocatalytic performance. These results also can be related to the highest absorption of the fluorinated sample in the visible region (Figure III.2.2) that could favor the TiO_2 photoefficiency in the glucose degradation. It is also important to consider that the high number of Pt nanoparticles on TiO_2 surface can limit the adsorption of the glucose on the photocatalyst surface, thus reducing the degradation rate of this substrate.

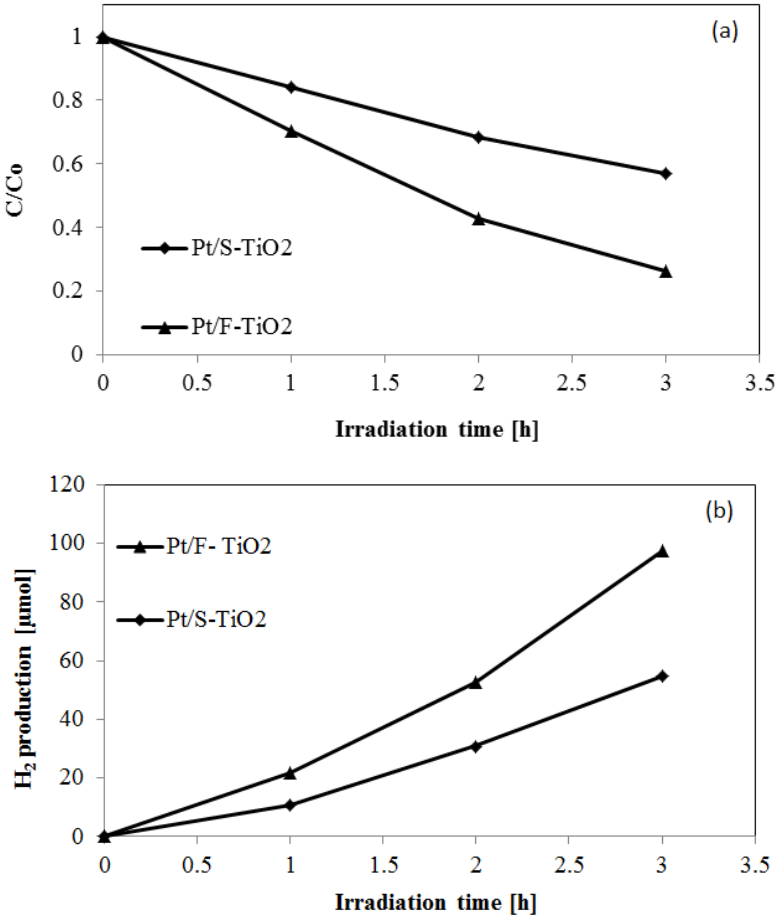

Figure III.2.7. *Behavior of glucose normalized concentration (a) and H_2 rate (b) during irradiation of fluorinated and sulfated TiO_2; catalyst dose: 1.5 g/L; initial glucose concentration: 2000 mg/L; pH=6.*

III.2.2.3 Effect of initial pH

Due to higher performances of Pt-F-TiO_2, this catalyst was chosen to evaluate the effect of initial pH over both the degradation of glucose and the production of hydrogen (Figure III.2.8). The degradation of glucose is higher at pH=6, reaching a value equal to 73% (Figure III.2.8a) while the best hydrogen evolution rate was obtained at pH=2 (Figure III.2.8b). It has been reported that, in acidic conditions, the redox potential of H^+/H_2 would become more positive, and this condition is advantageous for an efficient hydrogen photocatalytic generation (Jing et al., 2010b). Accordingly, the higher hydrogen yield was obtained in acidic condition (3 % after 3 hours of irradiation; H_2 production: 590 µmol h^{-1} g^{-1}). However, at pH=2, when the

glucose in the solution is mainly in molecular form, the degradation of glucose occurs in limited extent.

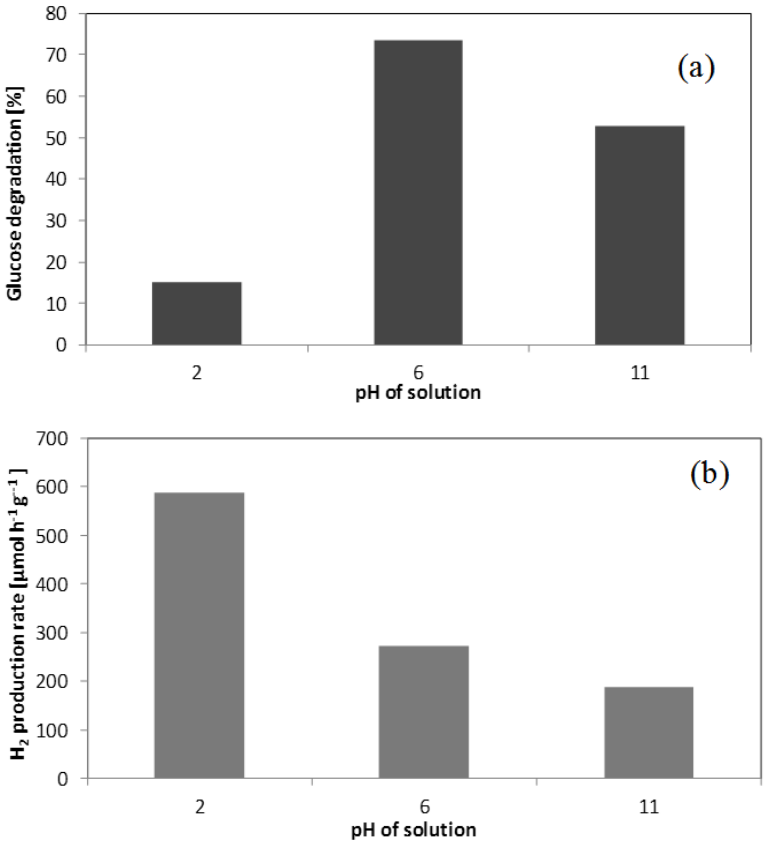

Figure III.2.8. *Effect of initial pH on glucose degradation (a) and H_2 production rate (b) for Pt-F-TiO_2 after 3 hours of irradiation; catalysts dose: 1.5 g/L; initial glucose concentration: 2000 mg/L.*

III.2.2.4 Possible reaction mechanism

It was also proposed a possible reaction mechanism for the photocatalytic hydrogen production from glucose aqueous solution. Usually, in the literature, the mechanism for the H_2 production is explained according to the classical reaction of glucose photoreforming (Fu et al., 2010) :

$$C_6H_{12}O_6(l) + 6\ H_2O(l) = 6\ CO_2(g) + 12\ H_2(l) \qquad \text{(III.8)}$$

In this reaction the H_2/CO_2 ratio is equal to 2. However, in our case, this ratio is never equal to 2, but it is in the range between 10 and 30, as it is possible to evince from experimental data reported in Figure 6. This indicates that the mechanism of production of H_2 from glucose does not take place according to the Eq.1. Moreover, from HPLC results, no formation of intermediate compounds resulting from the glucose conversion, such as arabinose (Li et al., 2010, Vohra et al., 2003), erythrose, glyceraldehyde or formic acid (Chong et al., 2014a) was observed during the irradiation. In fact, in the HPLC chromatogram obtained after 3 hours of UV irradiation, only the signal related to glucose was visible, with a peak that decreased with respect to the initial solution (Figure III.2.9). It is possible to highlight that there was not the presence of arabinose, which should appear in a different retention time from glucose (Figure III.2.10).

This result can be explained considering that the selectivity of the photocatalyst to arabinose and erythrose is influenced by the different crystalline phases of TiO_2 (anatase or rutile). In fact, literature data (Chong et al., 2014a) reports that the anatase TiO_2 displayed a lower selectivity to arabinose and erythrose than rutile phase. In our case, the crystalline phase of TiO_2 in Pt-F-TiO_2 catalyst is precisely in anatase form. The latter allows the cleavage C–C bond of glucose molecules adsorbed on photocatalyst surface more effectively than rutile phase(Chong et al., 2014a). For this reason, probably, the formation of arabinose and erythrose on Pt-F-TiO_2 is inhibited and the degradation of glucose to H_2, CO_2 and gluconic acid is promoted. This last observation has been confirmed by UV Vis spectrophotometric analysis that evidenced the presence of gluconic acid ($C_6H_{12}O_7$) as sole intermediate detected in the solution after 3 hours of UV irradiation.

Therefore, in agreement with the literature results (Li et al., 2010), a possible reaction mechanism for the photocatalytic H_2 production from glucose on Pt-F-TiO_2, providing the presence of gluconic acid in solution, is the following:

$$h^+ + H_2O = \bullet OH + H^+ \quad \text{(III.9)}$$

$$h^+ + OH^- = \bullet OH \quad \text{(III.10)}$$

$$H^+ + e^- = \tfrac{1}{2}\, H_2 \text{ (on Pt)} \quad \text{(III.11)}$$

$$RCHO + \bullet OH = RCO\bullet + H_2O \quad \text{(III.12)}$$

or

$$h^+ + RCHO = RCO\bullet + H^+ \quad \text{(III.13)}$$

$$RCO\bullet + H_2O = RCOOH + \bullet H \quad \text{(III.14)}$$

$$RCOOH + \bullet OH = R'OH\ (R''CHO) + CO_2 + \bullet H \quad \text{(III.15)}$$

$$2e^- + 2H^+ = \bullet H + \bullet H \quad \text{(III.16)}$$

$$\bullet H + \bullet H = H_2 \quad \text{(III.17)}$$

Where:

$RCHO = C_6H_{12}O_6$

$RCOOH = C_6H_{12}O_7$

The reaction is initiated by the photoexcitation of Pt-F-TiO_2 photocatalyst, leading to the formation of electron–hole pairs. Valence band holes (h^+) can be filled by the surface water molecules or hydroxyl ions to form hydroxyl radicals (Eqs. III.9-10) (Li et al., 2010) . Pt can trap photogenerated conduction electron (e^-), and consequently the electron acceptor (H^+) interacts with the electron to produce hydrogen on Pt (Eq. III.12) (Chen et al., 2010c). Glucose (RCHO) adsorbed on the catalyst can react with the hydroxyl radicals (Eq. III.12) forming gluconic acid (Eq. III.14) which would react further with hydroxyl radicals so that a decarboxylation reaction takes place (Eq. III.15) (Hoffmann et al., 1995b). The holes could react also directly with electron donor glucose (Eq. III.13). The produced •H radicals can form H_2 (Eq.III.16-17). The amount of CO_2 produced (Eq. III.15) was found higher on Pt-F-TiO_2 than on Pt-S-TiO_2, indicating the higher reactivity of unbounded •OH (produced on Pt-F-TiO_2) than •OH trapped on catalyst surface (produced on Pt-S-TiO_2).

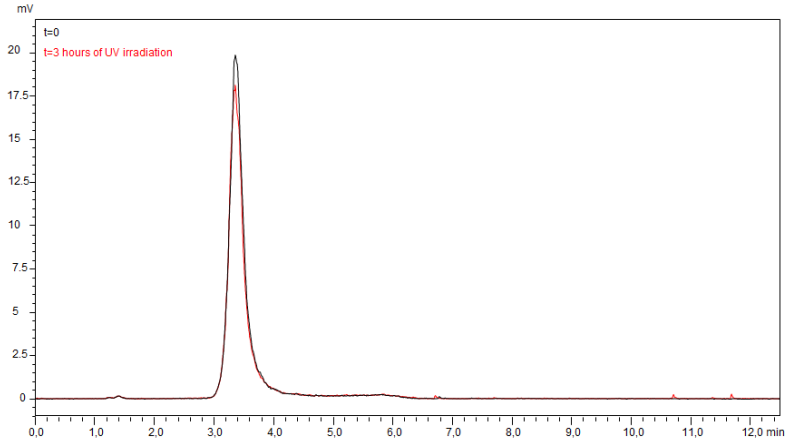

Figure III.2.9. *Typical HPLC chromatogram obtained during photocatalytic test on Pt-F-TiO_2 catalyst; initial glucose concentration : 2000 mg/L; initial pH =2.*

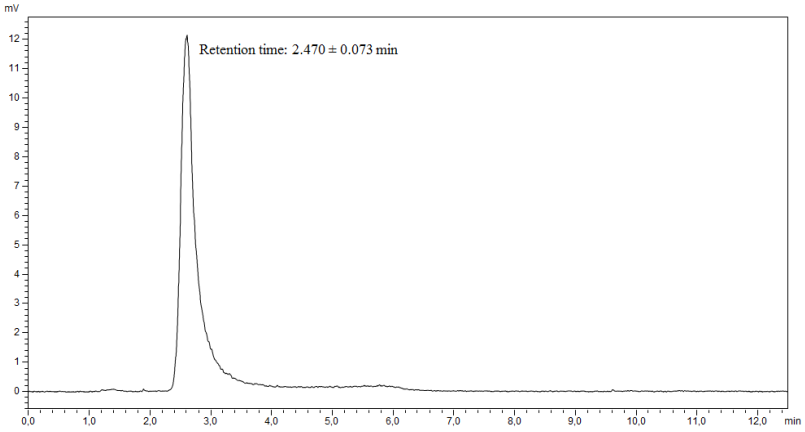

Figure III.2.10. *Typical HPLC chromatogram for a standard solution of arabinose.*

According to the results, fluorinated TiO_2 (F-TiO_2) represents an interesting support for noble metals to be used in the photocatalytic process for the hydrogen production sugars contained in water. In particular, Pt on F-TiO_2 (Pt-F-TiO_2) significantly enhanced the photocatalytic H_2 production compared to the other investigated catalysts. The increase of photocatalytic activity of Pt-F-TiO_2, with respect to Pt supported on sulfated TiO_2, is due to the formation of unbounded OH radicals that are more reactive, leading to a higher hydrogen production.

Experimental results: hydrogen and methane production from photocatalytic degradation of glucose on noble metals based photocatalysts

The higher hydrogen production was obtained under acidic conditions (pH=2), while the degradation of glucose was higher at pH=6. By HPLC and UV-Vis analyzes performed on the liquid samples, it was also confirmed that, using Pt-F-TiO_2, it is possible to produce hydrogen by the photocatalytic degradation of glucose obtaining gluconic acid as product.

IV Experimental results: hydrogen and methane production from photocatalytic degradation of glucose on perovskite based photocatalysts.

With respect the photocatalytc hydrogen production, titanium dioxide was the first material used for in the electrochemical water splitting reaction (Fujishima and Honda, 1972b) but different photocatalyst formulations like mixed oxides and perovskites, have been proposed and studied (Kudo, 2006). In particular, perovskite type photocatalysts are quite encouraging materials for water splitting owing to their stability in water. $LaFeO_3$ is one of the most common perovskite type oxide and a promising material with abundance of functionalities, having a general formula ABO_3, where position A is occupied by the rare earth ion, and position B by the transition metal ion. $LaFeO_3$ displays significant physical and chemical properties making them attractive in advanced technologies applications such as solid oxide fuel cells catalysts (Arendt et al., 2008), chemical sensors (Zhang et al., 2006), photocatalysis (Su et al., 2010) and biosensors (Thirumalairajan et al., 2012). The excellent catalytic activity of $LaFeO_3$ is related to its interesting properties such as high stability, non-toxicity and small band gap energy (2.07 eV), which make perovskite an interesting visible light active photocatalyst (Li et al., 2011).

The use of perovskites, particularly $LaFeO_3$, in the photocatalytic water splitting process has been reported in scientific literature but, typically, the use of sacrificial agents (such as ethanol) and co-catalysts based on noble metals, with the aim of enhance the production of H_2, is required (Parida et al., 2010, Li et al., 2007).

However, the use of $LaFeO_3$ for hydrogen production from sugar containing water has been never reported. Therefore, the effectiveness of the $LaFeO_3$ for hydrogen production during photocatalytic treatment of glucose

aqueous solutions was investigated under different light sources (UV or visible light irradiation by light-emitting diodes (LEDs)). In particular, it was first investigate the ability of undoped LaFeO3 in the photocatalytic hydrogen production and it was evaluated the performances of doped LaFeO3 using transition metals (suc as Rh and Ru) for enhance the photocatalytic hydrogen production from glucose solution under visible light.

IV.1 $LaFeO_3$ photocatalysts: Synthesis

$LaFeO_3$ was prepared by solution combustion synthesis using citric acid as organic fuel and metal nitrate as metal precursor (Hwang et al., 2010). Given amounts of $Fe(NO_3)_3 9H_2O$ (RiedeldeHaen, 97 wt%), $La(NO_3)_3 6H_2O$ (Fluka, 99%), and citric acid (Fluka, 99 wt%), were completely dissolved in 100 mL of distilled water, and the solution was kept under continuous stirring at 60 C. Ammonium hydroxide (Carlo Erba, 37 wt%) was slowly added to adjust the pH of the solution up to 7.0. The solution was dried at 130 C and then calcined at 300 °C for 3 h to ignite the solution combustion reaction.

Finally, three $LaFeO_3$ catalysts with different content of citric acid were prepared (Table IV.1). In a typical preparation citric acid, $La(NO_3)_3$ and $Fe(NO^3)^3$ in weight ratio 1/1.07/0.51 were used. In this way it was possible to evaluate the effect of the content of fuel on (i) the crystalline structure of the perovskite, (ii) the size of the crystallites and (iii) the photocatalytic activity.

Table IV.1.1 *List of photocatalysts and their characteristics*

Catalysts	**$La(NO_3)_3$ [g]**	**$Fe(NO_3)_3$ [g]**	**Citric acid [g]**	**SSA* [m^2/g]**	**Crystallite size [nm]**	**Band-gap energy [eV]**
$LaFeO_3$-A	1.78	1.66	0.86	4	37.6	2.0
$LaFeO_3$-B	1.78	1.66	1.72	18	22.3	2.0
$LaFeO_3$-C	1.78	1.66	2.15	24	6.4	2.0

IV.1.2 Photocatalysts characterization

IV.1.2.1 X-ray diffraction (XRD)

Figure IV.1 shows the XRD patterns of the $LaFeO_3$ photocatalysts prepared with different amount of citric acid. XRD showed well indexed diffraction peaks, clearly indicating the formation of orthorhombic perovskite type structure, as reported in literature. No significant impurity phases have been observed in the XRD spectra. The crystallite size of $LaFeO_3$ was calculated by using the Scherrer formula at diffraction line positioned at 2θ value of 32.16 degree , which corresponds to $LaFeO_3$ (h k l) (0 0 2) (Tijare et al., 2010). The results are reported in Table IV.1. The crystallite size decreased as the amount of citric acid used in the preparation of perovskites was increased. On the other hand, the different amounts of citric acid resulted in changes of the crystalline structure of perovskites.

In particular, $LaFeO_3$-C exhibits a partially amorphous structure with respect to $LaFeO_3$-A and $LaFeO_3$-B samples.

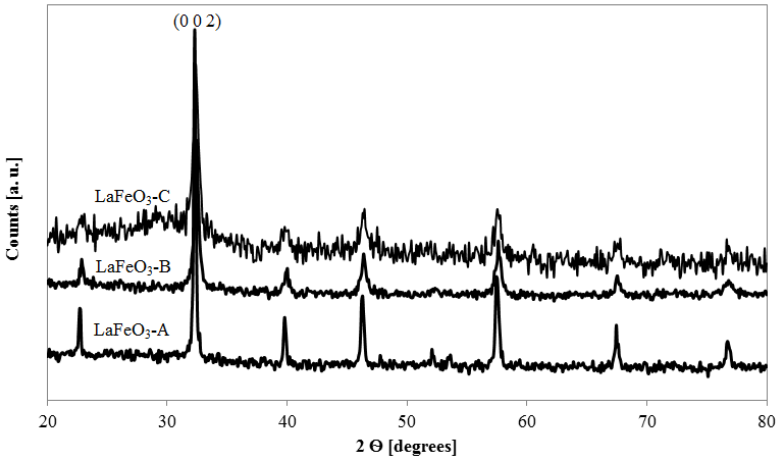

Figure IV.1. *XRD spectra of $LaFeO_3$-A, $LaFeO_3$-B and $LaFeO_3$-C photocatalysts.*

IV.1.2.2 BET surface area

BET surface area values (SBET) of the catalysts were strongly affected by the different amounts of citric acid used in the catalyst preparation (Table IV.1). In particular, SBET increased from 4 up to 24 m^2/g by increasing the amount of citric acid confirming that it plays an important role in the combustion of gel. It is worthwhile to note that at the combustion point, the organic fuel formed gases that tried to come out from the gel by breaking the gel in nanoporous and nanosized particles of $LaFeO_3$ (S.M.Khetre, 2011). This process was faster when the amount of citric acid was higher, allowing to obtain $LaFeO_3$ with higher surface area and smaller crystallite size (Table IV.1).

IV.1.2.3 UV-Vis Diffuse Reflectance spectra

The reflectance spectra of all the samples are shown in Figure IV.2. The typical absorption band edge of the $LaFeO_3$ semiconductor was observed at around 814 and 600nm for the samples $LaFeO_3$-A and $LaFeO_3$-B and attributed to electron transitions from valence band to conduction band ($O_{2p} \rightarrow Fe_{3d}$) (Parida et al., 2010). On the contrary, the sample $LaFeO_3$-C does not show the characteristic bands of perovskite. This result could be due to a partially amorphous structure, as confirmed by XRD results (Figure IV.1).

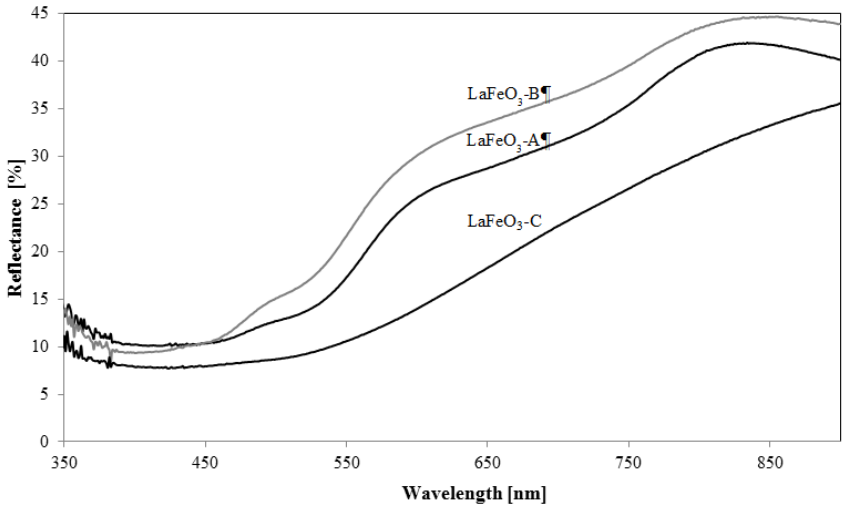

Figure IV.2. *UV-Vis DRS spectra of $LaFeO_3$-A, $LaFeO_3$-B and $LaFeO_3$-C photocatalysts in terms of reflectance as a function of wavelength*

The data obtained from UV–Vis reflectance spectra were used for evaluating the band-gap energy of $LaFeO_3$-A, $LaFeO_3$-B and $LaFeO_3$-C

catalysts. As shown in Figure IV.3, the increase in the amount of citric acid resulted in a decrease in band-gap energy from 3.0 (band-gap of $LaFeO_3$-A) to 2.0 eV for (band-gap $LaFeO_3$-B and $LaFeO_3$-C). These results are reported in Table IV.1.

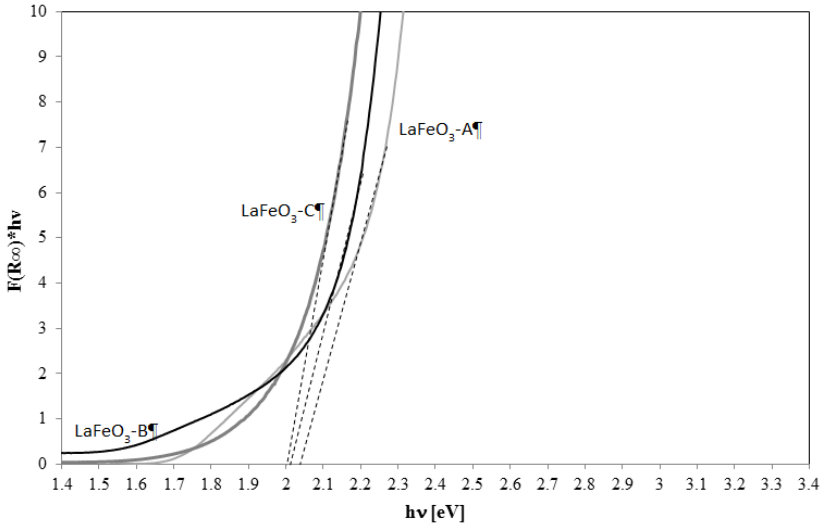

Figure IV.3. *Band-gap energy calculation for $LaFeO_3$-A, $LaFeO_3$-B and $LaFeO_3$-C photocatalysts.*

IV.1.2.4 Raman analysis

Raman spectra of $LaFeO_3$ photocatalysts, recorded using a 785 nm diode laser, are reported in Figure IV.4. All the samples showed bands in the range 100-1000 cm^{-1}, all associated to $LaFeO_3$ structure (Phokha et al., 2014). The modes caused by La vibrations are present below 200 cm^{-1}, at 153 and 176 cm^{-1}. The bands in the range 400-450 cm^{-1} are due to the oxygen octahedral bending vibrations.

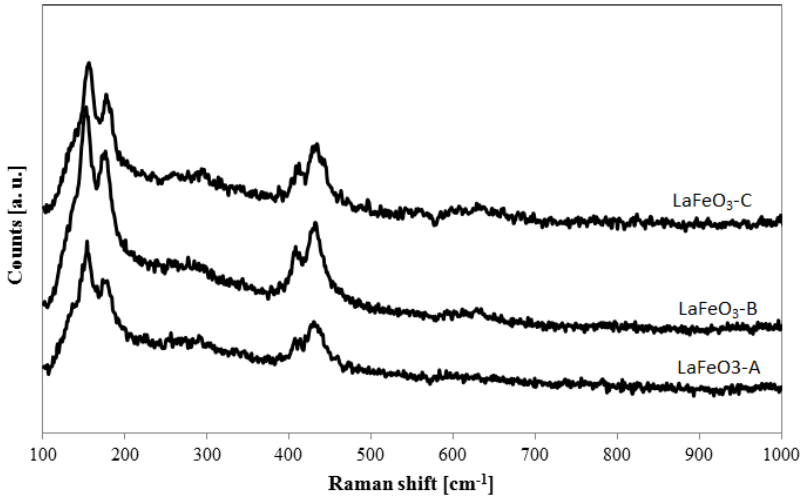

Figure IV.4. *Raman spectra.*

IV.2.1 Photocatalytic results

Typically, in the photocatalytic experiments, 0.12 g of catalyst was suspended in 80 ml of an aqueous solution containing 500 mg/L of glucose (D^+ Glucose VWR, Sigma-Aldrich). Moreover the activity in photowater splitting reaction was evaluated by tests carried out in the same conditions with only distilled water, in order to compare the production of H_2 obtained by the reaction of water splitting and that one obtained by the photocatalytic degradation of glucose on the same photocatalyst. Continuous mixing of the solution in the reactor was assured by external recirculation of water through a peristaltic pump. The photoreactor was irradiated with a strip of UV-LEDs (nominal power: 10W) with wavelength emission in the range 375–380 nm, or with a strip of visible LEDs with the main wavelength emission at 440 nm (nominal power: 10W).

Glucose degradation and hydrogen yield during the irradiation time were evaluated according to the following relationships:

$$X = \frac{(n^0 C_6H_{12}O_6 - nC_6H_{12}O_6)}{n^0 C_6H_{12}O_6} \cdot 100 \qquad \text{(IV.1)}$$

$$R_{H_2} = \frac{2 \cdot nH_2}{12 \cdot n^0 C_6 H_{12} O_6} \cdot 100 \qquad \text{(IV.2)}$$

Where:

X = glucose conversion, [%];

R_{H2} = hydrogen yield, [%];

nH_2=moles of hydrogen produced;

$n^0C_6H_{12}O_6$=moles of glucose in aqueous solution after dark adsorption

$nC_6H_{12}O_6$=moles of glucose in aqueous solution at the end of irradiation time.

IV.2.1.1 Hydrogen production on $LaFeO_3$ by photocatalytic water splitting reaction

Firstly, $LaFeO_3$ samples were tested to evaluate their activity in hydrogen generation through water splitting reaction under UV irradiation. The typical trend obtained during the irradiation is reported in Figure IV.5 with reference to the $LaFeO_3$-B photocatalyst; the production of hydrogen and oxygen increased as irradiation time increased. In particular, $LaFeO_3$- B resulted in 52 mmol hydrogen production after 4 h of irradiation. Moreover, the H_2/O_2 ratio was about 2 for all the catalysts (Figure IV. 6). This result confirms that hydrogen is produced from water splitting according the following reaction:

$$2H_2O \rightarrow 2H_2 + O_2 \qquad \text{(IV.3)}$$

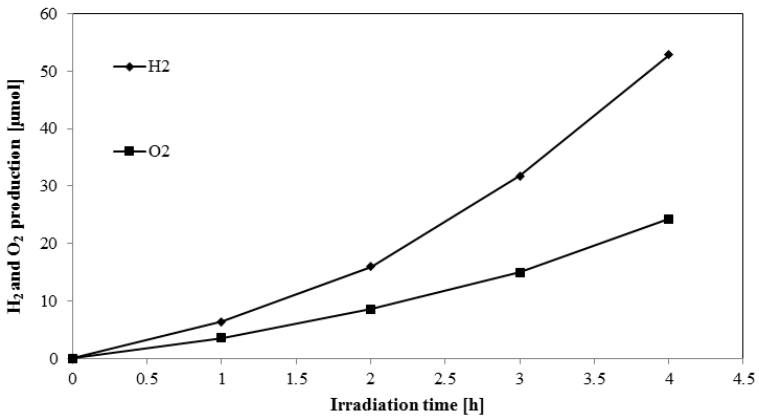

Figure IV.5. *H_2 and O_2 production by photocatalytic water splitting reaction on $LaFeO_3$-B photocatalyst; light source: UV-LEDs.*

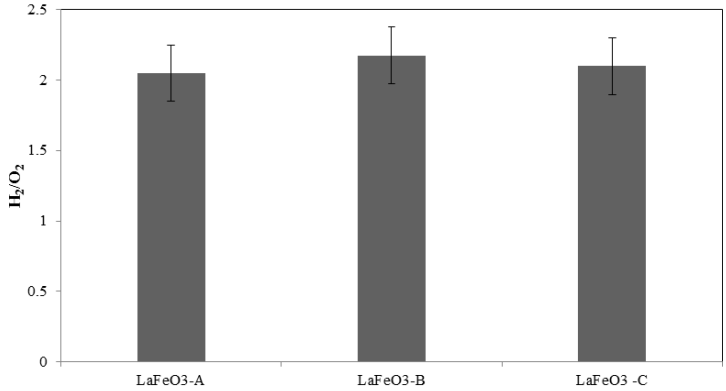

Figure IV.6. H_2/O_2 *molar ratio by photocatalytic water splitting reaction on $LaFeO_3$-A, $LaFeO_3$-B and $LaFeO_3$-C photocatalysts; irradiation time: 4 hours; light source: UV-LEDs.*

IV.2.1.2 Influence of the photocatalyst formulation on hydrogen production and glucose degradation under UV-LEDs irradiation.

In addition to the water splitting process, the performances of the photocatalysts in hydrogen production during glucose degradation were evaluated. The behavior of glucose relative concentration for all the prepared photocatalysts is shown in Figure IV.7. In particular, in dark phase, a decrease of the concentration of glucose due to the adsorption on the catalyst surface was observed and any product has been detected in gaseous phase.

The amount of glucose adsorbed increased with the increase of the specific surface area of the photocatalyst. When UV light was switched on, the degradation of glucose increased.

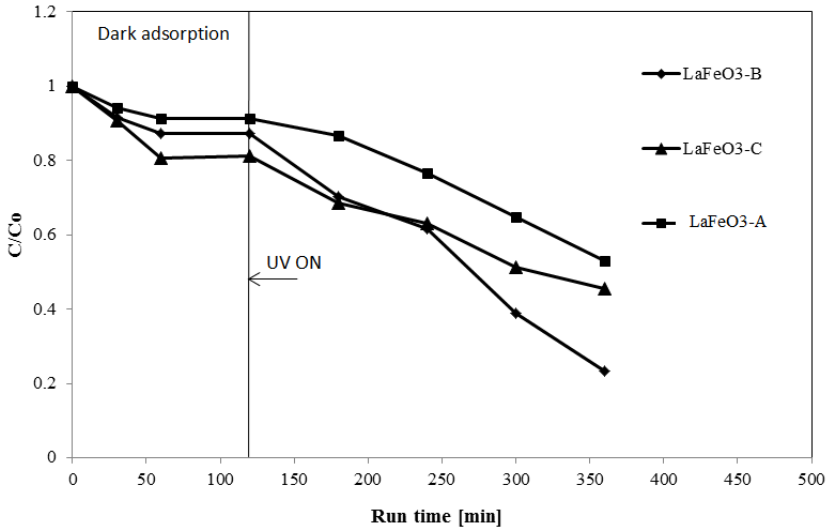

Figure IV.7. *Behavior of glucose concentration on $LaFeO_3$-A, $LaFeO_3$-B and $LaFeO_3$-C photocatalysts during the dark adsorption and during the irradiation time; light source: UV-LEDs.*

The photocatalytic degradation of glucose can be described by a first-order kinetic equation (Liu et al., 2010) with respect to the concentration of glucose. During irradiation, mass balance on glucose present in the aqueous solution can be written as:

$$\frac{dC(t)}{dt} = -k \cdot C(t) \cdot a \qquad \text{(IV.4)}$$

Where:

$C(t)$: concentration of glucose at given reaction time, [mg L^{-1}]

k: degradation kinetic constant, [L g_{cat}^{-1} h^{-1}]

a: dosage of catalyst [g_{cat} L^{-1}]

The initial condition is:

$t=0$ $\qquad C=C_0^*$

Where C_0^* is the glucose concentration after dark period.

Eq. (IV.4) was solved by the Euler iterative method. Primary goal of the simulation by the mathematical model is to identify the apparent kinetic constant k using nonlinear regression analysis of the experimental data reported in Figure IV.7 as a function of irradiation time. The nonlinear regression procedure was performed using the least-squares approach, based on the minimization of the sum of squared residuals between the experimental data and the values given by the mathematical model. The results of fitting procedure are reported in Figure IV. 8.

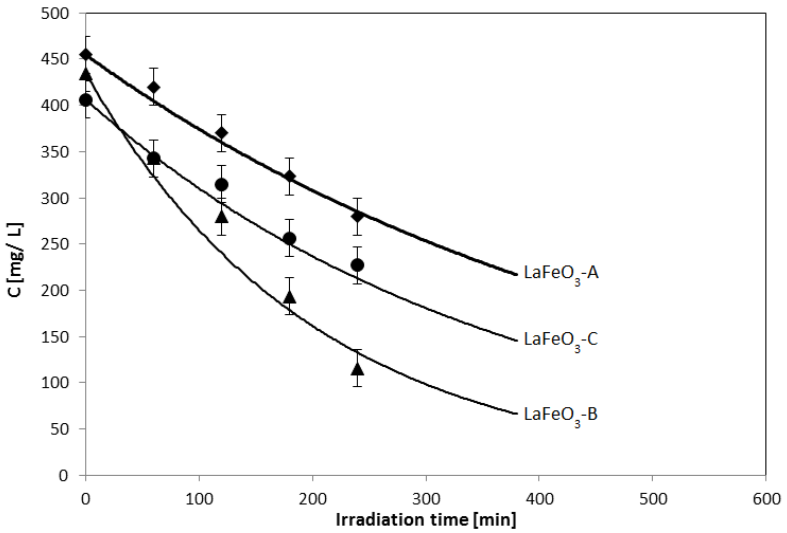

Figure IV.8. *Behavior of glucose experimental concentration (symbols) and predicted data (lines) as function of irradiation time for the different photocatalysts; light source: UV-LEDs.*

These results allowed to calculate the value of k, which is 0.0013, 0.0033 and 0.0018 L g_{cat}^{-1} h^{-1} for $LaFeO_3$-A, $LaFeO_3$-B and $LaFeO_3$-C, respectively. The best glucose degradation rate was obtained for $LaFeO_3$-B photocatalyst, reaching glucose degradation as high as 73% after 4 h of irradiation. Moreover, it was observed that the glucose degradation rate does not depend on the specific surface area of the catalyst and on the band-gap energy.

In fact, with $LaFeO_3$-C, characterized by the highest specific surface area (24 m^2 /g), the kinetic constant was equal to 0.0018 L g_{cat}^{-1} h^{-1} , while with $LaFeO_3$-B that has the same band-gap of the $LaFeO_3$-C catalyst, the value of

k was higher, despite its lower specific surface area (18 m^2 /g). These results could be explained considering that since $LaFeO_3$-C photocatalyst has partially amorphous structure, as confirmed by XRD analysis (Figure IV.1), its lower photocatalytic activity is likely due to the higher recombination rate of the photogenerated charge carriers (Hajaghazadeh et al., 2014). It has been proposed that the crystallinity quality of a given catalyst has a direct effect on the charge carrier separation (Tahiri Alaoui et al., 2012). Therefore, our findings suggest that the better performance of $LaFeO_3$-B is possibly due to the slow recombination of charge-carriers, because of the better crystalline structure compared to $LaFeO_3$-C catalyst. The amount of H_2 during the irradiation of $LaFeO_3$-A, $LaFeO_3$-B and $LaFeO_3$-C photocatalysts is shown in Figure IV.9. All the tested catalysts resulted in hydrogen production in the presence of UV irradiation, the highest yield being obtained with $LaFeO_3$-B sample, in agreement with the experimental data of glucose degradation. The formation of CO_2 was also observed during glucose degradation.

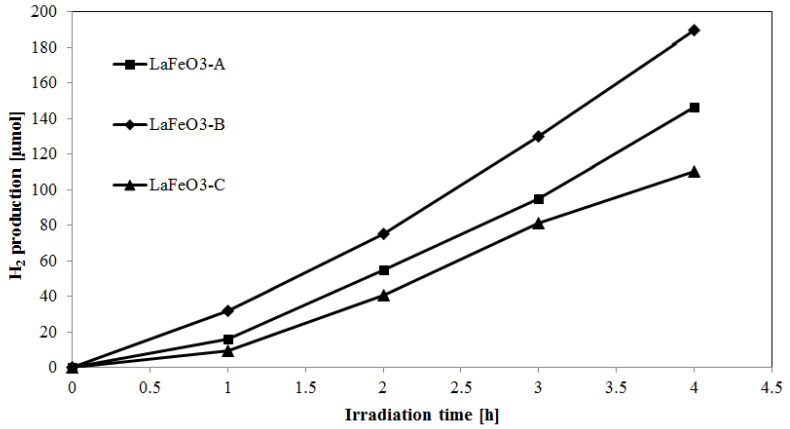

Figure IV.9. *Photocatalytic H_2 production from glucose solution during the irradiation time on $LaFeO_3$-A, $LaFeO_3$-B and $LaFeO_3$-C photocatalysts; light source: UV-LEDs.*

Photocatalytic hydrogen and carbon dioxide production could result from glucose reforming, according to the following reaction (Fu et al., 2010):

$$C_6H_{12}O_6 + 6H_2O = 6CO_2 + 12H_2 \qquad \text{(IV.5)}$$

but in this case, the H_2/CO_2 molar ratio (Figure IV.10) is never equal to 2

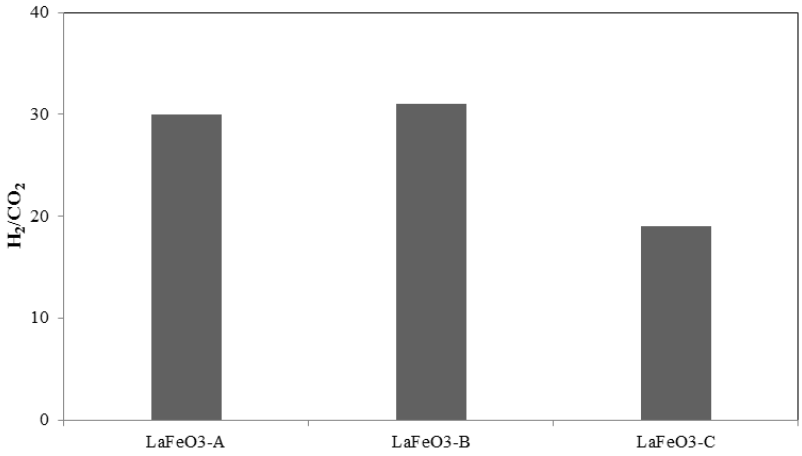

Figure IV.10. *H_2/CO_2 molar ratio on $LaFeO_3$-A, $LaFeO_3$-B and $LaFeO_3$-C photocatalysts by photocatalytic treatment of glucose solution; irradiation time: 4 hours; light source: UV-LEDs.*

On the other hand, during the irradiation time, the analysis of the liquid phase showed the presence of gluconic acid and he ratio between the moles of gluconic acid produced and the moles of glucose converted (Figure IV.11) is approximately equal to 1 for all the tested catalysts.

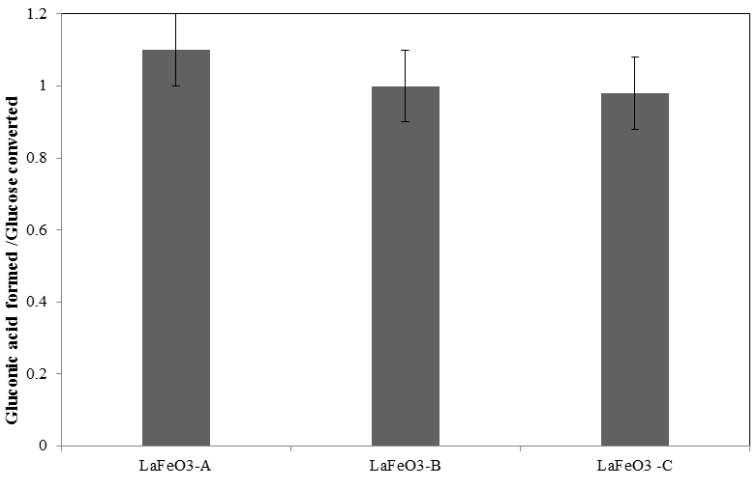

Figure IV.11. *Gluconic acid formed/glucose converted molar ratio on $LaFeO_3$-A, $LaFeO_3$-B and $LaFeO_3$-C photocatalysts by photocatalytic treatment of glucose solution; irradiation time: 4 hours; light source: UV-LEDs.*

Therefore, a possible reaction path to hydrogen production could pass through the formation of gluconic acid in solution according to the reactions proposed in literature (Hambourger et al., 2005, Li et al., 2010).

$$RCHO + OH\cdot = RCO\cdot + H_2O \quad \text{(IV.6)}$$

$$RCO\cdot + H_2O = RCOOH + H\cdot \quad \text{(IV.7)}$$

Glucose (RCHO) adsorbed on the catalyst can react with the hydroxyl radicals formed by the reaction of holes (h^+) with water molecules. In this way, gluconic acid (RCOOH) is formed according to the eq. IV.6 and eq. IV.7.

The holes react also with glucose forming gluconic acid, accoriding to the Eq. IV8 and Eq. IV9:

$$h^+ + RCHO = RCO^{\cdot} + H^{\cdot} \quad \text{(IV.8)}$$

$$RCO^{\cdot} + H_2O = RCOOH + H^{\cdot} \quad \text{(IV.9)}$$

$$H^{\cdot} + H^{\cdot} = H_2 \quad \text{(IV.10)}$$

The produced $H^{\cdot}$ radicals can form H_2 (eq.IV.10). Moreover, in a parallel way, hydrogen is also formed by water splitting mechanism promoted by $LaFeO_3$ (Parida et al., 2010).

Gluconic acid would react further with hydroxyl radicals so that a decarboxylation reaction takes place (Hoffmann et al., 1995b). But, taking into account that the amount of CO_2 produced is very low, this last reaction occurs in limited extend. On the basis of this last observation and considering the eqs. (IV.6) and (IV.9), the moles of gluconic acid formed are about equal to the moles of glucose converted explaining in this way the behavior shown in Figure IV.11. Specific productions of hydrogen and glucose degradation after 4 h of UV irradiation are shown in Figures IV.12 and IV.13, respectively. The highest glucose degradation (1.2 mmol g_{cat}^{-1}) and hydrogen production (1.6 mmol g_{cat}^{-1}), corresponding to a hydrogen yield equal to 16%, have been obtained for $LaFeO_3$- B.

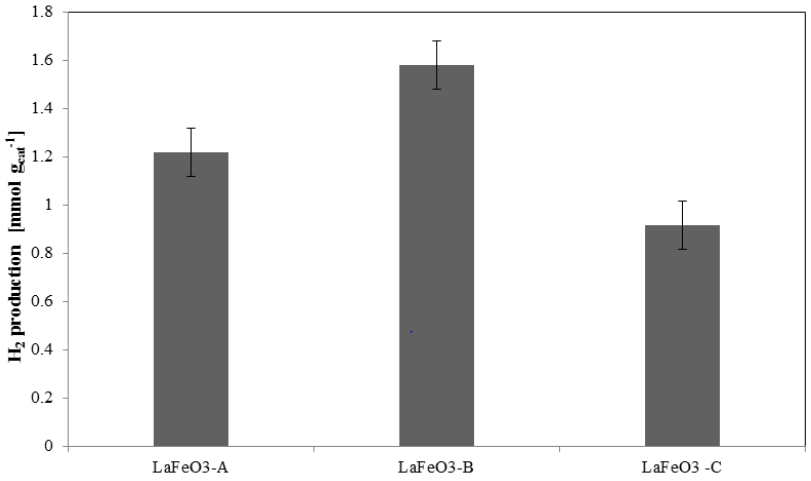

Figure IV.12. *Specific H_2 production on $LaFeO_3$-A, $LaFeO_3$-B and $LaFeO_3$-C photocatalysts by photocatalytic treatment of glucose solution; irradiation time: 4 hours; light source: UV-LEDs.*

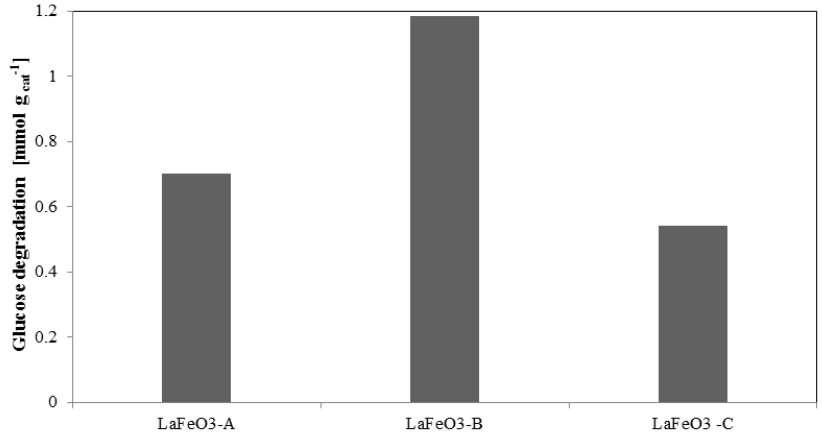

Figure IV.13. *Specific glucose degradation on $LaFeO_3$-A, $LaFeO_3$-B and $LaFeO_3$-C photocatalysts by photocatalytic treatment of glucose solution; irradiation time: 4 hours; light source: UV-LEDs.*

IV.2.1.3 Influence of initial glucose concentration on hydrogen production

The influence of initial glucose concentration on the hydrogen production was evaluated. In particular it was considered a range of glucose concentration from 500 to 4000 mg L^{-1}.

Figure IV.14 shows the influence of the initial glucose concentration on hydrogen production and glucose degradation during the UV irradiation time. By increasing the initial concentration of glucose in solution, hydrogen production increased (Figure 4a). In particular, at 500 and 4000 mg L^{-1} of glucose, 190 and 460 μmol of hydrogen after 4 h of irradiation were obtained, respectively (Figure IV.14a). Moreover, the highest sugar degradation was obtained with 1000 mg L^{-1} glucose initial concentration (Figure IV.14b). Figure IV.15 reports the trend of hydrogen production and glucose degradation after 4 h of UV irradiation, as a function of the initial concentration of glucose in solution. It is worthwhile that, as the initial concentration of glucose was increased, a linear increase of hydrogen production up to 1000 mg L^{-1} of initial concentration of glucose was observed. The same behavior was found for glucose degradation. Every further increase of the initial concentration of glucose did not result in a linear increase of the hydrogen production, and glucose degradation was almost unchanged. This typical kind of Langmuirian catalytic behavior suggests that the reaction depends of the glucose concentration on the catalyst surface rather than of the concentration in the solution (Fu et al., 2008a)

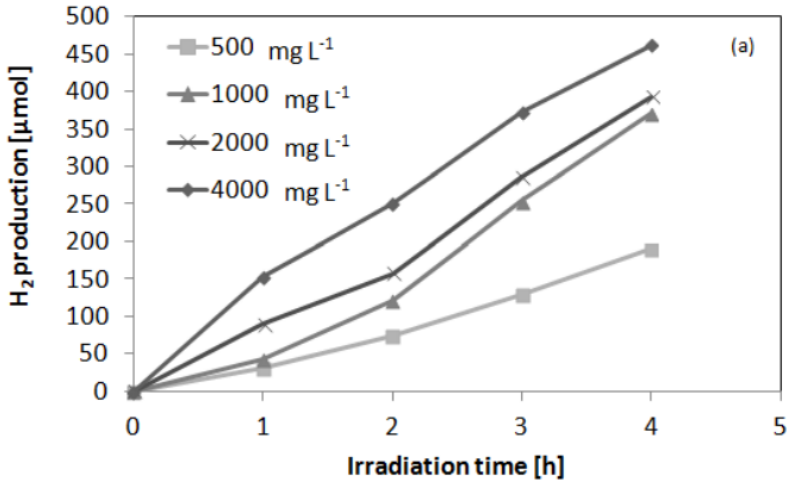

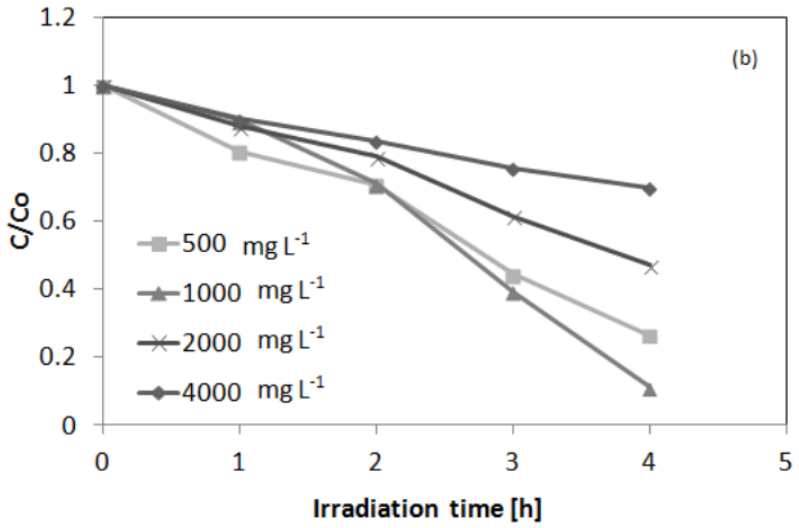

Figure IV.14. *Influence of the initial glucose concentration on hydrogen production (a) and glucose degradation (b), during the irradiation time under UV-LEDs. Catalyst dosage: 1.5 g L-1*

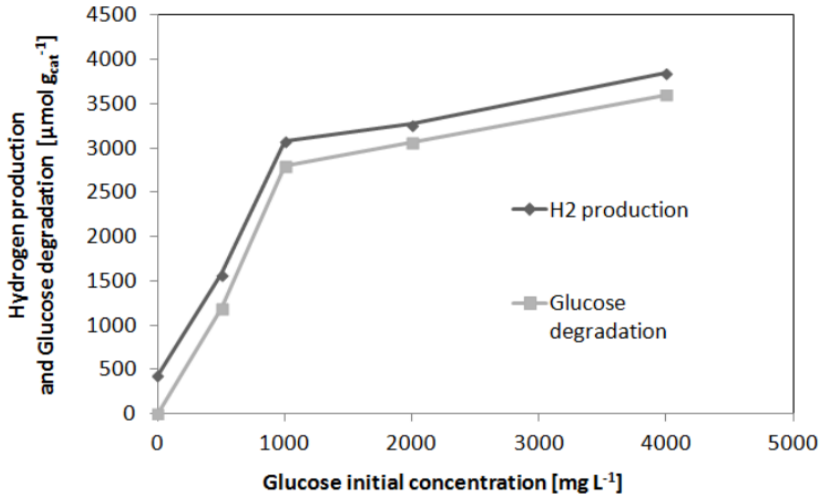

Figure IV.15. *Trend of hydrogen production and glucose degradation after 4 h of UV irradiation, as a function of the initial concentration of glucose in solution. Catalyst dosage: 1.5 g L-1.*

IV.2.1.4 Effect of different catalyst dosage

The influence of catalyst dosage on glucose conversion and hydrogen production after 4 h of UV irradiation was also evaluated (Figure IV.16).
The photocatalytic efficiency increased as the catalyst loading was increased up to 1.5 g L^{-1}. Further increase of catalyst loading resulted in a decrease of glucose conversion (Figure IV.16a) and H_2 production (Figure IV.16b). The presence of an optimal value for the catalyst dosage is likely related to the limiting effect of the interception of the light by the suspension on the degradation rate (Vaiano et al., 2014a).

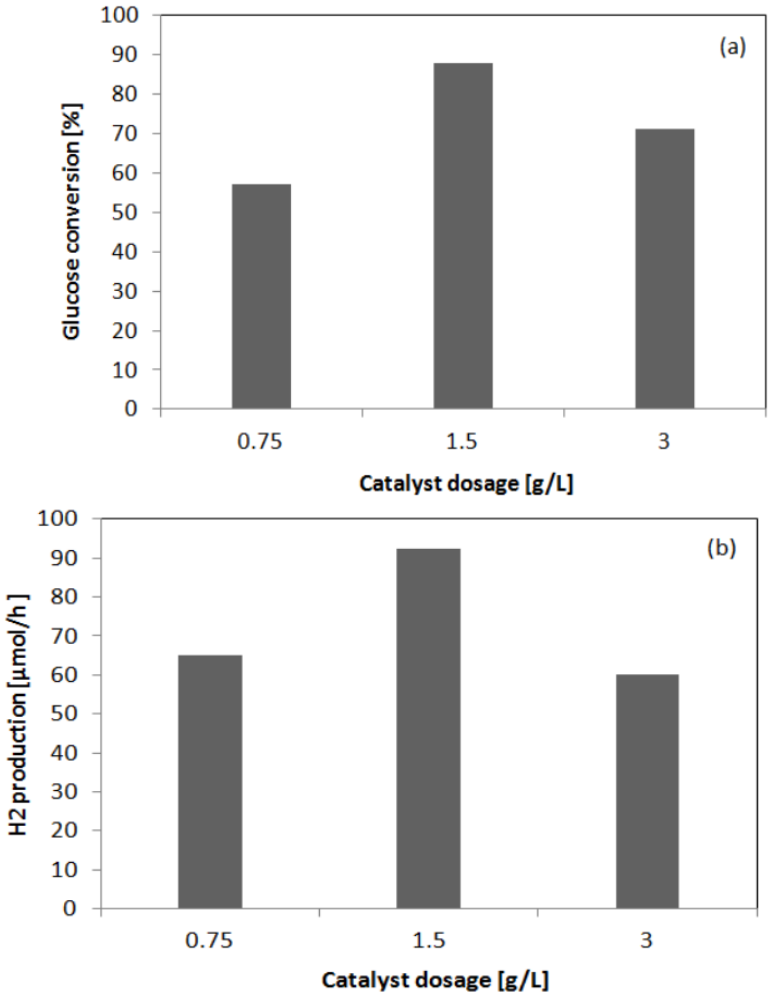

Figure IV.16. *Influence of catalyst dosage on glucose conversion (a) and hydrogen production (b) after 4 h of irradiation time; Light source : UV LEDs.; Glucose initial concentration : 1000 mg L-1.*

IV.2.1.5 Effect of different light source

The effect of different light sources (UV LEDs and visible LEDs) on the catalyst $LaFeO_3$-B, which showed the best performances, was evaluated. The results shown in Figure IV.17, confirm the activity of $LaFeO_3$-B sample also in the presence of visible light, as reported in the literature for photocatalytic water splitting (Tijare et al., 2010). In particular, after 4 h of visible light irradiation, the production of hydrogen was 140 mmol, with glucose degradation equal to about 35% .

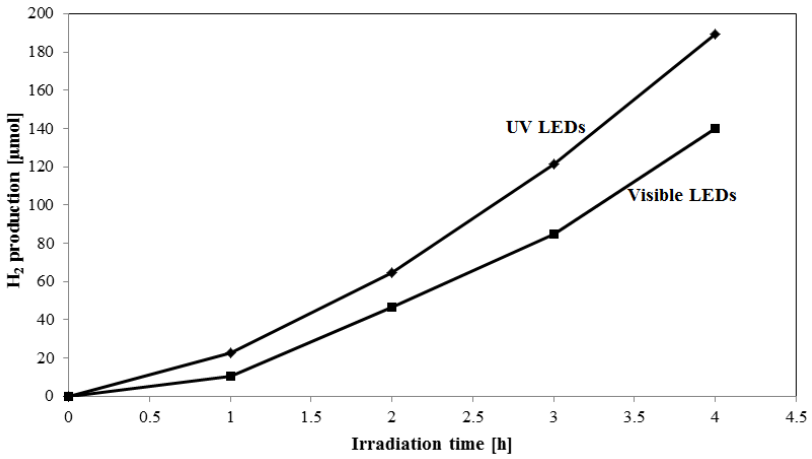

Figure IV.17. *Photocatalytic H_2 production from glucose solution during the irradiation time on $LaFeO_3$-B photocatalyst; light source: UV or visible LEDs*

From these results, it is possible to note that $LaFeO_3$ photocatalysts were successfully synthesized using the solution combustion synthesis method, with different content of citric acid as organic fuel. In a typical preparation, citric acid, $La(NO_3)_3$ and $Fe(NO_3)_3$ in weight ratio 1/2.07/1.93 were used. The influence of amount of citric acid (varied between 0.86 and 2.15 g) was evaluated. The specific surface area of perovskite increased from 4 to 24 m^2 /g as the amount of citric acid was increased from 0.86 to 2.15 g, with crystallite size of 38 and 6 nm, respectively. Moreover, the different amounts of citric acid used in the preparation of $LaFeO_3$ cause modifications of the crystalline structure of perovskite. In particular, $LaFeO_3$ prepared with 0.86 and 1.72 g of citric acid exhibited a crystalline structure. The sample, prepared with a higher amount of citric acid equal to 2.15 g ($LaFeO_3$-C), showed a partial amorphous phase. $LaFeO_3$ catalyst prepared with an amount of citric acid equal to 1.86 g, was the most active in the photocatalytic

production of H_2 (up to 1.6 mmol/gcat after 4 h of UV irradiation, corresponding to 16% hydrogen yield). With the same photocatalyst the simultaneous degradation of glucose was 73% after 4 h UV irradiation. The optimized photocatalyst showed also a significant photocatalytic activity under visible light irradiation, reaching hydrogen yield and glucose degradation equal to about 12 and 35%, respectively. The obtained results evidenced the possibility to produce hydrogen with a significant yield by using photocatalysts in the absence of noble metals.

IV.2 Doped perovskite: Enhanced photocatalytic hydrogen production from glucose aqueous solutions.

Usually, for enhancing the photocatalytic properties of perovskite, noble metals are used as dopants for photocatalyst. Various cation doped perovskites have been synthesized and tested (Ohno et al., 2005, Kim et al., 2005). Among these systems, Rh-doped $SrTiO_3$ appears to be the most promising for hydrogen production from ethanol aqueous solutions(Ohno et al., 2005)

No studies about the photocatalytic activity in the hydrogen production from aqueous solution containing sacrificial agents using $LaFeO_3$ doped with noble metals are present in literature.

Therefore, it may be interesting to study the effect of the doping of $LaFeO_3$ with a noble metal very effective and already used in the case of titania, that is rhodium.

Moreover, among the several possible dopants for perovskites, another interesting alternative to the noble metals is the use of transition metals for enhances the photocatalytic activity of perovskite. Ruthenium is the most suitable metals since a large Ru amount can be introduced within the perovskite network keeping it single-phase (Malavasi et al., 2005).

So, in these paragraphs it was reported the effect of the doping of $LaFeO_3$ with a noble metal very effective and already used in the case of titania, that is rhodium. The effect of different amount of rhodium used for the doping of $LaFeO_3$ prepared through solution combustion synthesis has been investigated. In addition, providing for the application of the photocatalyst to industrial level, the study has been directed to the formulation of a noble metal free photocatalyst that had good performance for the production of hydrogen and in the degradation of the sugars present in the solution. So, the effect of doping with transition metal (not noble metals) was investigated. In particular, Ru-doped $LaFeO_3$ was synthesized and characterized and its effectiveness in the photocatalytic hydrogen production from glucose aqueous matrices was investigated under UV or visible irradiation by light-

emitting diodes (LEDs). The influences of Ru loading and photoreactor configuration have been assessed. Moreover, in presence of this last photocatalytst, a mathematical model, able to predict the experimental data for different initial concentration of glucose, was developed. The optimized photocatalyst was also tested under visible light on a real wastewater taken from a brewing process.

IV.2.1 Rhodium doped $LaFeO_3$

IV.2.1.1 Synthesis and characterization results

The "solution combustion synthesis" was used for the preparation of catalysts based on perovskite doped with rhodium using citric acid as an organic fuel and metal nitrates as precursors. In detail, 1.66 g of $Fe(NO_3)_3 \cdot 9H_2O$ (Riedel-deHaen, 97 wt%), 1.78g of $La(NO_3)_3 \cdot 6H_2O$ (Fluka, 99%), 0.86g of citric acid (Fluka, 99 wt%) and a specific amount of $RhCl_3$ (Sigma Aldrich, 99%) used as dopant source, were completely dissolved in 100 ml of bidistilled water. The solution was kept stirred continuously at 60 °C for 5 minutes. Then, NH_3 (Carlo Erba, 37 wt %) was added to the solution until the pH reached a value of approximately 7. The solution was dried at 130° C and then calcined at 300° C for 3 hours to ignite the solution combustion reaction. Different amount of $RhCl_3$ was used for the doping of $LaFeO_3$. The Rh nominal loading is expressed as molar percentage and it was evaluated through Eq. 1:

$$\%molRh = \frac{nRh}{nLa + nFe} \cdot 100 \qquad \text{(IV.11)}$$

Where:

nRh is the number of moles of $RhCl_3$ used in the synthesis;

nLa is the number of moles of $La(NO_3)_3 \cdot 6H_2O$ used in the synthesis;

and nFe is the number of moles of $Fe(NO_3)_3 \cdot 9H_2O$ used in the synthesis.

In Table IV.2.1 it is reported the list of the photocatalysts prepared with different molar percentages of rhodium.

Table IV.2.1 *Summary of the characterization results*

Catalyst	Rh nominal amount [mol %]	Crystallite size (XRD) [nm]	Specific surface area [m^2/g]	Band gap (UV-Vis DRS) [eV]
$LaFeO_3$	0	37	4	2.12
0.12% Rh	0.12	37	4	2.08
0.23% Rh	0.23	36	4	2.08
0.37% Rh	0.37	34	4	2.06
0.47% Rh	0.47	32	4	2.00
0.70% Rh	0.70	26	6	1.93
1.16% Rh	1.16	31	5	1.88
2.33% Rh	2.33	30	5	2.05

IV.2.1.1.1 XRD

The XRD results are reported in Figure IV.18. As it can be seen, up to an Rh loading of 1.16 %, only signals due to the crystalline phase of the $LaFeO_3$ are visible. Only for the catalyst prepared with the highest percentage of rhodium (2.33%) it is possible to note the presence of RhO_2 segregated on the catalyst surface, evidenced by a peak at 35° (Demazeau et al., 2006). For the 1.16%Rh and 2.33%Rh photocatalysts, it is also possible to note an additional peak at about 48°, probably due to the presence of metallic rhodium (He et al., 2009). These results indicate that substitutional doping of up to 1.16 mol% of Rh cations did not introduce impurities in the final sample. Moreover, in comparison with undoped perovskite, no significant shift in the XRD patterns was observed for Rh-$LaFeO_3$. This last result could be explained considering that the ionic radii of Rh^{4+} (60.5 pm) and Fe^{4+} (58.5 pm) are very similar and therefore the replacement of Fe^{4+} with Rh^{4+} determined a very small structural changes of Rh-$LaFeO_3$ samples, as previously observed for Rh-$SrTiO_3$ (Shen et al., 2013a).

The photocatalysts crystallite size was calculated using the Scherrer's equation. The obtained results are reported in Table IV.2.1. It is possible to note that the crystallite size slightly decreased from 37 nm (for pure $LaFeO_3$) up to 26 nm when the Rh content was increased to 0.7%. Only for the photocatalysts prepared with the higher molar percentage of rhodium (1.16 and 2.33 %) a decrease in the crystallite size was observed.

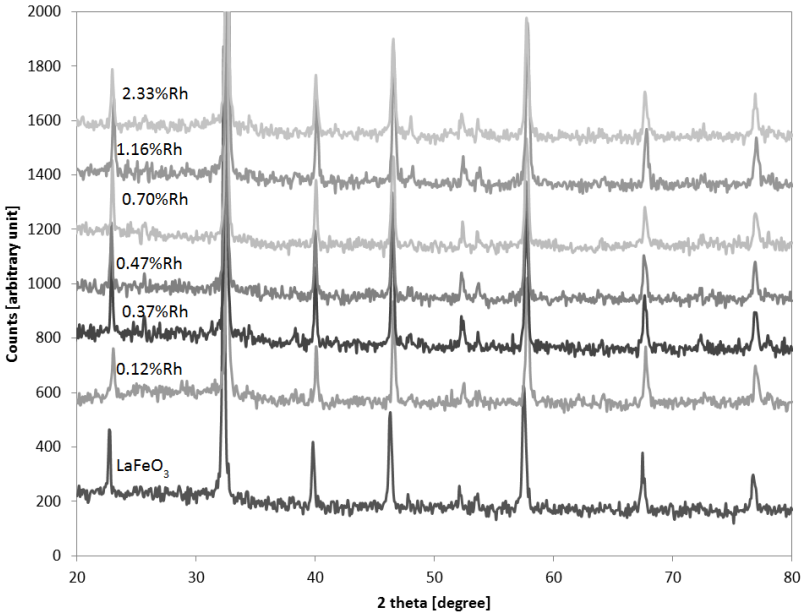

Figure IV.*18* *XRD spectra.*

IV.2.1.1.2 Raman analysis

Raman spectra of Rh-$LaFeO_3$ photocatalysts are reported in Figure IV.19. All the samples showed bands in the range 100-1000 cm^{-1}, associated to $LaFeO_3$ structure (Phokha et al., 2014). The modes caused by La vibrations are present below 200 cm^{-1}, at 153 and at 176 cm^{-1}. The bands in the range 400-450 cm^{-1} are due to the oxygen octahedral bending vibrations. From the Raman spectra no additional bands are noticed.

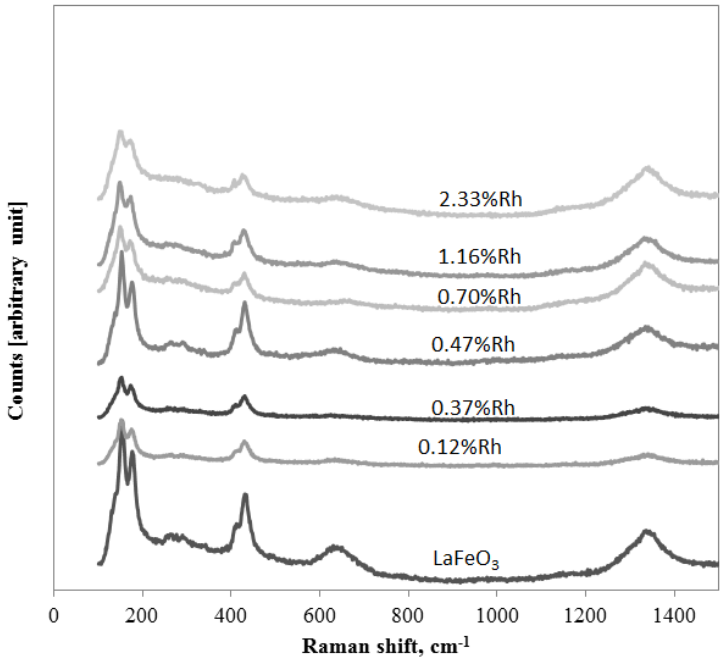

Figure IV.19 *Raman spectra.*

IV.2.1.1.3 UV-Vis Diffuse Reflectance spectra (UV-Vis DRS)

The reflectance spectra (Figure IV.20) showed the typical absorption band edge of the $LaFeO_3$ semiconductor at around 814 and 600 nm for all the samples and attributed to electron transitions from valence band to conduction band ($O_{2p} \rightarrow Fe_{3d}$) (Parida et al., 2010). It is worthwhile to note that these bands disappeared for the catalysts with the higher Rh content (1.16%Rh and 2.33%Rh). This result could be due to the presence of RhO_2 present on the $LaFeO_3$ surface, observed in XRD measurements (Figure IV.18).

The data obtained from UV–Vis reflectance spectra were used for evaluating the band-gap energy of the photocatalysts. The obtained results are reported in Table 1. The increase of Rh amount resulted in a decrease in band-gap energy from 2.12 (band-gap of undoped $LaFeO_3$) to 1.72 eV for 2.33%Rh. The decrease of band-gap energy was due to the electronic transition from donor levels formed with dopants to the conduction band of the host photocatalysts (Wang et al., 2015). In particular, as reported in literature about perovskite doped with Rh, the adsorption peak at 580 nm is assigned to an electronic transition from the valence band to Rh^{4+} acceptor levels in the band gap (Sasaki et al., 2009).

The latter results in occupied Rh^{3+} levels and photon absorption from these states to the conduction band give rise to the 580 nm peak. In summary the UV-Vis DRS analysis confirm the substitutional doping generated by the replacement of Fe^{4+} with Rh^{+4}.

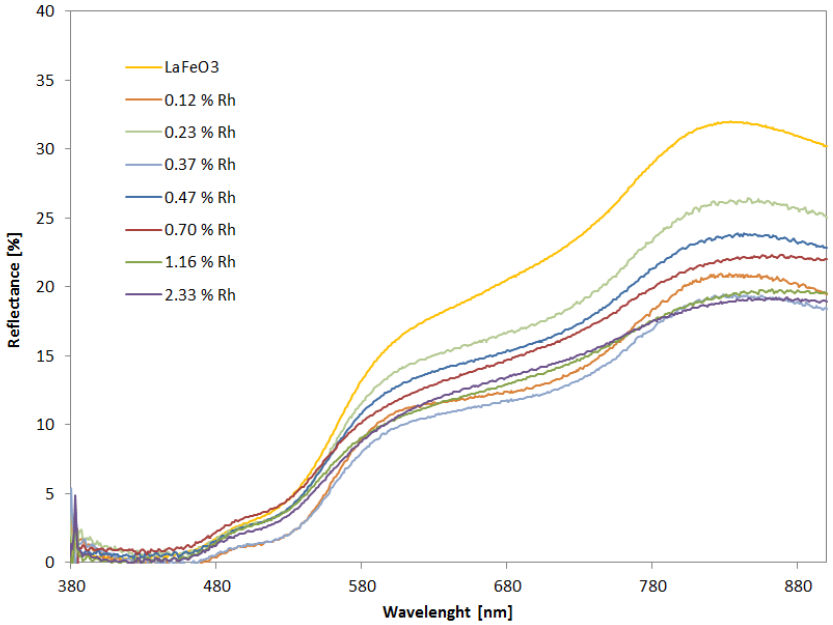

Figure IV.20. *UV Vis DRS spectra.*

IV.2.1.2 Photocatalytic results: Influence of Rh content on the photocatalytic performances

Typically, 0.12 g of catalyst was suspended in 80 ml of an aqueous solution containing 1000 mg/L of glucose (D + Glucose VWR, Sigma-Aldrich) using a pyrex cylindrical photocatalytic reactor (ID = 2.5 cm) equipped with a N_2 distributor device (Q=0.122 NL/min).

To ensure complete mixing of the solution in the reactor, a peristaltic pump was used. The photoreactor was irradiated with a strip of UV-LEDs positioned around the external surface of the reactor. The suspension was left in dark conditions for 2 hours to reach the adsorption-desorption equilibrium of glucose on the photocatalysts surface, and then the reaction was initiated under UV light for up to 4 hours.

Figure IV.21 reports the comparison in terms of H_2 photocatalytic production as a function of irradiation time for undoped and Rh-$LaFeO_3$ photocatalysts. It is possible to note that up to an Rh content of 1.16 mol%,

the photocatalytic activity improved. For 2.33%Rh sample, the photocatalytic activity worsened, probably due to the presence of RhO_2 on the catalyst surface. Anyway, for all the doped photocatalysts it was found an improvement in photocatalytic hydrogen production compared to the value obtained with the undoped $LaFeO_3$. In particular the highest value of H_2 production (1835 µmol/L) was achieved for 0.70%Rh after 4 hours irradiation time. This last value is higher than that one reported in the previous paragraph concerning the generation of hydrogen from the photocatalytic degradation of glucose on perovskites.

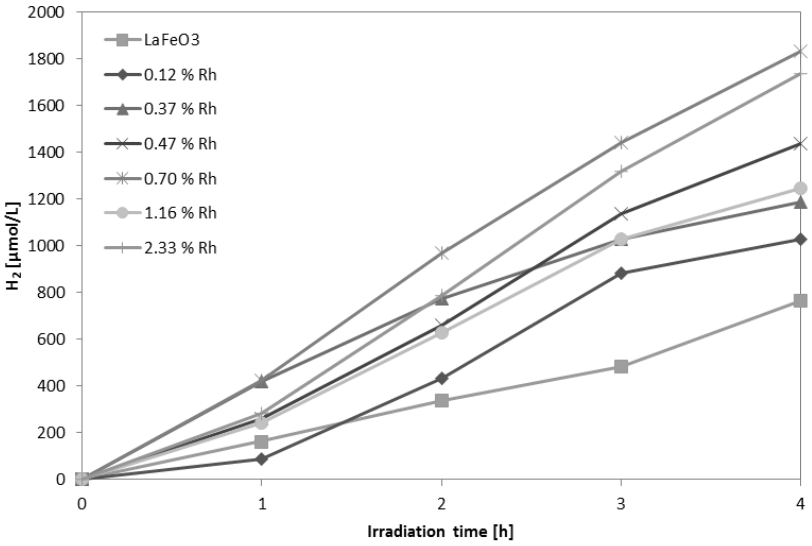

Figure IV.21. *Hydrogen production during the irradiation time for undoped and Rh doped photocatalysts.*

Figure IV.22 reports the hydrogen production and glucose degradation obtained for the different photocatalyst doped with rhodium and for undoped $LaFeO_3$ after 4 hours of irradiation time. The almost total glucose degradation was achieved after 4 hours of UV irradiation time for 0.7%Rh catalyst. Glucose degradation increased as Rh content was increased from 0.12 to 0.7, and decreased when Rh % was increased from 0.7 to 2.33 mol%.

The same trend was observed for H_2 production with the highest value (1835 µmol/L) achieved for 0.7%Rh after the same irradiation time.

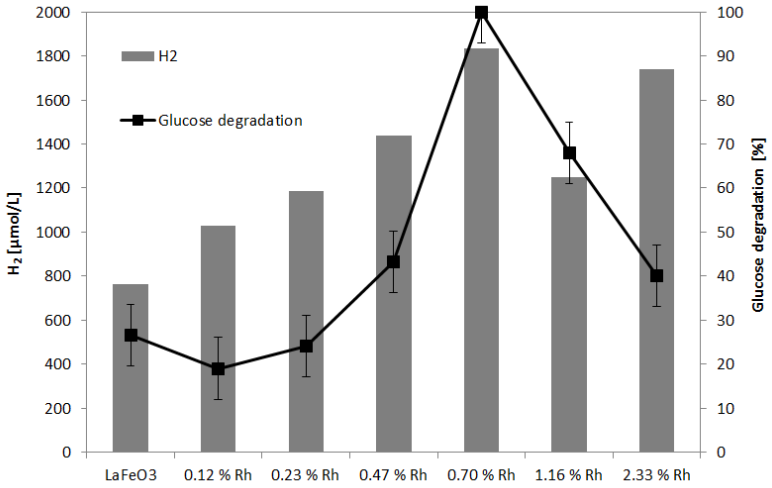

Figure IV.22 *Hydrogen production and glucose degradation after 4 hours of irradiation for undoped and Rh doped photocatalysts.*

The presence of Rh^{4+} in the crystalline structure of the perovskite could promote the separation of charge carriers efficiently, inhibiting the recombination of electron–hole pairs, and consequently causing the enhancement of the photocatalytic activity (Elsalamony and Mahmoud, 2012) This phenomenon may be predominant for an Rh content up to 0.7 mol%. The decreased photoactivity observed when Rh% was increased from 0.7 to 2.33 mol % is probably due to the presence of rhodium oxide on the catalyst surface, as observed from XRD analysis (Figure IV.18). The presence of rhodium oxide crystallites can act as recombination centers diminishing the H_2 production and the glucose degradation as observed for photocatalysts doped with Ru (Nguyen-Phan et al., 2016). These results evidenced that the optimal Rh loading was 0.7 mol%.

The same results was observed for the methane production, showed in figure IV.23, where it is possible to note that the highest CH_4 production equal to about 100 µmol/L was obtained for 0.7%Rh photocatalyst.

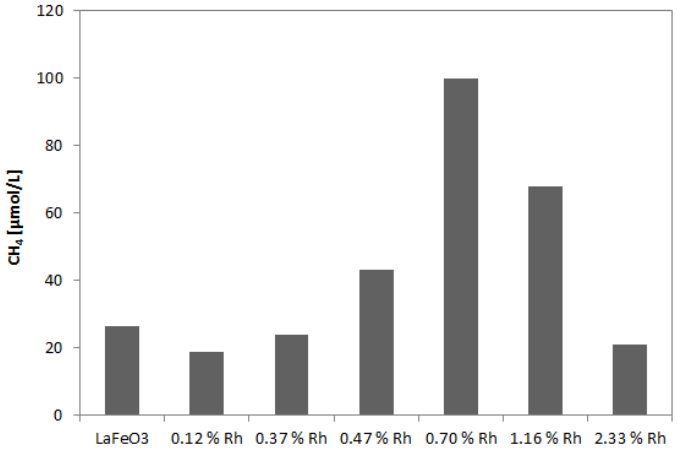

Figure IV.23 *Methane production after 4 hours of irradiation for undoped and Rh doped photocatalysts.*

So, from these results it was possible to observe that the substitutional doping generated by the replacement of Fe^{4+} with Rh^{+4} promotes the separation of charge carriers efficiently, inhibiting the recombination of the photogenerated electron–hole pairs, and consequently enhancing the photocatalytic activity. The total glucose degradation and the highest H_2 production have been achieved with an Rh content equal to 0.7 mol%.

IV.2.2 Ruthenium doped $LaFeO_3$

IV.2.2.1 Synthesis and characterization results

Ru-$LaFeO_3$ samples were prepared by solution combustion synthesis, using citric acid as organic fuel and metal nitrate as metal precursor (oxidizer) (Hwang et al., 2010). In detail, 1.66 g of $Fe(NO_3)_3 \cdot 9H_2O$ (Riedel-deHaen, 97 wt%), 1.78g of $La(NO_3)_3 \cdot 6H_2O$ (Fluka, 99%), 0.86g of citric acid (Fluka, 99 wt%) and a specific amount of $RuCl_3$ (Sigma Aldrich, 99%) used as dopant, were completely dissolved in 100 ml of bidistilled water. The solution was kept stirred continuously at 60 °C for 5 minutes. Then, ammonium hydroxide (Carlo Erba, 37 wt %) was slowly added to regulate the pH of the solution up to 7.0. The solution was dried at 130° C and then calcined at 300° C for 3 hours to ignite the solution combustion reaction (Iervolino et al., 2016b). Different amount of $RuCl_3$ was used for the doping of $LaFeO_3$ to obtain photocatalysts with different amount of Ru (Table 1). The Ru nominal loading is expressed as molar percentage and it was evaluated through eq. IV.12:

$$\%molRu = \frac{nRu}{nLa + nFe} \cdot 100 \qquad \text{(IV.12)}$$

Where:

nRu is the number of moles of $RuCl_3$ used in the synthesis;

nLa is the number of moles of $La(NO_3)_3 \cdot 6H_2O$ used in the synthesis;

and *nFe* is the number of moles of $Fe(NO_3)_3 \cdot 9H_2O$ used in the synthesis.

Table IV.2.2 *Summary of the characterization results*

Catalyst	Ru nominal amount [mol %]	Ru measured amount (XRF) [mol %]	Crystallite size (XRD) [nn]	Specific surface area [m^2/g]	Band gap (UV-Vis DRS) [eV]
$LaFeO_3$	0	0	37	4	2.12
0.12% Ru	0.12	0.11	29	5	2.08
0.23% Ru	0.23	0.19	30	5	2.04
0.38% Ru	0.37	0.35	30	5	2.01
0.47% Ru	0.47	0.49	29.5	5	1.98
0.70% Ru	0.70	0.72	31	5	1.85
1.16% Ru	1.16	1.22	28.5	5	1.90
2.33% Ru	2.33	2.43	30	5	1.72

IV.2.2.1.1 XRD

Figure IV.23 shows the XRD patterns of the Ru-doped $LaFeO_3$ photocatalysts doped with different amount of ruthenium. XRD showed well indexed diffraction peaks, clearly indicating the formation of orthorhombic perovskite type structure, as reported in literature (Tijare et al., 2010, Iervolino et al., 2016b). No significant impurity phases and no splitting of peaks were observed underlining that no orthorhombic distortion occurred, according to literature for perovskite samples doped with ruthenium (Gurav et al., 2012).

Additional peaks due to ruthenium oxide were not observed up to a Ru loading of 1.16 mol %. In fact, for the catalyst 1.16%Ru, XRD patterns showed an additional diffraction peak at 2θ value of about 35 degree due to the presence of RuO_2 on the surface, indicating only a partial doping of perovskite structure (Senthilnanthan et al., 2010). The crystallite size of the samples was calculated by Scherrer formula for a diffraction line positioned at 2θ value of 32.16 degree, which corresponds to $LaFeO_3$ (h k l) (0 0 2) (Tijare et al., 2010) (Table IV.2.2).

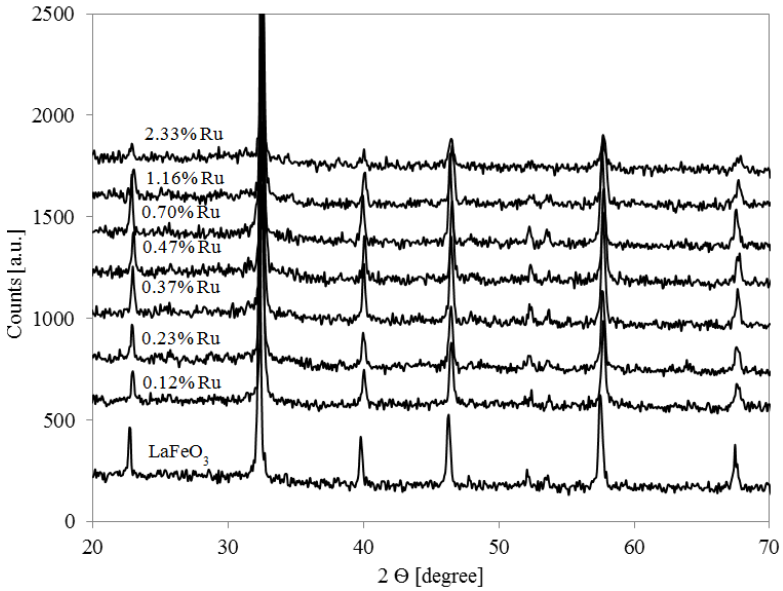

Figure IV.23. *XRD spectra for undoped and Ru-doped $LaFeO_3$*

Comparing doped and undoped $LaFeO_3$, it can be observed that the doping process induced a slight decrease of photocatalysts crystallite size, though no clear relationship could be established between Ru contents (Figure IV.23). A similar result was observed for $SrTiO_3$ perovskite doped with Ru (Gurav et al., 2012).

IV.2.2.1.2 BET surface area and XRF results

BET surface area values (S_{BET}) of the catalysts are shown in Table 1. In agreement with XRD results, S_{BET} values did not change when Ru amount used in the catalyst preparation was increased. In particular, S_{BET} increased from 4 up to 5 m^2/g for undoped $LaFeO_3$ and Ru-doped $LaFeO_3$, respectively. The total amount of ruthenium in the samples was determined by XRF (Table IV.2.2). In every case, the real Ru content well agrees to the nominal metal content indicating a good yield of the synthesis process.

IV.2.2.1.3 UV-Vis Diffuse Reflectance spectra

The reflectance spectra (Figure IV.24) showed the typical absorption band edge of the $LaFeO_3$ semiconductor at around 814 and 600 nm for all the samples and attributed to electron transitions from valence band to conduction band ($O_{2p} \rightarrow Fe_{3d}$) (Parida et al., 2010). It is worthwhile to note that these bands disappeared for the catalysts with the higher Ru content (1.16%Ru and 2.33%Ru). This result could be due to the presence of RuO_2

present on the $LaFeO_3$ surface, observed in XRD measurements (Figure IV.18).

The absorption edge of Ru-doped $LaFeO_3$ catalysts has a red shift and also a stronger absorption than the pure $LaFeO_3$ in the visible region. Similar results were observed for Li-doped $LaFeO_3$ samples (Hou et al., 2006).

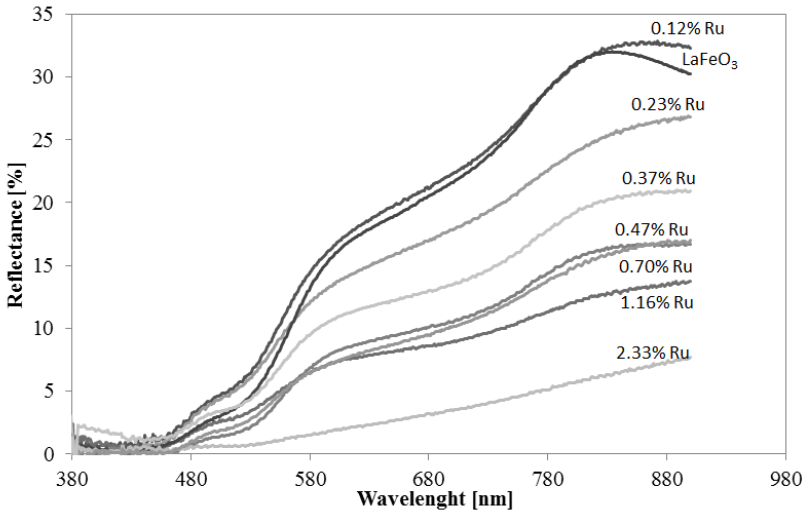

Figure IV.24. *UV Vis DRS spectra for undoped and Ru-doped $LaFeO_3$*

The data obtained from UV–Vis reflectance spectra were used for evaluating the band-gap energy of the photocatalysts (Figure IV.25). The obtained results are reported in Table IV.2.2. The increase of Ru amount resulted in a decrease in band-gap energy from 2.12 (band-gap of undoped $LaFeO_3$) to 1.72 eV for 2.33%Ru. The decrease of band-gap energy was due to the electronic transition from donor levels formed with dopants to the conduction band of the host photocatalysts (Wang et al., 2015). In our case, the dopant could exist as a trivalent ion (Ru^{3+}) on the Fe^{4+} site, which forms a donor level at a lower potential than the top of the valence band composed of O 2p orbitals, and the apparent band-gap energy consequently became narrowed (Wang et al., 2015).

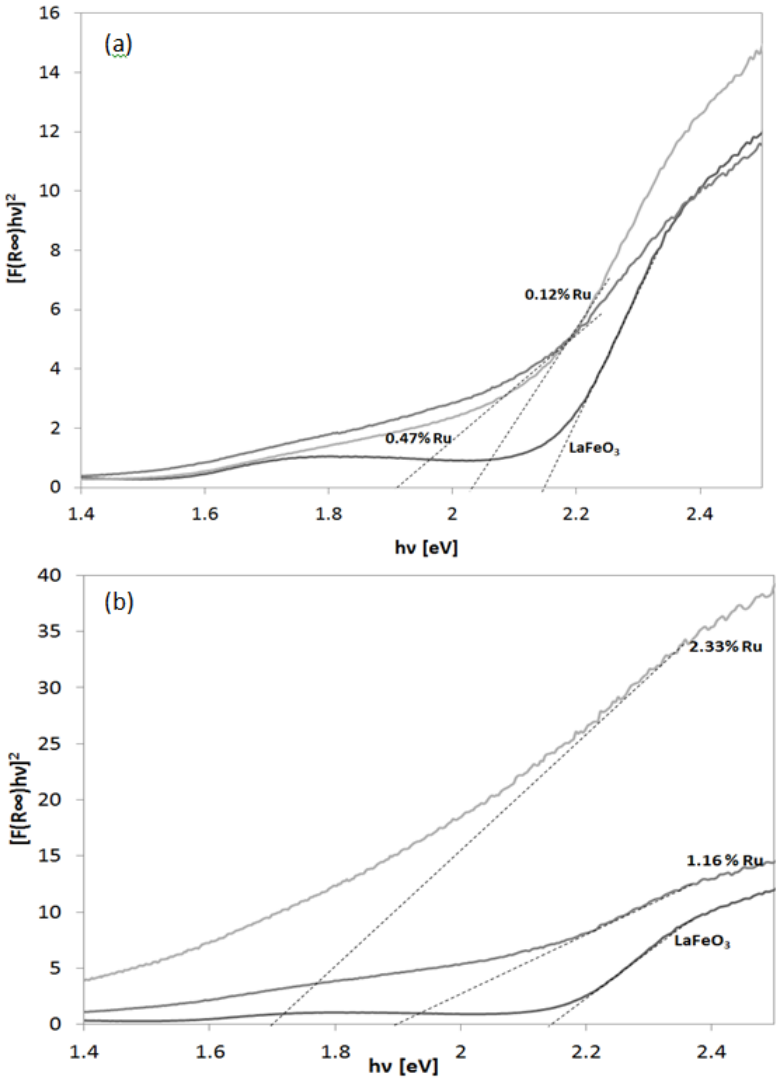
(a)
[F(R∞)hν]²
hν [eV]
0.12% Ru
0.47% Ru
LaFeO3
(b)
[F(R∞)hν]²
hν [eV]
2.33% Ru
1.16 % Ru
LaFeO3

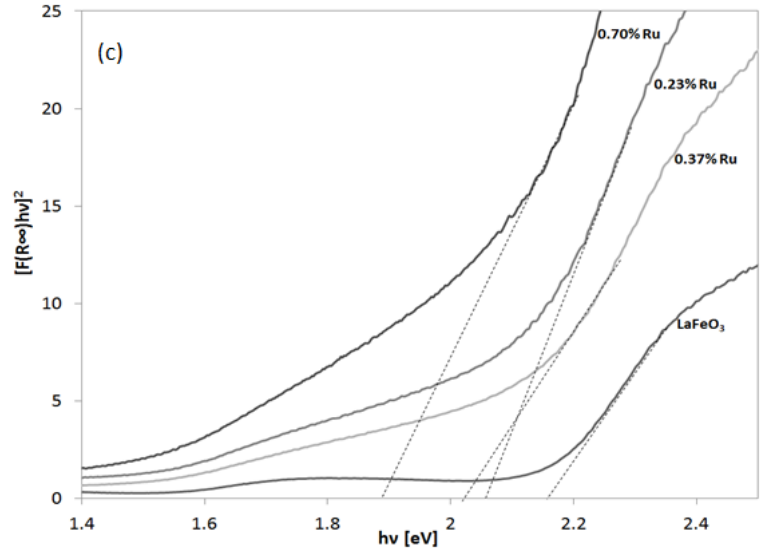

Figure IV.25. *Evaluation of band gap for undoped and Ru-doped $LaFeO_3$*

IV.2.2.1.4 SEM analysis

The morphology of the $LaFeO_3$ and Ru-doped $LaFeO_3$ photocatalysts was investigated by SEM microscopy and the obtained results are presented in Figure 4. For sake of brevity, together with undoped $LaFeO_3$, only the analysis on 0.47%Ru photocatalyst are reported, being similar the results obtained for all the others Ru-doped $LaFeO_3$ samples.

The SEM pictures show that the size of photocatalysts particles is not uniform due to agglomeration phenomena induced by particle-particle interactions. However, porous structure is clearly seen in the SEM images revealing the low density product, loose and porous material (Khetre et al., 2010) due to the role of citric acid in the combustion of gel formed after the drying process at 130°C. In particular, at the combustion point, the citric acid generates gases that tried to come out from the gel by breaking the gel and generating the porous structure of $LaFeO_3$ (Figure IV.26 a) and Ru-doped $LaFeO_3$ (Figure IV.26b) photocatalysts (Khetre et al., 2010).

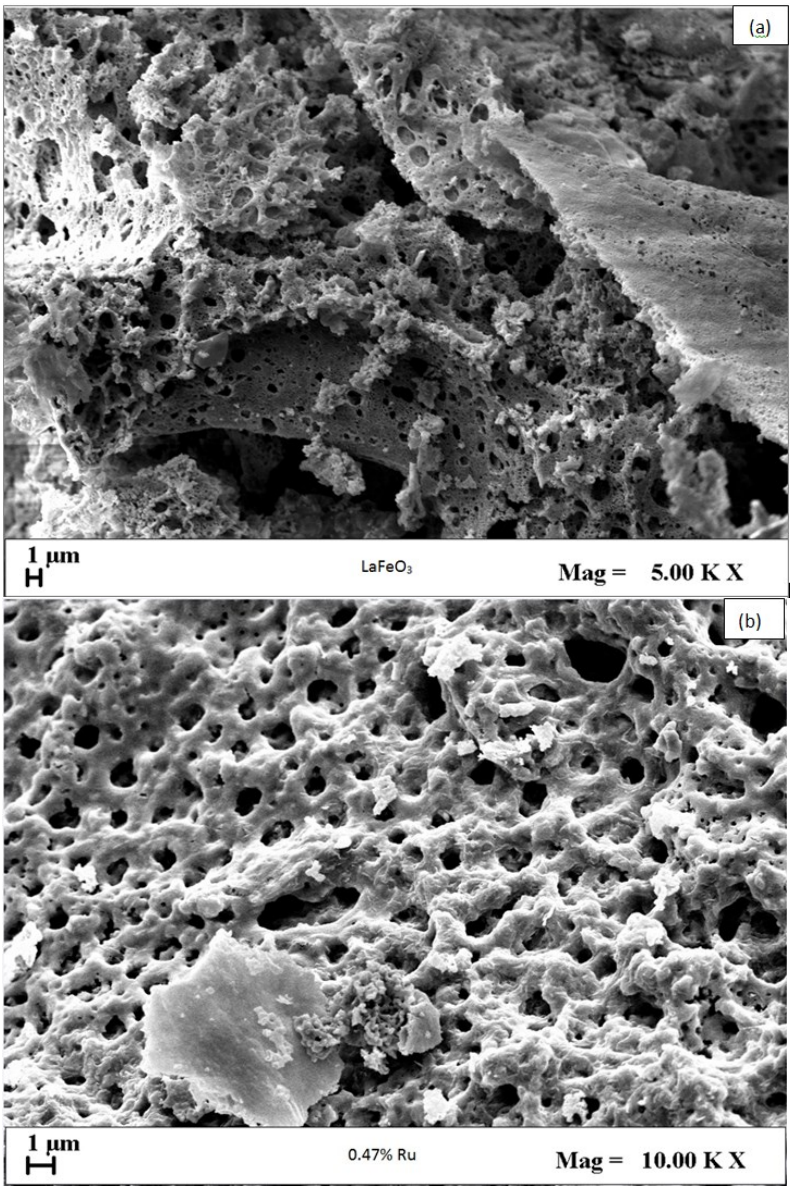

Figure IV.26. *SEM image of $LaFeO_3$ (a) and 0.47%Ru (b) photocatalysts.*

IV.2.2.2 Photocatalytic results

In a typical photocatalytic test, 0.12 g of catalyst was suspended in 80 ml of an aqueous solution containing 1000 mg/L of glucose (D^+ Glucose VWR, Sigma-Aldrich). To ensure complete mixing of the solution in the reactor, a peristaltic pump was used. The photoreactor was irradiated with a strip of UV-LEDs with wavelength emission in the range 375–380 nm, or with a strip of visible LEDs with the main wavelength emission at 440 nm positioned around the external surface of the reactor.

To evaluate the effect of reactor design, another photoreactor (R2) with a nominal volume equal to the first one (R1) but with an internal diameter equal to half (1.25cm) was also investigated. Finally, to evaluate the effect on real wastewater containing glucose, the optimized photocatalyst was tested under visible light on a wastewater sample taken from a brewing process (pH 6, TSS 450 mg/L, TOC 1000 mg/L).

IV.2.2.2.1 Effect of Ru content on H_2 photocatalytic production and glucose degradation.

During the dark phase a decrease of the concentration of glucose, due to the adsorption on the catalyst surface, was observed and any product has been detected in gaseous phase. Figure IV.27 report the behavior of relative glucose concentration (C/C_0) and hydrogen production under UV-LEDs light at the spontaneous pH of solution (pH=6).

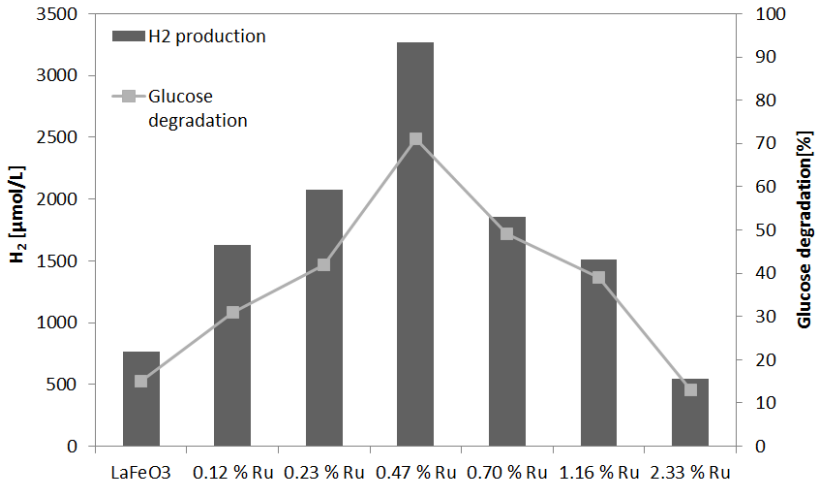

Figure IV.27. *Behavior of glucose degradation and hydrogen production after 4 hours of irradiation for all the photocatalysts; light source: UV-LEDs; glucose initial concentration: 1000 mg/L; catalyst dosage: 1.5 g/L.*

All the Ru-doped $LaFeO_3$ photocatalysts demonstrated a better activity compared to undoped $LaFeO_3$. The higher glucose degradation (about 70 %) was achieved after 4 hours of UV irradiation time for 0.47%Ru catalyst.

Glucose degradation efficiency increased as Ru% was increased from 0.12 to 0.47, and decreased when Ru% was increased from 0.47 to 2.33. In parallel, the same trend was observed for H_2 production with the higher value (3270 µmol/L) achieved for 0.47%Ru after the same irradiation time, higher than that one reported in the literature concerning the generation of hydrogen from the photocatalytic degradation of glucose on perovskites (Iervolino et al., 2016b).

Also for the methane production was observed the same trend (Figure IV.28). In fact, all the catalysts doped with ruthenium show a methane production higher than the undoped $LaFeO_3$. The highest methane production was obtained with the catalyst 0:47% Ru for which it is achieved a production of about 90 µmol/L.

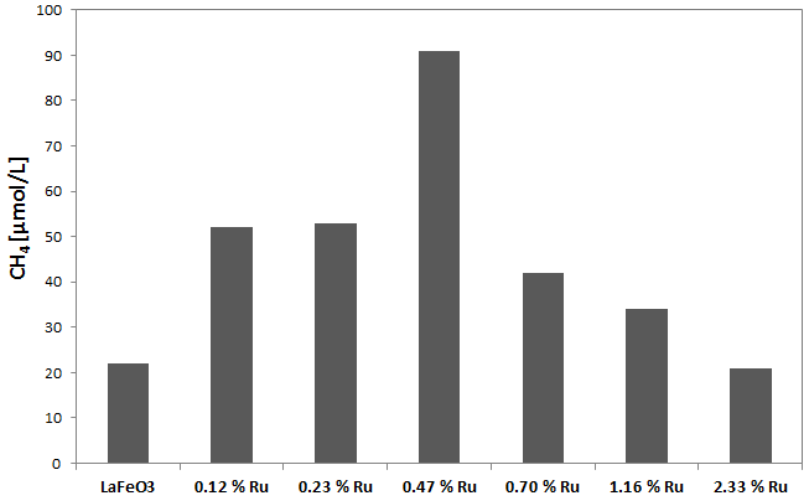

Figure IV.28 *Methane production after 4 hours of irradiation for undoped and Ru doped photocatalysts.*

The introduction of Ru in the crystalline structure of the $LaFeO_3$ resulted in the change of the electronic environment of perovskite (Figure IV.19) and may promote the separation of charge carriers efficiently, inhibiting the recombination of electron–hole pairs, and consequently causing the enhancement of the photocatalytic activity (Elsalamony and Mahmoud, 2012). This effect could be predominant for a Ru loading up to 0.47 mol%. The decreased efficiency observed when Ru% was increased from 0.47 to 2.33 is probably due to the presence of RuO_2 on the catalyst surface, as evinced from XRD analysis (Figure IV.28). The presence of RuO_2

crystallites may reduce the light penetration, retarding the activation of the photocatalyst and the generation of photoinduced charge carriers or can act as recombination centers diminishing the H_2 production and the glucose degradation (Nguyen-Phan et al., 2016, Antoniadou et al., 2013).

According to these results 0.47 mol% of Ru loading was considered to be the optimal value for the studied reaction.

IV.2.2.2.2 Effect of different metal for $LaFeO_3$ doping: Ru vs Pt.

Noble metals are widely used as dopants to improve the photocatalytic activity of semiconductor exploiting the properties of the recombination of charged inhibitors, usually positively influencing photocatalytic activity (Tijare et al., 2010). In order to demonstrate the enhanced efficiency of the perovskite doped without noble metals in the photocatalytic hydrogen production, a comparison between $LaFeO_3$ doped with ruthenium (0.47% Ru) and the same catalyst doped with platinum was carried out. To make the comparison as much reliable as possible, the catalyst doped with platinum (0.47%Pt) was prepared with the same method and with the same molar percentage of Pt used for the catalyst 0.47%Ru and using platinum chloride (Sigma Aldrich, 99%) as a precursor salt. The comparison between the two catalysts in terms of glucose degradation during the irradiation time is shown in Figure IV.28a.

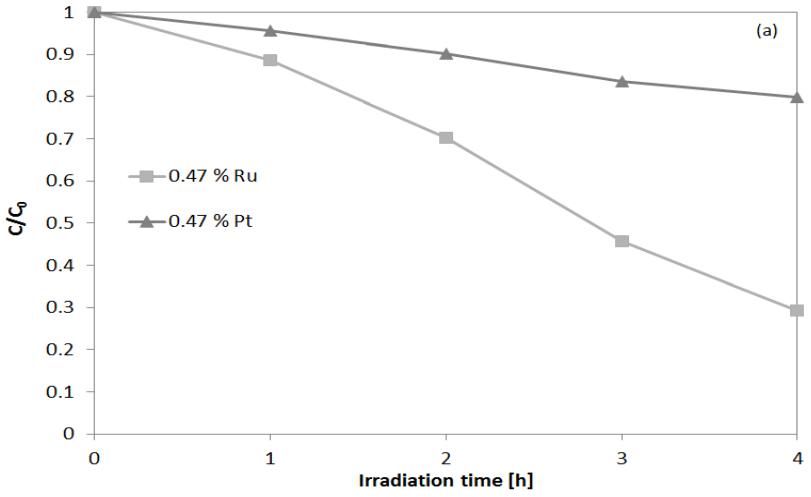

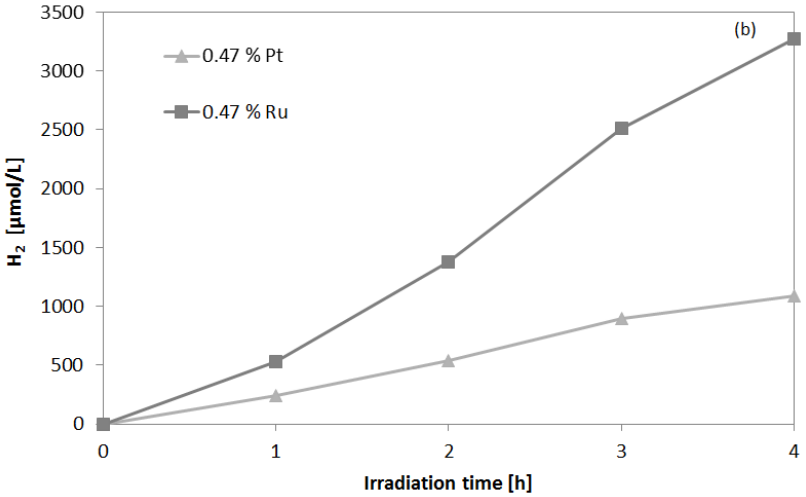

Figure IV.28. *Glucose degradation (a) and hydrogen production (b) as a function of irradiation time on 0.47%Ru and 0.47Pt photocatalysts; light source: UV-LEDs; glucose initial concentration: 1000 mg/L; catalyst dosage: 1.5 g/L.*

Ru-doped photocatalyst was significantly more efficient than Pt-doped photocatalyst in glucose degradation. In particular, 0.47%Ru experiment resulted in a 70 % glucose reduction after 4 hours of irradiation compared to only 20% reduction observed for 0.47%Pt under the same irradiation time. The same result was observed in terms of hydrogen production. In fact with 0.47%Ru catalyst, test showed a hydrogen production as high as 3270 µmol/L after 4 hours of UV irradiation, about three times higher than that observed for 0.47%Pt (Figure IV.28). Considering that Ru or Pt act as a mediator in the vectorial electron-transfer process, their Fermi energy levels are supposed to affect the interfacial charge transfer and thus the charge separation (Hudson, 1998). In general, the higher Fermi level of the noble metal leads to the better the photocatalytic activity (Halas and Durakiewicz, 1998a). In this context, it was found that, for Fermi level, the order of metals is Ru > Pt (Shen et al., 2010a), explaining in this way, the better photocatalytic activity of Ru-doped $LaFeO_3$ with respect to Pt-doped $LaFeO_3$ catalyst.

IV.2.2.2.3 Influence of the reactor configuration on the photocatalytic activity

The optimum condition of Ru percentage (0.47) in terms of glucose degradation and hydrogen production was used to investigate the influence of the reactor configuration. In particular a new set of experiments was carried out with the new reactor (R2) with a nominal volume equal to the

first one (R1) but with an internal diameter equal to half (1.25cm). The aim was to enhance the photonic transport by increasing the photons flow that intercept the photocatalysts particles dispersed into the glucose solution.

Figure IV.29 shows the comparison in terms of photocatalytic activity between the two reactor configurations. R2 resulted in a significantly higher glucose degradation compared to R1: in particular, an almost complete sugar degradation after 3 hours of UV irradiation was observed for R2 compared to 70% removal in 4 hours of UV irradiation observed for R1 (Figure IV.29a). Noteworthy, glucose degradation had already reached about 70% after 2 hours of irradiation in R2 experiments.

Moreover, in parallel the hydrogen production (Figure IV.29b) was higher with the photoreactor R2 (6079 μmol/L) compared to that one obtained with the photoreactor R1 (3270 μmol/L).

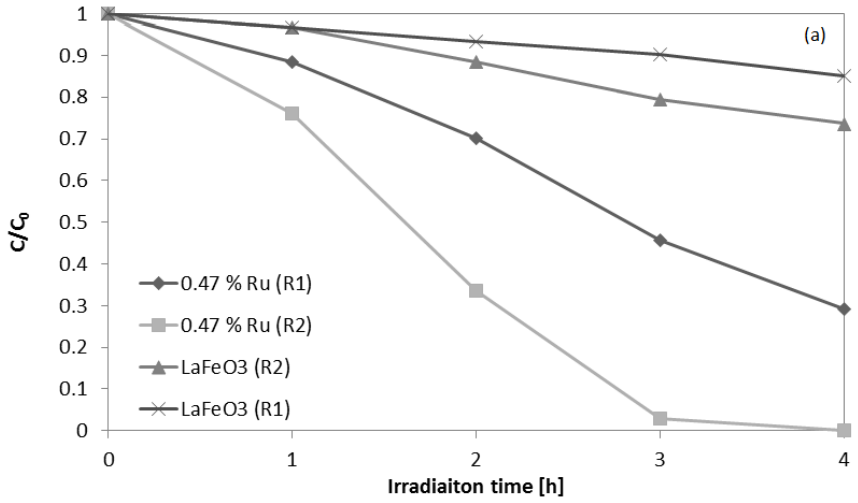

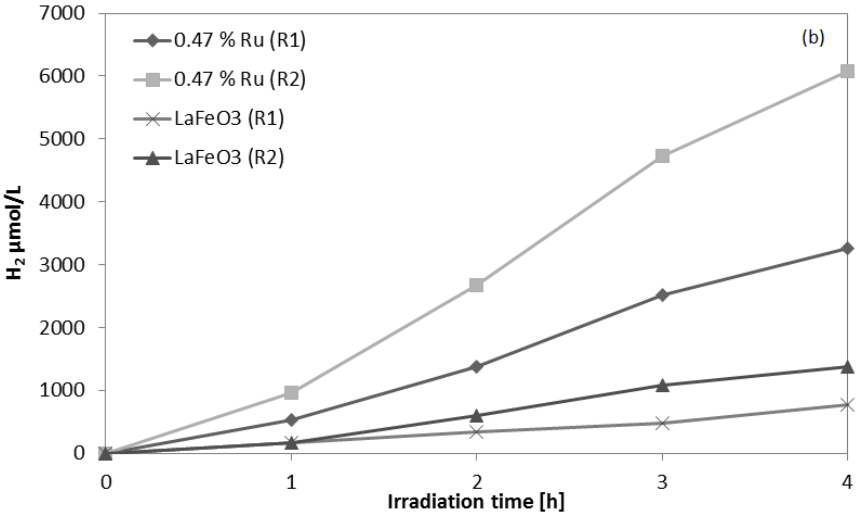

Figure IV.29 *Influence of reactor configuration on glucose degradation (a) and hydrogen production (b) with 0.47%Ru photocatalyst; light source: UV-LEDs; glucose initial concentration: 1000 mg/L; catalyst dosage: 1.5 g/L.*

These results are in agreement with a previous work where a similar photoreactor configuration was investigated in the removal of chemical oxygen demand (COD) of a highly polluted wastewater (Hajaghazadeh et al., 2014). It is underlined that the percentage of irradiated catalyst volume is different. For an ID of 1.25 cm (photoreactor R2), it is larger than that obtained for an ID of 2.5 cm (photoreactor R1) indicating that the attenuation of the available light energy is a key parameter that influences the photocatalytic performances of the reactor as previously found (Chiovetta et al., 2001, Palma et al., 2010).

IV.2.2.2.4 Optimization of catalyst dosage for photocatalytic tests

The optimization of the catalyst dosage was carried out under UV irradiation with the photoreactor R2 by testing different dosages of 0.47%Ru photocatalyst, in the range 0.75-3 g/L. Photocatalytic efficiency increased as catalyst loading was increased up to 1.5 g/L (Figure IV.30).

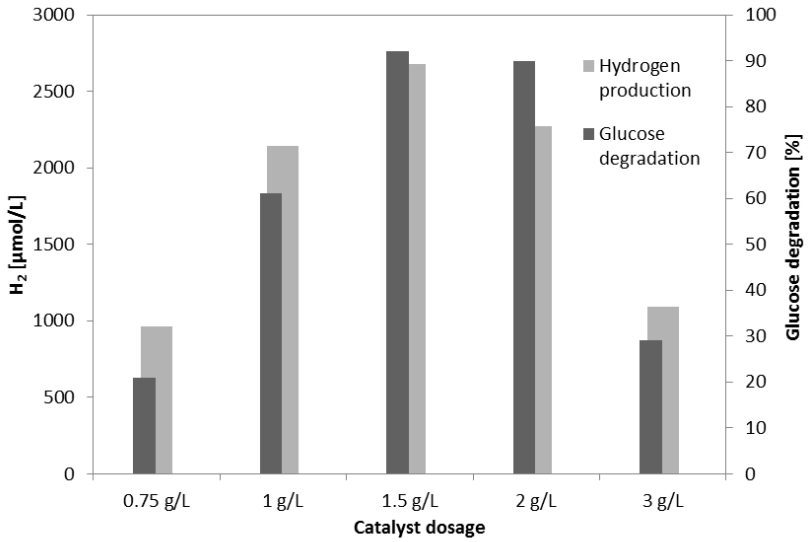

Figure IV.30 *Influence of catalyst dosage on glucose degradation and hydrogen production after 2 hours of irradiation; photocatalyst: 0.47%Ru; light source: UV-LEDs; glucose initial concentration: 1000 mg/L; photoreactor R2.*

Further increase in catalyst loading resulted in a decreased degradation of glucose and lower H_2 production. Possibly, the increase in the catalyst dosage over the optimum value resulted in a decreased light penetration through the solution because of the increased opacity of the aqueous suspension, a typical behavior reported in literature when the amount of the catalyst was increased in a similar photoreactor configuration (Vaiano et al., 2016a).

IV.2.2.2.5 Influence of initial glucose concentration

Figure IV.31 shows the effect of the initial glucose concentration on its degradation (Figure IV.31a) and hydrogen production (Figure IV.31b) under UV light. In particular, glucose degradation decreased as the initial concentration was increased. It is worthwhile to note that, as the initial concentration of glucose was increased, an increase of the hydrogen production was observed up to 1000 mg/L of initial concentration of glucose, in agreement with the results available in scientific literature (Fu et al., 2008b).

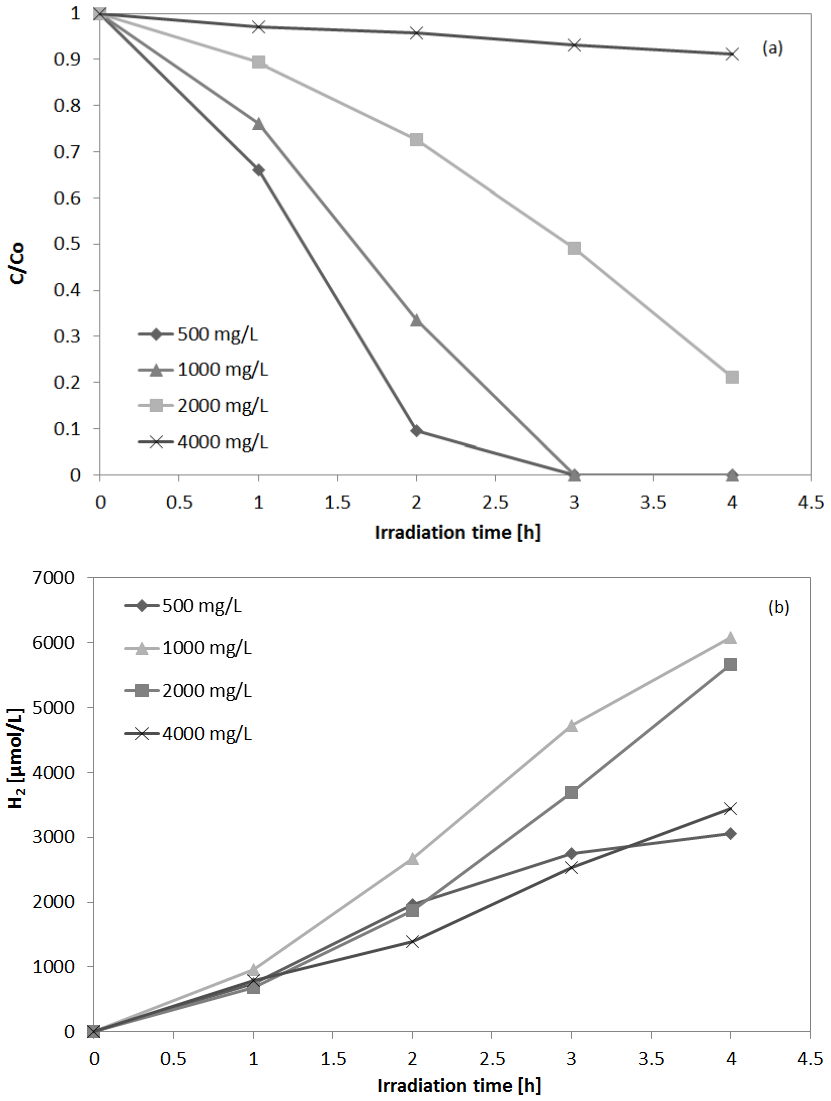

Figure IV.31. *Glucose degradation (a) and hydrogen production (b) as a function of irradiation time for different glucose initial concentrations; photocatalyst: 0.47%Ru light source: UV-LEDs; catalyst dosage: 1.5 g/L; photoreactor R2.*

The H_2 production from glucose degradation could be obtained according to the sugar photoreforming reaction:

$$C_6H_{12}O_6 + 6H_2O = 12H_2 + 6CO_2 \qquad \text{IV.13}$$

In this reaction the H_2/CO_2 ratio is equal to 2. However, in our case, the ratio H_2/CO_2 is in the range 28 – 46, as initial glucose concentration was varied, and never equal to 2 (Figure IV.32a).

On the other hand, the analysis of the liquid phase showed that gluconic acid is formed during photocatalytic process and the ratio between the moles of gluconic acid produced and the moles of glucose converted is approximately equal to 1 for all the tested concentrations (Figure IV.32b), as previously observed on $LaFeO_3$ based photocatalysts.

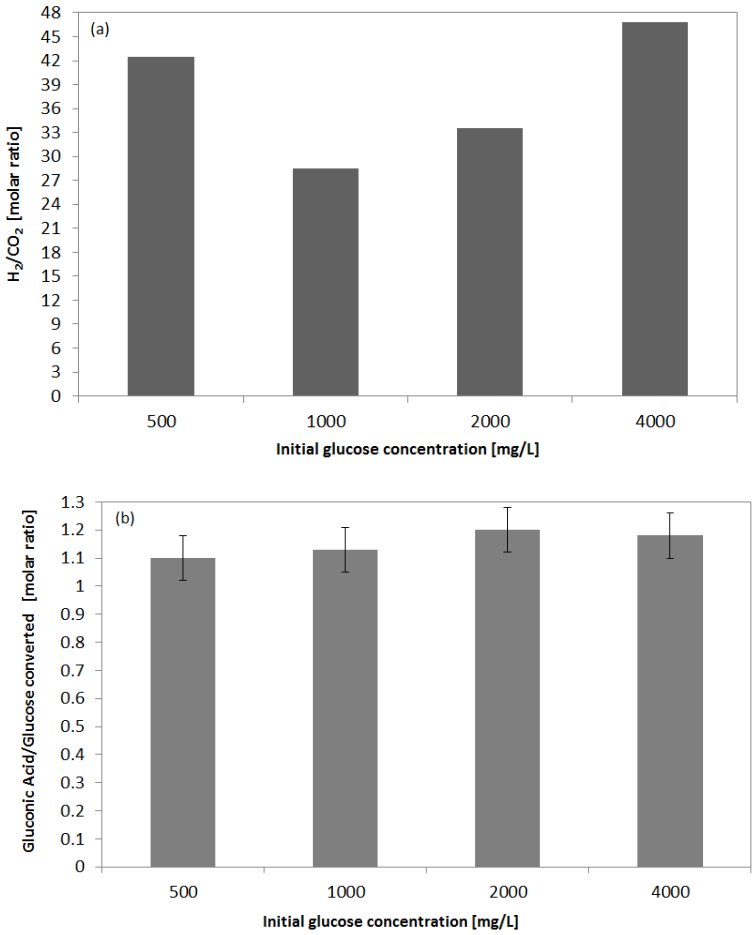

Figure IV.32. *Influence of initial glucose concentration on CO_2/H_2 molar ratio (a) and gluconic acid formed/glucose converted molar ratio (b) for different initial glucose concentrations; irradiation time: 4 h; photocatalyst: 0.47%Ru; light source: UV-LEDs; catalyst dosage: 1.5 g/L; photoreactor R2.*

Part of the additional CO_2 produced could come from the decarboxylation reaction of gluconic acid (Hoffmann et al., 1995a, Iervolino et al., 2016a). But, taking into account the results reported in Figure IV.32a, this last reaction occur at a limited extend. On the basis of these observations and considering the behavior shown in Figure IV.32b, H_2 and gluconic acid could be mainly produced from the photocatalytic degradation of glucose, according to the following reaction:

$$C_6H_{12}O_6 + H_2O = H_2 + C_6H_{12}O_7 \qquad \text{IV.14}$$

IV.2.3 Mathematical modeling for Ru doped $LaFeO_3$ photocatalyst

IV.2.3.1 Water splitting reaction on 0.47%Ru photocatalyst

Before assessing the mathematical model of photocatalytic hydrogen formation from the degradation of glucose in aqueous solution, the ability of 0.47%Ru photocatalyst in the hydrogen production through water splitting reaction (without glucose) under UV irradiation was evaluated (Figure IV.33). The amount of hydrogen produced progressively increased, as irradiation time increased, reaching a value of 64 μmol (after 4 hours of irradiation) corresponding to 2133 μmol/L, significantly lower than that obtained in presence of glucose. In fact, to promote photocatalytic water splitting, various oxidizing sacrificial agents have been added to water; the role of sacrificial agent being to scavenge the coproduced O_2 due to water splitting, and, thus, to prevent the reverse reaction of O_2 with H_2 to H_2O (Kawai and Sakata, 1980, Zieliñska et al., 2008). Typically, the sacrificial compounds are hydrocarbons such as saccharides, alcohol and acetic acid (Deguchi et al., 2011). However it must be taken into account that, in our case, the water splitting reaction plays an important role in the photocatalytic hydrogen production.

The amount of hydrogen produced through water splitting reaction during the photocatalytic process followed a linear trend (Figure IV.33); accordingly, the zero-order kinetic model (eq.IV.15) perfectly represents experimental data:

$$\frac{dnH_2}{dt} = k_{ws} \cdot W \qquad \text{(IV.15)}$$

Where W is the amount of photocatalyst used in the test (0.12 g), nH_2 is the millimoles of hydrogen produced, t is the irradiation time (min) and k_{ws} is the kinetic constant of water splitting reaction (mmol/(g_{cat}*min).

The initial condition for eq.IV.15 was:

$t = 0 \qquad nH_2=0$

Eq. IV.15 was solved with Euler iterative method together with the initial condition finding a k_{ws} value equal to 0.00513 mmol/ (g_{cat}*min).

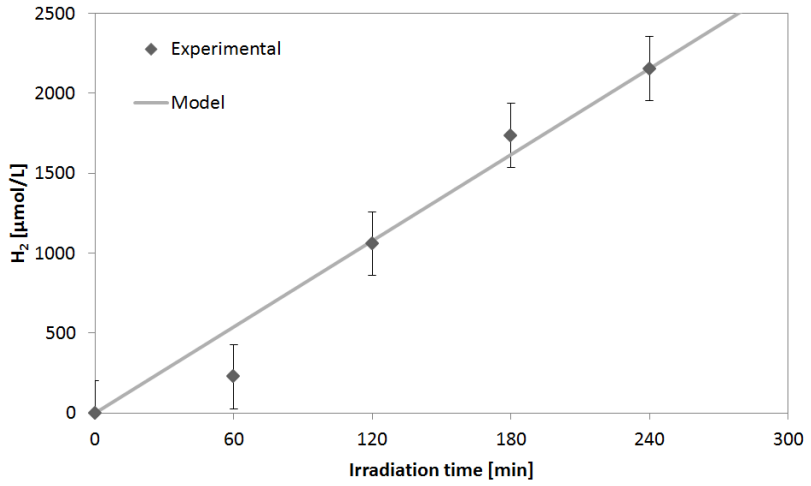

Figure IV.33. *Fitting of experimental data with zero-order kinetic model for water splitting reaction. Photocatalyst: 0.47%Ru; light source: UV-LEDs; catalyst dosage: 1.5 g/L; photoreactor R2.*

IV.2.3.2 Adsorption of glucose on 0.47%Ru photocatalyst in dark conditions

Glucose adsorption on the active surface of the photocatalyst (0.47%Ru) (C*) was evaluated as a function of the equilibrium concentration (C_{eq}) under dark conditions (Figure IV.34).

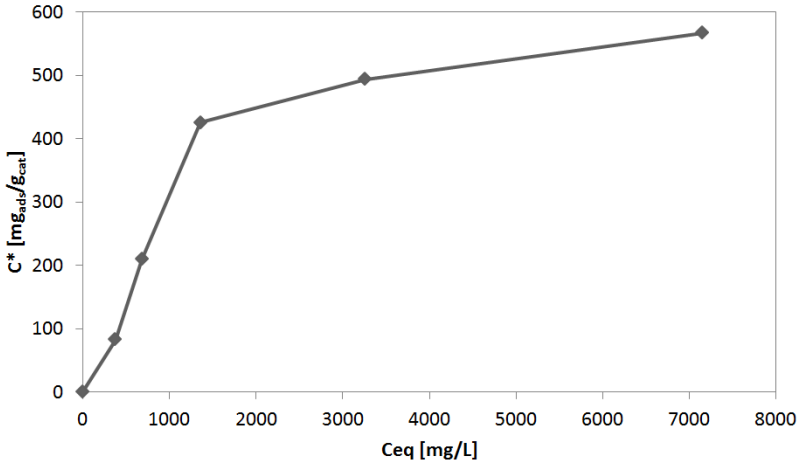

Figure IV.34. *Evaluation of glucose adsorbed on 0.47%Ru sample. Catalyst dosage: 1.5 g/L.*

Different assumptions were made to understand the best model able to fit the obtained experimental data. In particular a first fitting attempt was made with Langmuir isotherm (Eq.5):

$$C^* = \frac{C_m \cdot b \cdot C_{eq}}{1 + b \cdot C_{eq}} \qquad \text{IV.16}$$

Where:
C^* is the amount of glucose adsorbed on catalyst surface [$mg_{glucose}/g_{cat}$];
C_{eq} is the glucose equilibrium concentration after dark phase [mg/L];
C_m is the maximum amount of glucose adsorbed on catalyst surface [$mg_{glucose}/g_{cat}$];
b is the adsorption equilibrium constant [L/mg].

The values of b and C_m were achieved using nonlinear regression analysis of the experimental data to fit the Langmuir function for glucose adsorption as a function of C_{eq}. The nonlinear regression procedure was performed using the least-squares approach, based on the minimization of the sum of squared residuals, obtaining 0.00073 and 699 for b and C_m, respectively. Unfortunately, the calculated values did not fit well experimental data (Figure IV.35). This means that Langmuir isotherm is unable to well represent the behaviour of glucose adsorption on the 0.47%Ru surface.

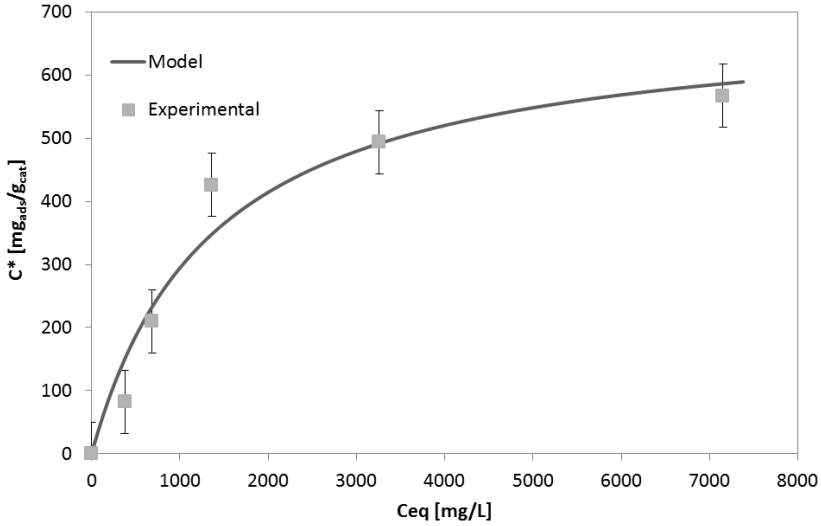

Figure IV.35. *Fitting of adsorption experimental data with Langmuir–Hinshelwood (L–H) isotherm for the evaluation of adsorption constant b. Sample: 0.47%Ru; catalyst dosage: 1.5 g/L.*

The second attempt to find an adsorption law able to fit experimental data was made with Freundlich isotherm (IV.17):

$$C^* = k \cdot C_{eq}^{1/n} \qquad \text{IV.17}$$

Where:

k is the Freundlich constant that corresponds to adsorption capacity (Desta, 2013);

n is the adsorption intensity (Desta, 2013)

Constants k and 1/n were evaluated as 0.97 and 0.80, respectively by fitting the experimental data as a function of C_{eq} (Figure IV.36).

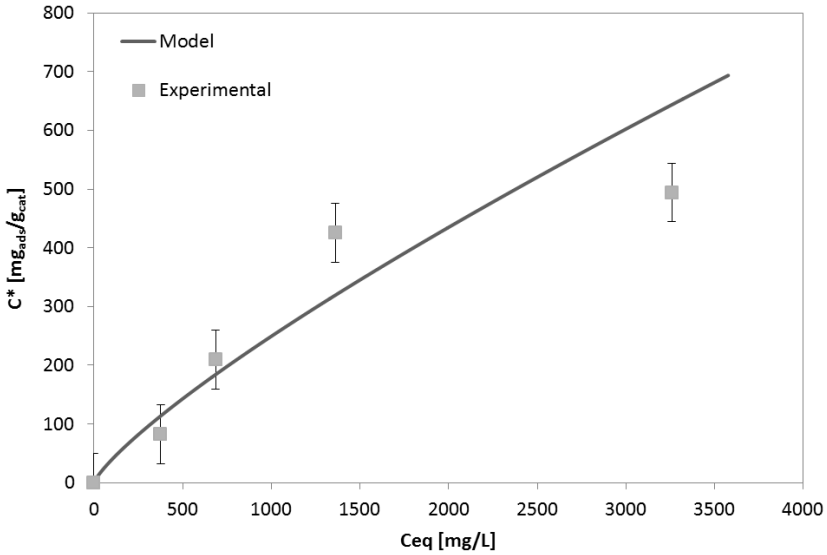

Figure IV.36. *Fitting of adsorption experimental data with Freundlich isotherm. Sample: 0.47%Ru; catalyst dosage: 1.5 g/L.*

Unfortunately, also Freundlich isotherm model was not able to well represent the behavior of the experimental data. However, possible alternative approach for the definition of an adsorption model in catalytic reactions is represented by the Langmuir-Freundlich isotherm (Jeppu and Clement, 2012) .The Langmuir-Freundlich isotherm is a versatile isotherm expression that can simulate both Langmuir and Freundlich behaviors (Nahm et al., 1977). A general form of Langmuir-Freundlich isotherm can be written as follow (Eq. IV.18):

$$C^* = \frac{C_m \cdot (b \cdot C_{eq})^n}{1 + (b \cdot C_{eq})^n} \qquad \text{IV.18}$$

Also in this case the fitting procedure was finalized by using the least squares approach, whose results are reported in Figure IV.37. The fitted values of b and n are 0.0012 and 2.21, respectively.

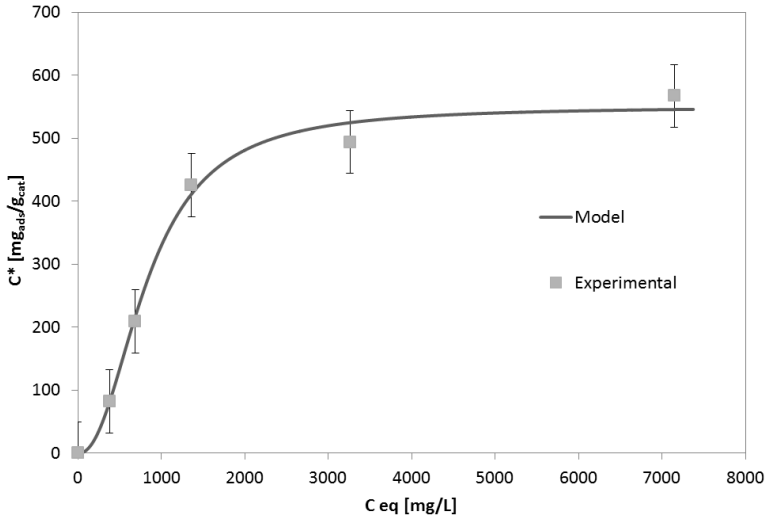

Figure IV.37. *Fitting of adsorption experimental data with Langmuir-Freundlich (L-F) isotherm. Sample: 0.47%Ru; catalyst dosage: 1.5 g/L.*

The comparison between the experimental data and those ones calculated by isotherm equation (Eq. IV.17) clearly indicates that the Langmuir-Freundlich can be used to describe the behavior of the amount of adsorbed glucose as a function of its equilibrium concentration. The non-linear behavior occurring for glucose concentrations lower than 1000 mg/L may happen because adsorbate-adsorbate interactions are stronger than adsorbate-adsorbent interactions (Jeppu and Clement, 2012).

IV.2.3.2 Kinetic modelling of the photocatalytic glucose degradation and hydrogen production on 0.47%Ru photocatalyst

Before to develop the kinetic modeling of the photocatalytic glucose degradation and hydrogen production on 0.47%Ru photocatalyst, the fluid dynamics of the system was preliminarily evaluated by the determination of the Reynolds number (Eq. IV.19):

$$\mathrm{Re} = \frac{D \cdot \nu \cdot \rho}{\mu} = 15963 \qquad \text{IV.19}$$

Where:

D is the reactor diameter = 1.25 cm;

ν is the velocity of the liquid inside the reactor = 118 cm/min;

ρ is the density of the liquid solution (approximately equal to that water) =1g/cm^3;

μ is the water dynamic viscosity = 0.01 g/cm s.

The obtained value for Reynolds number (15963) indicates a very turbulent regime inside the reactor, being Re> 2100. This result allows to assume the absence of external mass-transfer limitations since the simultaneous presence of the flow turbulence and a good stirring is usually enough for the effect of external transfer to vanish (Bouchy and Zahraa, 2003). Moreover it was possible to neglect the liquid-gas transport phenomena in the kinetic model.

Considering these simplifications and the experimental results reported in Figure IV.32 and in Figure IV.33, the mathematical modeling on 0.47%Ru was developed considering that, in the batch photoreactor R2, occur mainly the following reactions:

$$C_6H_{12}O_6 + H_2O = H_2 + C_6H_{12}O_7 \qquad \text{IV.20}$$

and

$$H_2O = H_2 + ½O_2 \qquad \text{IV.21}$$

In order to determine the best kinetic model for the degradation of glucose using the experimental data with an initial concentration of glucose equal to 2000 mg/L, three different models were evaluated: Langmuir-Freundlich-Hinshelwood (L-F-H) kinetic type model, first order kinetics; and zero-order kinetics.

The L-F-H kinetic model can be written as follows:

$$V\frac{dC}{dt} = -k \cdot \frac{C_m \cdot (b \cdot C_{eq})^n}{1 + (b \cdot C_{eq})^n} \cdot W \qquad \text{IV.22}$$

This equation can be arranged as:

$$\frac{dt}{dC} = \alpha \cdot \left(\frac{1}{(b \cdot C)^n}\right) \qquad \text{IV.23}$$

$$\alpha = \frac{V}{k \cdot W \cdot C_m \cdot} \qquad \text{IV.24}$$

Where b and n are the constant previously evaluated, C is the glucose concentration during the irradiation time, k is the apparent kinetic constant, V is the solution volume and t is the irradiation time.

The experimental data as well as the correlation coefficient (R^2) are shown in (Figure IV.38).

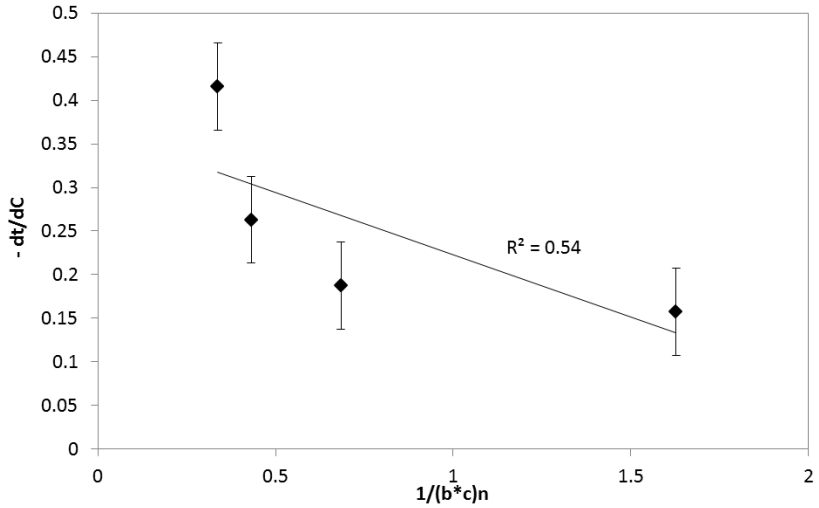

Figure IV.38. *Langmuir-Freundlich-Hinshelwood (L-F-H) kinetic model for the evaluation of k. Initial glucose concentration: 2000 g/L; photocatalyst: 0.47%Ru; light source: UV-LEDs; catalyst dosage: 1.5 g/L; photoreactor R2.*

Unfortunately, the correlation coefficient R^2 in this case was equal to 0.54, indicating that the L-F-H kinetic model is not able to describe the degradation of glucose during the irradiation time.

The second assumption was the first order kinetic. The first-order model describes the systems where degradation rate depends on the amount of glucose molecules in the solution:

$$-\ln\frac{C}{C_0} = k \cdot \frac{W}{V} \cdot t \qquad \text{IV.25}$$

Where C_0 is the concentration of glucose in aqueous solution after the dark phase.

Also in this case, the kinetic model doesn't fit the experimental data. In fact, the R^2 value was equal to 0.82 (Figure IV.39).

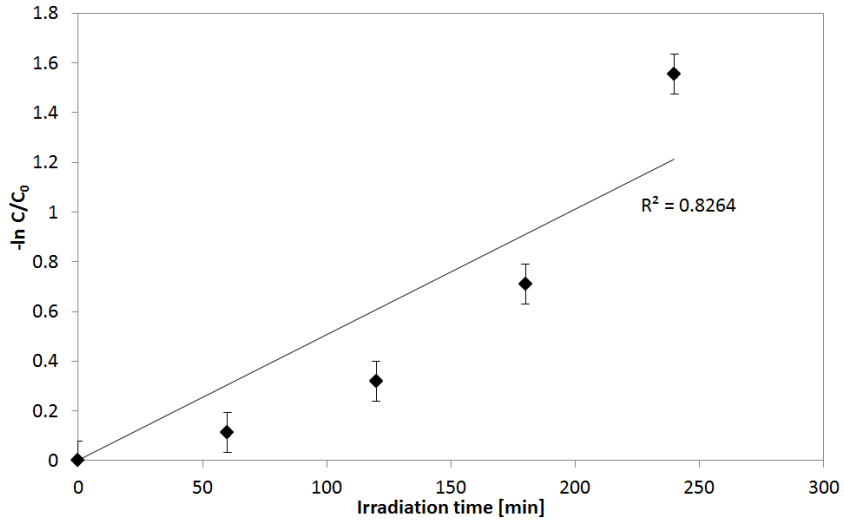

Figure IV.39. *First-order kinetic model. Initial glucose concentration: 2000 g/L; photocatalyst: 0.47%Ru; light source: UV-LEDs; catalyst dosage: 1.5 g/L; photoreactor R2.*

The last hypothesis investigated was the zero order kinetic models (Eq.14):

$$C - C_0 = -k \cdot \frac{W}{V} \cdot t \qquad \text{IV.26}$$

In this case (Figure IV.40) the experimental data are well described by the zero order kinetic models, being the R^2 value equal to 0.95. This model was used for the estimation of the apparent kinetic constant of glucose degradation.

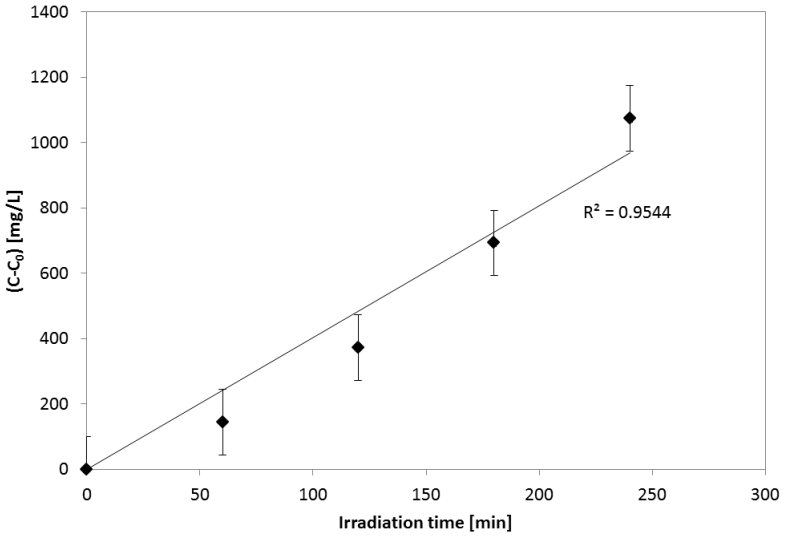

Figure IV.40 *Zero-order kinetic model. Initial glucose concentration: 2000 g/L; photocatalyst: 0.47%Ru; light source: UV-LEDs; catalyst dosage: 1.5 g/L; photoreactor R2*

Considering the amount of photocatalyst (W=0.12 g) and the solution volume (V= 80 mL) used in the experimental test, the slope of the straight line reported in Figure IV.40 allows to obtain the value of k, which resulted equal to 2.1±0.3 [mg/(g min)]. Finally, the experimental data obtained with different initial glucose concentrations were compared with the calculated values to analyze the ability of the model to predict the experimental data at 500, 1000, 2000 and 4000 mg/L initial glucose concentration.

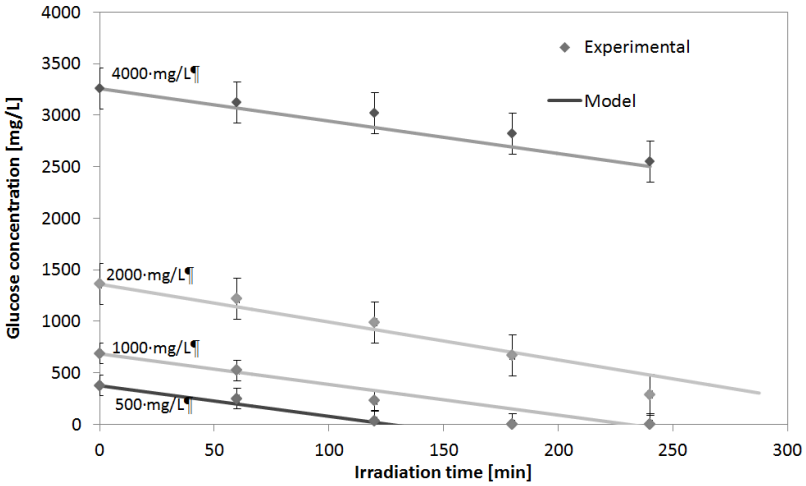

Figure IV.41. *Comparison between model calculation and experimental data for different glucose concentrations. Photocatalyst: 0.47%Ru; light source: UV-LEDs; catalyst dosage: 1.5 g/L; photoreactor R2.*

The calculated values are in good agreement with all the experimental data (Figure IV.41). It is important to note that also for the higher initial dye concentration (4000 mg/L), this system is able to predict the glucose degradation trend with a single value of kinetic constant.

Using the k value of the glucose degradation, it was calculating the value of water splitting kinetic constant (k_{ws}) in presence of the target sugar in the aqueous medium using the experimental data with an initial glucose concentration of 2000 mg/L and optimizing the model for the hydrogen production that can be expressed as:

$$\frac{dnH_2}{dt} = k \cdot \frac{W}{Mw} + k_{ws} \cdot W \qquad \text{IV.27}$$

Where M_w is the molecular weight of glucose and nH_2 is the millimoles of hydrogen produced during the irradiation time.

The initial condition for Eq. IV.27 was:

t = 0 nH_2=0

The calculated data and the experimental ones in terms of H_2 production for the different initial concentration of glucose are included in supplementary material (Figure IV.42).

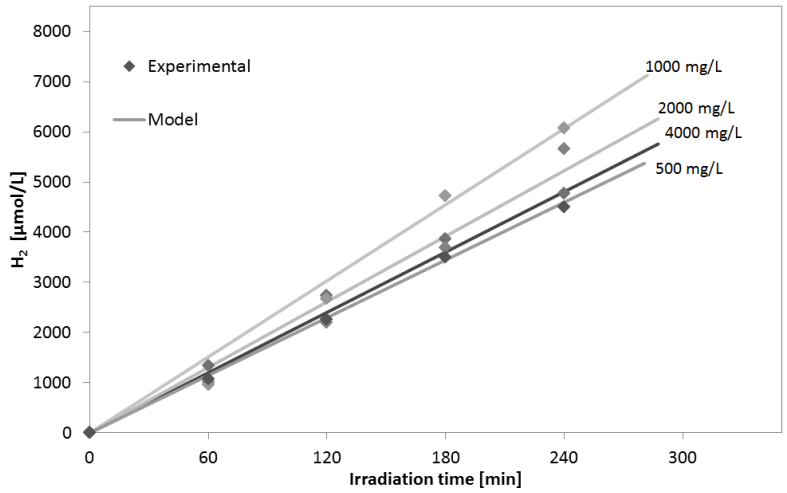

Figure IV.42. *Comparison between model calculation and experimental data for hydrogen production at different glucose initial concentrations. Photocatalyst: 0.47%Ru; light source: UV-LEDs; catalyst dosage: 1.5 g/L; photoreactor R2.*

The fitting procedure was finalized using the same procedure used for the estimation of the kinetic constant of glucose degradation, obtaining the k_{ws} value equal to 0.003±0.2 [mmol/ (g min)], different from the k_{ws} evaluated in the water splitting experiment. In particular, in the presence of glucose, the k_{ws} value was lower than that one obtained in the water splitting reaction (without glucose in aqueous solution), indicating that the hydrogen production preferentially comes from the glucose degradation reaction that inhibits the water splitting reaction.

The calculated values are in good agreement with all the experimental data also for the photocatalytic hydrogen production obtained at different glucose initial concentrations.

IV.2.3.3 Photocatalytic activity of 0.47%Ru under visible light irradiation

The effect of different light sources (UV or visible LEDs) was evaluated on the 0.47%Ru catalyst, which showed the best performances. According to UV-Vis DRS results, this catalyst could be active also in the presence of visible light (band-gap equal to 1.98 eV). In particular, the photocatalytic experiment was carried out with a solution containing 1000mg/L of glucose, a catalyst dosage equal to 1.5g/L and the optimized R2 configuration. The

observed glucose degradation was equal to 40% after 4 hour of visible light irradiation (Figure IV.43a) and the hydrogen production was equal to 1919 µmol/L (Figure IV.43b) after the same irradiation time. These results, also if lower than that obtained in presence of UV light, confirm the activity of the optimized photocatalyst also in presence of visible light irradiation.

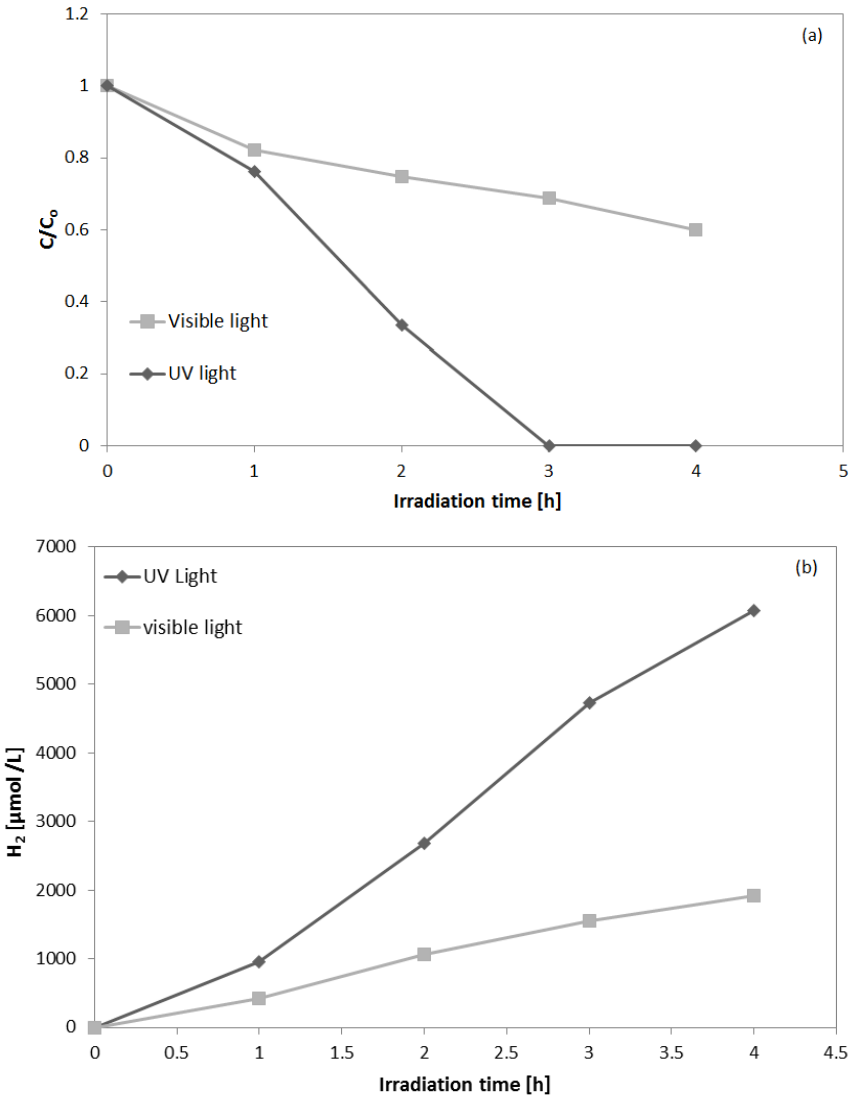

Figure IV.43. *Hydrogen production (a) and glucose degradation (b) during UV and visible light irradiation. Photocatalyst: 0.47%Ru; initial glucose concentration: 1000 mg/L; catalyst dosage: 1.5 g/L; photoreactor R2*

IV.2.3.4 Photocatalytic hydrogen production from brewing wastewater with 0.47%Ru catalyst under visible light

Since the investigated photocatalytic process was really effective in the hydrogen production from glucose-containing solutions, the effect of the phtocatalyst 0.47% Ru was also investigated in the treatment and valorization of real wastewater from brewing process.

Before the photocatalytic process, the wastewater sample was filtered to remove the suspended solids (initial TSS 450 mg/L). Typically the main component of this type of wastewater is maltose ($C_{12}H_{22}O_{11}$), a sugar of the family of glucides disaccharides, consisting of two glucose molecules bonded by an oxygen atom (Kawai and Sakata, 1980). The degradation of maltose during photocatalytic process (visible light) was evaluated by measuring absorbance changes at the wavelength of 268 nm (Figure IV.44a).

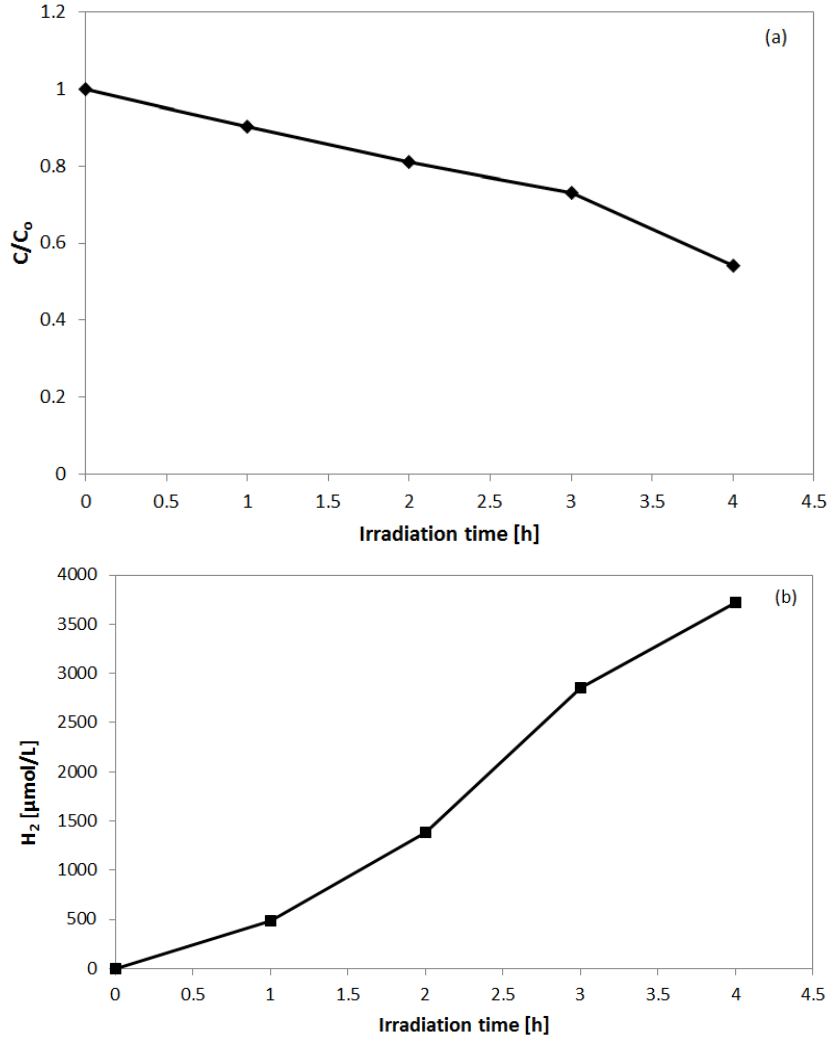

Figure IV.44. *Maltose degradation (a) and hydrogen production (b) from real wastewater. Photocatalyst: 0.47%Ru; light source: visible LEDs; catalyst dosage: 1.5 g/L; photoreactor R2.*

After 4 hours of visible light irradiation, a degradation of maltose equal to 50% was observed. In parallel photocatalytic hydrogen production reached the value of about 3700 µmol/L within four hours of irradiation (Figure IV.44b).

These results confirm the applicability of the photocatalytic process also to a real wastewater and the possibility to valorize the wastewater obtaining hydrogen from the degradation of maltose under visible light.

Form these results it is possible to observe that the introduction of Ru in the crystalline structure of the $LaFeO_3$ promotes the separation of charge carriers efficiently, inhibiting the recombination of electron–hole pairs, and consequently causing enhancement of the photocatalytic activity. For Ru content higher than 0.47 mol%, the photocatalytic activity decreased because of the presence of RuO_2 on the catalyst surface. Therefore 0.47 mol% of Ru loading is considered to be an optimal value for the studied reaction. In particular, after 4 hours of UV irradiation with 0.47%Ru, glucose degradation and hydrogen production were equal to 70% and 3270 μmol/L, respectively.

It is important to underline the effect of the reactor configuration on the hydrogen production and degradation of glucose. The results showed that with the same volume but reducing the diameter of the photocatalytic reactor from 2.5 to 1.25 cm, the photonic transport was enhanced and consequently the activity of the 0.47%Ru increased. In particular, under UV light, the hydrogen production passed from 3270 to 6079 μmol/L and the glucose degradation was complete after 3 hours of irradiation.

V Photocatalytic hydrogen production using Ru-$LaFeO_3$ coupled with Fe_2O_3 magnetic particles in presence of visible light irradiation

After the photocatalytic treatment of wastewaters, it is necessary to remove the photocatalysts particles from the depurated effluent. Generally this step is difficult and requires different precautions for the process.

The use of suspended and dispersed photocatalysts has some unique advantages: (1) great specific area for fast degradation rate of the pollutants; (2) effective absorbance of light irradiation for the efficient utilization of light energy; and (3) facilitating fast transportation of pollutants between the powder surface and aqueous medium due to its small diameter. However, the recovery and cyclic utilization of photocatalysts are limited due to the difficult separation of the small particles from the medium. To overcome these drawbacks, the photocatalysts are immobilized on supports such as glass beads (Serpone et al., 1989), lamp walls (Sakkas et al., 2010), glass plates (Anderson et al., 1988), fiberglass mesh (Al-Ekabi et al., 1991), porous films (Sabate et al., 1992), fiber optic cable reactor (Peill and Hoffmann, 1996), cellulose matrix (Zeng et al., 2010), silica (Ilisz et al., 2003) , alumina (Zhe et al., 2001), zeolite (Reddy et al., 2003).

Although the immobilization can make them recoverable, the photocatalytic activities undergo a large decrease due to the low specific area caused by the supports and of mass transfer limitations. The photocatalysts are incorporated in the activated carbon, leading to an increase in catalytic efficiencies due to the synergistic effect; however, the composite materials are still difficult to recover (Ao and Lee, 2004).

For the hydrogen production, in particular for the photoelectrocatalytic process, catalysts immobilized on macroscopic support are used. For

example in literature it was reported the use of nanoparticulate titania (np-TiO_2) films deposited on FTO transparent electrodes (Pop et al., 2015b).

However with regard to a photocatalytic process for the hydrogen production, typically slurry reactors are used (Chapter II). For this type of reactor, the kinetics reaction is very high. To preserve these performances it would be ideal to use a separable photocatalyst but likely to make the most of the typical characteristics of the slurry reactor (well-mixed liquid phase, catalytic particles distributed in a uniform way). An interesting alternative is represented by magnetic particles as supports for the photocatalysts.

The magnetic photocatalysts are defined as catalysts that possess both photocatalytic functions under light irradiation and magnetic separation functions by using an external magnetic force.

The first magnetic separation was described by William Fullarton, who used a magnet to separate iron minerals in 1792 (Yavuz et al., 2009). In 1873, Hay received the first US patent for a water treatment device that employed a magnetic field (Hay, 1873). Currently, magnetic separation techniques are used in a variety of areas, ranging from steel production to biotechnology and environmental protection (Ambashta and Sillanpaeae, 2010).

During the fabrication process of the magnetic photocatalysts, magnetite (Fe_3O_4), maghemite (γ-Fe_2O_3), and MFe_2O_4 (where M stands for Ba^{2+}, Ni^{2+}, Co^{2+}, Zn^{2+} divalent metallic cations) are the three most widely used magnetic materials.

The first magnetic photocatalyst was designed by Hiroshi et al. and was prepared through the deposition of titanium dioxide onto a magnetite core in 1994 (Horikoshi et al., 2002). Atsuya and Mutsuo developed photocatalyst particles containing ferromagnetic metal particles in 1997. In 1998, Beydoun synthesized titania-coated magnetic photocatalysts, in which titanium dioxide particles were directly coated with the Fe_3O_4 magnetic material(Beydoun et al., 1998) to form the core/shell structure. Other core/shell magnetic photocatalysts studied include $BaFe_2O_4/TiO_2$ (Lee et al., 2002), $NiFe_2O_4/TiO_2$ (Rana and Misra, 2005), $BaFe_{12}O_{19}/TiO_2$ (Fu et al., 2006), $ZnFe_2O_4/TiO_2$ (Zhang et al., 2006), and Fe_3O_4/BiOCl (Zhang et al., 2009). The use of magnetic core Fe_3O_4 and N-doped TiO_2 shell nanoparticles was reported also in the photocatalytic removal of phenol from water (Vaiano et al., 2016b).

Generally, the synthesized magnetic photocatalysts were composed of two components: a magnetic core with the separation function by an external magnetic force, and a semiconductor shell with the photocatalytic function under irradiation. But the photocatalytic activities and stability were decrease because the direct contact between the magnetic particles and photocatalysts led to the photogenerated electron-hole recombination and the photodissolution of the Fe_3O_4 magnetic particles under the irradiation.

To overcome the drawbacks of the low activities and the photodissolution, Cao and Chen pioneered a three-component magnetic photocatalyst of γ - Fe_2O_3 /SiO_2/TiO_2 in 1999, in which γ-Fe_2O_3 was used as the magnetic core, SiO_2 interlayer as insulator, and TiO_2 as photocatalytic shell (Ghasemi et al., 2016). It is reported in literature the use of Fe_2O_3 nanoparticles for the photocatalytic hydrogen production from ethanol (Carraro et al., 2014).

Considering the performance of Fe_2O_3 as magnetic support, in this work the optimized photocatalyst (0.47%Ru) was coupled with Fe_2O_3 particles, and was tested in the photocatalytic hydrogen production from glucose degradation under visible light irradiation. In literature, no data was reported on the use of coupling between perovskite and Fe_2O_3 magnetic particles to be used in a slurry reactor for the hydrogen production from glucose solution. In particular, it was optimized the perovskite amount in the final magnetic composite. This recyclable sample was finally tested in the treatment of a real wastewater from the washing process of the fruit (especially cherries). Finally, it has been evaluated the possibility to couple the photocatalytic reactor (used primarily for the valorization of the wastewater through the production of hydrogen and /or methane) with a photo-Fenton system able to mineralize the unconverted organics coming from the photoreactor and for the removal of not-biodegradable substances still present in the wastewaters.

V.1 Synthesis of magnetic Fe_2O_3 particles

Fe_2O_3 particles were prepared by solution combustion synthesis, using citric acid as organic fuel and metal nitrate as iron oxide precursor.

In detail, 1.66 g of $Fe(NO_3)_3 \cdot 9H_2O$ (Riedel-deHaen, 97 wt%), and 0.86g of citric acid (Fluka, 99 wt%) were completely dissolved in 100 ml of bidistilled water. The solution was kept stirred continuously at 60 °C for 5 minutes. Then, ammonium hydroxide (Carlo Erba, 37 wt %) was slowly added to regulate the pH of the solution up to 12. The solution was dried at 130° C and then calcined at 300° C for 3 hours to ignite the solution combustion reaction.

V.2 Synthesis of Ru-$LaFeO_3$ coupled with magnetic Fe_2O_3 particles

Ru-$LaFeO_3$ was coupled with magnetic Fe_2O_3 particles following a specific procedure. In particular a physical mixture between 0.47%Ru catalyst (at different amount) and 0.3 grams of Fe_2O_3 particles was created in order to ensure a tight contact between the two solid phases.

The physical mixture was dispersed in 22.5 mL of distilled water and maintained under mechanical stirring until to obtain a uniform dispersion. Then, 0.45 mL of TEOS, 3mL of ethanol and 4.5mL of NH_3 were added to the aqueous suspension. The mixture was kept under stirring for 12 h at 25 °C and then centrifuged. Finally, the recovered sample was calcined at 450° C for 30 min to obtain the Ru-$LaFeO_3$/Fe_2O_3 composite. Table V.1 reports all the prepared composites.

Table V.1 *List of prepared composites*

Catalyst	Amount of Fe_2O_3 (g)	0.47%Ru loading (wt %)
33Ru	0.3	33
50Ru	0.3	50
67Ru	0.3	67

V.3 Characterization results

V.3.1 X-ray diffraction

XRD measurement results for Fe_2O_3 particles and for Ru-$LaFeO_3$/Fe_2O_3 prepared with different amount of 0.47%Ru photocatalyst are shown in Figure V.1.

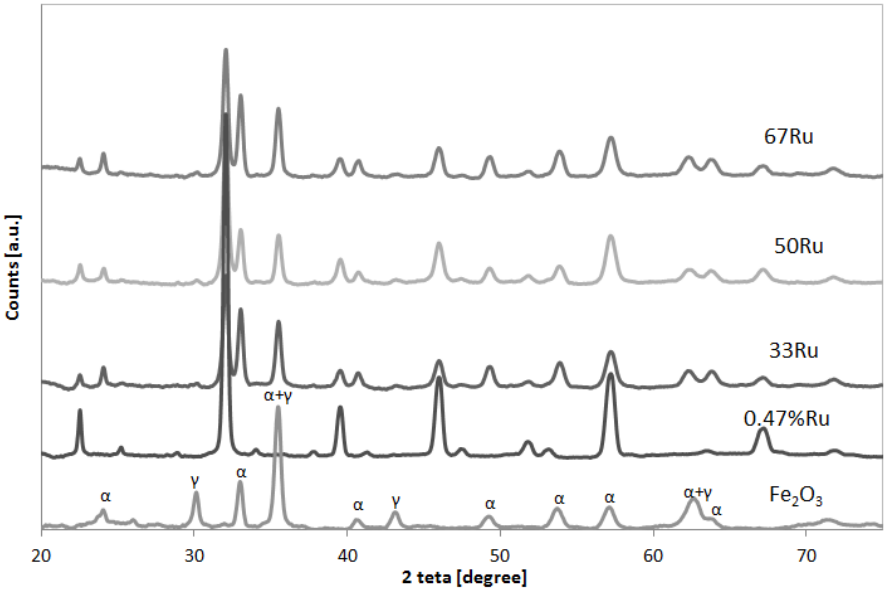

Figure V.1 *: XRD spectra.*

The XRD patterns for Fe_2O_3 evidenced the presence of γ-Fe_2O_3 (peaks marked as 'γ') particles along with α-Fe_2O_3 (peaks marked as 'α') as it is also reported in literature (Basavaraja et al., 2007). However, for the other samples (33Ru, 50Ru and 67Ru) over the peaks relative to the Fe_2O_3, it is possible to note the presence of peaks characteristic of perovskite (at 32.04°,39.55°, 45.99° and 57.15°) in particular for the 67Ru photocatalyst, confirming the simultaneous presence of 0.47%Ru photocatalyst and of Fe_2O_3 particles.

V.3.2 UV Vis

The data obtained from UV–Vis reflectance spectra were used for evaluating the band-gap energy of all photocatalysts. The band gap evaluation for Fe_2O_3, 0.47%Ru and 67Ru sample is reported in figure VI (a, b and c). These results of the other samples are reported in Table V.2.

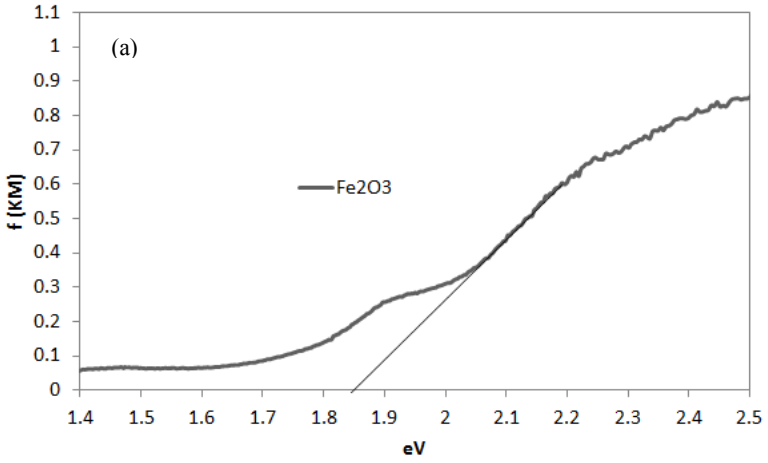

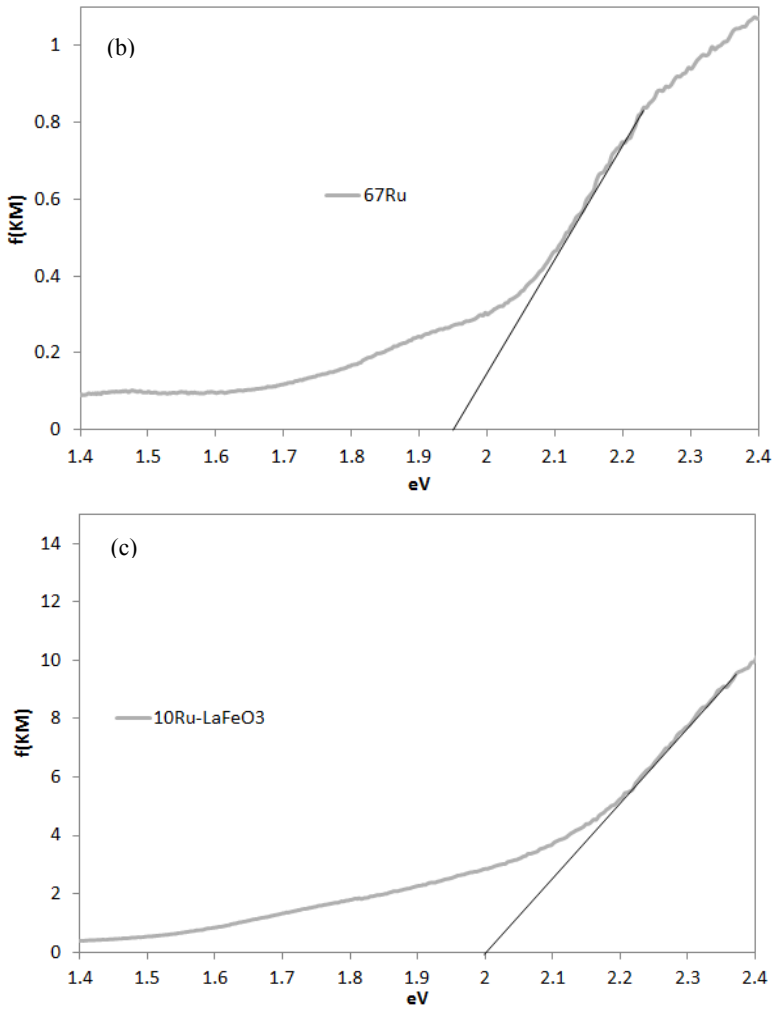

Figure V.2 : *Band gap evaluation*

Table V.2 *Band gap energy value (eV) for different photocatalyst.*

Catalyst	Band gap (eV)
Fe_2O_3	1.98
0.47%Ru	2.01
33Ru	1.98
50Ru	1.95
67Ru	1.93

V.3.3 M(T) measurements

The M(T) measurements of Magnetization as function of the Temperature were performed using the Zero Field Cooling (ZFC)-Field Cooling (FC) procedure. More precisely, the samples were first cooled down to 5 K in presence of a zero magnetic field, then the field was turned on at 0.1 Tesla and the data were acquired for increasing temperature (ZFC) up to 300 K.

After that, the samples were cooled down again while acquiring FC magnetization. In Figure 1 the M(T) for the pure Fe_2O_3 nanoparticles is showed, while in Figures 2,3 and 4 the M(T) for the samples covered with 25%, 50% and 100% Ru-$LaFeO_3$ respectively are reported.

The M(T) measurement for the pure Fe_2O_3 nanoparticles (Figure 1) is characterized by a maximum in the ZFC branch with a little bump at about 125 K and a plateau in the FC branch, which can be ascribed to the γ-Fe_2O_3 phase nanoparticle (Martínez et al., 1996, Jeong et al., 2004, Pascal et al., 1999).

Nevertheless, the presence of the α-Fe_2O_3 phase, for which a much lower signal than the revealed one is expected due to the presence of a Morin transition (for nanoparticles diameter above 20 nm (Ozdemir et al., 2008, Zysler et al., 2003), cannot be excluded.

The analysis of the experimental results on the Fe_2O_3 nanoparticles covered with several concentrations of the catalyst Ru-$LaFeO_3$ (in particular 25%, 50% and 100% of the Fe_2O_3 nanoparticles weight), shows that these samples maintain the same general magnetic behavior as the pure sample. In fact, in the M(T) curves of Figure 2, 3 and 4, we observe the same characteristics in both ZFC and FC curves as the pure Fe_2O_3, although with a lower magnetic signal. Furthermore, as it can be seen in Figure 5, the temperature of the maximum in the ZFC branch does not show relevant variations with Ru-$LaFeO_3$ concentrations

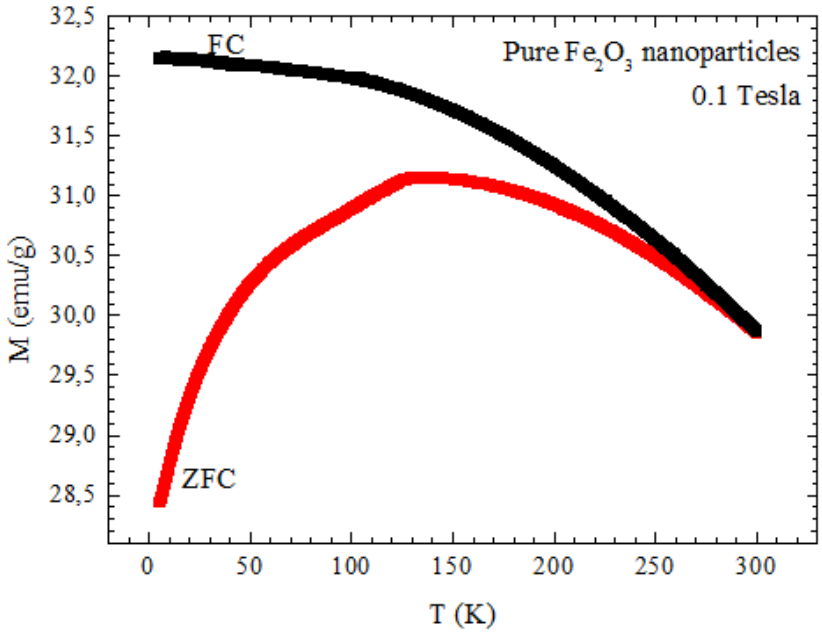

Figure V.3 *ZFC and FC magnetizations as a function of temperature with an external applied field of 0.1 T for pure Fe_2O_3 nanoparticles.*

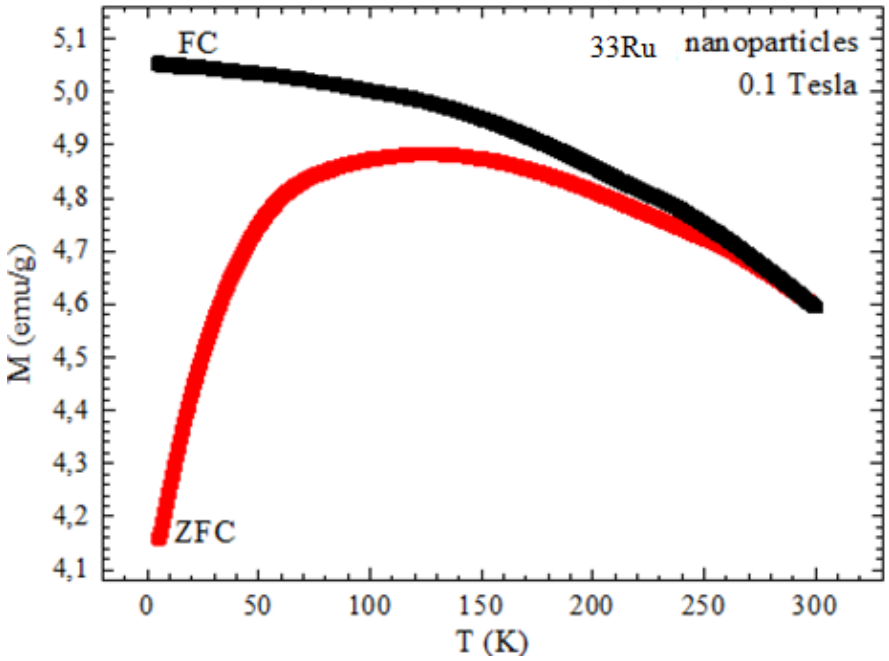

Figure V.4 *ZFC and FC magnetizations as a function of temperature with an external applied field of 0.1 T for Fe_2O_3 + 25% Ru-$LaFeO_3$ nanoparticles.*

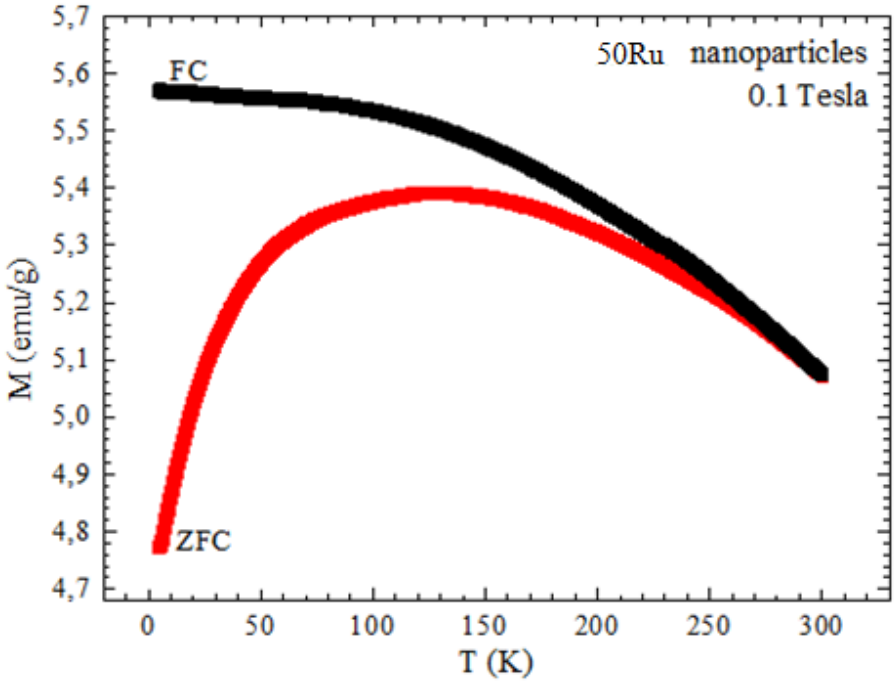

Figure V.5 *ZFC and FC magnetizations as a function of temperature with an external applied field of 0.1 T for Fe_2O_3 + 50% Ru-$LaFeO_3$ nanoparticles*

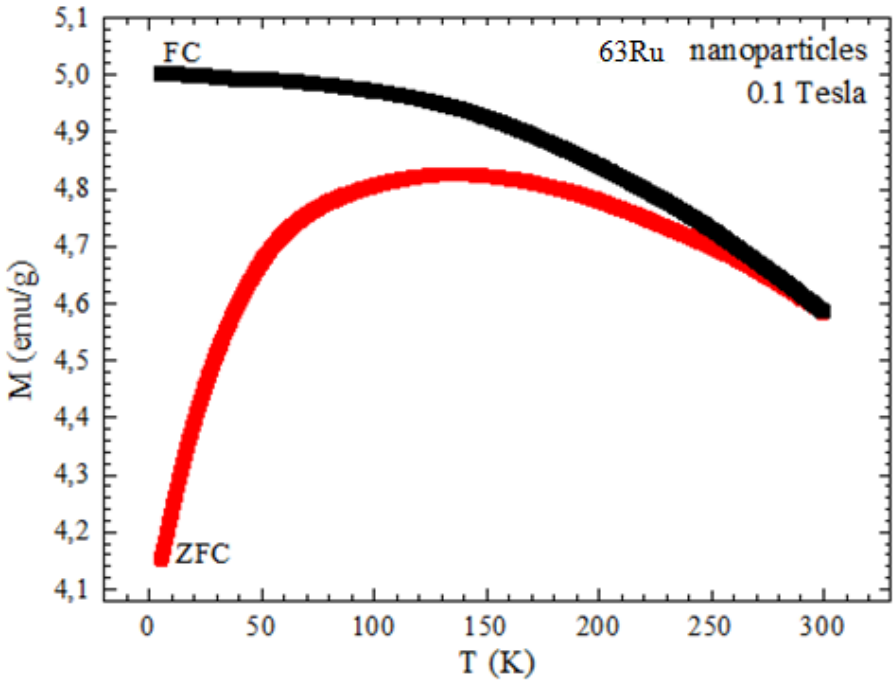

Figure V.6 *ZFC and FC magnetizations as a function of temperature with an external applied field of 0.1 T for Fe_2O_3 + 100% Ru-$LaFeO_3$ nanoparticles.*

In Figure V.7 all the previous M(T) curves are reported in the same plot (only the ZFC branch).

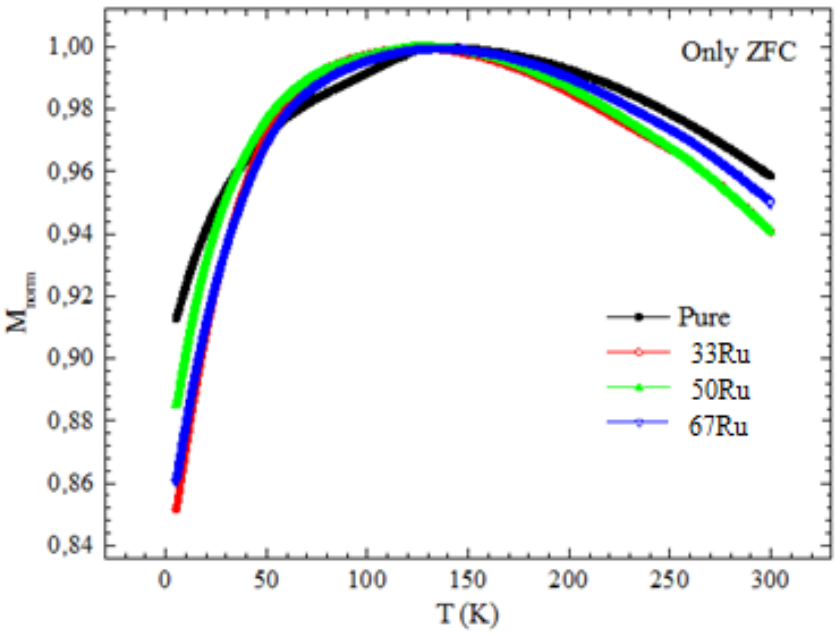

Figure V.7 *Comparison among the normalized (to the maximum value) ZFC M(T) curves.*

V.3.4 M(H) measurements

For the measurements of magnetization as function of the magnetic field M(H), the samples were first cooled down to the measurement temperature in absence of magnetic field and thermally stabilized for about 20 minutes.

Then, the field was increased with a sweep rate of 0.01 T/s to reach +9 T, then decreased to -9 T, and finally to +9 Tesla again with the same sweep rate in order to acquire the complete hysteresis loop.

In Figure V.8 the M(H) for the pure Fe_2O_3 nanoparticles is showed, while in Figures V.9, V.10 and V.11the M(H) for the samples covered with 33Ru 50Ru and 67Ru respectively are reported. In Figure 10 the M(H) for the Ru-$LaFeO_3$ is reported.

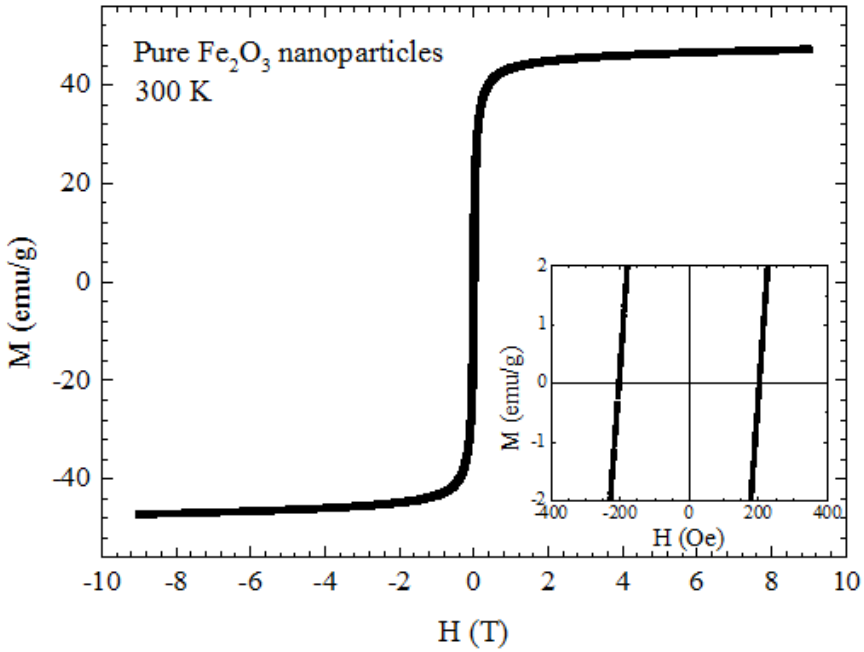

Figure V.8 *M(H) at T = 300 K on pure Fe2O3 nanoparticles. The inset shows the M(H) curve near zero field.*

The M(H) curve shows an open hysteresis (Figure V.9) with a non-zero coercive field which is what expected for the α-Fe_2O_3 phase nanoparticles (Jiao and Zhao, 2016, Mitra et al., 2007, Cao et al., 2006).

Nevertheless, also in this case the measured curve cannot exclude the presence of the γ-Fe_2O_3 phase, since this phase shows a M(H) curve without hysteresis, i.e. with coercive field equal to zero. Therefore, the analysis of these curves suggest that the results are compatible with the presence of both α-Fe_2O_3 and the γ-Fe_2O_3 phases inside our Fe_2O_3 nanoparticles sample, and this presence is confirmed also by the μ-XRD analysis.

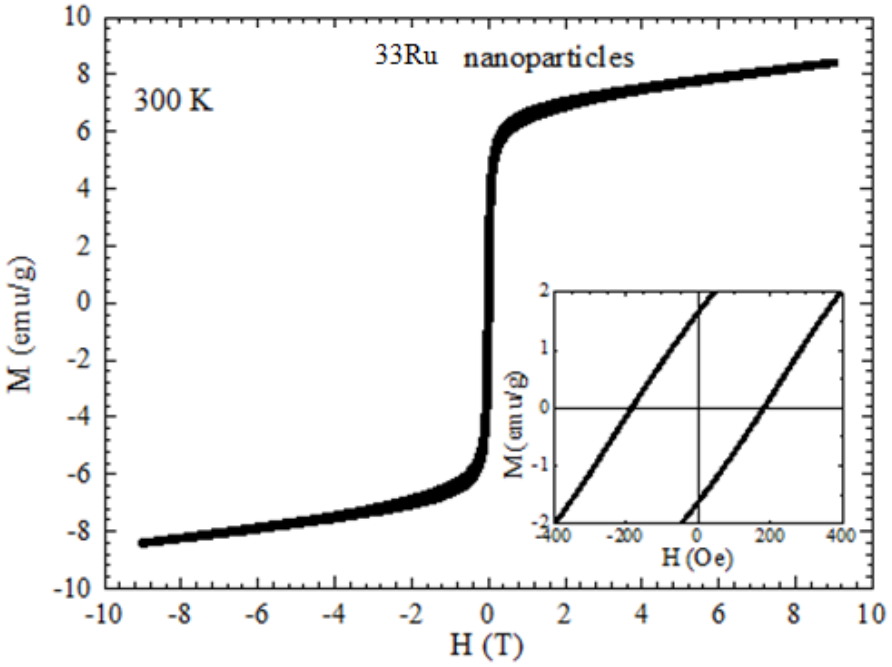

Figure V.9 *M(H) at T = 300 K on Fe_2O_3 + 25% Ru-$LaFeO_3$ nanoparticles. The inset shows the M(H) curve near zero field.*

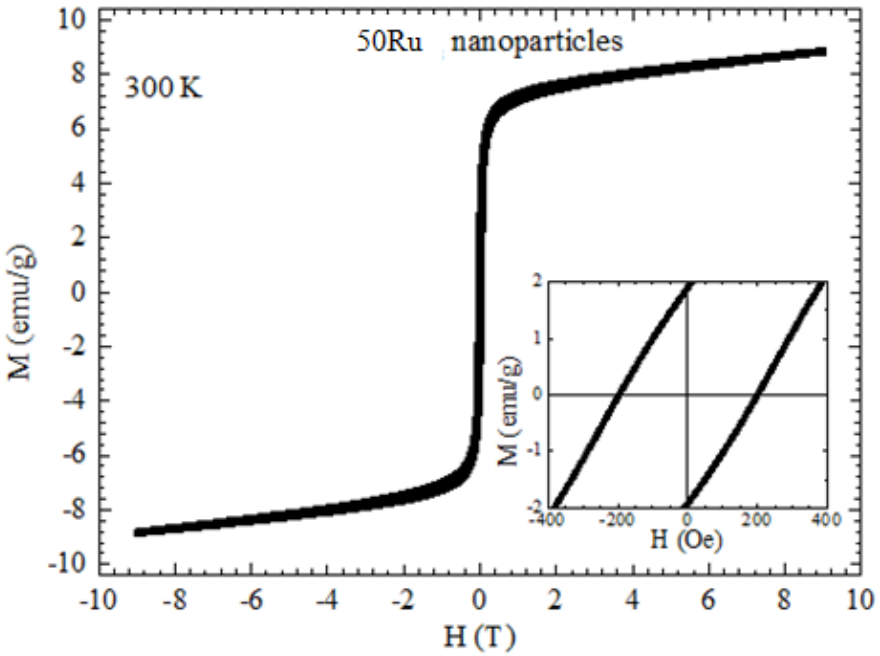

Figure V.10 *M(H) at T = 300 K on Fe_2O_3 + 50% Ru-$LaFeO_3$ nanoparticles. The inset shows the M(H) curve near zero field.*

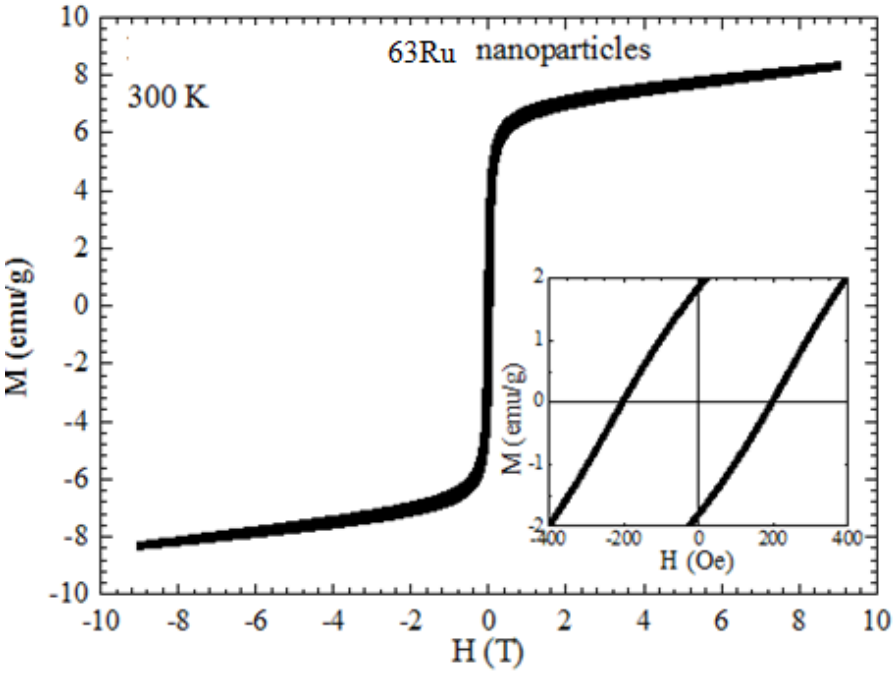

Figure V.11 *M(H) at T = 300 K on Fe_2O_3 + 100% Ru-$LaFeO_3$ nanoparticles. The inset shows the M(H) curve near zero field*

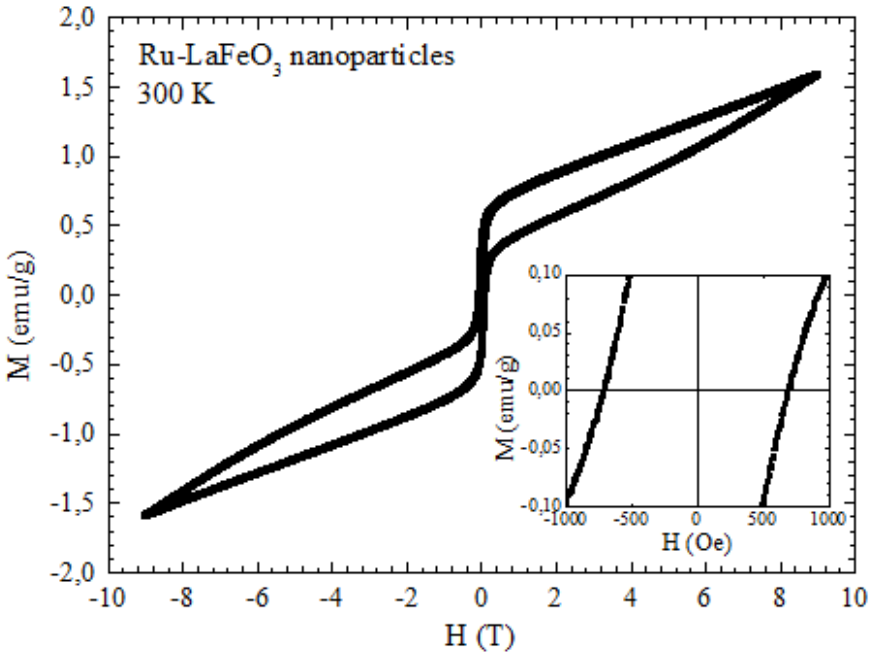

Figure V.12 *M(H) at T = 300 K on Ru-$LaFeO_3$ nanoparticles. The "bee waist" type hysteresis loop, due typically to a coexistence of a soft and hard phase not well exchanged and coupled to each other inside the sample [9,10], is visible. The inset shows the M(H) curve near zero field.*

In the main panel of Figure V.13 all the previous M(H) curves are reported in the same plot. In the inset a magnification of the zero field regions is reported.

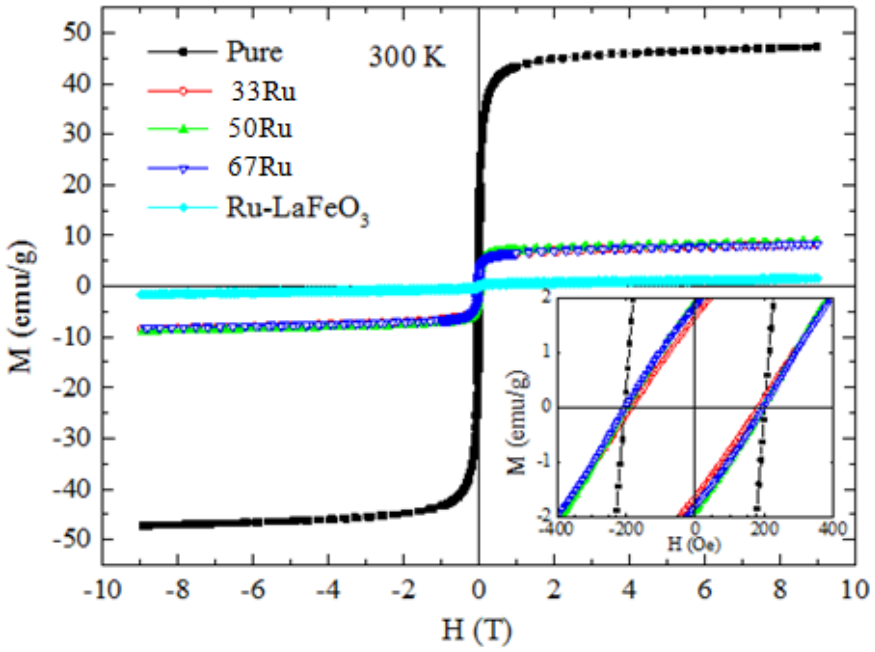

Figure V.13 *Comparison among the M(H) curves. Inset: The inset shows the M(H) curves near zero field. The Ru-LaFeO3 is not reported. It can be noted how the addition of the catalyst to the Fe_2O_3 nanoparticles does not change substantially the coercive field of the samples. On the other hand the catalyst causes a net decrease of the magnetic signal*

For what concerns the M(H) curves (see Figure V.9, V.10 and V.11), we observe that the Fe_2O_3 nanoparticles covered with catalyst exhibit a similar behavior respect to the pure Fe_2O_3 sample. Moreover, none of the samples reaches the complete saturation at the maximum field (9 T) and the coercive fields remain comparable for all the samples as reported in the inset of Figure 11 and in Table V.2. Also the saturation magnetization of the covered nanoparticles samples remains definitely comparable to each other, although this value is significantly reduced respect to the pure Fe_2O_3, as can be seen in the main panel of Figure V.13 This can be explained considering that also the catalyst has a magnetic signal different from zero, as showed in Figure 10, although it is much lower than the corresponding pure Fe_2O_3 nanoparticles signal. This low magnetic signal is the reason of the fact that, in spite of the larger coercive field of the catalyst, we detect values of the coercive field for the covered samples which are very similar to the pure sample ones.

It is also worth to underline the different slope of the M(H) curves at low fields, well visible in the inset of Figure V.13, of the covered samples with

respect to the pure Fe_2O_3 nanoparticles, that indicates how easily the magnetic moments of the nanoparticles orient with the applied magnetic field. This different response velocity influences the value of the magnetic field corresponding to the 80% of the maximum signal, as showed in Table 1, although for the covered samples we have to apply a magnetic field of just about 0.5 Tesla, not much different in absolute terms from the field of 0.3 Tesla to apply for the pure sample.

In Table V.2 we report the coercive field, the value of the maximum magnetization at 9 Tesla, M_{max} (9 T), and the value of the magnetic field where the magnetization reaches the 80% of its maximum value, H (80% M_{max}), for all the analyzed samples.

Table V.2 *Magnetic features of the samples*

Catalyst	Coercive field (Oe)	M_{max} (9 T) (emu/g)	H (80% M_{max}) (T)
Fe_2O_3	∓ 200	47.2	0.3
33Ru	∓ 183	8.4	0.5
50Ru	∓ 197	8.9	0.5
67Ru	∓ 200	8.3	0.5

V.4 Photocatalytic activity results

In a typical photocatalytic test, 0.0675 g of catalyst was suspended in 45 ml of an aqueous solution containing 1000 mg/L of glucose (D^+ Glucose VWR, Sigma-Aldrich). To ensure complete mixing of the solution in the reactor, a peristaltic pump was used. The photoreactor was irradiated with a strip of visible LEDs with the main wavelength emission at 440 nm positioned around the external surface of the reactor.

In particular these experiments were carried out on a reactor configuration previously optimized, called R1, with an internal diameter equal to 1.25 cm. At the end of the photocatalytic test, the photocatalysts particles were removed by using an external magnetic force.

It was tested the recyclability of the photocatalyst recovered after the tests. The photocatalytic tests were carried out also on a real water matrix, containing chlorides and carbonate that can act as radical scavengers. The effect of these compounds was evaluated on the hydrogen production after 4 hours of irradiation time.

V.4.1 Effect of the amount of 0.47%Ru photocatalyst in the magnetic composite

Figure V.14 and V.15 reports the behavior of glucose relative concentration (C/C_0) and the hydrogen production during the 4 hours of irradiation. All the photocatalysts demonstrated a better activity compared to pure Fe_2O_3. As it can be seen from both figures, the best performance was obtained with 67Ru photocatalyst. In particular with this photocatalyst it was obtained a glucose degradation equal to 100% after 4 hours of irradiation and the production of hydrogen equal to 5460 μmol/L. From this very high value, it is possible to note the synergic effect of the Ru-$LaFeO_3$ photocatalyst coupled with Fe_2O_3, being itself semiconductor with a band gap equal to 2.2eV, so active in presence of visible light, as demonstrated in figure V.2(a).

Moreover, this catalyst, in addition to ensuring excellent productions of H_2 and the total glucose degradation after 4 hours of irradiation, ensures an optimal separability at the end of the photocatalytic process, thereby maintaining the magnetic characteristics, as reported in the characterization results (paragraph V.3).

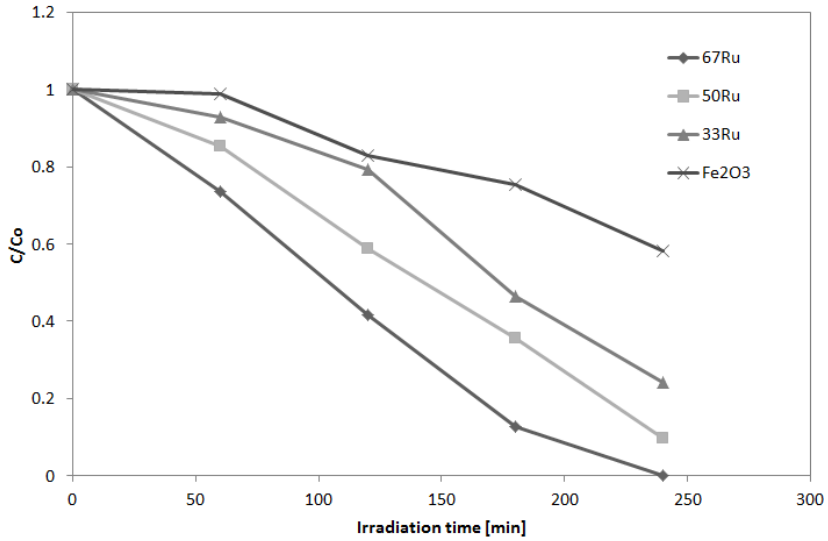

Figure V.14 Photocatalytic glucose degradation under visible LEDs. Initial glucose concentration : 1000 mg/L.

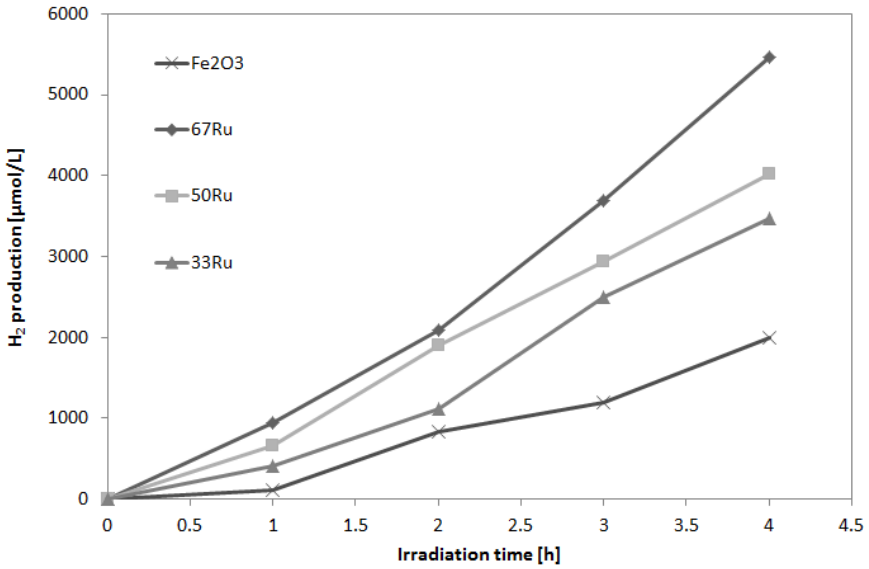

Figure V.15. *Photocatalytic hydrogen production under visible LEDs. Initial glucose concentration : 1000 mg/L.*

The optimal composite (67Ru) was used to investigate the influence of different operating condition. In particular catalyst dosage was optimized. The optimization of the catalyst dosage was carried out under visible led irradiation by testing different dosages of 67Ru photocatalyst, in the range 0.75-3 g/L.

Photocatalytic efficiency in the hydrogen production and glucose degradation increased as catalyst loading was increased up to 1.5 g/L (Figure V.16).

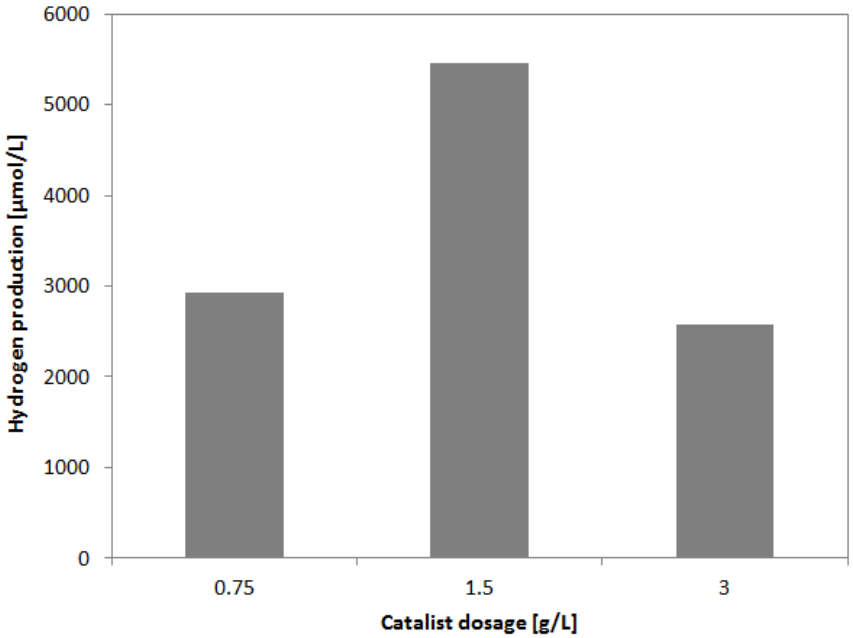

Figure V.16. *Effect of catalyst dosage on the photocatalytic hydrogen production after 4 hours of visible light irradiation. Initial glucose concentration : 1000 mg/L. Photocatalyst: 67Ru.*

As already seen from the other results reported in the previous chapters, the increase in the catalyst dosage over the optimum value resulted in a decreased light penetration through the solution because of the increased opacity of the aqueous suspension; a typical behavior reported in literature when the amount of the catalyst was increased in a similar photoreactor configuration (Vaiano et al., 2014d).

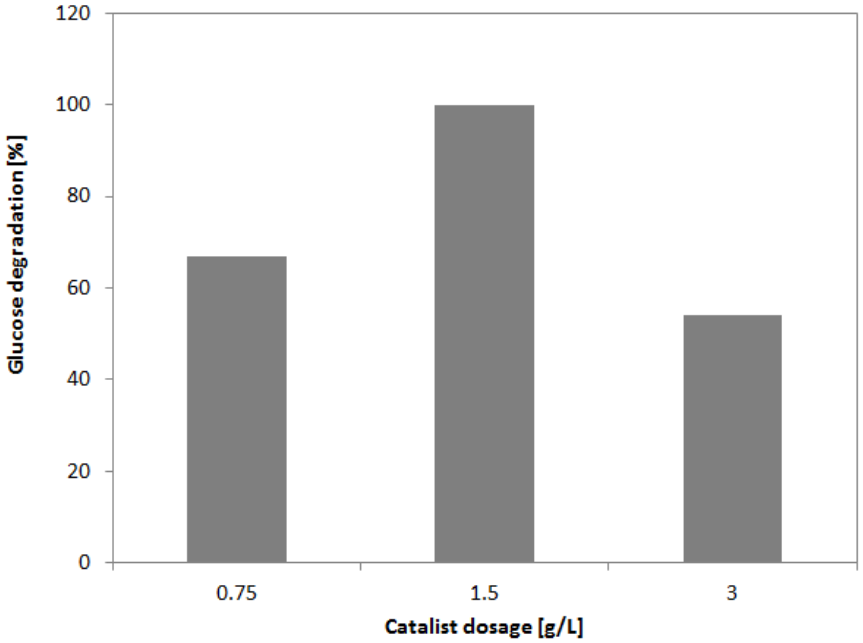

Figure V.17 *Effect of catalyst dosage on the photocatalytic degradation of glucose after 4 hours of visible light irradiation. Initial glucose concentration : 1000 mg/L. Photocatalyst: 67Ru.*

Recyclability is one of the most important factors in catalysis research (Vaiano et al., 2016b, Linley et al., 2014). To confirm the recyclability of 67Ru sample, the photocatalytic degradation of glucose with the hydrogen production was repeated up to seven cycles (Figure V.18 and V.19).

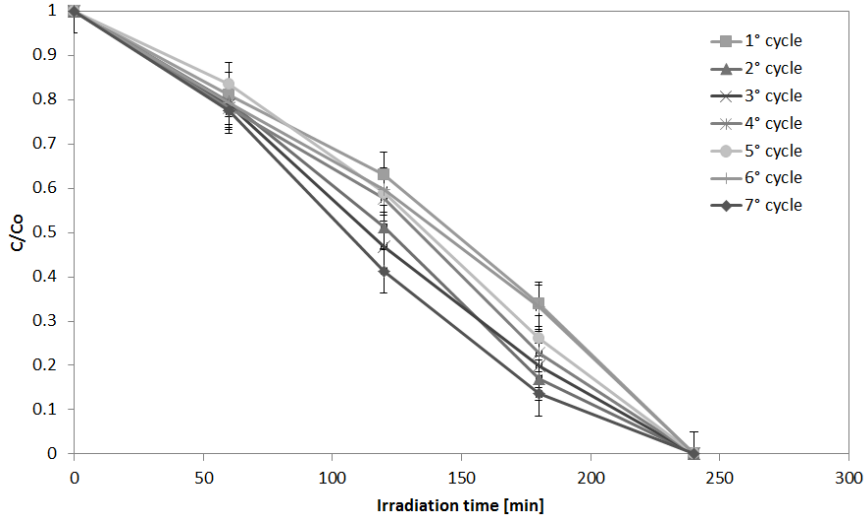

Figure V.18. *Evaluation of glucose degradation during the irradiation time on 67Ru catalyst for different cycles; initial glucose concentration: 1000 mg/L; catalyst dosage: 1.5 g/L*

After seven cycles, it is possible to obtain the complete glucose degradation. These results evidenced the stability of the photocatalyst coupled with Fe_2O_3 particles.

The same results were obtained for the hydrogen production (Figure V.19). The hydrogen production was equal to about 5700 μmol/L after all the cycles.

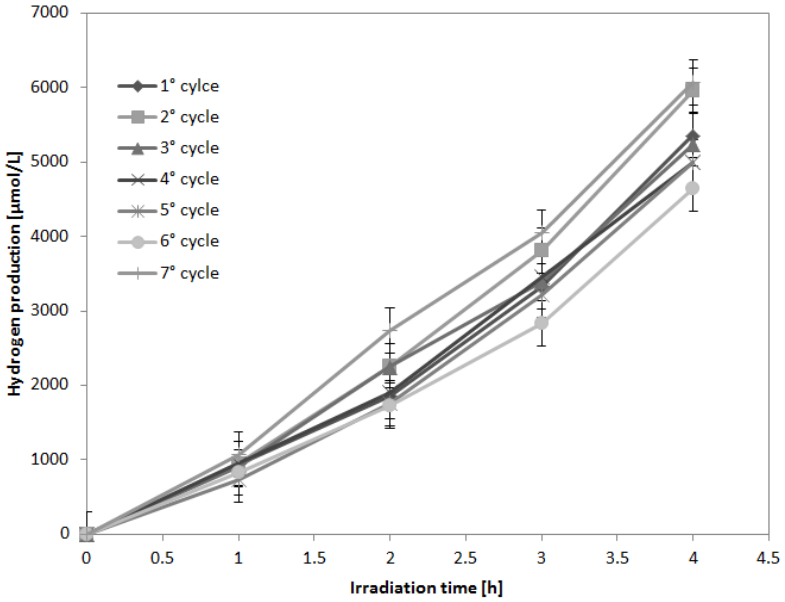

Figure V.19 *Evaluation of hydrogen production during the irradiation time on 67Ru catalyst for different cycles; initial glucose concentration: 1000 mg/L; catalyst dosage: 1.5 g/L*

Whereas it the ratio between the hydrogen product and the glucose degraded during the photocatalytic reaction does not follow the reforming reaction stoichiometrically, it is possible to confirm the presence of reaction by-products such as gluconic acid, whose presence has been demonstrated in the previous chapter.

So to ensure the complete degradation of the TOC present in solution after the photocatalysis, the photocatalytic process that guarantees the valorization of the wastewater, was coupled to the heterogeneous photo Fenton process that instead ensure the complete removal of residual organic substances still present in solution.

After the photocatalytic treatment, the TOC present in solution was equal to 280 mg/L.

Photo-Fenton tests were carried out on 160 ml of solution in sealed stainless-steel batch cylindrical photoreactor. The spontaneous pH of the solution (pH=6.6) were used in the tests. An 8 W mercury vapors lamp emitting at 254 nm was used as light source. 13 g of the monolith catalysts (with 4.5 wt.% $LaFeO_3$ placed in the reactor).

The reactor was maintained in the absence of irradiation at 25°C for t=180 min to reach the adsorption equilibrium of organic substance on catalysts surface. During the tests, a continuous dosage of H_2O_2 (0.038 mol h^{-1}) was used. The results are shown in figure V.19.

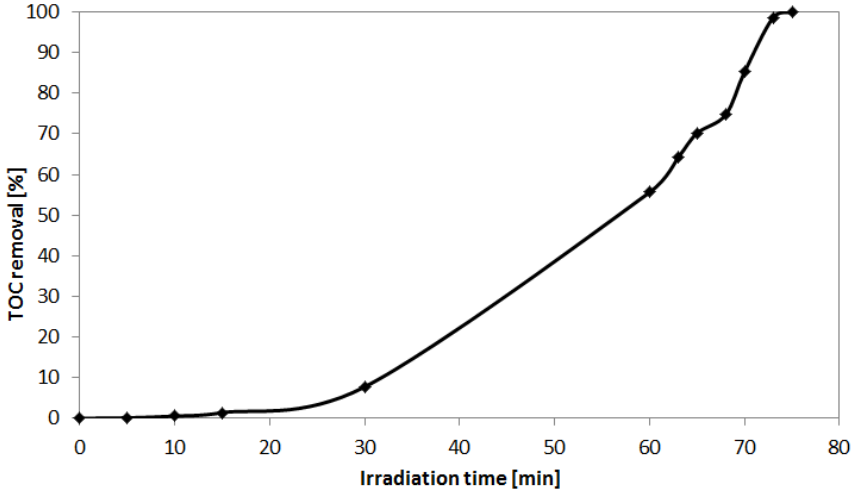

Figure V.20 *Evaluation of TOC removal during the photo-Fenton treatment. Initial TOC concentration : 280mg/L. Synthetic solution.*

In figure V.20 it was reported the behavior TOC removal during the irradiation time. It is possible to observe that during the first 25 minutes of irradiation no removal of TOC was observed due to the formation of reaction intermediates. However, after 30 minutes of irradiation, it is possible to note a progressive removal of the organic substance present in solution, which reaches values equal to 100% removal after about 75 minutes of irradiation.

These results demonstrate that the coupling of the photocatalytic process with the heterogeneous photo-Fenton treatment is a good solution for the valorization and for the treatment of wastewater containing sugars.

V.4.2 Photocatalytic tests on a real water matrix: effect of the presence of carbonates and chlorides

All the photocatalytic and photo-Fenton tests shown in the previous paragraphs were carried out on a synthetic solution prepared in the laboratory. To obtain a behavior similar to that of real solutions, photocatalytic tests were also performed on a real consisting of water solution containing chlorides and carbonates, to which a known amount of glucose was added.

In particular, the physical chemical characteristics of water used are shown in the TableV.3.

Table V.3 *Physical chemical characteristics of water*

Substance	Quantity [mg/L]
Carbonates	249
Calcium	58
Sulphates	3.4
Nitrates	7.10
Chlorides	6
Sodium	3.16
Potassium	1.08
Fluorides	0.076
Magnesium	12.9

The presence of the elements shown in the table, and in particular the presence of chlorides and carbonates can affect the photocatalytic performance. In fact, these substances act as radical scavengers in the photocatalytic processes. The final solution prepared contains 1000 mg/L of glucose.

Also in this case, recyclability tests were carried out. As it is possible to note from the results reported in figure V.21 and V.22, the complete glucose degradation was not obtained (76% after 4 hours of irradiation), and the production of hydrogen is lower than that obtained using synthetic solutions (3878 mol/L).

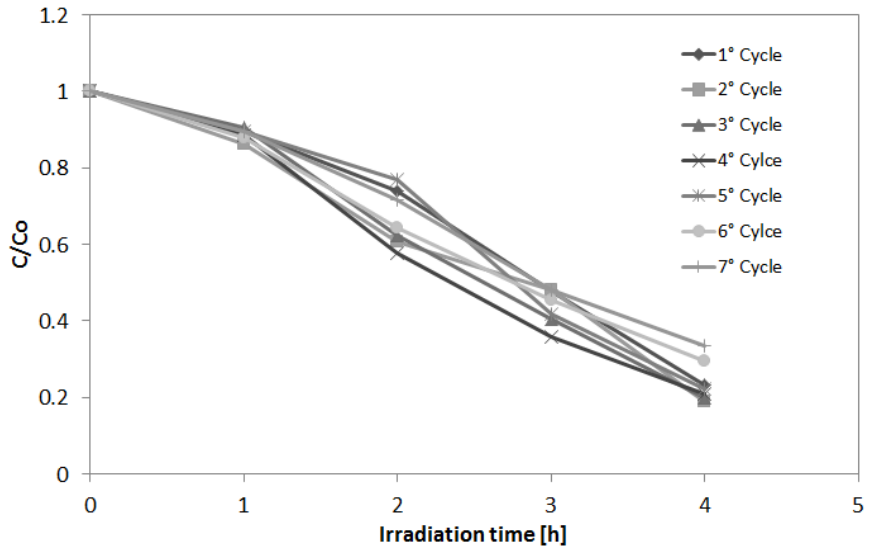

Figure V.21. *Evaluation of glucose degradation during the irradiation time*

on 67Ru catalyst for different cycles; initial glucose concentration: 1000 mg/L; catalyst dosage: 1.5 g/L. Real water.

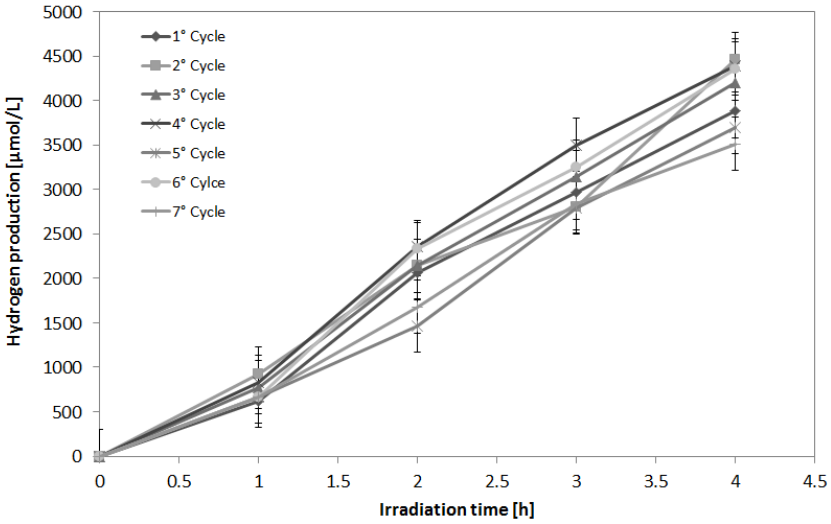

Figure V.22. *Evaluation of hydrogen production during the irradiation time on 67Ru catalyst for different cycles; initial glucose concentration: 1000 mg/L; catalyst dosage: 1.5 g/L. Real water.*

However, the results obtained in presence of real water matrix demonstrated that there is only a small reduction in the efficiency of the catalyst, both for glucose degradation and hydrogen production, evidencing again the stability of the photocatalyst coupled with Fe_2O_3 particles.

After the photocatalytic treatment, the TOC present in solution was equal to 278 mg/L. As in the case of synthetic solution, with the aim to remove the TOC present in solution after the photocatalytic process, the real water was treated with the photo-Fenton process.

In figure V.23 it was reported the behavior TOC removal during the irradiation time.

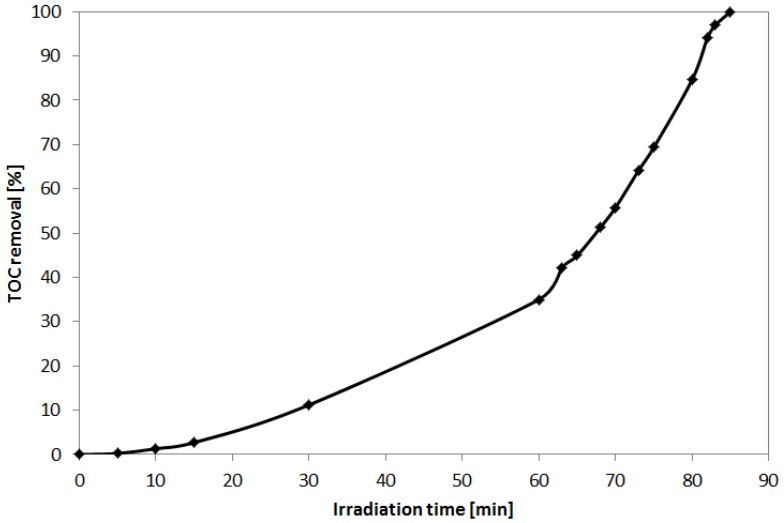

FigureV.23. *Evaluation of TOC removal during the photo-Fenton treatment. Initial TOC concentration : 278mg/L. Real water.*

It is possible to observe that during the first 15 minutes of irradiation no removal of TOC was observed due to the formation of reaction intermediates. However, after 20 minutes of irradiation, it is possible to note a progressive removal of the organic substance present in solution, which reaches values equal to 100% removal after about 85 minutes of irradiation.

Compared with the synthetic solution, in this case, the degradation of organic substance required a longer time, probably due to the presence of substances which act as radical scavengers (chlorides and carbonates).

From these results it is possible to claim that the photocatalytic process coupled to the photo-Fenton process for the simultaneous valorization and treatment of the organic substances present in aqueous matrices allows to obtain interesting results.

For this reason, having regard to the good performance obtained on a real waters matrices containing also other substances (such as carbonates and chlorides), it was decided to apply the whole process, with the catalyst optimized, on a wastewater from the cherries washing process. The experimental tests and the results are shown in the following chapter.

VI Experimental results: AOPs for the valorization and treatment of wastewater from the cherries washing process

Considering the excellent results obtained by applying the advanced oxidation processes both on synthetic solutions and on real water containing chlorides and carbonates, the experimental tests were carried out also on real wastewaters from cherries wash water of a food industry. This wastewater is rich of different types of sugars, and it is characterized by a high concentration of TOC. The valorization for the hydrogen and methane production was obtained by the application of the photocatalytic process under visible light and using the optimized photocatalyst reported in the previous chapter. For the total removal of TOC, the photocatalytic process was coupled to the heterogeneous photo-Fenton process able to remove the organic substance still present in wastewater.

In this chapter it is reported the characteristic of the wastewater, the analysis of the liquid phase by HPLC method and the photocatalytic results in terms of hydrogen and methane production. In addition it is shown the results in terms of TOC removal after the application of photo-Fenton process.

VI.1 Characteristics of the wastewater

The wastewater, object of study, comes from a food industry after the phase of the cherries wash. It has a yellow-brownish color, and it is characterized by the presence of suspended solids.

First it was necessary to remove suspended solids. In particular, the sample was centrifuged at 6000 rpm for 10 minutes at 25°C. At the end of centrifugation, the supernatant was subjected to filtration using Whatman filters 540 and finally analyzed by HPLC (Ultra High Performance Liquid Chromatography). During the HPLC analysis it was found to contain anthocyanins, water-soluble pigments belonging to the flavonoid family.

Anthocyanins are among the most important groups of pigments found in plants, and find themselves in the flowers and fruits as well as the bushes and in the autumn leaves. The color of anthocyanin can range from red to blue and depends on the pH of the medium in which they are located and by the formation of salts with heavy metals present in those tissues.

Anthocyanins are polyaromatic polyhydroxylated compounds capable of reacting with the oxidants such as molecular oxygen and free radicals thus reducing the damage that can cause these molecules to cells and tissues.

Thanks to their antioxidant and anti-radical, these substances can be very useful for their use in medicine. These pigments protect against capillary fragility (Bell and Gochenaur, 2006), and against various aging processes or cellular changes caused by oxygen, including inflammatory processes and carcinogenic amended (Hou, 2003, Hannum, 2004). Some of these activities are the same as those found in wine (Dell'Agli et al., 2004). The presence of anthocyanins has been demonstrated by the chromatographic profile obtained by HPLC analyzes, reported in Figure VI.1.

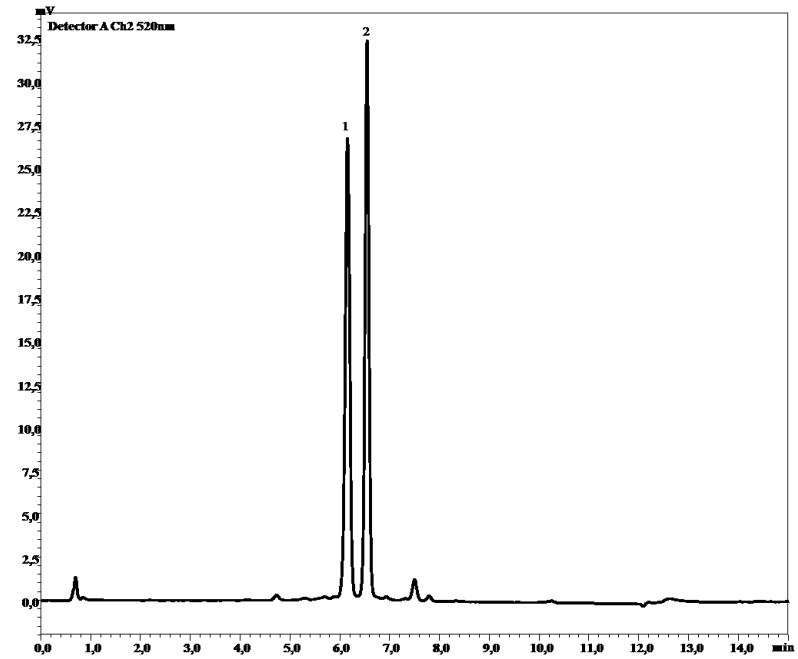

Figure VI.1 *Chromatographic profile of anthocyanins present in the water of cherry vegetation*

The HPLC method for the quantitative characterization of antocianine.ha allowed to identify two main molecules.

The HPLC method for the quantitative characterization of anthocyanins has allowed us to identify two main molecules.

The analysis showed that the two anthocyanins are present in solution at a concentration of 13.62 ± 0.01 mg/L and 13.91 ± 0:04 mg/L, respectively for the peak 1 and 2 (Figure VI.1). Due to the presence of anthocyanins, it was considered interesting to evaluate the opportunity to recover these compounds from wastewater for use in cosmetics and medicine.

Furthermore, in order of the valorization of the wastewater, it is interesting to understand the effect of anthocyanins on the hydrogen and methane yields. For this reason, the photocatalytic tests were carried out on wastewater in presence of anthocyanins and on wastewater without anthocyanins. For the extraction of anthocyanins, 50 mL of cherry washing waters were subjected to solid phase extraction using polymeric cartridges (Strata-X, 500 mg/6 mL). The HPLC analysis of the wastewater revealed the presence of three sugars: glucose, fructose and sorbitol. The concentration of these organic compounds was equal to 37000, 32000 and 13000 mg/L respectively. In figure VI.2 it is reported the chromatographic profile of the

sample with anthocyanins and in the Figure VI.3 that of the sample without anthocyanins.

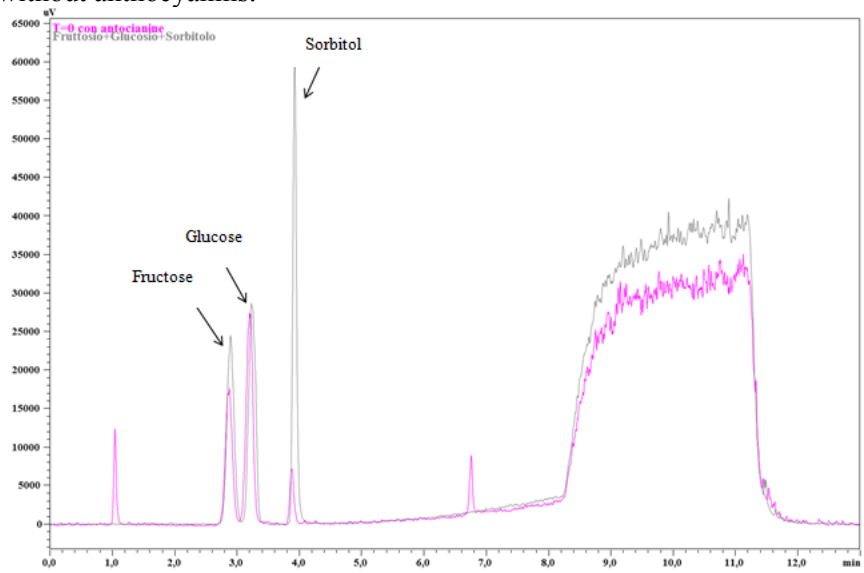

Figure VI.2 *Chromatographic profile of sample with anthocyanin.*

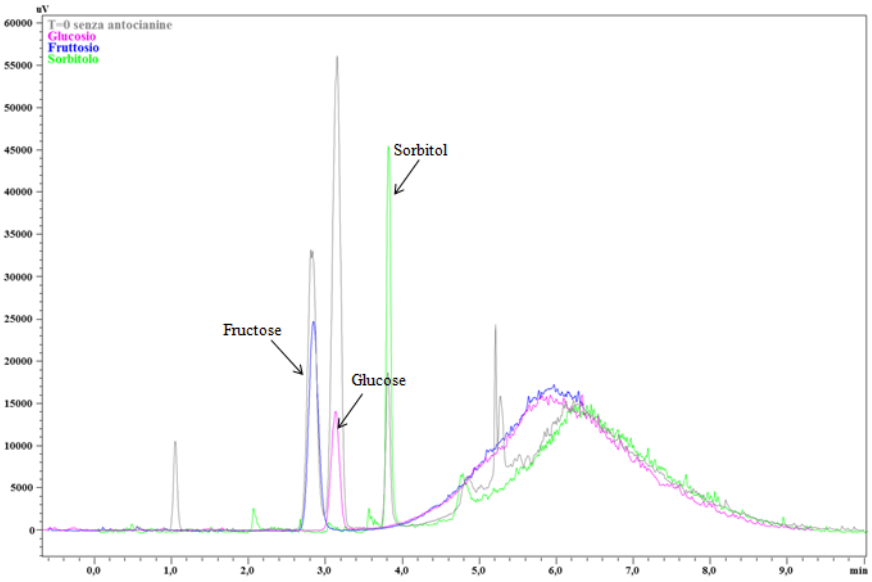

Figure VI.3 *Chromatographic profile of sample without anthocyanin.*

VI.2 Experimental results

For the valorization of the wastewater, the photocatalytic process was applied. In particular, it was used the optimized photocatalyst (called "67Ru") easily removable at the end of the process due to the magnetic properties.

The photocatalytic tests were carried out on the reactor configuration previously optimized, called R1, with an internal diameter equal to 1.25 cm.

Catalyst dosage equal to 1.5g/L was used and the volume of wastewater used during the photocatalytic experiment was 45 ml. To ensure complete mixing of the solution in the reactor, a peristaltic pump was used. The photoreactor was irradiated with a strip of visible LEDs with the main wavelength emission at 440 nm positioned around the external surface of the reactor.

Before the photocatalytic experiment, the wastewater was centrifuged at 6000rpm in order to remove solids in suspension. The initial total organic carbon (TOC) measured for the wastewater containing the anthocyanin was equal to 38000 mg/L.

In Figure VI.4 and VI.5 it is reported the hydrogen and methane production during the irradiation time for the wastewater containing the anthocyanin.

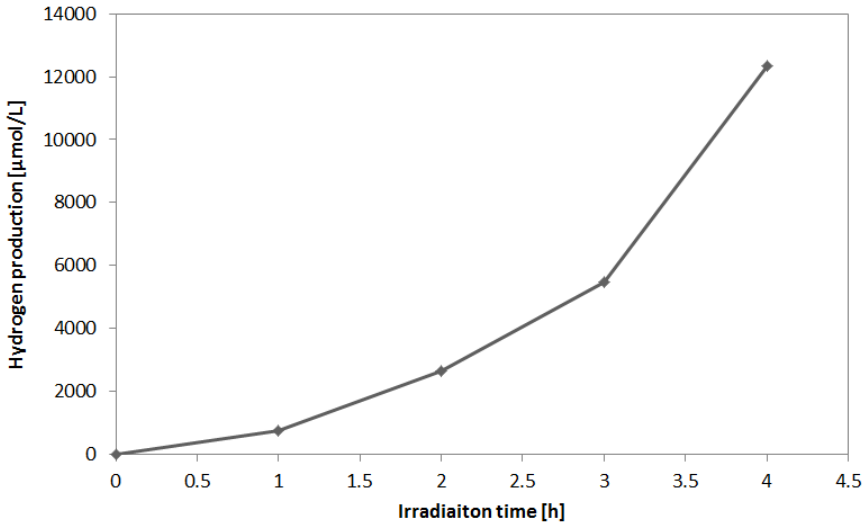

Figure VI.4 *Hydrogen production from the wastewater containing the anthocyanin.*

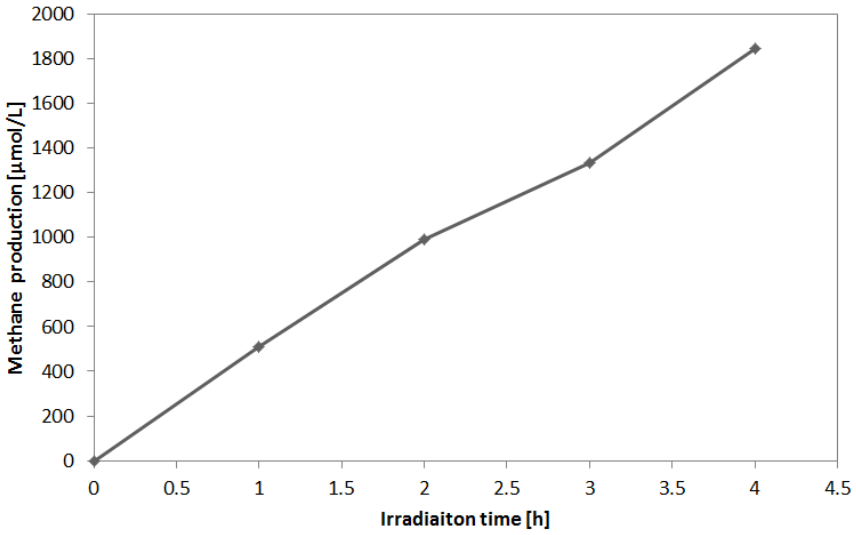

Figure VI.4 *Methane production from the wastewater containing the anthocyanin.*

As it is possible to observe in Figure VI.3 the hydrogen production is very high and after 4 hours of irradiation time it was obtain a value equal to 12340 µmol/L. This result is very interesting and confirms the ability of the photocatalytic process in the valorization of a food industry wastewater. The same result was obtained also for the methane production, equal to 1840 µmol/L.

As regards the degradation of sugars present in solution, after 4 hours of irradiation time it was observe a degradation equal to 790, 800 and 220 mg/L for fructose, glucose and sorbitol respectively.

At the end of the photocatalytic process, the TOC value was equal to 37960 mg/L. In fact, during the irradiation time, the removed TOC was only equal to 36.86 mg/L.

This means that the photocatalytic process has promoted the valorization of the wastewater by converting a portion of the sugars in H_2 and CH_4, but the organic content, responsible for the high TOC value, is still present in solution.

In order to make the wastewater comply with the limits imposed by the legislation, the organic content has been completely degraded through the photo-Fenton process.

The use of this advanced oxidation process has allowed to obtain the complete degradation of the organic substance, as evidenced by the results shown in the figure VI.5 in terms of TOC removal.

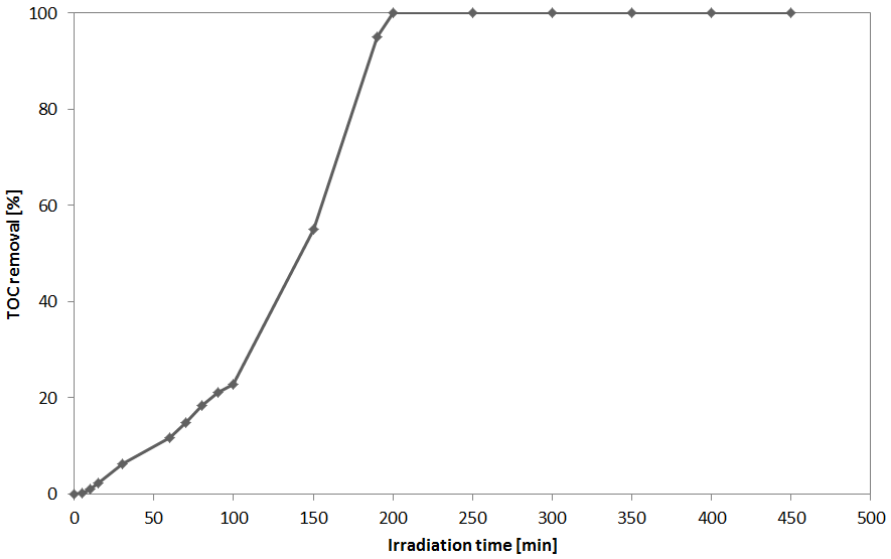

Figure VI.5 *TOC removal during photo-Fenton treatment for wastewater containing anthocyanins.*

It is possible to observe that after 200 min of irradiation the complete TOC removal was obtained. This result demonstrated that also for a food industry wastewater with very high concentration of TOC, the coupling of the photocatalytic process with the photo-Fenton allows to obtain a good valorization and an effective wastewater treatment, by completely removing the organic substance and hardly biodegradable compounds (such as food dyes).

To evaluate the effect of anthocyanins on the production of hydrogen and methane, and to determine if it is convenient to proceed with the extraction and recovery of these organic compounds, photocatalytic tests were performed on wastewater subjected to a process for the extraction anthocyanins.

The wastewater, in this case, is characterized by an initial TOC equal to 34032 mg/L.

The obtained results (hydrogen and methane production) from photocatalytic tests are reported in figure VI.6 and VI.7.

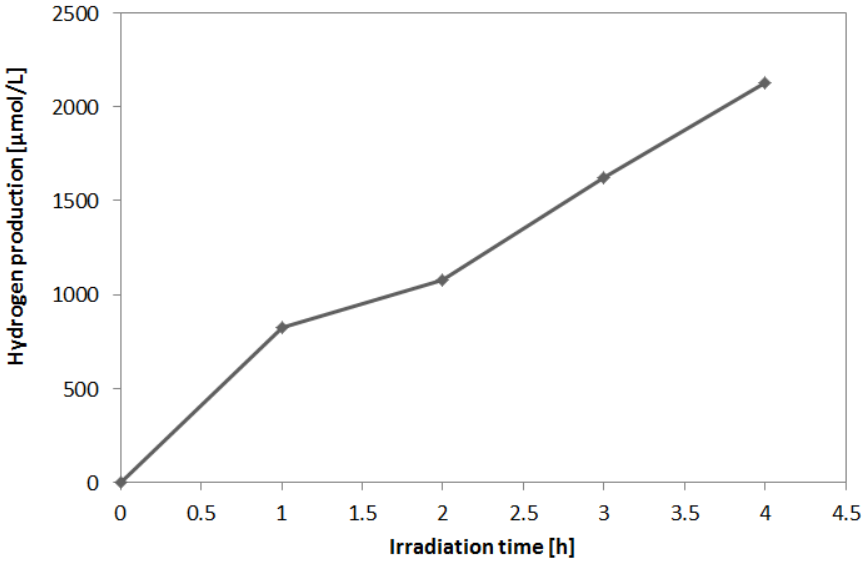

Figure VI.6 *Hydrogen production from the wastewater without the anthocyanin.*

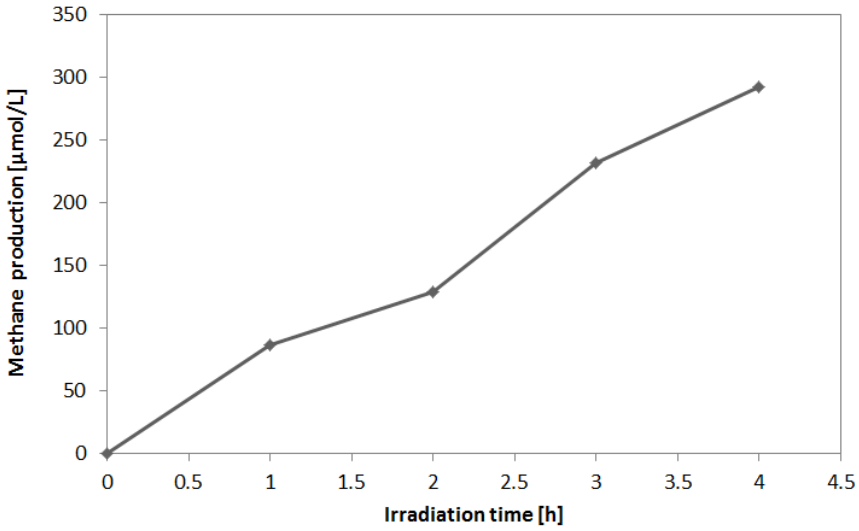

Figure VI.7 *Methane production from the wastewater without the anthocyanin.*

The presence of anthocyanins drastically reduces the production of hydrogen and methane.

In this case, at the end of the photocatalytic process, the TOC value was equal to 34023 mg/L. In fact, during the photocatalytic process the TOC removed was equal to 8.31 mg/L.

The results in terms of TOC removal during the photo-Fenton treatment is shown in figure VI.8.

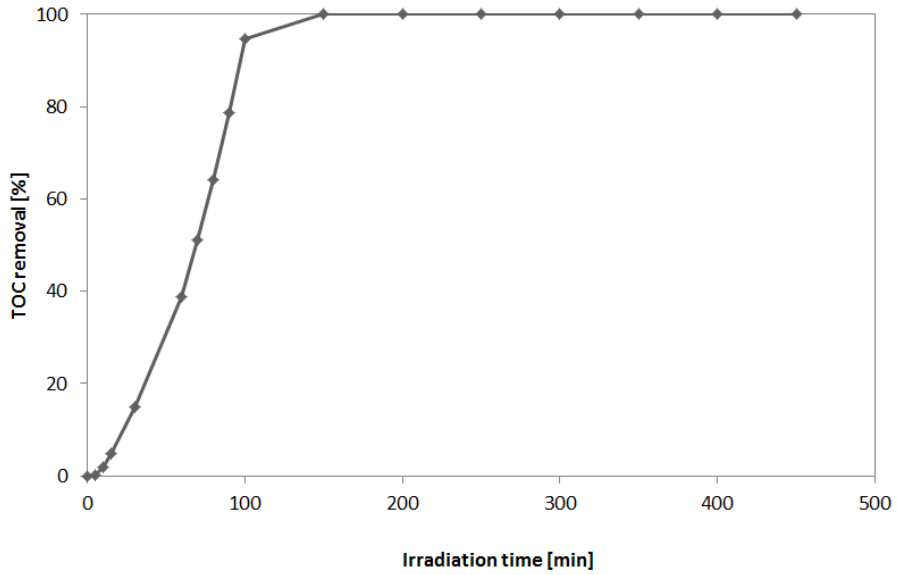

Figure VI.8 *TOC removal during photo-Fenton treatment for wastewater containing anthocyanins.*

It is possible to observe that after 150 minutes of irradiation time the complete TOC removal was obtained.

Compared to the wastewater with anthocyanins, in this case the removal of TOC was faster.

The effect of the presence of anthocyanins is highlighted in the production of hydrogen and in the removal of TOC.

In order to better understand this phenomenon, it was evaluated the effect of anthocyanins in the production of hydrogen from a solution containing only glucose at a concentration equal to 1000 mg/L.

It was added a quantity of anthocyanins equal to that present in the waste water previously reported. This has allowed us to understand the role of anthocyanins in photocatalytic hydrogen production from solutions containing sugars. The result was reported in Figure VI.9.

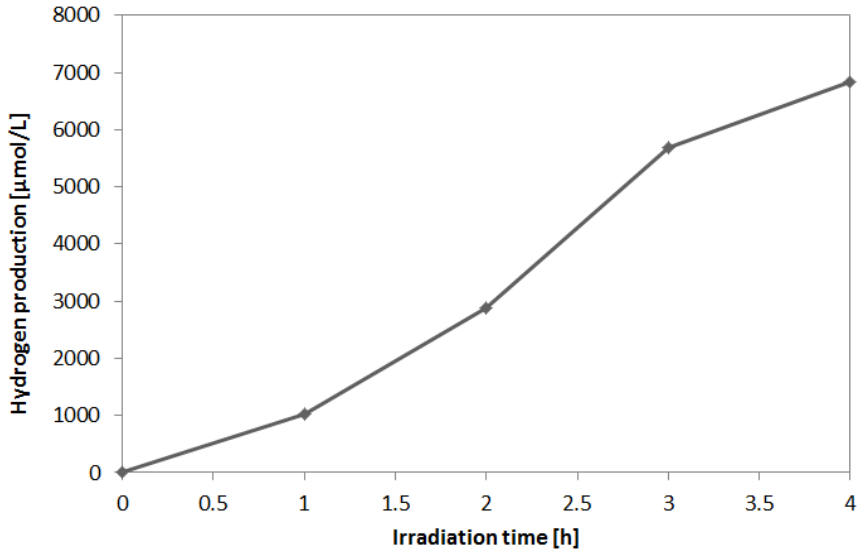

Figure VI.9 *Hydrogen production from the glucose solution (1000 mg/L)in presence of anthocyanin.*

It is possible to note that in this case the hydrogen production after 4 hours of irradiation time was equal to 6836 µmol/L, higher than that obtained in the case of solution containing only 1000 mg/L of glucose without anthocyanins (5460 µmol/L).

This result confirms the behavior of hydrogen production observed in the case of cherry wash wastewater with and without anthocyanins.

VII Experimental results. Photoelectrocatalytic hydrogen production on metal-doped Fe_2O_3 photoanodes.

Advanced oxidation processes and in particular photoelectrocatalysis, allow to obtain interesting results in terms of hydrogen production from the degradation of the organic compounds present in wastewater (Wu et al., 2015). The generation of H_2 by means of photoelectrocatalysis allows for a sustainable green fuels production and it is particularly attractive among the low-cost technologies in the hydrogen–based energy system (Fu et al., 2008b).

With regard to the photoproduction of hydrogen, different semiconductors with photocatalytic and photoelectrochemical properties have been tested in the water splitting reaction (Dholam et al., 2009).

Several works have demonstrated that hydrogen can be produced by the photoelectrocatalytic decomposition of ethanol, methanol and other oxygenates (Michal et al., 2014, Antoniadou et al., 2011, Strataki et al., 2010, Antoniadou et al., 2009, Zhang et al., 2015a), but also the photoelectrocatalytic degradation of other organic compounds such as glucose, sorbitol and other saccharides come from food industry wastewaters could also lead to interesting hydrogen yield (Vaiano et al., 2015a, Zhang et al., 2015b, Zhang et al., 2016). Among the different semiconductors, hematite (α-Fe_2O_3) has become a very attractive material to be used as photoanode in photoelectrochemical cells because of its bandgap ($Eg \approx 2.2eV$) that allows utilization of a considerable portion of solar energy (Bora et al., 2013, van de Krol et al., 2008, Dholam et al., 2009). Moreover, hematite is an environmental friendly, abundant, non-toxic material and it is very stable in aqueous solutions. However, hematite, at its pure phase, has some limitations with regard to the desired efficiency for solar water splitting due to its poor charge transfer characteristics, low electron mobility, short hole diffusion length and its high recombination rate of the

photogenerated holes and electrons (Sivula et al., 2010, Cardillo et al., 2013). A promising method to improve the photoelectrochemical properties of hematite is to introduce dopant atoms such as Zr, Cr, Mo, Zn, Cd, Ni, Pt, Ti, Si and Ge (Bora et al., 2013, Bak et al., 2011, Fu et al., 2014).

There are several methods to synthesize doped hematite such as hydrothermal method (Cardillo et al., 2013, Rajendran et al., 2014), spray pyrolysis (Cesar et al., 2006), sol-gel method (Park et al., 2009) and electrochemical deposition (Fu et al., 2014, Schrebler et al., 2007, Zheng et al., 2015, Kumar et al., 2011). The latter method is advantageous, being inexpensive in both materials and energy consumption because it is performed at low temperatures (Fu et al., 2014). Also, the deposition could be applied straight on FTO glass which can be used in a photoelectrochemical cell.

So, hematite photoanodes doped with several metals and deposited on FTO glass by the electrochemical deposition have been studied in a photoelectrochemical cell configuration, in order to increase the photoelectrocatalytic hydrogen yield by the decomposition of organic compounds present in a simulated food industry wastewater.

VII.1 Preparation and characterization of Fe_2O_3 films on FTO

Hematite (Fe_2O_3) films were deposited on FTO transparent electrodes by the electrochemical deposition procedure. An FTO glass was cut in the appropriate dimensions and was carefully cleaned first with soap and then by sonication in isopropanol, water and acetone. The FTO glass was immersed into the electrodeposition solution containing 5 mM $FeCl_3$, 5 mM KF, 0,1 M KCl, 1 M H_2O_2. The volume of the solution was 100 ml. The deposition of the hematite film was performed by cyclic voltammetry, applying 50 potential cycles between -0.4 to 0.5 V vs Ag/AgCl with scan rate of 100 mV s^{-1} at 50 ºC. As counter electrode a 2.5 cm^2 Pt foil was used. The distance between the anode and the cathode was approximately 1cm. After deposition, the hematite-modified FTO electrode was rinsed with three distilled water. Finally, the film was calcined up to 750 ^oC for 10 min in air atmosphere at a rate of 20^oC/min. The geometrical area of the deposited film on FTO was 17.5 cm^2 (5 cm x 3.5 cm) when it was used for hydrogen production. The metal-modified photoanodes were prepared with the same method, introducing in the electrodeposition solution containing 5 mM $FeCl_3$, 5 mM KF, 0,1 M KCl, 1 M H_2O_2 and the following metals: Co, Ti, Cu, Sn, Ni as chlorides nitrates. The atomic ratio of the single metal with Fe was in the range 0.5-3%. The samples are named xMe-Fe_2O_3, where x is the atomic ration of modifier (%) and Me is the metal.

For the fabrication of the counter electrode, a commercial carbon paste (Elcocarb C/SP (Solaronix)) was applied on FTO by doctor blading and was annealed at 450^oC for 30 minutes. Pt was then deposited on the top using a solution of Diamminedinitritoplatinum(II) (Aldrich) in ethanol and casted on warm film lying on a hot plate at 40^oC. The film was subsequently annealed again at 450^oC. The final quantity of Pt on the film was calculated to be 0.1 mg/cm^2. The geometrical area of the film was 17.5 cm^2 (5 cm x 3.5 cm). The photocatalyst and electrocatalyst were deposited on separate FTO electrodes and connected by external wires. In that case, hydrogen production rate could be enhanced by applying an external electrical bias.

VII.1.1 Photocurrent characterization results

Figure V.1 shows the photocurrent density-applied potential (J–V) plots for pristine hematite thin films. In dark conditions, the J–V responses for all the samples are similar and show no evidence of PEC activity due to the metal modifier. The pristine hematite thin film gave a photocurrent density equal to 0.36 mA/cm^2 at 0.5 V. This value is one of the highest photocurrents reported for bare hematite prepared by electrodeposition method (Rahman and Joo, 2013).

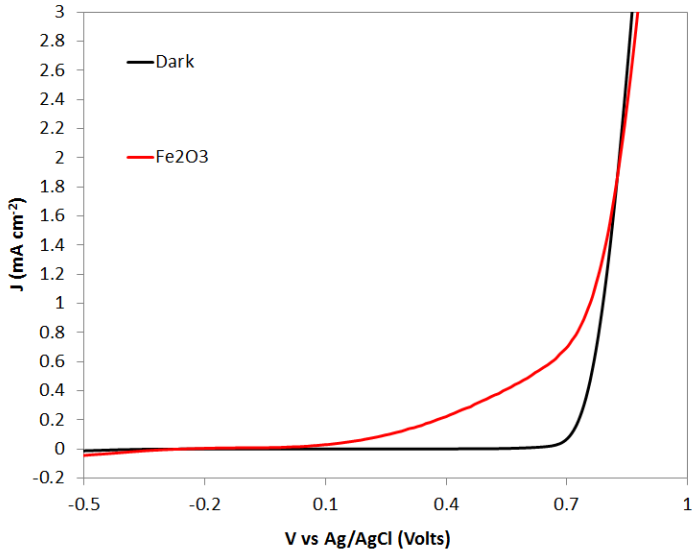

Figure VII.1 *Photocurrent-potential (J-V) curves collected for undoped Fe_2O_3 film, in 1 M NaOH solution.*

The comparison for different amounts of modifiers is shown in Figures V.2-V.6. With metal-modified hematite films, it was possible to observe an increase of photocurrent values for specific amount of dopant in agreement with literature about the performance of hematite films doped with different metals (Atabaev et al., 2015). In general, metal modifiers (M^+) in hematite may act in several ways: i) first, metal may act as an electron donor due to the substitution of Fe^{3+} by M^+ in hematite lattice. The increased donor concentration improved the conductivity of the photoactive film and decreases the carrier recombination; ii) second, the increased donor concentration would increase the electric field across the space charge layer resulting in higher charge separation efficiency (Atabaev et al., 2015). However, at high concentrations, M^+ would have defect scattering/recombination properties and finally negate the increased separation efficiency (Atabaev et al., 2015). For each metal modifier, the experimentally obtained optimum level may balance these competing effects and yield the best PEC performances (Atabaev et al., 2015). In fact, for hematite modified with Ni, the optimal loading of modifier was 1 % while for Ti was 3 %, both nominal loadings.

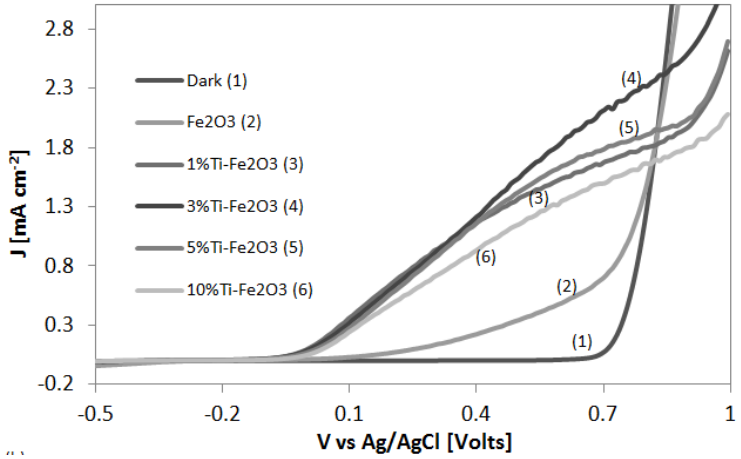

Figure VII.2 *Photocurrent-potential (J-V) curves collected for Ti doped Fe_2O_3 film, in 1 M NaOH solution.*

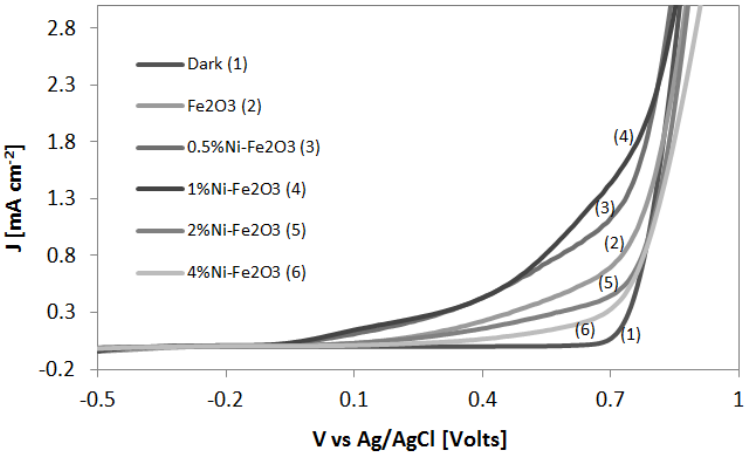

Figure VII.3 *Photocurrent-potential (J-V) curves collected for Ni doped Fe_2O_3 film, in 1 M NaOH solution.*

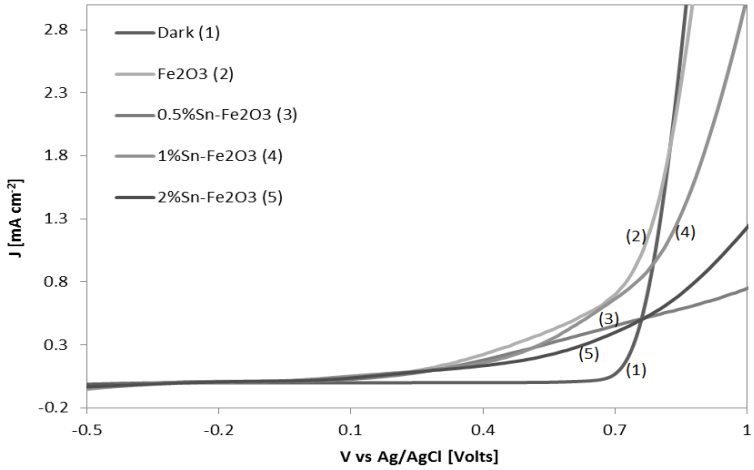

Figure VII.4 *Photocurrent-potential (J-V) curves collected for Sn doped Fe_2O_3 film, in 1 M NaOH solution.*

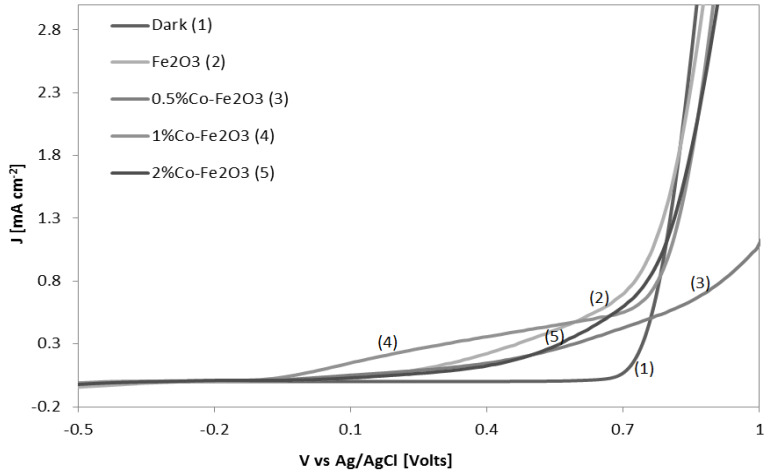

Figure VII.5 *Photocurrent-potential (J-V) curves collected for Co doped Fe_2O_3 film, in 1 M NaOH solution.*

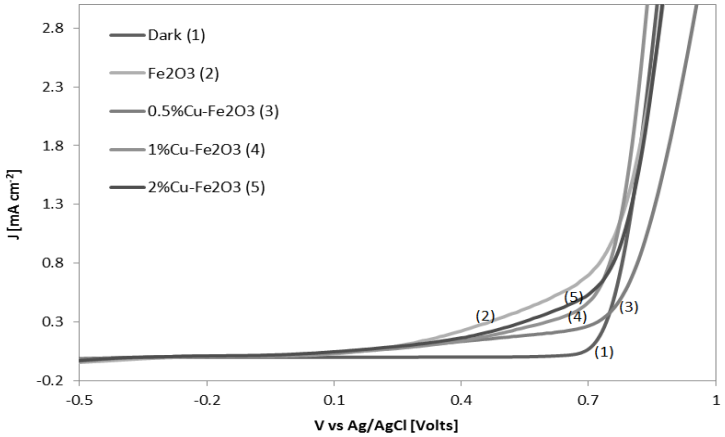

Figure VII.6 *Photocurrent-potential (J-V) curves collected for Cu doped Fe_2O_3 film, in 1 M NaOH solution.*

After choosing the optimal amount of doping for each single metal-modified hematite film, a comparison of the J–V responses in the presence of various metals was made to determine which one was able to improve the photoelectrochemical performances of hematite (Figure V.7).

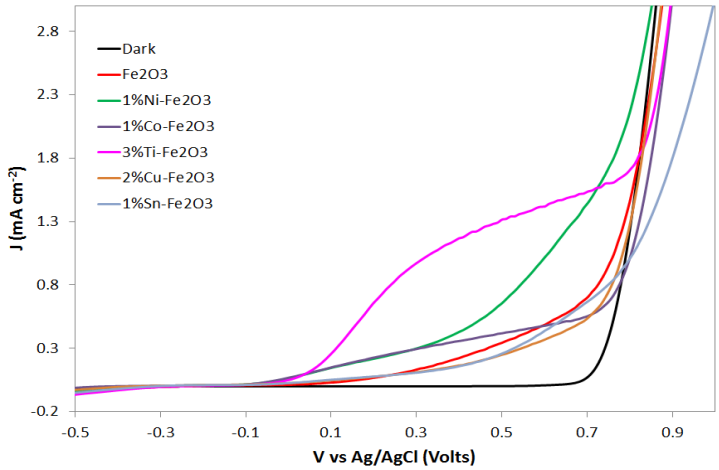

Figure VII.7 *Photocurrent-potential (J-V) curves collected for Cu doped Fe_2O_3 film, in 1 M NaOH solution.*

The Ti-doped hematite and Ni-doped hematite thin films show a much higher photocurrent than that obtained with other modifiers. In particular with the 3%Ti-Fe_2O_3, it was possible to obtain a photocurrent value equal to 1.32 mA/cm^2 for a bias potential equal to 0.5 V vs Ag/AgCl. In this case, the

amount of produced photocurrent increased by about 3 times with respect to pure Fe_2O_3.

With 1%Ni-Fe_2O_3, the photocurrent values were lower than those obtained with 3%Ti-Fe_2O_3 (0.67 mA/cm^2), but still better than the pure Fe_2O_3 (0.46 mA/cm^2) at the same potential (0.5V vs Ag/AgCl).

In the literature there are already studies on the efficiency of doping hematite with Ti for photoelectrochemical purposes (Fu et al., 2014). However, the photocurrent yield obtained with 3%Ti-Fe_2O_3 (1.32 mA/cm^2 at 0.5 V) was higher than that reported in literature, since a comparable value of photocurrent was obtained at remarkably higher potential (1.4 mA/cm^2 at 1.23 V) (Wang et al., 2013, Atabaev et al., 2015).

Following the excellent results obtained from photocurrent measurements, which showed the best performance of the samples 1% Ni-Fe_2O_3 and 3% Ti-Fe_2O_3 it proceeded with the characterization of the latter.

VII.1.2 XRD

The crystal structures of the samples were analyzed by XRD analysis (Figure V.8).

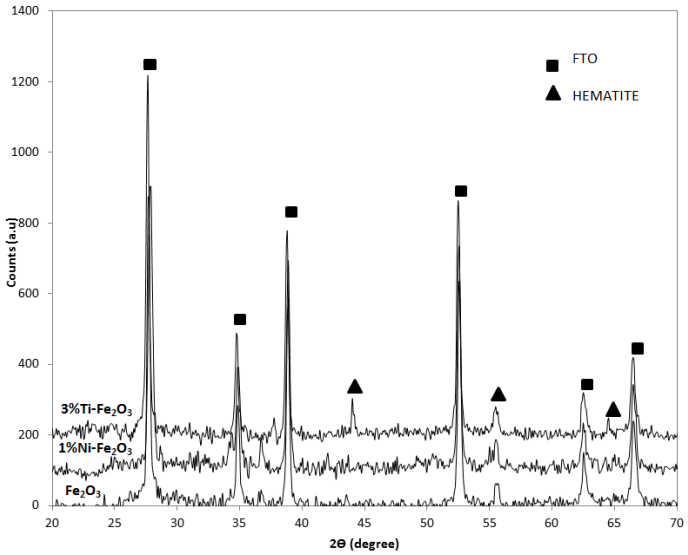

Figure VII.8 *: XRD spectra.*

Excluding peaks associated with the FTO substrate, only peaks that can be assigned to α-Fe_2O_3 were observed, suggesting that the metal incorporation (Ti or Ni) is not associated with any new long-range order in the crystals. In particular, both pure and 1%Ni-Fe_2O_3 or 3%Ti-Fe_2O_3 films showed diffraction peaks at 44, 55 and 64.0° degree, corresponding to the

(110) and (300) diffraction planes of hematite phase, as reported in literature (Chong et al., 2014c). The crystallite size of Fe_2O_3, 1%Ni-Fe_2O_3 and 3%Ti-Fe_2O_3 calculated by the Scherrer equation at (1 0 1) diffraction plane is listed in Table V.1.

Table VII.1 *Crystallite sizes obtained by XRD analysis*

PHOTOANODE	CRYSTALLITE SIZE (nm)
Fe_2O_3	21
1%Ni-Fe_2O_3	26
3%Ti-Fe_2O_3	20

The ratio between the intensity of FTO main peak (at 27.66 degrees) and that one of hematite phase (at 55.66 degree) is directly correlated to the thickness of the electrodeposited film (Shen et al., 2013b).

The obtained value of this ratio was 0.10 for 1%Ni-Fe_2O_3 while it was equal to 0.072 and 0.078 for Fe_2O_3 and 3%Ti-Fe_2O_3, respectively. These results indicate that the thickness of film for 3%Ti-Fe_2O_3 sample was lower than that one for 1%Ni-Fe_2O_3 sample. This might explain the lower photocurrent values of 1%Ni-Fe_2O_3 compared to those ones of 3%Ti-Fe_2O_3. In fact, as reported in literature, the film thickness should be optimized to facilitate carrier transport to interfaces as well as maximize the light absorption (Shen et al., 2013b).

It was thus shown that in the case of thicker Fe_2O_3 films, a higher number of photons are absorbed (Shen et al., 2013b). However, these films are subject to an increased recombination rate of the charges, which reduces the photocatalytic activity. For thinner Fe_2O_3 films, larger portions of photogenerated carriers reach the interface, but only a small number of photons are absorbed. In this case, an important role is represented by doping, which enhances the activity of the photoanode in the production of photocurrent, such as for 3%Ti-Fe_2O_3.

VII.1.3 Raman

Raman spectroscopy was also used to examine the phase of the films, as shown in Figure V.10. For all the samples, the optical modes of hematite were observed (225, 244, 292, 409, 496 and 611 cm^{-1}). It was possible to state that for the sample 3%Ti-Fe_2O_3, there is no signal typical due to the TiO_2 phase (generally at 145, 399, 516 and 640 cm^{-1}) (Leong et al., 2015), and also for 1%Ni-Fe_2O_3 sample, the typical modes of nickel oxide which

should appear at 460 and 500 cm^{-1} (Wang et al., 2001) are not visible, possibly due to low modifier concentration.

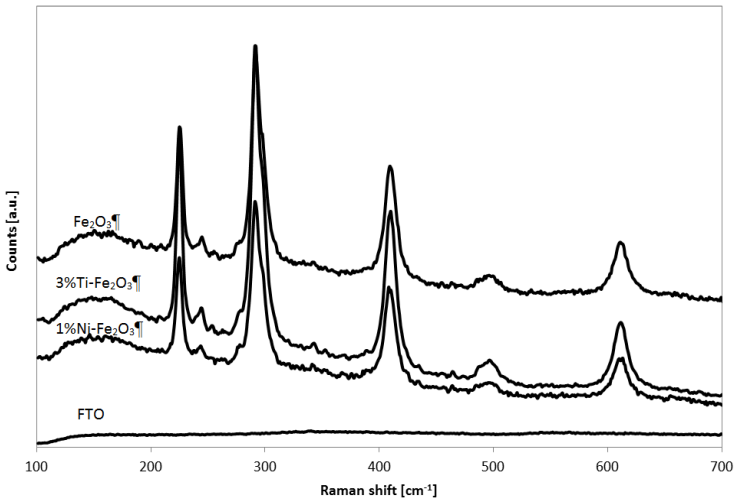

Figure VII.10 *Raman spectra.*

VII.1.4 UV Vis

The UV-visible spectrum reported in Figure V.11 in terms of Kubelka Munk function shows the absorption bands of α-Fe_2O_3 at 450 nm and 550 nm. In particular, the shoulder around 550 nm and the bands around 450 nm can be attributed to the indirect transition and direct charge transfer, respectively (Liu et al., 2012b).

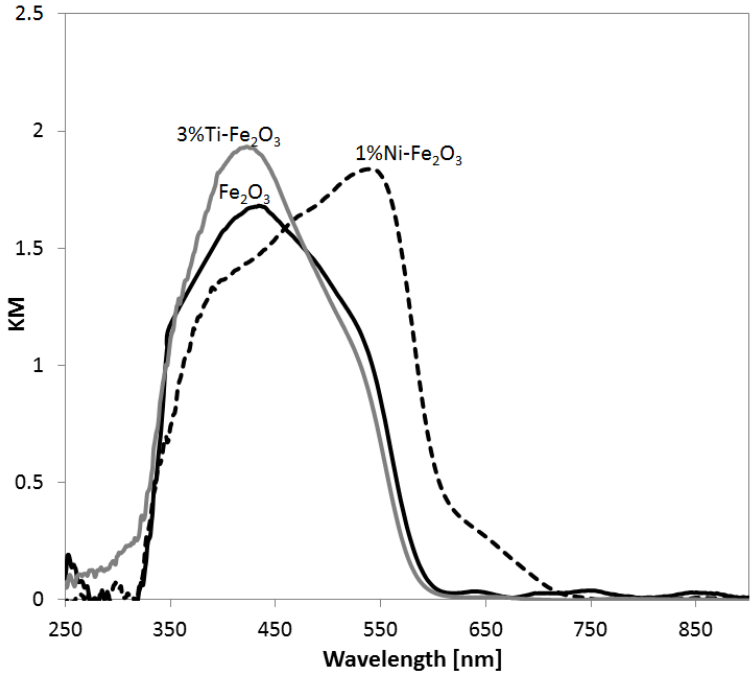

Figure VII.11 *UV-Vis DRS spectra*

It is noted that in the presence of hematite with titanium (3%Ti-Fe_2O_3), the band at 450 nm, responsible of the direct charge transfer, was enhanced, while for hematite doped with nickel (1%Ni-Fe_2O_3) the band at 550 nm was enhanced, responsible of the indirect charge transfer. As shown in literature, for the direct charge transfer phenomenon, the photo-generated holes are directly extracted from the valence band and the photocurrent follows the voltage variations of the hole density at the surface (Bertoluzzi et al., 2016). For the indirect charge transfer, the photogenerated holes are trapped in surface states and they can subsequently oxidize water or recombine with trapped electrons.

As it was possible to observe from Figure V.12, the band gap of Fe_2O_3, 3%Ti- Fe_2O_3 and 1%Ni-Fe_2O_3 was equal to 2.2, 2.1 and 2 eV, respectively.

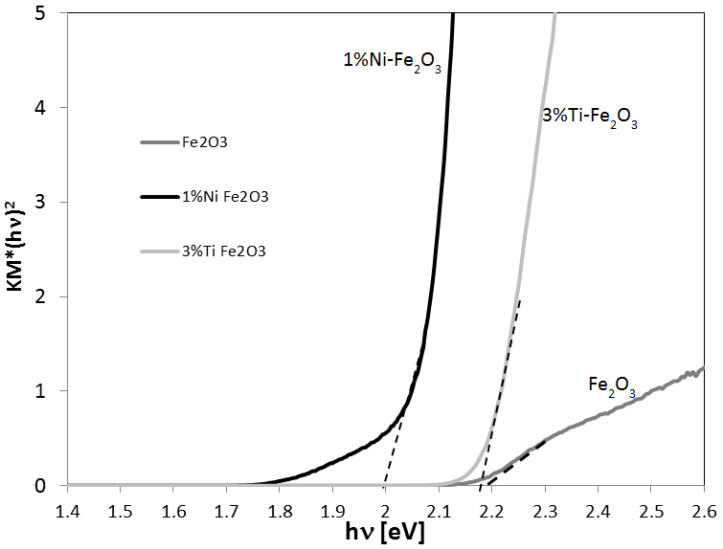

Figure VII.12. *Band gap evaluation (b).*

Despite the value of the band gap in the case of 1%Ni-Fe_2O_3 is the lowest (2eV), the sample which showed the better photoelectrochemical properties was the hematite doped with titanium. This result can be justified considering the optical properties of the samples in terms of direct and indirect charge transfer. In particular, considering the J-V graph reported in Figure V.7, it is possible to note a different behavior for the samples 3% Ti-Fe_2O_3 and 1% Ni-Fe_2O_3. According to the literature data, for 3% Ti-Fe_2O_3 photoanode, the behavior of photocurrent is typically of a direct charge transfer and, in particular, it can be an indication that the photo-generated holes are directly extracted from the valence band (Bertoluzzi et al., 2016). For 1% Ni-Fe_2O_3, the trend of photocurrent curve is typically of an indirect charge transfer meaning that the direct hole transfer competes with indirect charge transfer from the surface states (Bertoluzzi et al., 2016).

This may be the cause of the lower production of photocurrent in the case of 1% Ni-Fe_2O_3 photoanode compared to 3% Ti-Fe_2O_3.

VII.1.5 XPS analysis

XPS was also used to examine the presence and the atomic ratio of each component of the films. The examined dopants were 1% Ni or Co and a variation of ratios in the case of Ti (2-7%). Modification of Fe_2O_3 with Co, Ni and Ti by electrodeposition does not have the same effect for the three dopants, as shown in Table V.2. Apparently, Co and Ni are entering the hematite film at very small quantities and for this reason XPS method failed

to detect their presence. On the contrary, Ti uptake is much higher than the nominal percentage of Ti in the precursor solution. For this reason, one

lower and two higher ratios than 3% were examined to detect the influence of the solution ratio to the surface ratio on the film. Thus the atomic percentage of Ti in the film ranged between 10 and 39% while the nominal concentration ranged between 2 to 7%. This is in agreement with our previous results (Kalamaras et al., 2016).

Table VII.2 *Detected elements and dopant atomic ratios for doped hematite*

Dopant (D) atomic ratio (D/Fe) in the solution (%)	Detected elements	Valence	Atomic ratio (%)	Surface dopant atomic percentage with respect to Fe (%)
1% Co	Fe, O, C, NO Co	Fe^{3+}	45%Fe, 55%O	n.d.
1% Ni	Fe, O, C, NO Ni	Fe^{3+}	39%Fe, 61%O	n.d.
2% Ti	Fe, O, C, Ti	Fe^{3+}, $Ti^{4+}(TiO_2)$	35%Fe, 59%O, 4% Ti	10
3% Ti	Fe, O, C, Ti	Fe^{3+}, $Ti^{4+}(TiO_2)$	27%Fe, 66%O, 7% Ti	21
5% Ti	Fe, O, C, Ti	Fe^{3+}, $Ti^{4+}(TiO_2)$	21%Fe, 66%O, 13% Ti	38
7% Ti	Fe, O, C, Ti	Fe^{3+}, $Ti^{4+}(TiO_2)$	24%Fe, 61%O, 14% Ti	39

VII.1.6 SEM characterization

The morphology of the undoped Fe_2O_3 and 1%Ni-Fe_2O_3 photoanodes was investigated by SEM microscopy and the obtained results are presented in Figure V.13. The results of 3%Ti-Fe_2O_3 are not shown since they are presented in another previous paper evidencing a mesostructure composed of nanoparticles (with a size ranging from 40 to 400 nm) with substantial size polydispersity (Kalamaras et al., 2016). It can be seen the doping with Ni at nominal loading of 1% induced a deposited film with morphology similar to that of the undoped Fe_2O_3 with particle aggregates between 100 and 400 nm, higher than those ones observed for 3%Ti-Fe_2O_3.

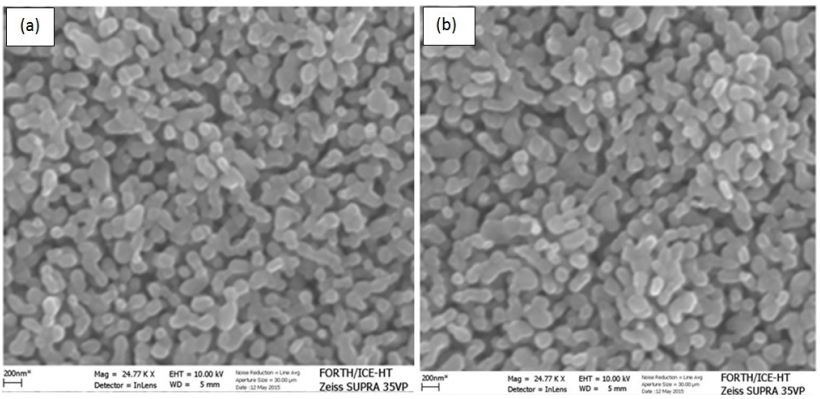

Figure VII.13 *SEM images of electrochemically deposited hematite films: (a) undoped and (b) doped with 1% Ni. Scale bar is 200 nm.*

VII.2 Photoelectrocatalytic activity in the H_2 production

The photoelectrocatalytic performances of the best photoanode (3%Ti-Fe_2O_3) were also analyzed in terms of H_2 production from the degradation of organic compounds present in water (Figure V.14). As control test, a photoelectrocatalytic test was carried out also in presence of only electrolyte solution (1M NaOH), without additive.

After a first transient phase (about 1.5 hours), the hydrogen production rate remained almost constant, confirming the absence of deactivation phenomena during the irradiation time.

As general remark, the presence of organic compounds in the solution enhanced the photoelectrocatalytic performances with respect to those ones achieved in presence of only electrolyte solution.

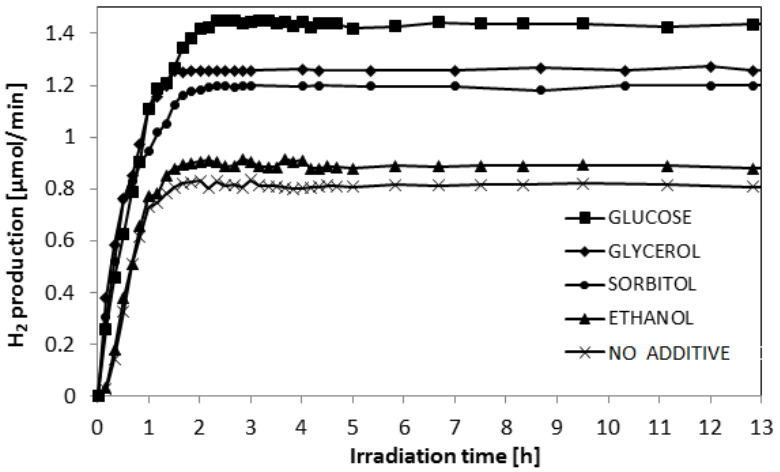

Figure VII.14*: Photoelectrocatalytic hydrogen production by using 3%Ti-Fe_2O_3 photoanodes and 1g/L of various organic additives*

The highest H_2 production (1.46 µmol/min) was obtained in the presence of glucose, followed by glycerol (about 1.26 µmol/min), sorbitol (1.19 µmol/min) and ethanol (0.9 µmol/min).

Generally, for hydrogen production by photocatalysis or photoelectrocatalysis, sugars are used as sacrificial agents (Vaiano et al., 2015a, Iervolino et al., 2016b, Lu et al., 2014). In fact, the feasibility of hydrogen evolution from carbohydrates, such as glucose, under light irradiation was demonstrated in a pioneering work by Kawai and Sakata (Kawai and Sakata, 1980) in which it was reported that the presence of many hydroxy groups in sugars enables their easy activation on semiconductor surfaces.

In addition, the mechanism for hydrogen evolution from alcohols with the use of metal oxide semiconductors includes the release of H^+ from the sacrificial agent (organic compound) and the formation of different oxygenated radicals, which are powerful oxidizing species. The result is the reduction of protons to H_2 and the concomitant full oxidation of the organic compounds to CO_2 through various intermediates, including aldehydes and carboxylates (Chen et al., 2010b)

Kondarides et al. (Kondarides et al., 2008b) described the photoreforming of glycerol (and other biomass-derived compounds, such as saccharides and organic acids) to H_2 and CO_2 over Pt/TiO_2 photocatalysts under non aerated conditions and with UV irradiation. In this case the hydrogen production rate increased by an order of magnitude in the presence of glycerol in the aqueous solution compared to that obtained by pure water.

However, in the present study, when ethanol was used in the aqueous solution, the hydrogen production was lower than that obtained with the

other organic compounds. Nevertheless it must be considered that, typically, the concentration of ethanol used to study the photoelectrocatalytic production of hydrogen was much higher than 1000 mg/L (Pop et al., 2015a, Antoniadou et al., 2013), used in this work.

The obtained photoelectrochemical results confirm that the valorization of sugar or of other organic substance (such as glycerol) present in wastewater is very interesting, and it is a valid alternative to the conventional water splitting reaction for H_2 production. In fact, with this process, in addition to hydrogen production, it was possible to observe also a significant degradation degree of the tested organic compounds. In particular, in the case of glucose, sorbitol and glycerol, after 4 hours of irradiation, the number of moles degraded were equal to 2.22, 2.36 and 2.17 mmol/L respectively,

Figure V.15 shows the effect of increasing the potential (bias) on the photoelectrochemical production of hydrogen from solution containing glucose. As expected, there was an increase of H_2 production with the increase of external bias from 0.5 V to 0.7 V. In particular after 4 hours of irradiation, the hydrogen production was 1.46 µmol/min with 0.5 V and 2.28 µmol/min with 0.7 V.

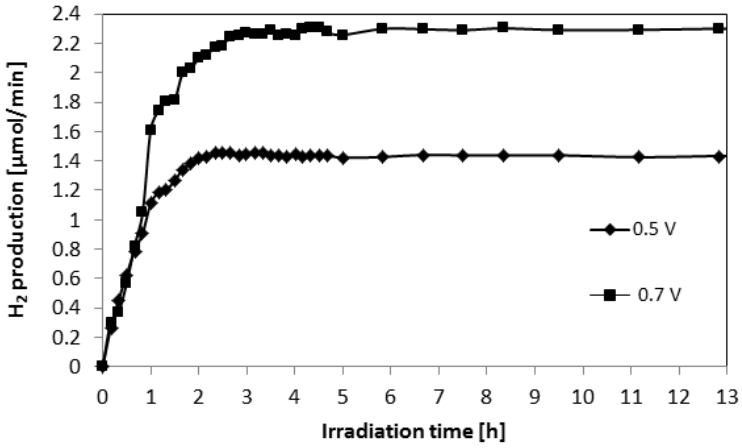

Figure VII.15 *: Photoelectrocatalytic hydrogen production by using 3%Ti-Fe_2O_3 photoanodes and 1g/L of glucose at two different bias.*

Since glucose showed the best results, this substance was chosen to compare the H_2 production obtained using 3%Ti-Fe_2O_3, 1%Ni-Fe_2O_3 and undoped Fe_2O_3 with an external bias of 0.5 V. The obtained results are reported in Figure V.16.

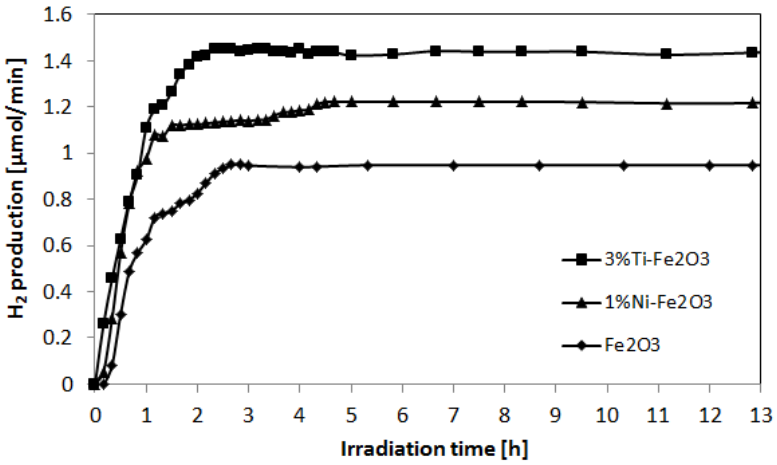

Figure VII.16 *Photoelectrocatalytic hydrogen production by using pristine or metal-modified Fe_2O_3 photoanodes and 1g/L of glucose.*

In the steady state conditions, both doped-Fe_2O_3 films showed an enhanced performance if compared to undoped Fe_2O_3. It must be noted that 3%Ti-Fe_2O_3 allowed to reach a H_2 production higher than 1%Ni-Fe_2O_3. This last result is in agreement with the UV-Vis DRS data, XRD analysis and photocurrent production. Possibly, as reported in the discussion about characterization data, with 3%Ti-Fe_2O_3, a perfect holes selective contact without surface states is obtained, determining an increase of the photoelectrocatalytic activity compared to 1%Ni-Fe_2O_3 for which the direct hole transfer competes with indirect charge transfer from the surface states, worsening the photoelectrocatalytic performances.

Considering these results it is possible to conclude that the photoelectrocatalytic process applied to solutions containing organic substances represents a valid alternative to the conventional water splitting reaction for H_2 production.

In particular it was confirmed that the valorization of sugars or of other organic substances (such as glycerol) present in wastewater is very interesting. In fact, with this process, in addition to hydrogen production, it was possible to observe also a significant degradation degree of the tested organic compounds.

Using the electrodeposition method, the hematite (Fe_2O_3) film was deposited on transparent FTO and it was used as photoanode. The efficiency of various metal modifiers (Ti, Ni, Sn, Co and Cu) has been tested by monitoring the photoelectrochemical behavior of the modified Fe_2O_3 photoanodes. With Ti-doped hematite photoanode a perfect holes selective

contact without surface states is obtained, determining an increase of the photoelectrocatalytic activity.

In fact, the experimental results showed that the highest photocurrent production has been achieved with the Ti-modified Fe_2O_3 photoanode. The highest hydrogen production (1.43 μmol/min at 0.5 V and 2.30 μmol/min at 0.7 V vs Ag/AgCl) was obtained on a Ti-modified hematite photoanode in the presence of alkaline aqueous electrolyte solution containing 1 g/L glucose as sacrificial agent.

VIII Experimental results. AOPs for food dyes removal: photocatalysis and photo-Fenton application

A substantial amount of hazardous organic compounds are introduced into the environment as a result of the industrial activities. Currently, dyestuffs coming from textile and food industries are important pollutants in water effluents. These dyes represent a serious problem for the human and animal health. For that reason, the degradation of these pollutants has acquired increasing attention. The traditional processes for treatment of these effluents prove to be insufficient to purify the important quantity of waste waters after the different operations of textile dyeing and washing. Some methods such as combined coagulation, electrochemical oxidation, active sludge have recently been investigated and proved to be adequate (Lin and Peng, 1994). Other methods such as flocculation, reverse osmosis and adsorption on activated carbon have also been tested (Ramakrishna and Viraraghavan, 1997).

The drawbacks of these methods are mainly the creation of a more concentrated pollutant-containing phase. The processes by bacterial beds are less adapted because of the fluctuations of the wastewater composition (Lachheb et al., 2002).

As has been already mentioned in Chapter I, the use of advanced oxidation processes for the removal of dyes is increasingly sponsored for their complete ability in the mineralization of these compounds. In this section it is reported the results about the application of heterogeneous photocatalysis and heterogeneous photo-Fenton processes for the food industry wastewaters containing organic dyes. The relevant aspect is related to the use of catalysts doped with noble metals, or of catalysts active in the visible region of light characterized by the presence of organic phosphors able to exploit as best as possible the light source, capable of also degrade hardly biodegradable organic dyes.

Furthermore, the application of the heterogeneous photo-Fenton process for the mineralization of food dyes such as tartrazine and red allura gave interesting results especially for the use of a structured catalyst capable of operating at neutral pH.

VIII.1 Photocatalytic removal of Patent Blue V dye on Au-TiO_2 and Pt-TiO_2 catalysts

Heterogeneous photocatalysis has been studied in the decomposition of a wide range of undesirable chemical contaminants and it appears to be a feasible process for the degradation of dyes in water courses by using solar or artificial light illumination (Duta and Visa, 2015, Kordouli et al., 2015, Murcia et al., 2014, Vaiano et al., 2015b). TiO_2 is the semiconductor most widely studied and used in photocatalytic processes. In order to improve the photoactivity of this oxide, many strategies, such as sulfation and noble metal addition, have been employed (Murcia et al., 2014, Sannino et al., 2012a, Murcia et al., 2013). For the noble metal addition on TiO_2 surface, many methods have been employed, resulting in different metal particle sizes. The presence of metal nanoparticles decreases the electron-hole recombination, thus improving the TiO_2 efficiency in the photodegradation reactions. It has been reported that it is very important to control the synthesis parameters in order to obtain highly effective photocatalysts based on modified TiO_2.

Among the different considered food dyes, for the purpose of food industry wastewater treatment, it has been considered a dye not easily biodegradable, the Patent blue V (PB), a recognized dye in food industry. This compound is difficult to remove with conventional treatments such as adsorption or coagulation. As alternative the photocatalytic degradation of PB has been investigated and reported in literature by using TiO_2 in presence of different electron acceptors such as H_2O_2 or $KBrO_3$ (Saquib et al., 2008, Dalbhanjan et al., 2015) or using TiO_2-coated nonwoven fibers (Fernandez et al., 2009).

In this work it was evaluated the photodegradation of the PB over sulfated and metallized TiO_2 (Au-TiO_2 and Pt-TiO_2), considering the effect of the Au or Pt addition and the synthesis parameters over the efficiency of these materials in the PB removal.

The synthesis and the photocatalytic results have been reported.

VIII.1.1 Synthesis of the photocatalysts

VIII.1.1.1 Sulfated TiO_2

TiO_2 used as starting material was prepared by the hydrolysis of titanium tetraisopropoxide (Aldrich, 97%) in isopropanol solution (1.6 M) by the slow addition of distilled water (volume ratio isopropanol/water 1:1). Afterward, the generated precipitate was filtered, dried at 110°C overnight and calcined at 650 °C for 2 hours. Sulfation treatment was applied to TiO_2 before calcination; the TiO_2 powders were sulfated by immersion in H_2SO_4 aqueous solution 1 M for 1 hour and afterward calcinated at 650 ºC for 2 hours (S-TiO_2). Sulfation treatment was carried out for two reasons; on one hand, previous results have shown that sulfation stabilizes the anatase phase up to high temperatures and protect the catalyst from the loss of surface area by sintering (Colon et al., 2003). On the other hand, at the calcination temperature of 650 ºC, the elimination of sulfate groups promotes the creation of high number of oxygen vacancies, which have been reported as preferential sites for noble metal adsorption (Okazaki et al., 2004).

The S-TiO_2 powders were also modified by noble metal addition. Two different methods were employed: the photochemical deposition and chemical reduction method. The typical procedure is described as follows.

VIII.1.1.2 Photochemical deposition (PD) of gold and platinum over S-TiO_2

Gold (III) chloride trihydrate ($HAuCl_4.3H_2O$, Aldrich 99.9%) or Hexachloroplatinic acid (H_2PtCl_6, Aldrich 99.9%) were used as metal precursors for Au and Pt, respectively. Under an inert atmosphere (N_2), a suspension of S-TiO_2 in distilled water containing isopropanol (Merck 99.8%) which acts as sacrificial donor, was prepared. Then, the appropriate amount of metal precursor to obtain a nominal Pt or Au loading of 0.5 weight total (wt %) to TiO_2 was added. Final pH of the suspensions was 3. Photochemical deposition of Pt or Au was then performed by illuminating the suspensions with an Osram Ultra-Vitalux lamp (300W) with a sun-like radiation spectrum and a main emission line in the UVA range at 365 nm, using 15 and 120 minutes of photodeposition time. Light intensities on the TiO_2 surface were low intensity 0.15 W/m^2 (LI) and high intensity 140 W/m^2 (HI) for Pt and Au photochemical deposition, respectively.

After noble metal deposition, the powders were recovered by filtration and dried at 110 °C overnight. The metallized samples were called Au-TiO_2 and Pt-TiO_2.

VIII.1.1.3 Chemical reduction (CR) of gold over S-TiO_2

Chemical reduction of gold was carried out by using sodium citrate as both reducing and stabilizing agent following a procedure described in the literature (Kimling et al., 2006). Appropriate amount of $HAuCl_4$ for nominal content of deposited Au of 0.5 wt. % with respect to TiO_2 was dissolved in distilled water (1 mg $HAuCl_4$/10 mL water). Then, suspensions of the different TiO_2 samples (1 g) in sodium citrate solutions (0.2 g/10 mL distilled water) were added. The final suspensions were heated to reflux for 1 h under N_2 atmosphere to avoid gold re-oxidation. After this time, the powders were washed, filtered and dried at 110 °C overnight.

All the photocatalysts synthesized are enlisted in Table VI.1a and b.

Table VIII.1a *Summary of the characterization results*

Catalyst	Method for metal addition	Light intensity (W/m^2)	Deposition time (min)	S_{BET} (m^2/g)	Metal particle size (nm)
S-TiO_2	-	-	-	58	-
Au-TiO_2	Chemical reduction (CR)	-	-	52	0.39
Au-TiO_2	Photochemical Deposition (PD)	0.15 (LI)*	15	57	0.29
			20	58	0.32
		140 (HI)*	15	54	30-40
			20	53	40-50
Pt-TiO_2	Photochemical Deposition (PD)	140 (HI)*	15	53	2-3
			20	59	4-6

Table VIII.1b *Summary of the characterization results*

Catalyst	$D_{ANATASE}$ (nm)	Band gap (eV)	wt% metal content**	Binding Energy Ti $2p_{3/2}$	O 1s
S-TiO_2		3.2	-	458.5	529.8
Au-TiO_2 (CR)	-	3.22	0.39	458.3	529.7
Au-TiO_2 (PD)	0.15 (LI)*	3.19	0.29	459.0	530.3
		3.24	0.32	458.5	529.8
	140 (HI)*	3.20	0.36	459.6	530.8
		3.21	0.45	458.8	530.1
Pt-TiO_2 (PD)	140 (HI)*	2.80	0.26	458.5	529.9
		2.80	0.41	458.4	529.6

*(LI) = Low intensity and (HI) = High intensity- **: XRF

VIII.1.2 Characterization of the photocatalysts

In order to correlate the physicochemical properties of the catalysts with their photocatalytic activity, all the materials were widely characterized by using different techniques and the results obtained are summarized in Table 1 and presented below.

VIII.1.2.1 N_2 physisorption

The specific surface areas (S_{BET}) of the photocatalysts analyzed are listed in Table 1. As it can be observed, the BET surface area of S-TiO_2 is 58 m^2/g. After the metal addition a slight decrease of the S_{BET} value was detected, probably due to pore blocking by metal nanoparticles homogeneously distributed on surface. As it can be seen in Table 1, this effect is much more noticeable in the catalysts prepared by chemical reduction and also in the materials prepared by photochemical deposition method using 15 minutes of deposition time.

VIII.1.2.2 Microscopic analysis

In order to obtain information about the metal deposits size and dispersion, all the samples modified by gold or platinum addition were studied by SEM. Figure 1 shows representative SEM images of the metallized samples prepared by chemical reduction (CR) and photochemical deposition method (PD), using 140 W/m^2 of light intensity (HI) and different deposition times (15 and 120 min). Images of the samples prepared using low intensity (LI = 0.15 W/m^2) are not provided for the sake of brevity. In all the samples, gold or platinum particles can be seen as white spots placed over the larger TiO_2 particles. As it can be observed, there are significant differences in particles sizes and morphology between samples prepared by PD or by CR. Thus, in the catalyst Au-TiO_2 prepared by CR (Figure 1C), the gold particles are more homogeneously distributed on TiO_2 surface than the gold particles observed in the samples prepared by PD (Figure 1A and B). The higher number of gold particles covering the TiO_2 surface can explain the lowest S_{BET} value observed in the sample prepared by CR (Table 1).

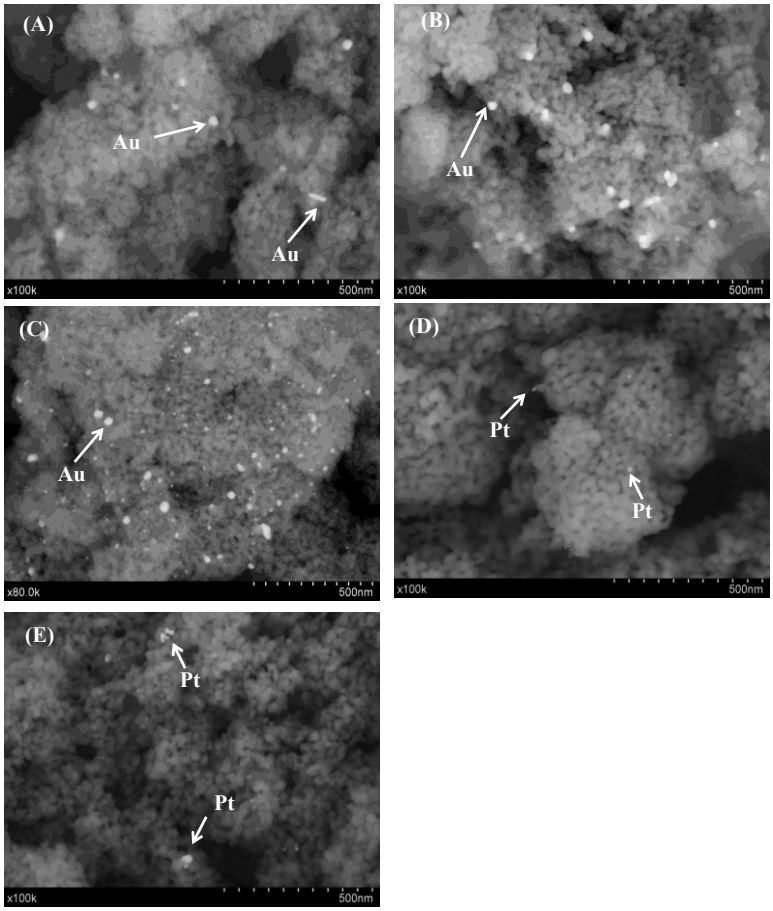

Figure VIII.1. *SEM images of photocatalysts synthesized using different methods: photodeposition (PD) and chemical reduction (CR). (A) Au-TiO_2(PD-HI)15min; (B) Au-TiO_2(PD-HI)120min; (C) Au-TiO_2(CR); (D) Pt-TiO_2(PD-HI)15min and (E) Pt-TiO_2(PD-HI)120min.*

It was also possible to observe that the platinum particles are smaller than the gold particles in the metallized samples prepared by PD, and in all the cases the number and size of the metal particles increase with the deposition time from 15 to 120 min. The average particle size of the noble metal (Au or Pt) particles, obtained by TEM analysis is presented in Table 1; selected TEM images of the samples metallized prepared by photochemical deposition method, using the highest light intensity and different deposition times are presented in Figure 2.

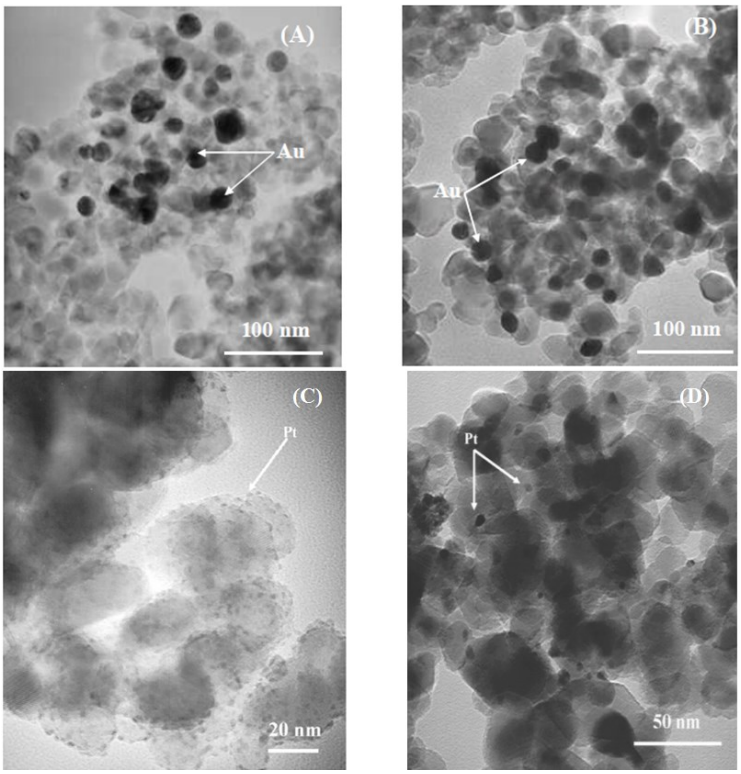

Figure VIII.2. *TEM images of metallized S-TiO_2. (A) and (B) Au-TiO_2 catalysts prepared by PD method using 140 W/m^2 of light intensity and different deposition time 15 and 120 min, respectively. (C) and (D) Pt-TiO_2 samples prepared by photodeposition method and different deposition time 15 and 120 min, respectively.*

In these images it is possible to observe that gold particles with higher sizes are heterogeneously distributed and partially covering the TiO_2 surface; the number and the size of the gold particles increases with the deposition time. On the contrary, in the case of the Pt-TiO_2 sample, platinum particles with the lowest sizes are homogeneously covering the titania surface.

VIII.1.2.3. X-ray diffraction (XRD)

XRD was used to analyze the effect of the metal addition on the crystallite structure and phase composition of sulfated TiO_2. Figure 3 shows the XRD patterns of the sulfated TiO_2 and the metallized catalysts prepared by CR and PD using high light intensity and 120 min of deposition time.

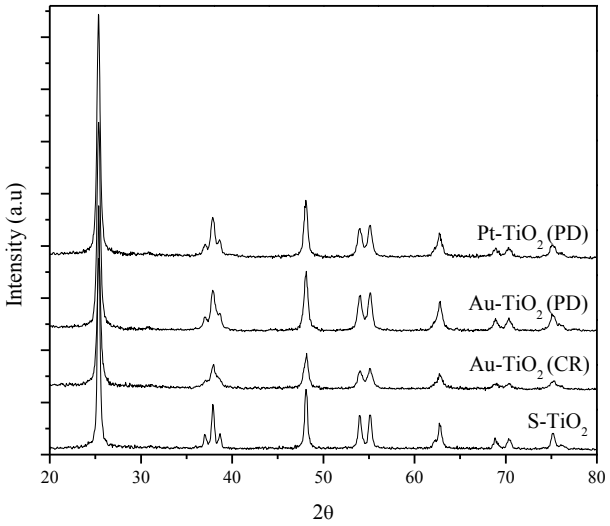

Figure VIII.3. *XRD patterns for TiO_2 and M-TiO_2 photocatalysts (M=Au or Pt) prepared by chemical reduction (CR) and photochemical deposition (PD) using 120 min of deposition time.*

In all the analyzed samples, only anatase peaks (25.3°, 38.0°, 48.0° and 54.7° 2θ) were detected. The stabilization of anatase phase of the TiO_2 by the sulfation pretreatment can be noticed here, as no traces of rutile were found even after the high calcination temperature used during the preparation of the catalysts (Colon et al., 2003).

The anatase crystallite size in the different samples was determined from the broadening of corresponding X-ray diffraction peaks by using Scherrer equation and these data are listed in Table 1. As it can be observed, for sulfated samples the anatase crystallite size was about 20 nm, any important influence of the synthesis parameters over this value was observed. No peaks ascribed to platinum or gold species were detected in the XRD patterns of the metallized samples; surely due to the low metal content in the samples or due to the detection limit of this technique.

XRD patterns of the catalysts prepared by PD under low light intensity are not included for the sake of brevity, but the diffraction peaks are similar than the observed for the samples obtained at high light intensity.

VIII.1.2.4 UV–Vis diffuse reflectance spectra (UV–Vis DR)

The UV-Vis DR spectra of selected samples are shown in Figure 4. The typical band edge of the TiO_2 semiconductor was observed at around of 370 nm for all the samples. Gold or platinum addition did not alter substantially the absorption properties of the samples; however, a slight increase of absorbance throughout the visible range of the spectrum was observed due to

the purple or grey color of the metallized materials, respectively. In the Au-TiO_2 catalysts, the surface plasmon resonance band of metallic gold can be observed; this characteristic plasmon is located around 550 nm. It is known that for colloidal gold nanoparticles there is a strong dependence between particle size and plasmon bandwidth and position (Min et al., 2009, Link and El-Sayed, 1999, Hidalgo et al., 2009).

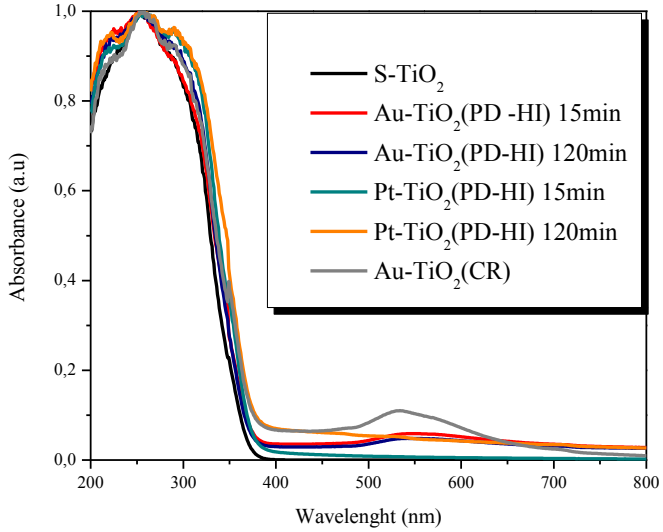

Figure VIII.4. *UV-Vis DRS spectra for the investigated photocatalysts*

From the UV–Vis DR spectra, band gaps energies were calculated and the obtained results are reported in Table 1, being 3.20 eV for the S-TiO_2 sample. Any important modification of this value was observed after gold addition. A slight decrease of the band gap value was observed in the Pt-TiO_2 samples.

VIII.1.2.5. X-ray fluorescence

The real gold and platinum content in the metallized samples was measured by XRF and the results are enlisted in Table 1. As it can be seen, these values are under the nominal metal content used to prepare these materials (0.5 wt.%), thus indicating an incomplete reduction of the metal precursor on TiO_2 surface during the synthesis process. However, it was observed that the amount of deposited gold or platinum increases with the deposition time and with the light intensity in the materials prepared by PD method.

XRF analysis revealed that a certain amount of S and Cl^- species remained on the solids after preparation. The sulfur content in the samples

was under 0.16 wt %; the Cl^- content in all the platinized samples was under 0.10 wt %; this content comes from the gold and platinum precursors.

VIII.1.2.6 X-ray photoelectron spectroscopy (XPS)

XPS analyzes were also carried out and the binding energies (BE) of the main XPS peaks (Ti $2p_{3/2}$ and O 1s) for the different samples are enlisted in Table 1. The Ti $2p_{3/2}$ core level spectra were similar for all the analyzed samples with peaks centered at 458.4±0.1 eV, corresponding to Ti^{4+} in the TiO_2 network as the main component. In the O 1s region, a peak located at a binding energy of 529.8±0.2 eV was registered in all the samples. This peak is assigned to lattice oxygen in TiO_2, with a broad shoulder at higher binding energies ascribed to oxygen in surface hydroxyl groups.

From the XPS data, O/Ti ratios were also calculated and it was found that for S-TiO_2 sample the O/Ti value was 1.70 indicating the presence of a certain amount oxygen vacancies on the surface of this oxide, in agreement with previous reported results (Colon et al., 2003) that showed the development of oxygen vacancies on TiO_2 surfaces due to the sulfation process. The ratios O/Ti for the metallized samples were higher than the observed in the S-TiO_2 sample, suggesting that the oxygen vacancies are partially annihilated during the Pt or Au photochemical deposition over the sulfated oxide. The atomic percentage of metal was calculated by XPS and it was found to be < 0.2% in all the catalysts; in correlation with the XRF results, the metal atomic content increases with the deposition time and also with the light intensity used in the catalysts preparation.

VIII.1.3 Photocatalytic activity results

VIII.1.3.1 Patent blue V photodegradation on Au-TiO_2

The efficiency of the photocatalysts prepared and characterized was evaluated in the PB removal. In order to verify that the target dye was converted in a heterogeneous photocatalytic process, blank experiments were performed. In particular, tests carried out in dark conditions did not evidence any oxidation activity. Moreover, additional control tests were carried out in the presence of PB dye and irradiating the photoreactor with UV-LEDs (photolysis reaction) and in the absence of photocatalyst. Also in this case, no degradation of the target dye was detected.

Figure 5 shows the evolution of the discoloration of the PB as a function of run time, obtained over Au-TiO_2 photocatalysts in comparison with S-TiO_2. In dark conditions a decrease of PB concentration was observed during the first 30 minutes of the test and it was almost unchanged up to 120 minutes, indicating that the adsorption equilibrium of dye on catalyst surface

was reached. After the dark period, the solution was irradiated with UV light and the reaction started to occur. As it can be observed, an important

decrease of the dye concentration was obtained in presence of Au on titania surface. The highest discoloration was observed on the catalyst Au-TiO_2 prepared by photochemical deposition method, using high light intensity (140 W/m^2) and 15 minutes of deposition time.

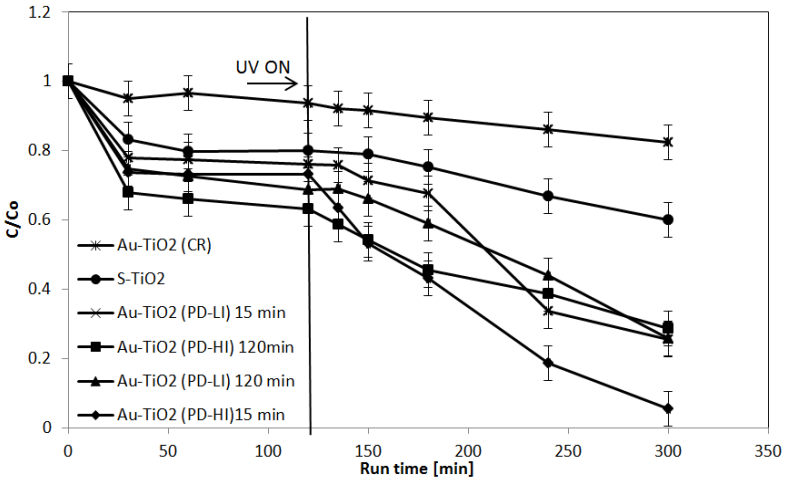

Figure VIII.5. *Discoloration of the Patent blue V as a function of run time over the photocatalysts analyzed; Patent blue V initial concentration: 7 mg/L; catalyst dosage: 3 g/L.*

The evaluation of the TOC during the run time was also analyzed and the obtained results are represented in Figure 6. In this case it was also observed that the highest mineralization of the dye was achieved on the sample Au-TiO_2(PD-HI)15 min. In particular, with this catalyst, a discoloration and a TOC removal (evaluated starting from the irradiation time) of 93 and 67% respectively, were obtained after 180 minutes of UV irradiation. These values are higher than that obtained on S-TiO_2 (discoloration and TOC removal of about 25% and 3%, respectively).

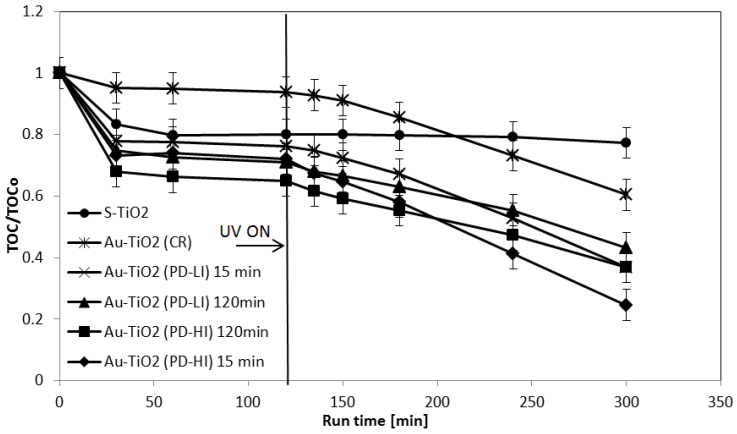

Figure VIII.6. *Total Organic Carbon (TOC) removal as a function of run time over the catalysts analyzed. Patent Blue V initial concentration: 7 mg/L; catalyst dosage: 3 g/L.*

The percentage of discoloration and mineralization of the PB evaluated starting from the irradiation time is summarized in Table 2.

In the case of the Au-TiO_2 samples prepared with the highest deposition time (120 min), the decrease of the photocatalytic activity could be due to the big cluster of gold particles which can act as a recombination centers, thus reducing the effectiveness of these samples (Murcia et al., 2015a). The best photocatalytic behavior was observed over the catalyst Au-TiO_2 prepared by photochemical deposition method, using high light intensity (140 W/m^2) and 15 minutes of deposition time. It could be due to a combined effect between two factors: (i) the presence of the gold nanoparticles, which act as a sink for the electrons, retarding the electron-hole recombination, thus leading to an improvement of the TiO_2 photoefficiency; (ii) in this catalyst, the gold nanoparticles are heterogeneously distributed on TiO_2 surface. The lower number of the gold particles allows to the dye molecule to be adsorbed with the TiO_2 surface. In this case the azo or sulfate groups in the molecule of dye can act as electron donor (Murcia et al., 2015a), leading to a better interaction between substrate and catalyst surface, thus increasing the dye discoloration efficiency.

In the case of the catalysts with the lowest metal particle sizes, such as Au-TiO_2 prepared by chemical reduction or Pt-TiO_2 catalysts, many particles with low metal particle sizes could covering the TiO_2 surface, thus leading to difficult adsorption of the dye.

Finally, it is important to note that the lowest PB discoloration was obtained over the catalyst Au-TiO_2 prepared by CR. The discoloration obtained over this catalyst is even lower than the obtained with the starting S-TiO_2. This behavior could be related with the presence of remaining

material on catalyst surface coming from the preparation procedure, mainly due to the sodium citrate used as reducing agent. Thus the remaining material on surface could have a detrimental effect over effectiveness of the Au-TiO_2(CR) catalyst on the dye photodegradation. These results can suggest that photodeposition is a suitable method to prepare active and efficient catalysts for PB photocatalytic removal.

Table VIII.2 *Percentage of discoloration and mineralization of the Patent blue V; initial dye concentration: 7 mg/L; catalyst dosage: 3 g/L.*

Catalyst	Discoloration (%)	Mineralization (%)
S-TiO_2	25	3
Au-TiO_2(CR)	12%	35%
Au-TiO_2(PD-LI)15min	67%	51%
Au-TiO_2(PD-LI)120min	63%	37%
Au-TiO_2(PD-HI)15min	93%	66%
Au-TiO_2(PD-HI)120min	55%	29%
Pt-TiO_2(PD-HI)15min	74%	45%
Pt-TiO_2(PD-HI)120min	85%	44%

VIII.1.3.2 Patent blue V photodegradation on Au-TiO_2 – Effect of the initial dye concentration

Taking into account that the best photocatalytic behavior in the PB removal was obtained on Au-TiO_2(PD-HI)15min catalyst, the effectiveness of this catalyst in the degradation of different initial concentrations (3, 7 and 12 mg/L) of the dye was evaluated.

Figure 7, shows the dye discoloration on the Au-TiO_2(PD-HI)15 min catalyst. After 120 minutes of dark adsorption, the photocatalytic test started. After 180 minutes of irradiation, the final value of the discoloration was 100% in the case of 3 mg/L, 92% in the case of 7 mg/L and 20% in the case of 12 mg/L PB initial concentration.

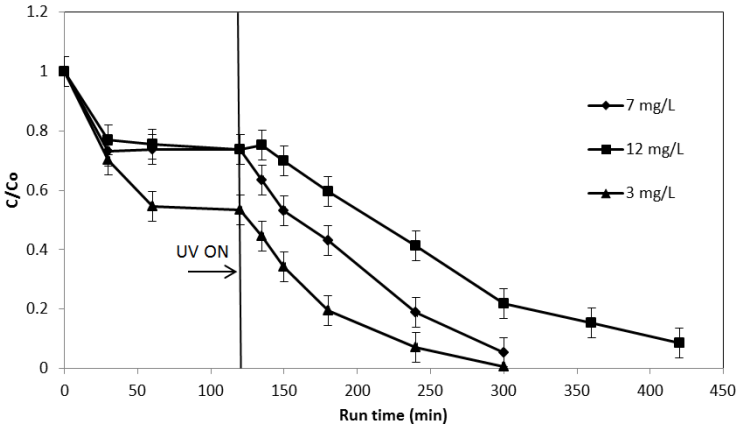

Figure VIII.7. *Patent blue V discoloration over Au-TiO_2(PD-HI)15min catayst, varying the initial concentration of the dye; catalyst dosage: 3 g/L*

For the interpretation of the effect of the dye initial concentration on the photodegradation performances, the Langmuir-Hinshelwood model has been used (Sannino et al., 2013b).

Considering that the adsorption equilibrium was reached after 120 min of run time, the behaviour of the amount of PB adsorbed on catalyst as a function of the dye initial concentration (C_0) is similar to a Langmuir adsorption isotherm (Figure 8 insert). Thus for the evaluation of PB adsorption on the active surface, the following equation was used:

$$C^* = \frac{b \cdot C_0^*}{1 + b \cdot C_0^*} \qquad \text{Eq. (1)}$$

Where C* is the amount of PB adsorbed on catalyst (g_{dye}/g_{cat}); C_0^* is the concentration of PB in solution after dark adsorption (mg/L); b is the adsorption constant (L/mg).

The Langmuir isotherm can be rearranged to give:

$$\frac{C_0^*}{C^*} = \frac{1}{b \cdot C_m} + \frac{1}{C_m} C_0^* \qquad \text{Eq. (2)}$$

Accordingly, a plot of C_0^*/C^* as a function of C_0^* produces a straight line with slope = $1/C_m$ and intercept = $1/bC_m$ (Figure 8). C_m is the maximum absorbable value of C*.

The value of b was calculated from Eq. (2) utilizing the data reported in Figure 8 and it was equal to 0.32 (L/mg).

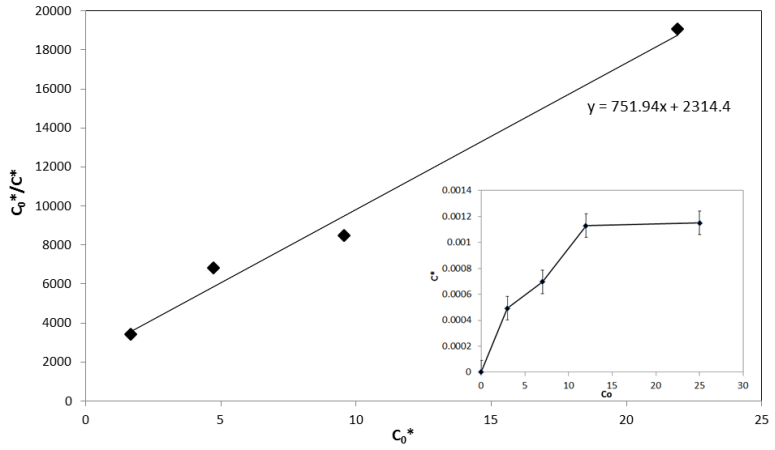

***Figure VIII.8**. Evaluation of Patent blue V adsorption constant on Au-TiO_2(PD-HI)15min catalyst; catalyst dosage: 3 g/L.*

With this value it was evaluated the apparent kinetic constant for all the initial concentration of dye, using the following equation:

$$\frac{dC(t)}{dt} = -K \cdot \frac{b \cdot C(t)}{1 + b \cdot C(t)} \cdot a \qquad \text{Eq. (3)}$$

Where C(t) is the PB concentration (mg/L) as a function of irradiation time; *a* is the e catalyst dosage (g_{cat}/L) and K is the kinetic constant (mg/(g min)).

The initial condition of Eq.(3) is:

t =0 $C(t)=C_0^*$

Eq. (3) together with the initial condition was solved with Euler iterative method to identify the constants K by fitting the experimental data as a function of irradiation time for the initial dye concentration of 7 mg/L. The fitting procedure was realized by using the least squares approach obtaining the value of K: 0.02 [mg/(g min)]. After obtaining the value of K, the experimental data obtained with different initial dye concentrations were fitted to analyze the ability of the model to predict the experimental data at 3 and 12 mg/L initial PB concentration. The obtained results are shown in Figure 9.

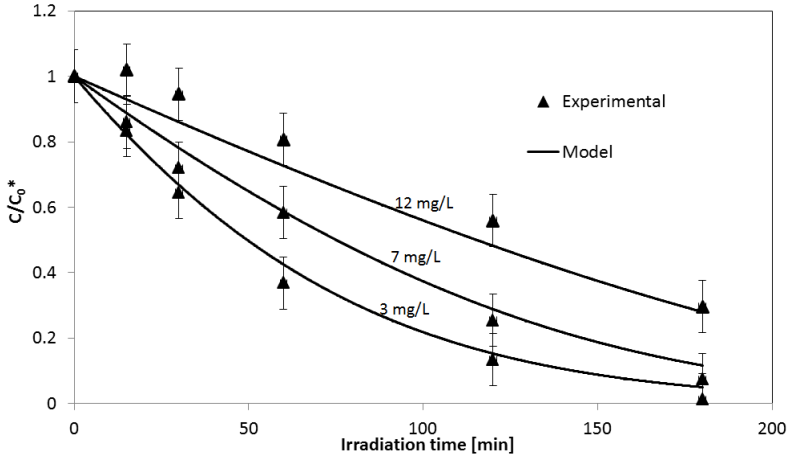

***Figure VIII.9**. Experimental and predicted data as a function of Patent blue V initial concentration on Au-TiO_2(PD-HI)15min; catalyst dosage: 3 g/L.*

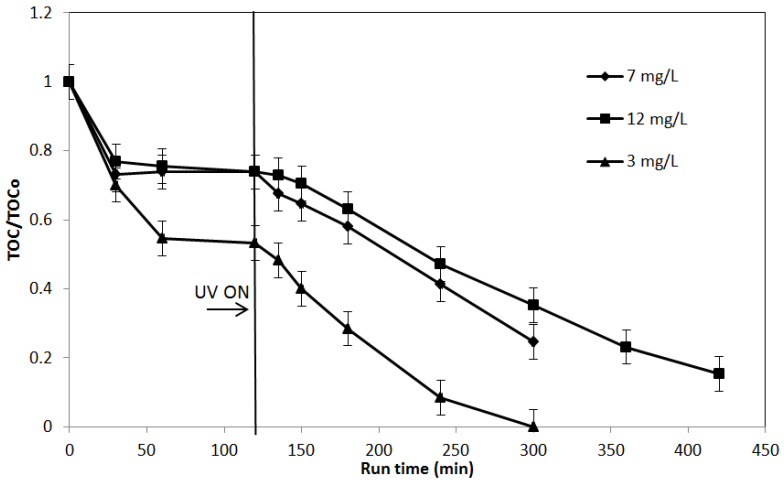

***Figure VIII.10.** Total Organic Carbon (TOC) removal over the Au-TiO_2(PD-HI)15min catayst, varying the initial concentration of the dye; catalyst dosage: 3 g/L*

The calculated values are in good agreement with all the experimental data. It is important to note that also for the higher initial dye concentration (12 mg/L), this system is able to predict the discoloration trend with a single value of kinetic constant. Thus the photocatalytic activity is not dependent by the increase of the intensity of the color meaning that the path length of photons inside the solution didn't decrease allowing to obtain in an effective way also the mineralization of the dye (Figure 10).

VIII.1.3.3 Patent blue V photodegradation on Au-TiO_2 – Effect of the catalyst dosage

The effect of the catalyst dosage over the effectiveness of the sample Au-TiO_2(PD-HI)15min was evaluated in the range 3-12 g/L and the results of discoloration and TOC removal are presented in Figures 11 and 12, respectively.

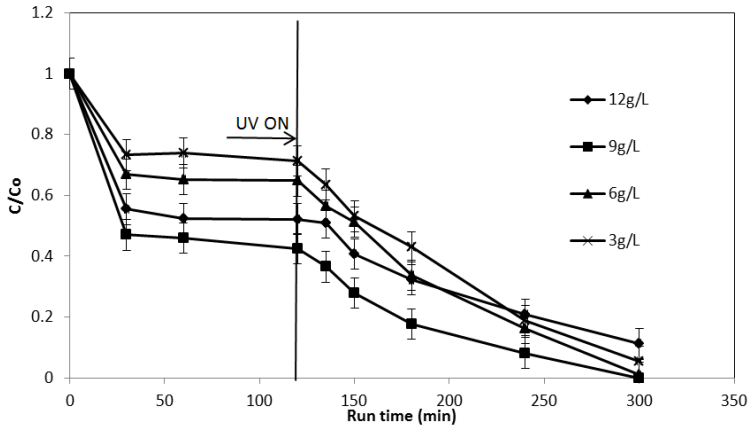

Figure VIII.11. *Patent blue V discoloration over the Au-TiO_2(PD-HI)15min catayst, varying the dosage of the photocatalyst (g/L); Patent blue V initial concentration: 7 mg/L.*

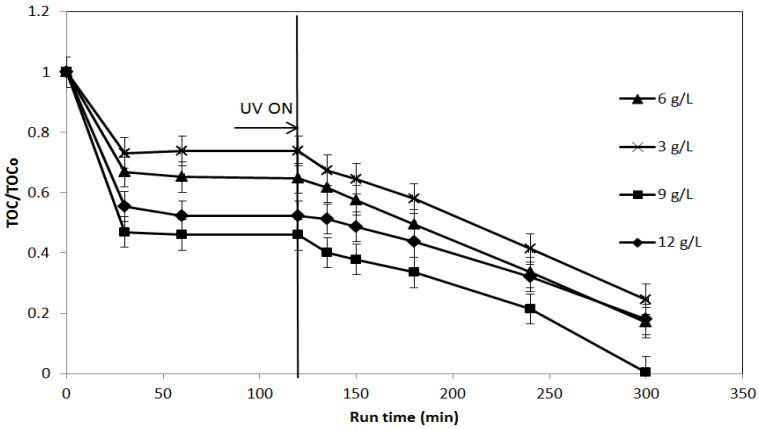

Figure VIII.12. *Total Organic Carbon (TOC) removal over the Au-TiO_2(PD-HI)15min catayst, varying the dosage of the photocatalyst (g/L); Patent Blue V initial concentration: 7 mg/L.*

After these experiments, it is possible to confirm that the best dosage of catalyst is 9 g/L, obtaining the highest discoloration and mineralization of PB. Photocatalytic efficiency increased as catalyst loading was increased up to 9 g/L. When the load of catalyst was increased from 9 to 12 g/L, the discoloration and the mineralization of the dye decreased. Possibly, the increase in the catalyst dosage over the optimum value resulted in a decreased light penetration through the solution because of the increased opacity of the aqueous suspension (Vaiano et al., 2015a).

VIII.1.3.4 Patent blue V photodegradation on Pt-TiO_2

The effectiveness of the platinized samples in the dye photodegradation was also evaluated. Figure 13 shows the evolution of the discoloration of the PB as a function of run time, obtained over Pt-TiO_2 photocatalysts in comparison with S-TiO_2.

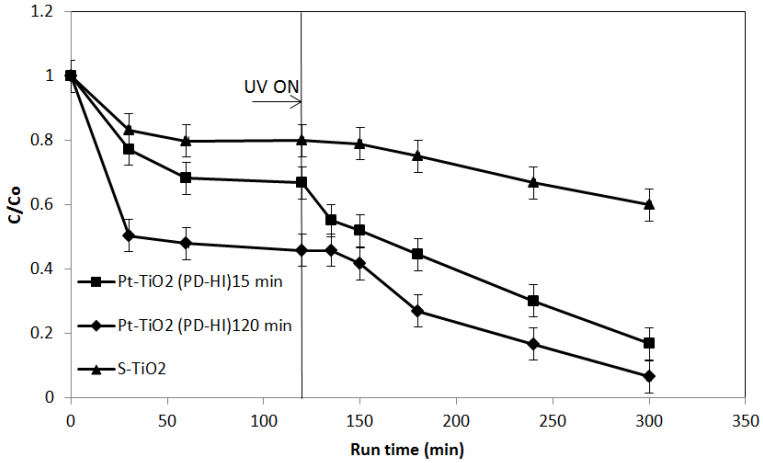

Figure VIII.13. *Patent blue V discoloration over the Pt-TiO_2 photocatalyst prepared with 140 W/m^2 of light intensity and different deposition time (15 and 120 min); Patent blue V initial concentration: 7 mg/L; catalyst dosage: 3 g/L.*

Also with these catalysts, in dark conditions a decrease of PB concentration was observed during the first 30 minutes of the test and it was almost unchanged up to 120 minutes. After the dark period, the solution was irradiated with UV light. During the irradiation time, it can be observed an increase of the dye degradation. The best discoloration (85%) and dye mineralization (44%) (Figure 14) was obtained over the catalyst Pt-TiO_2 prepared by photochemical deposition method and using 120 minutes of deposition time in the synthesis. These results may be due to the higher Pt content of the photocatalyst prepared with the highest deposition time.

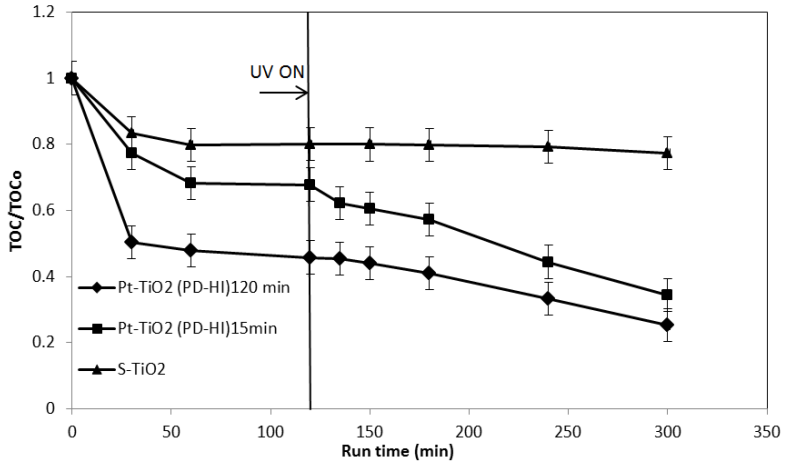

Figure VIII.14. *Total Organic Carbon (TOC) removal over the Pt-TiO_2 photocatalyst prepared with 140 W/m^2 of light intensity and different deposition time (15 and 120 min); Patent Blue V initial concentration: 7 mg/L; catalyst dosage: 3 g/L.*

VIII.1.3.5 Patent blue V photodegradation - Effect of the kind of noble metal (Au or Pt)

A comparison between the results obtained on the best Au-TiO_2 and Pt-TiO_2 photocatalysts is shown in Figure 15. As it can be observed, the best performances are obtained with the Au-TiO_2 catalyst since the TOC removal and discoloration rate under UV irradiation are higher than that obtained for Pt-TiO_2 catalyst.

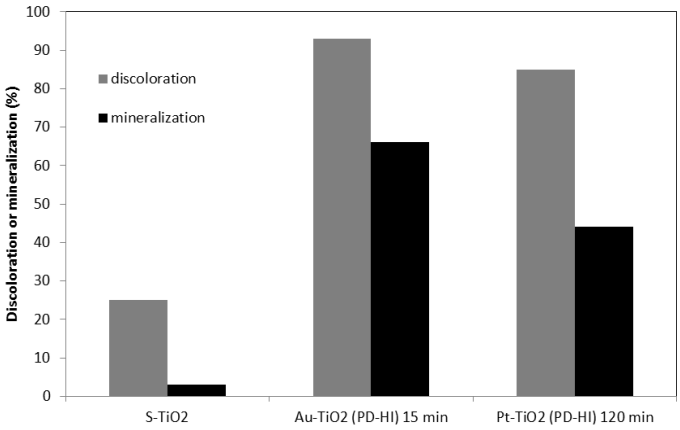

Figure VIII.15. *Comparison of the Patent blue V discoloration and mineralization over the S-TiO_2 and the most effective M-TiO_2 photocatalysts; Patent blue V initial concentration: 7 mg/L; catalyst dosage: 3 g/L.*

From the results reported in Table 1, it is possible to note that the catalyst Pt-TiO_2(PD-HI)120min has Pt particle size comprised in the range 4-6 nm, while the catalyst Au-TiO_2(PD-HI)15min has Au particle size in the range of 30-40 nm, so one would expect that the catalyst Pt-TiO_2(PD-HI)120 min presents a better photocatalytic activity. From the experimental results, instead, it is noted that the best photocatalytic efficiency is obtained with the catalyst in the presence of Au. In fact, the literature results reports that Au-TiO_2 shows higher catalytic activity than Pt (Maicu et al., 2011). Considering that the noble metals act as a mediator in the vectorial electron-transfer process, their Fermi energy levels are supposed to affect the interfacial charge transfer and thus the charge separation (Hudson, 1998). In general, the higher Fermi level of the noble metal leads to the better the photocatalytic activity (Halas and Durakiewicz, 1998b).

In this context, it was found that, for Fermi level, the order of noble metals is of Au > Pt (Shen et al., 2010b), explaining in this way, the better photocatalytic activity of Au-TiO_2 with respect to Pt-TiO_2 catalyst.

VIII.1.3.6 Recyclability of Au-TiO_2 photocatalyst

Recyclability is one of the most important factors in catalysis research (Vaiano et al., 2015d, Vaiano et al., 2014a). To confirm the recyclability of Au-TiO_2(PD-HI)15min sample, the photocatalytic degradation of PB was repeated up to four cycles (Figure 16). The reduction of discoloration and mineralization percentage was as low as 1-2% in 60 min of irradiation time. So, these results evidenced the stability of the photocatalyst and the reproducibility of the process in the PB degradation.

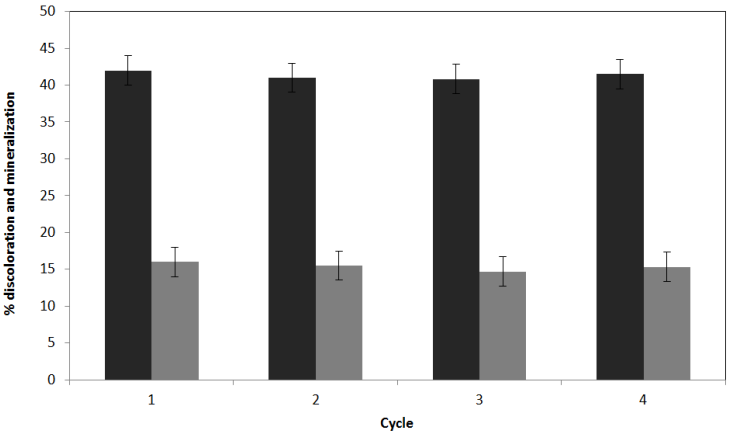

***Figure VIII.16**. Evaluation of Patent blue V discoloration and mineralization after 60 minutes of irradiation on Au-TiO_2(PD-HI)15min catalyst for different cycles; Patent blue V initial concentration: 4.7 mg/L; catalyst dosage: 3 g/L.*

From these experimental results it was possible to observe that the presence of Au or Pt on TiO_2 enhances the PB photodegradation and it was also found that metal distribution on TiO_2 and noble metal particle size are important factors influencing the dye degradation. There are significant differences in particles sizes and morphology between samples prepared by PD or by CR. In fact, for the Au-TiO_2 catalyst prepared by CR, the gold particles are more homogeneously distributed on TiO_2 surface than that observed in the samples prepared by PD. This causes a reduction in the value of the specific surface area for the sample prepared by CR. The highest dye degradation was obtained over the Au-TiO_2 catalyst prepared by PD method, using high light intensity and 15 minutes of deposition time during the synthesis.

In this catalyst, the Au nanoparticles are heterogeneously distributed and present in lower number on TiO_2 surface, allows to the dye molecule to have a best contact with the TiO_2 surface.

For Pt-TiO_2 catalysts the best discoloration and dye mineralization were obtained over the catalyst prepared by photochemical deposition method and using 120 minutes of deposition time in the synthesis. These results may be due to the higher Pt content of the photocatalyst prepared with the highest deposition time. Comparing the performance of the different catalysts, it can be concluded that the presence of the noble metal on the TiO_2 surface enhances the removal efficiency of the dye and that in particular the catalyst with gold showed a better efficiency of removal of PB.

VIII.2 Enhanced visible light photocatalytic activity by up-conversion phosphors modified N-doped TiO_2

Since the discovery of the semiconducting properties of TiO_2 (band-gap energy: 3.2 eV) (Fujishima and Zhang, 2006), great research efforts have been directed to a better exploitation of solar energy in photocatalysis. However, despite the great number of photocatalyst formulations proposed, most of them are only active under ultraviolet (UV) radiation, which is only a little fraction (5%) of solar light. To be of practical use for photocatalysis, the photo-response of the transition metal oxides should be within the visible light (43%) of the electromagnetic radiation reaching the planet's surface.

Therefore, an appropriate photocatalyst should work in the visible-light region (420 nm < λ < 800 nm) with a band gap of less than 3 eV.

Different approaches to improve the exploitation of sun light in photocatalytic processes have been proposed, especially oxide semiconductors doping (Khan et al., 2002) or titania photosensitization (Zhao et al., 2005). However, both approaches still suffer from disadvantages. For example, the introduction of impurities strongly affects the lifetime of the photogenerated $e^- h^+$ pair, and doping can also decrease the corrosion resistance of the material (Kisch and Macyk, 2002). Moreover, titania photosensitization with organic dyes still presents major limitations for applications in photocatalysis, due to the poor stability of the dye, which can undergo desorption, photolysis and oxidative degradation, and fast back electron transfer, resulting in low quantum yield for the photocatalytic reaction (Zhao et al., 2012).

Good visible photocatalytic activity results were found on N-doped TiO_2, both under visible irradiation and under solar simulated radiation in the removal of several pollutants such as emerging contaminants (Vaiano et al., 2015e, Senthilnathan and Philip, 2011) and bacteria inactivation (Rizzo et al., 2013, Liu et al., 2007). The photocatalytic performance of a semiconductor material is mainly limited by its intrinsic optical properties as the occurrence of the photocatalytic reaction requires an excitation source with energy equal or greater than the band gap of the semiconductor (Yang et al., 2014).

So, a main issue emerged, since the photocatalytic activity is related to the light propagation inside the overall volume of photoreactors (Hajaghazadeh et al., 2014). Therefore, since the improving of the photocatalytic reactivity is correlated to an efficient irradiation of the catalytic surface, the chance to get this improvement by modifying a photocatalyst with light carriers such as emitting phosphorescent particles (generally known as phosphors) has been successfully verified to confer additional radiation emission or to decrease the optical path of irradiation towards the photocatalyst (Ciambelli et al., 2011b, Wu et al., 2013). A

reasonable consequence of such an approach for the intensification of the photocatalytic process seems to be the use of up-conversion phosphors able to convert low-energy into high-energy photons (Wang and Liu, 2009). Few examples report the use of inorganic up-conversion phosphors in a photocatalytic system. To this purpose, active carbon supported undoped TiO_2 catalyst (C-TiO_2) was modified with Er^{3+}:$YAlO_3$ up-conversion phosphors that convert visible light into UV light able to photoexcite TiO_2 (Dong et al., 2015).

It is worthwhile to highlight that the photocatalytic tests were carried out with a visible light source that is not able to activate undoped TiO_2.

Moreover, in order to utilize visible light directly, C-TiO_2 catalyst was modified by blue, green and red colour emitting inorganic up-conversion phosphors through calcination assisted solvothermal method. The characterization data demonstrated that such photocatalysts could be excited by UV, visible and NIR light simultaneously (Wu et al., 2014). In this case, all the composites exhibited excellent induced rhodamine B degradation activity under the irradiation of 980 nm NIR laser, although uncoupled phosphors and C-TiO_2 showed no destruction ability (Wu et al., 2014). However, it is very important to underline that only 35 % of dye decolourization has been achieved after 5 h of irradiation (Wu et al., 2014) .

Recently, triplet−triplet annihilation up-conversion luminescence has emerged as an efficient process with anti-Stokes shift upon excitation by low power light intensity (Liu et al., 2012a). When compared to rare-earth up-conversion phosphors, the organic ones have several advantages including more intense absorption coefficient of sensitizer and higher quantum yield (Singh-Rachford and Castellano, 2010).

In the context of this PhD thesis, in view of the photocatalytic treatment of food industry wastewater containing dyes, a visible active N-doped TiO_2 photocatalyst was modified by organic up conversion phosphors and studied. The photocatalytic performances were evaluated in the degradation of a wide range of organic dyes in the presence of white LEDs visible light irradiation.

VIII.2.1 Synthesis of N-doped TiO_2 and blue-emissive up-conversion organic nanoparticles

N-doped TiO_2 (NdT) was prepared by hydrolysis reaction between titanium tetraisopropoxide and 30 wt% ammonia aqueous solution (Vaiano et al., 2014e). The preparation was carried out at 0° C and under stirring until the formation of a gel. The obtained gel was centrifuged and washed with distilled water and then placed in a furnace at 450° C for 30 min. The molar ratio N/Ti is 18.6, the same as in the catalyst formulation optimised in a previous work (Sacco et al., 2012, Rizzo et al., 2013). The characterization

of NdT catalyst, yellow in colour, by different analytical techniques has been reported in previous papers (Rizzo et al., 2013, Sacco et al., 2012). In particular, UV–vis spectra evidenced the ability of NdT to absorb visible light, as shown by the band gap value (2.5 eV) (Sacco et al., 2012).

Blue-emissive up-conversion organic nanoparticles (OP) (with a size ranging between 10 and 22 nm (Liu et al., 2012a)) were prepared following the method reported by Liu et al. (Liu et al., 2012a). In particular, 2.0 g of Pluronic F127, 1.0 mg of Pd complex octaethylporphyrin (PdOEP), and 10 mg of diphenylanthracene (DPA) were carefully solubilised in 20 mL of toluene. Toluene was evaporated from the homogeneous organic solution by means of a gently nitrogen flow until to obtain a pink solid residue (OP).

VIII.2.2 Preparation of NdT/OP catalyst

OP nanoparticles (0.4 g) were dissolved under magnetic stirring in 25 mL of HCl (0.85 mol L^{-1}) aqueous solution. First TEOS (2 mL), and then NdT (0.12 g) were added to the solution. The mixture was kept under stirring for 48 h at 25 °C and then centrifuged to recover the final NdT/OP solid phase. The nominal loading of NdT in the catalyst was 30 wt % (Sacco et al., 2015).

VIII.2.3 Characterization results of the samples

All the catalysts are listed in Table 1, together with nominal and measured NdT loading, specific surface area (BET), equivalent band-gap energy, and NdT average crystallites size.

Table VIII.1 *List of the catalysts and their characteristics*

Sample	TiO_2 nominal loading wt/%	TiO_2 measured loading (XRF) wt/%	Specific surface area m^2/g	TiO_2 average crystallites size nm	Equivalent Band gap energy eV
NdT	100	100	30	17	2.5
OP	-	-	1	-	-
NdT/OP	30	28	8	17	-

The specific surface area (SSA) of pure NdT, after calcination in air at 450°C, is 30 m^2/g, while a lower value (1 m^2/g) was found for OP. It is worthwhile to note that the SSA of NdT/OP catalyst increased up to 8 m^2/g after the deposition of NdT on the surface. The increase of surface area could be ascribed to the formation of NdT coating on the OP surface.

The total amount of titania in NdT/OP catalyst, determined by XRF, well agrees with the nominal TiO_2 amount, indicating that the preparation method is a suitable way to couple NdT with OP phosphors.

Crystal phase composition and crystallinity of the materials were determined by XRD (Fig.4). Anatase was the only TiO_2 crystalline phase detected for both NdT and NdT/OP. This result suggests that the preparation method used for obtaining the catalyst did not induce any change in the NdT crystalline structure, as also evidenced by the same value of crystallite size, evaluated at diffraction plane (101) through the Scherrer equation (Table 1). In the case of NdT/OP, a broad band with low intensity centered at $2\theta = 23°$ appears, attributed to silica obtained from the hydrolysis of TEOS (Yusof and Johan, 2014). The main diffraction signals of OP disappeared in NdT/OP pattern, due to the covering of OP surface by silica and NdT.

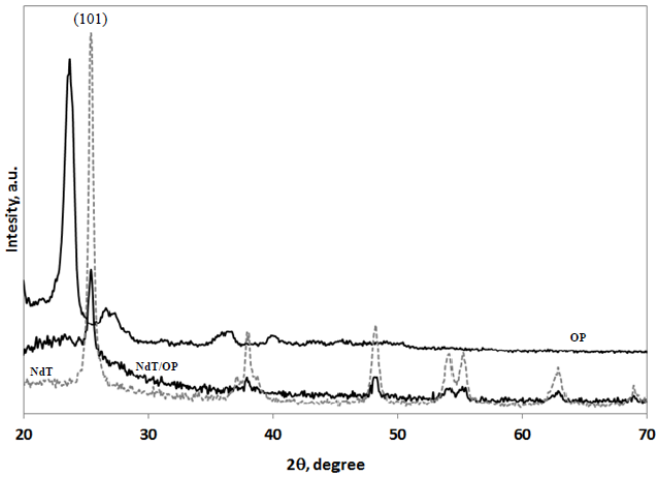

Figure VIII.17 *XRD analysis of NdT, OP and NdT/OP*

Raman spectra of NdT, OP and NdT/OP are shown in Fig. 5. In the range 100-1000 cm^{-1} (Fig. 5a), NdT showed bands at 144, 396, 514, 637 cm^{-1} and a weak shoulder at 195 cm^{-1}, due to the Raman-active fundamental modes of anatase (Ciambelli et al., 2008).

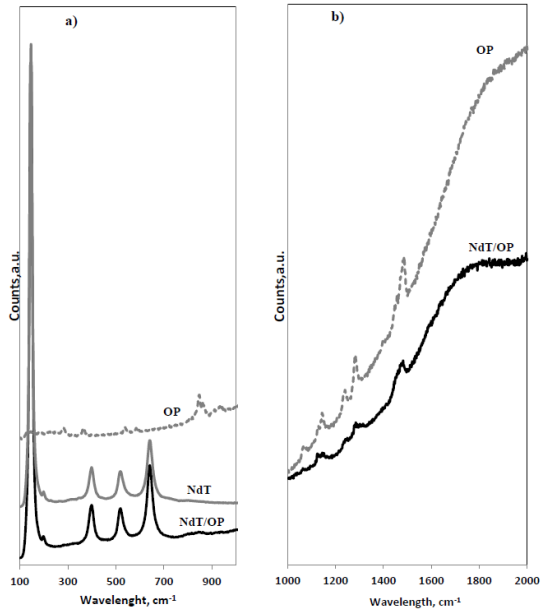

Figure VIII.18 *Raman spectra of the samples OP, NdT and NdT/OP in the range: a) 100-1000cm^{-1} and b) 1000-2000 cm^{-1}*

The NdT/OP catalyst also shows the presence of some bands of NdT without any shift in their positions. This indicates that the dispersion of NdT on the OP surface did not cause modification in the crystalline structure of NdT catalyst, as shown by XRD analysis.

In the range 100-1000 cm^{-1}, the spectrum of OP displayed signals at 281, 366, 536, 582, 847 and 926 cm^{-1}, less intensive than those ones of NdT. These signals disappear when NdT is supported on the surface of OP. On the contrary, in the range 1000-2000 cm^{-1} (Figure VIII.18b), the OP spectrum displayed signals at 1065, 1146, 1233, 1280, 1455 and 1486 cm^{-1}, that are present also in NdT/OP, but with lower intensity (Figure VIII.18b).

Figure VIII.19 depicts the photoluminescence (PL) spectrum of OP excited at 532 nm wavelength, accordingly with the spectral distribution of green LEDs employed to irradiate the photoreactor. A wide emission band between 400 and 500 nm was detected, with a blue peak centered at about 434 nm and two blunter peaks located at 418 and 450 nm, in good agreement with the data previously published (Liu et al., 2012a).

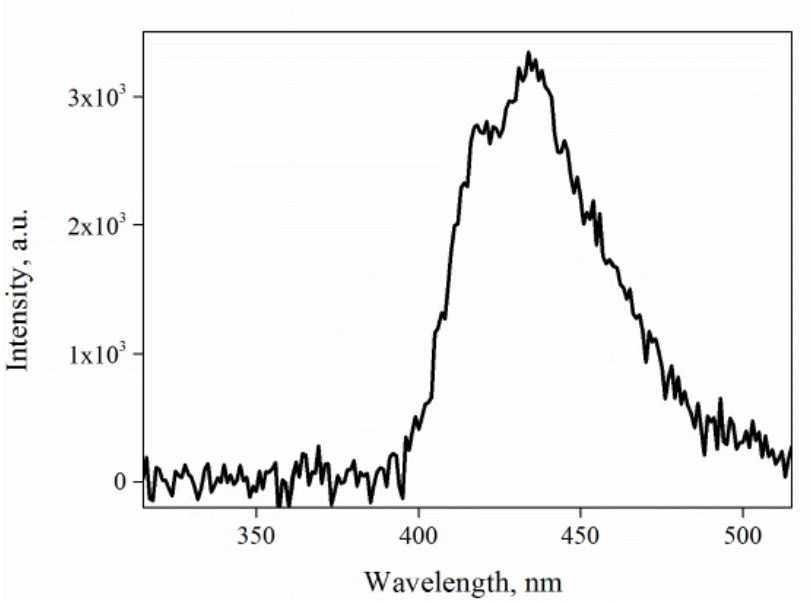

Figure VIII.19 *Photoluminescence spectrum of OP sample excited by a 532 nm source*

VIII.2.4 Photocatalytic activity tests with green LEDs as light source

To understand the influence of OP blue emission on NdT photoactivity, a photocatalytic test was carried out with MB dye solution (initial concentration of 10 mg/L) and green LEDs as light source. As reported in the Figure VIII.20 (insert), photocatalytic test on NdT showed that the MB concentration reached a maximum value, likely due to MB desorption from the NdT surface, and then decreased. After 240 min of irradiation, the MB degradation reached a value of about 3 % indicating that NdT has only a negligible photoactivity in the presence of green LEDs. It is worthwhile to consider that at these operating conditions no photolysis of MB occurred (not shown).

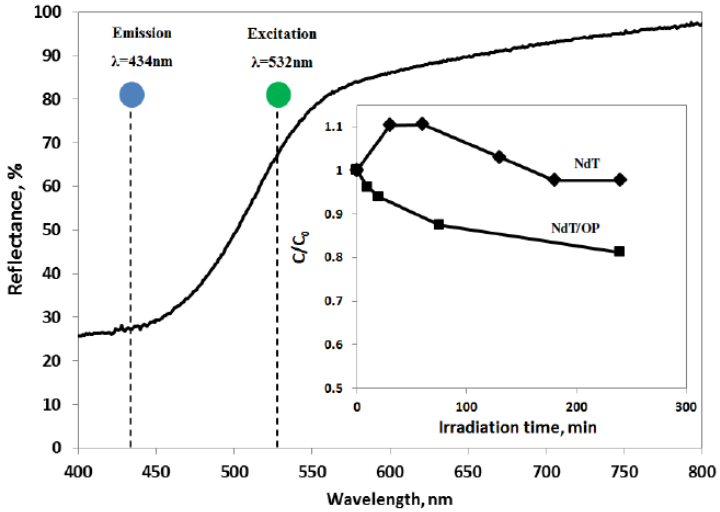

Figure VIII.20 *Reflectance spectrum of NdT sample and behavior of MB concentration as a function of irradiation time on NdT and NdT/OP composite; light source: green LEDs.*

A dramatically different trend was found for the NdT/OP catalyst, which showed MB degradation of about 20% after 4 hours of irradiation. These results clearly indicate that the photocatalytic activity under green light is only due to the presence of OP, that has up-conversion property and emits at 434 nm, wavelength able to photoexcite the nitrogen-doped titania deposited on OP surface, as also confirmed by the UV-vis DRS spectrum of NdT (Fig. 7). Indeed, the NdT catalyst evidenced a reflectance value of about 27% at excitation wavelength of 434 nm, corresponding to the blue emission of OP. On the contrary, with excitation wavelength of 532 nm (corresponding to the maximum emission of green LEDs), the NdT catalyst showed a very higher reflectance value with respect to that one at 434 nm. In summary, when NdT/OP is excited at 532 nm with green LEDs, OP nanoparticles emit at 434 nm, subsequently, the up-converted visible photons were absorbed by NdT leading to a better efficiency in MB photocatalytic degradation than NdT photocatalyst following a mechanism similar to that one found by Zhang and coworkers (Zhang et al., 2012).

VIII.2.5 Photocatalytic activity tests with white LEDs as light source

In order to verify that the dyes were converted in a heterogeneous photocatalytic process, blank experiments were performed. In particular, tests carried out in dark conditions with all the investigated dyes did not evidence any oxidation activity. Moreover, additional control tests were

carried out in the presence of each dye and irradiating the photoreactor with white LEDs (photolysis reaction) and in the absence of photocatalyst. Also in this case, no degradation of the target dye was detected.

The results of photocatalytic activity testing with NdT and NdT/OP for MB, CV, RhB, EBT, TRZ and RED are reported in Figs. VIII.21-23.

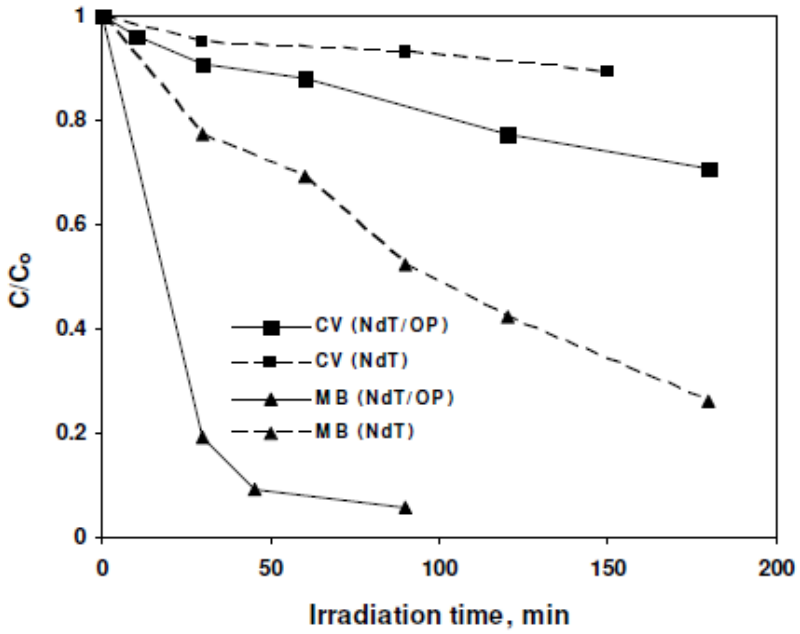

Figure VIII.21. *Photocatalytic decolourization of MB and CV on NdT and NdT/OP.; light source: white LEDs. This phenomenon increases the activity of the catalyst when it is irradiated with the white LEDs.*

For all the dyes a very strong increase of photocatalytic activity was found with NdT/OP with respect to NdT.

In particular, Figure VIII.21 gives a clear evidence of the dramatic enhancement of the photocatalytic decolourization rate of MB due to the presence of OP; NdT/OP allows to obtain 80 % MB degradation after only 30 min of irradiation time, while with the NdT only 30 % degradation was achieved after the same irradiation time.

Moreover, while the photocatalyst NdT did not allow to reach an effective degradation of CV dye, the NdT/OP catalyst improved the efficiency of the process reaching 30% degradation after 180 min of irradiation, much higher than that obtained with NdT (about 11%) after the same irradiation time.

The same trend was found for RhB, EBT, TRZ and RED dyes (Figure VIII.22 and VIII.23).

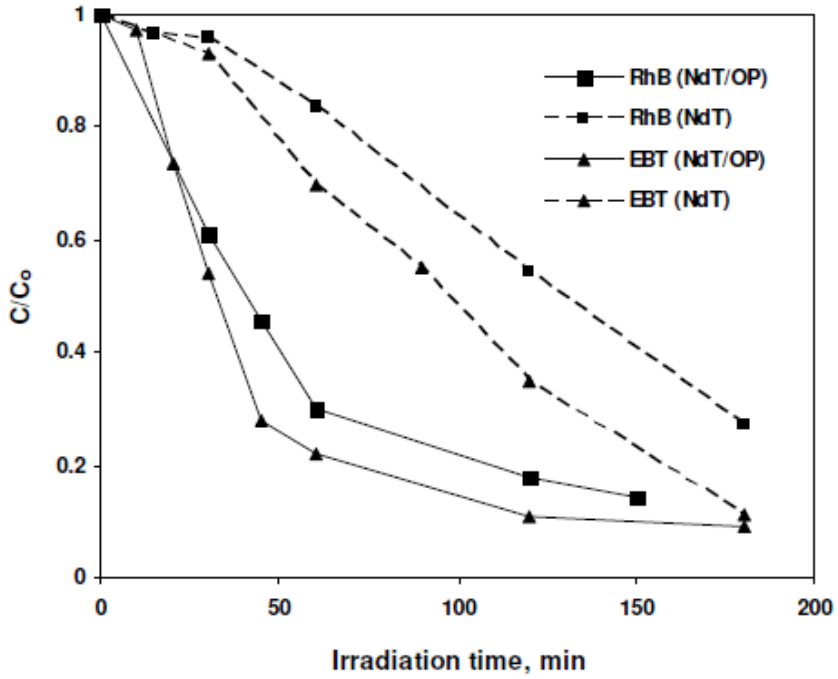

Figure VIII.22 *Photocatalytic decolourization of RhB and EBT on NdT and NdT/OP.; light source: white LEDs.*

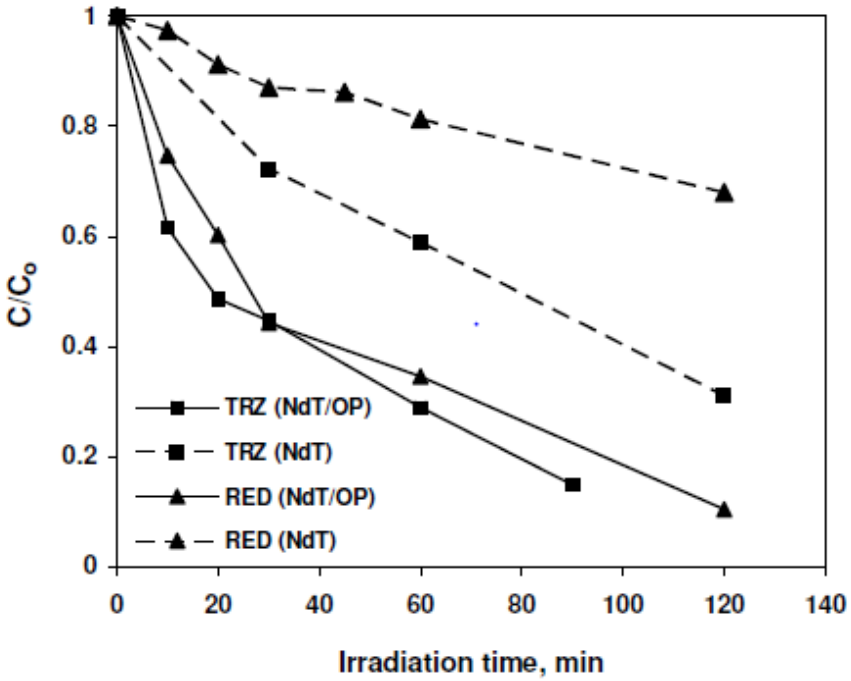

Figure VIII.23 *Photocatalytic decolourization of TRZ and RED on NdT and NdT/OP.; light source: white LEDs.*

The dramatic enhancement of photocatalytic activity obtained in this work is related to the specific formulation of the NdT/OP photocatalyst. It is possible to retain that NdT supported on the OP surface is excited both by the blue component of the emission spectrum of the white LEDs, and by the blue emission of the phosphors (OP), excited in turn by the green component emitted by the white LEDs. This phenomenon contributes to strongly enhance the NdT/OP photoactivity when it is irradiated with white LEDs.

Considering these results, it is possible to confirm that the photocatalytic activity of visible active N-doped TiO_2 (NdT) can be strongly enhanced when it is promoted by the presence of organic up-conversion phosphors (OP) in the catalyst formulation. A wide range of organic dyes was photocatalytically degradated in the presence of visible light irradiation emitted by green or white LEDs. It is possible to retain that the photocatalytic activity of N-doped TiO_2 supported on up-conversion phosphors (NdT/OP) under green light is due to the presence of the phosphors, that has up-conversion property and emits at 434 nm, wavelength able to photoexcite the NdT deposited on the OP surface. The NdT/OP catalyst shows high photocatalytic activity when white LEDs are used as light source. In this case, the NdT supported on the OP surface is excited

both by the blue component of the emission spectrum of the white LEDs, and by the blue emission of the phosphors (OP), excited by the green component emitted by white LEDs. This phenomenon contributes to strongly enhance the photocatalytic activity of NdT/OP photocatalyst in the decolourization process of all the tested dyes.

The obtained results make the visible active NdT photocatalyst modified with organic up-conversion phosphors, a very suitable system to achieve high photocatalytic activity with solar light.

VIII.3 Food azo-dyes removal from water by heterogeneous photo-fenton with $LaFeO_3$ supported on honeycomb corundum monoliths

Tartrazine E102 (TRZ) and red allura E129 (RED), are the most commonly used food dyes. They appear to cause the most allergic and/or intolerance reactions in comparison with the others azo dyes (Wawrzkiewicz and Hubicki, 2009). Moreover they are not recommended for consumption by children. The removal of TRZ and RED from wastewater is an important issue because of their potential toxicity (Dinc et al., 2002, Pourreza et al., 2011).

Due to the low biodegradability of dyes, conventional biological treatment processes are not very effective in treating dye wastewaters (Mafra et al., 2013).

Therefore, chemical and chemical-physical processes such as coagulation, flocculation, adsorption, chemical oxidation, are typically used in azo dyes wastewater treatment. Unfortunately, the most of them are separation processes resulting in the production of sludge that must be properly treated and disposed of. An interesting alternative for the treatment of food azo dyes is represented by the photo-Fenton process. Fenton process belongs to the family of advanced oxidation processes (AOPs) that can degrade recalcitrant compounds under mild conditions (Bouasla et al., 2010, Vaiano et al., 2014d, Vaiano et al., 2014e, Vaiano et al., 2014f, Vaiano et al., 2014b). The active sites in the Fenton process are iron ions which act as catalyst to produce hydroxyl radicals from hydrogen peroxide molecules.

In the scientific literature only a few works deals with the removal of TRZ and RED by AOPs. In particular, for TRZ a method based on Al, Fe-pillared clays as catalysts was investigated in the discoloration of aqueous solutions (Banković et al., 2012). In this case, bentonite clay from coal mines was used as catalyst in Fenton-like degradation of TRZ, and the homogeneous and heterogeneous photocatalytic oxidation were investigated.

In photo-assisted Fenton systems the rate of Fenton reaction can be further enhanced by the application of ultraviolet irradiation (Lofrano et al., 2009, Aleksić et al., 2010). In the homogeneous phase, the chemical changes that take place are solely dependent on the nature of the interactions between Fenton's reagents and compounds to be degraded (Soon and Hameed, 2011). Drawbacks due to the application of homogeneous catalysts, such as low pH (≅3), production of Fe containing sludge, and deactivation could be overcome by heterogeneous catalytic systems. Various studies have been carried out on the heterogeneous photo-Fenton system (Kuznetsova et al., 2004). The immobilization of Fe ions on clays, bentonite and laponite for the oxidation of the azo dye Orange II has been reported (Feng et al., 2005). Similar works have been also described for the degradation of different azo-dyes over iron oxides such as goethite and hematite under non controlled pH conditions (He et al., 2002). Heterogeneous Fe(III) catalyst is often used as suspended particles in the liquid reaction medium (Bossmann et al., 1998a). But the main disadvantage lies in the fact that a separation process is necessary after treatment, to remove the catalyst before effluent disposal, increasing operation costs. The use of structured catalysts could be an interesting option to avoid this additional process and save money for wastewater treatment (Sannino et al., 2011a, Vaiano et al., 2014c). $LaFeO_3$ perovskite supported on honeycomb monoliths has been successfully investigated in photo-Fenton treatment of organic contaminants such as acetic acid (Sannino et al., 2011a). However no papers regarding the use of structured catalysts for the photo Fenton treatment of food azo dyes are present in literature. Therefore, the aim of this work was to evaluate the efficiency of $LaFeO_3$ perovskite supported on honeycomb monoliths for the removal of food azo dyes from wastewater by photo-Fenton process. Process efficiency was evaluated in terms of both dyes discoloration and mineralization (total organic carbon (TOC) removal). The influence of $LaFeO_3$ loading, also in the presence of low amounts of Pt, was investigated.

VIII.3.1 Structured catalysts characteristics

The structured catalyst were prepared following the procedure reported elsewhere (Isupova et al., 2002, Isupova et al., 2005). $LaFeO_3$ was supported on corundum honeycombs by impregnation of thin wall (0.25 and monolithic support. A thin wall (0.25 mm) of the monolithic support (triangular channel size = 2.5 mm) was treated with solutions of nitrate salts in the presence of citric acid and ethylene glycol. The obtained samples were calcined in air at 900 °C for 4 h. Pt metal (0.1 and 0.16 wt%) was supported by wet

impregnation from H_2PtCl_6 on the corundum substrate containing $LaFeO_3$ loading of about 11 wt%. (Sannino et al., 2011a).

Table 1 reports the list of the structured catalysts tested in the Photo-Fenton process.

Table VIII.2 *Characteristics of the investigated corundum supported catalysts*

Catalyst	$LaFeO_3$ loading [wt%]	Pt loading [wt%]	Geometrical surface */volume** ratio [mm^2/mm^3]
2.2 La	2.23	0	2511
4.5 La	4.5	0	2513
10 La	10.64	0	2846
17 La	17.39	0	2577
0.1 Pt	11.39	0.1	2536
0.16 Pt	11.23	0.16	2513

*by the sum between the external area of cylindrical monolith and the area of all internal triangular channels; **volume of the single piece of monolith

VIII.3.2 Photo-Fenton oxidation tests

Photo-Fenton tests were carried out on 160 ml of solution in a properly designed sealed stainless-steel batch cylindrical photoreactor (Sannino et al., 2011a). Model aqueous solutions containing an initial concentration of RED and TRZ equal to 40 mg/L, corresponding to 14 and 17 mg TOC/L respectively, at the spontaneous pH of the solution (pH=6.6) were used in the tests. An 8 W mercury vapours lamp emitting at 254 nm was used as light source. 13 g of the monolith catalysts were placed in the reactor.

The reactor was maintained in the absence of irradiation at 25°C for t=180 min to reach the adsorption equilibrium of food dyes on catalysts surface. During the tests, a continuous dosage of H_2O_2 (0.038 mol h^{-1}) was used.

VIII.3.2.1 Discoloration of RED and TRZ

Figure VIII.24 shows the discoloration of RED and TRZ under different experimental condition: UV, UV+H_2O_2,UV+H_2O_2+4.5La.

Dye discoloration has been reported as A/A_0 where A is the absorbance at reaction time t and A_0 is the initial absorbance, respectively.

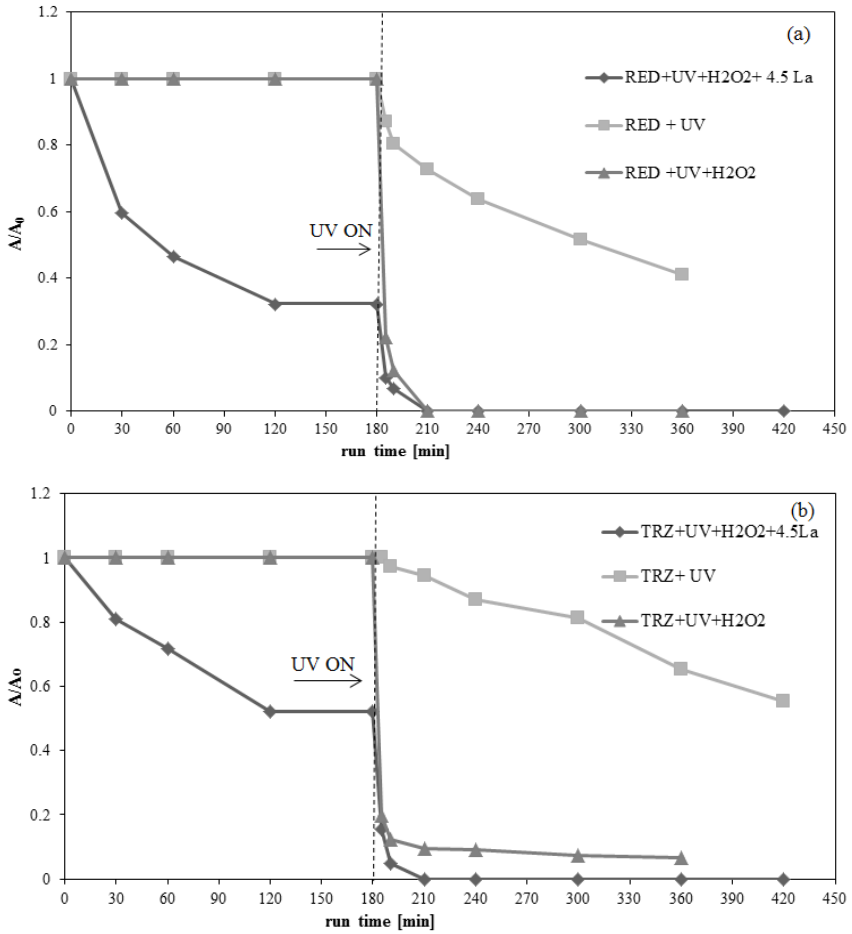

Figure VIII.24: *Discoloration of red allura (RED) and tartrazine (TRZ) under different experimental conditions : UV, UV+H_2O_2,UV+H_2O_2+4.5La*

In the case of UV alone, the discoloration occurs very slowly and not completely. In particular, 36 and 20 % discoloration was observed in 120 min of irradiation for RED and TRZ, respectively. Process efficiency enhanced when H_2O_2 was added to the solution. The combined action of UV and H_2O_2 resulted in the total discoloration in 60 min of irradiation for RED. While for TRZ, after the same time of irradiation, the discoloration was 90% and doesn't change for higher irradiation time.

Photo-Fenton process (4.5La catalyst) resulted in a drastic water discoloration (100% in 60 min of irradiation) for both dyes.

It is very important to underline that the presence of the catalyst has an important role in the dark phase, during which there has been a discoloration

(66% for RED and 45% for TRZ in 180 min of run time) due to the adsorption of the dye on the surface of the catalyst.

On the other hand, the progress in the absorbance spectrum of dyes solution was also monitored between 400 nm and 700 nm wavelengths. In all cases, reductions in the absorbance values at 426 and 506 nm indicate the degradation of the parent dyes molecules to smaller colorless oxidation intermediates, according to literature data (Tekbaş et al., 2008).

VIII.3.2.2 Influence of $LaFeO_3$ loading on the discoloration process.

Figure VIII.25 shows the influence of $LaFeO_3$ loading in the discoloration process.

During the dark period it is possible to note that there is a difference in the amount of dye adsorbed on the catalyst as a function of $LaFeO_3$ loading. In the presence of UV light, however, no significant differences in the discoloration can be observed among the different catalysts.

For RED (Figure VIII.25 a), the best catalyst is 4.5La since it allows an higher dye adsorbed amount compared to the other catalysts, corresponding to a discoloration of 66% after 3h in dark.

Moreover, in the presence of UV light and H_2O_2, 4.5La enhanced the discoloration of the solution, completely removing the color after 1h of irradiation time.

For TRZ (Figure VIII.25 b), the best catalyst is 2.2La. With this catalyst, after a dark period of 3 h, it was obtained a dye removal equal to 90% due to the TRZ adsorption on the catalyst surface. Moreover, with the same catalyst the complete discoloration is obtained after only 5 min of photo-Fenton process. In a previous work the total discoloration of a TRZ solution by homogeneous photo-Fenton process was achieved after 20 min of irradiation time (Oancea and Meltzer, 2013a), confirming the better performances of heterogeneous processes in presence of structured photocatalysts. However, in the case of RED, no literature data are available for comparison.

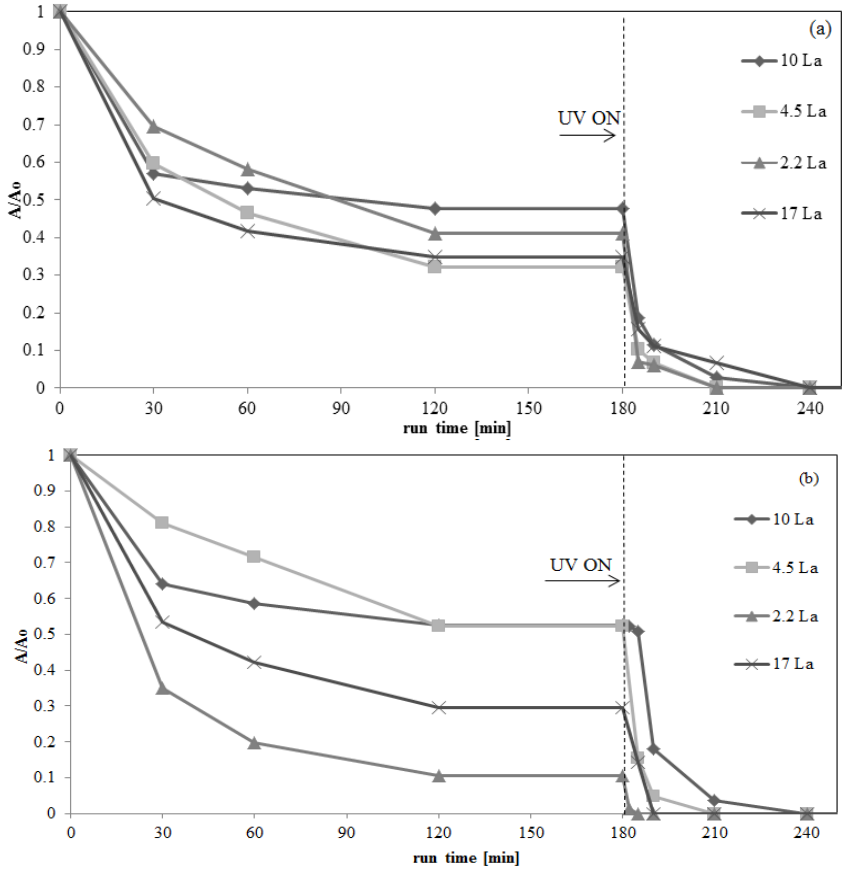

Figure VIII.25: *Influence of LaFeO3 loading on the discoloration process of RED (a) and TRZ (b).*

VIII.3.2.3 Influence of Pt loading on discoloration

Photo-Fenton tests were also performed using 0.1Pt and 0.16Pt to analyze the influence of Pt loading in TRZ and RED discoloration (Figure VIII.26 3).

The results from experiments with and without Pt were compared. For TRZ (Figure VIII.26 a), the efficiency of the discoloration reaction increased as Pt content was increased. In particular, already after one hour in dark, 0.16Pt catalyst allowed a discoloration of 96%, due to the adsorption of the dye on the catalyst surface. When the UV light was switched on, a complete discoloration was observed after only 5 minutes of reaction.

Differently, the best performance for RED solution was observed for the lower Pt loading (0.1 wt%), (Figure VIII.26 b).

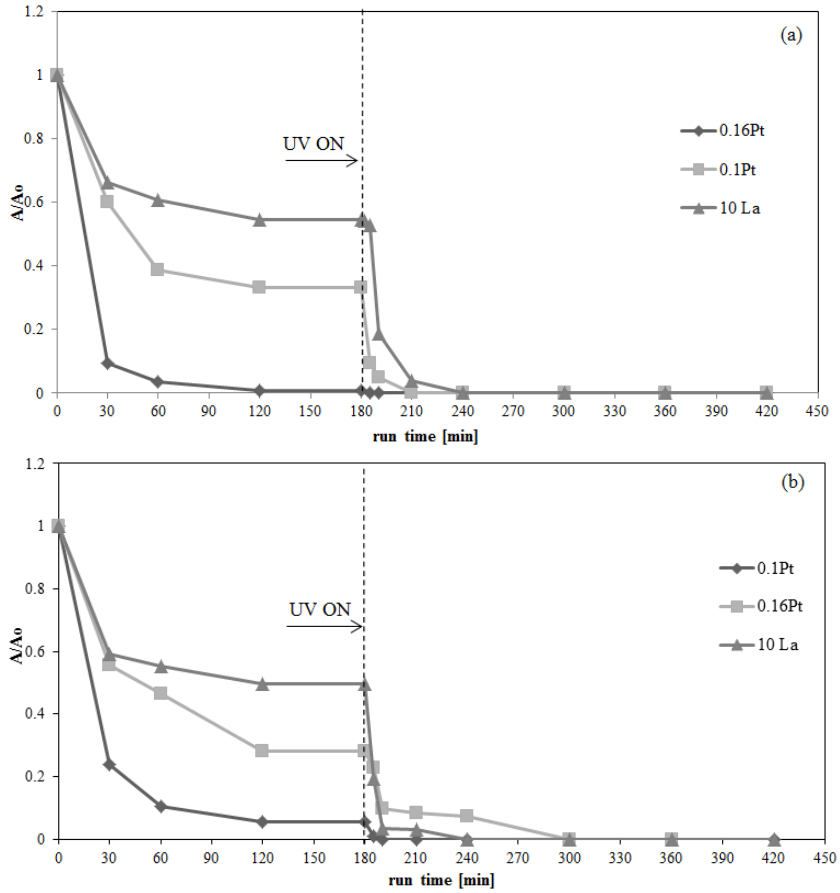

Figure VIII.26: *Discoloration of TRZ(a) and RED (b) with catalysts containing Platinum (0.1Pt, 0.16 Pt).*

VIII.3.2.4 Kinetic of discoloration process

Previous studies have indicated that the kinetics of photo-Fenton discoloration process is a pseudo-first order reaction (Chen et al., 2010a, Lucas and Peres, 2006).

Thus, the photo-Fenton discoloration process of RED and TRZ can be described hypothesizing first-order kinetics (Equation 1) with respect to the absorbance values at 426 and 506 nm for TRZ and RED, respectively.

$$\frac{dA(t)}{dA_0} = -k_{dec} \cdot A(t) \qquad \text{Eq (1)}$$

A(t): A is the absorbance at reaction time t, [-]

k_{dec}: apparent discoloration kinetic constant, [min^{-1}]

The initial conditions are:

t=0 $A=A_0$

where A_0 is the initial absorbance value.

The equation 1, together with the initial condition, was solved by the Euler iterative method to identify the constant k_{dec} by fitting experimental data reported in Figure 2 and Figure 3 as a function of irradiation time. The fitting procedure was realized by using the least squares approach.

Figure VIII.27a shows the trend of k_{dec} for RED dye. It is possible to observe that k_{dec} for catalysts with different percentages of $LaFeO_3$ doesn't change and it is comparable with the kinetic constant of homogeneous phase ($UV+H_2O_2$). This evidences that the color removal, for RED dye, occurs primarily in homogeneous phase.

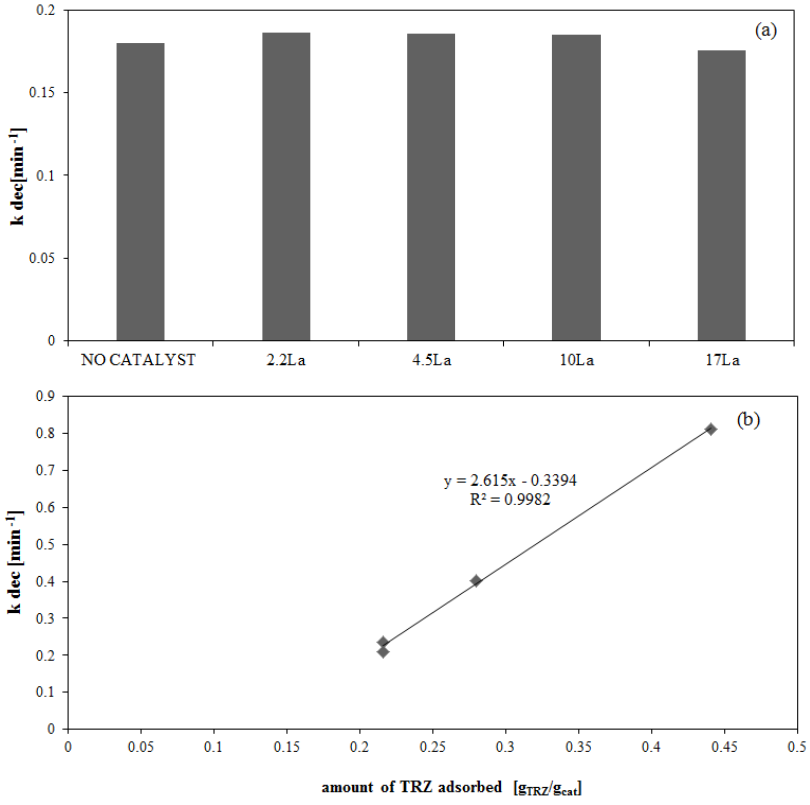

Figure VIII.27 *: Trend of the discoloration kinetic constant (k_{dec}) for RED (a) and TRZ(b).*

The values of k_{dec} for TRZ are reported in Figure VIII.27b as a function of the amount of TRZ adsorbed on catalyst surface.

It is evident that k_{dec} increased linearly with the amount of TRZ adsorbed meaning that the dye adsorption process is the key step for the photo-Fenton discoloration of TRZ.

The behavior of k_{dec} obtained for Pt based catalyst is reported in Figure VIII.28 . For RED (Figure VIII.28a) k_{dec} reached the maximum value for a Pt loading equal to 0.1 wt%, confirming the existence of an optimal content of Pt which guarantees the best discoloration of the aqueous sample.

Also for catalysts containing Pt, k_{dec} for TRZ was reported as a function of dye adsorbed in dark conditions (Figure VIII.28b). In this case, it can be noted that k_{dec} increases linearly with the amount of dye adsorbed on the catalyst. The highest value of k_{dec} corresponds to the catalyst with the highest adsorption ability, namely the one with a Pt percentage equal to 0.16 wt%.

In summary, the photo-Fenton discoloration process on structured catalysts strongly depends on the dye type. In particular, in the case of RED, the discoloration occurs primarily in homogeneous phase and only the presence of Pt can enhance the performance of the process.

Different results are obtained for TRZ. For this food dye, the discoloration rate is strongly influenced by the adsorption ability of structured catalysts. More higher is the amount of TRZ adsorbed, more higher is the reaction rate.

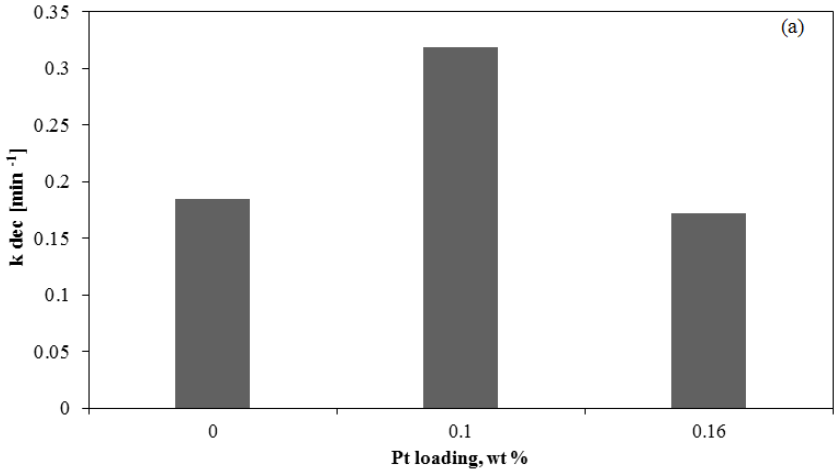

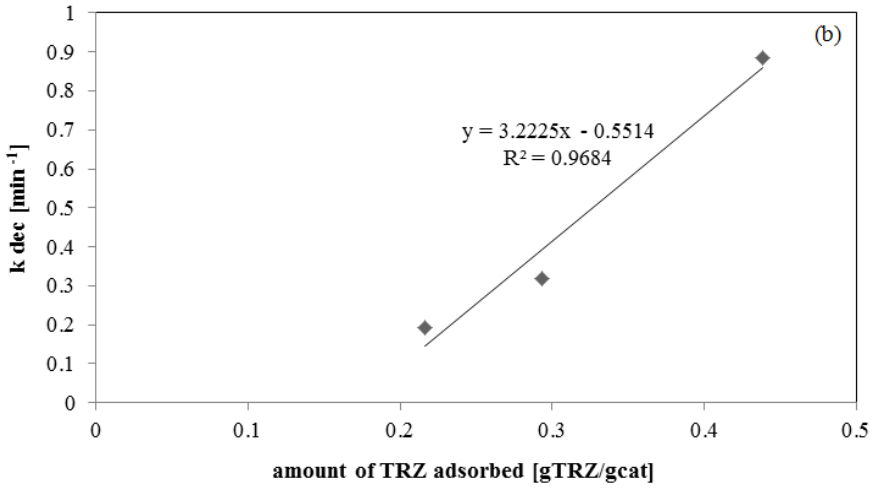

Figure VIII.28*: Trend of the discoloration kinetic constant (kdec) on the Pt based catalysts for RED (a) and TRZ (b).*

VIII.3.3 Mineralization study

The discoloration of dyes does not necessary correspond to the oxidation and mineralization of the molecule. Moreover, it is known that reaction intermediates that can be formed during the oxidation of azo dyes could be more toxic than their parent compounds (Lucas and Peres, 2006, Rizzo, 2011).

Therefore, it is necessary to understand the mineralization degree of the azo dye RED and TRZ to evaluate the mineralization level by heterogeneous photo-Fenton processes. To quantitatively characterize the mineralization of azo dyes, the TOC content of solution used in this study is defined as follows:

TOC content of solution = TOC/TOC_0

where TOC and TOC_0 are the TOC values at reaction time t and the initial TOC, respectively.

VI.3.3.1 Effect of UV, UV+H_2O_2, UV+H_2O_2+Structured catalyst

In Figure VIII.29 6, it was reported the behavior of TOC for RED and TRZ under different experimental conditions: UV, UV+H_2O_2, UV+H_2O_2+4.5La. It is possible to note how the presence of the catalyst plays a crucial role in the TOC removal both for TRZ and for RED. For TRZ, the structured catalyst allows a TOC removal of 50% after only 15 minutes of irradiation. In the presence of UV alone, no TOC removal was observed, while for UV+H_2O_2, only 3% of TOC was removed after 15 minutes of

irradiation. In the case of RED, in presence of 4.5La catalyst, a TOC removal of about 70 % was achieved after only 15 minutes of irradiation. As well as for TRZ, in the presence of UV alone, no TOC removal was observed, while for UV+H_2O_2, only 25% of initial TOC was removed after 15 minutes of irradiation.

In summary, in the presence of only UV and UV+H_2O_2, although the discoloration rate was high (Figure VIII.24), the TOC was not removed in the case of UV alone, and only partially removed in the case of UV+H_2O_2. These results indicated that in the absence of structured photocatalysts, the two dyes are degraded to small colorless molecules that are not completely mineralized in the absence of structured photocatalyst. The latter, on the contrary, is able to enhance the mineralization rate of the colorless intermediates (Figure VIII.29), leading to the complete removal of TOC, as observed in the homogeneous photo Fenton removal of azo dyes (Oancea and Meltzer, 2013a, Lucas and Peres, 2006).

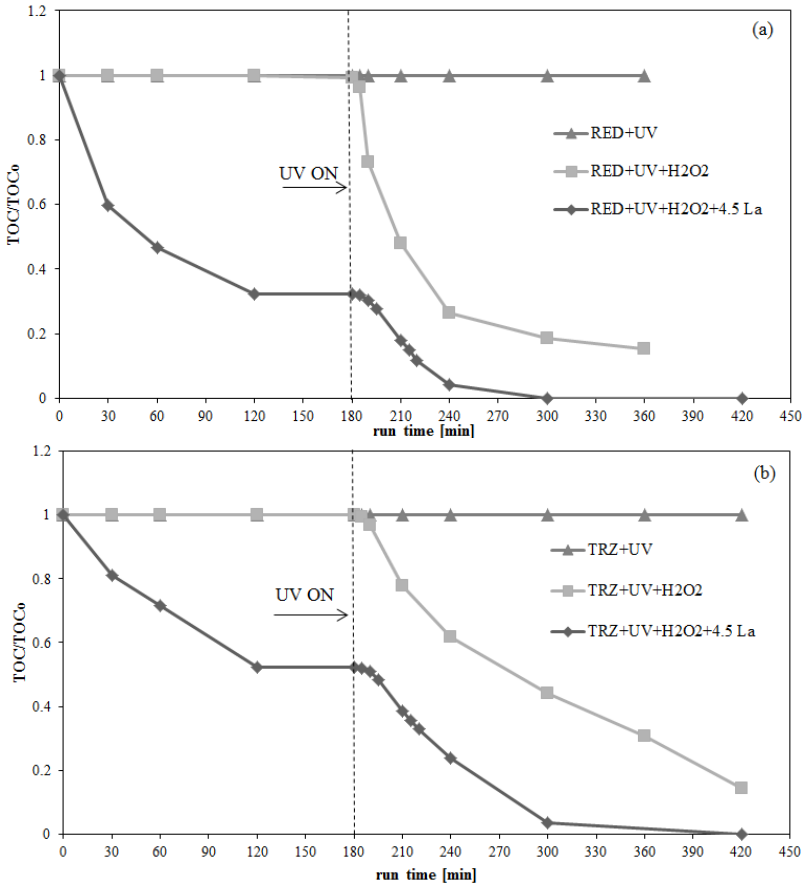

Figure VIII.29: *Trend of TOC for RED (a) and TRZ (b) under different experimental conditions : UV, UV+H2O2,UV+H2O2+LaFeO3.*

VIII.3.3.2 Effect $LaFeO_3$ loading on TOC removal

It was evaluated the influence of $LaFeO_3$ loading on TOC removal from aqueous samples. As for the step of discoloration, even in the mineralization process, the best catalysts were 4.5La and 2.2La for RED and TRZ, respectively.

In Figure VIII.30 it is reported the TOC profiles as function of run time obtained on catalysts with different percentage of $LaFeO_3$. For both dyes, it is possible to observed that during the dark period, a TOC removal was observed due to the dye adsorption on the catalysts. After 1 hour of irradiation time, the TOC has been completely removed.

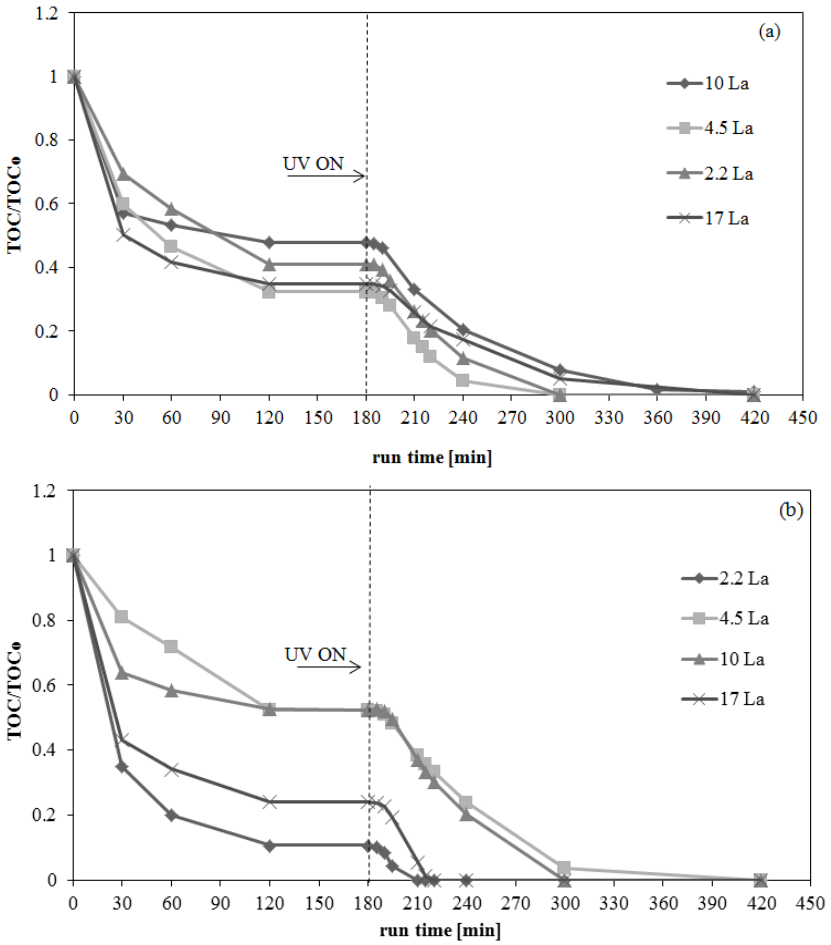

Figure VIII.30 *: Effect $LaFeO_3$ loading on TOC removal for RED(a) and TRZ(b).*

VIII.3.3.3 Influence of Pt loading on TOC removal

Figure 8 reports the trend of TOC for RED and TRZ on Pt-$LaFeO_3$ catalysts. Even for TOC removal it is possible to do the same assessments made for discoloration process.

In fact, for RED dye (Figure VIII.31a), as well as for the discoloration, the complete TOC removal from the wastewater has been achieved after only 5 minutes of irradiation time on the structured catalyst with a Pt content of 0.1wt %. For TRZ dye (Figure VIII.31b), instead, the Pt content that promotes the better TOC removal is higher (0.16% Pt), as happened for the discoloration. This Pt percentage allows to obtain the complete TOC removal after only 5 minutes of irradiation time.

These results well agree with those ones obtained on perovskites based monoliths for which the Pt addition improved the catalytic performances of the photo-Fenton process for the removal of not-biodegradable substances (Sannino et al., 2011a). As happens for the acetic acid (Sannino et al., 2011b), probably also for TRZ and RED, the addition of Pt showed relevant effect on the activity of $LaFeO_3$ based sample, suggesting a high activation of dyes molecules, which occurs during the dark adsorption step.

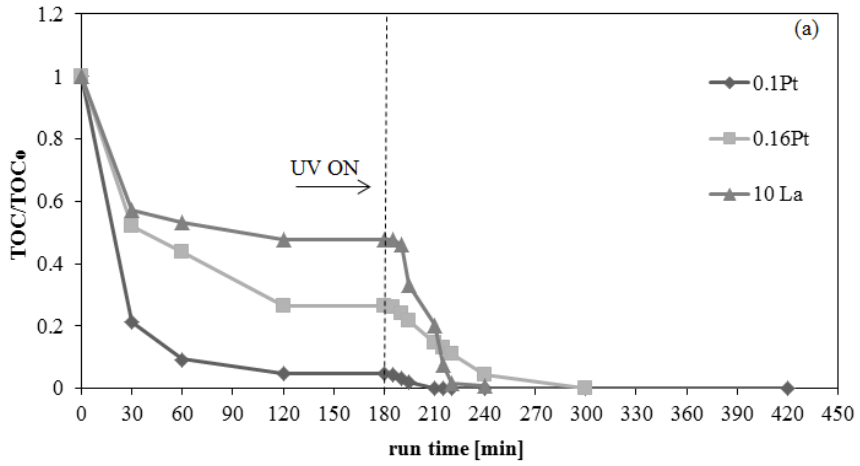

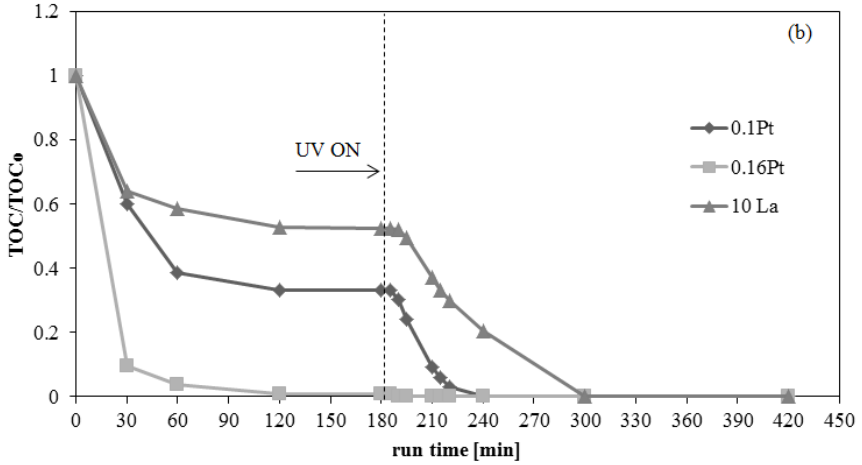

Figure VIII.31: *Influence of Pt loading on TOC removal for RED(a) and TRZ (b)*

VIII.3.3.4 Kinetic of photo-Fenton process for mineralization

Mass balance on organic content of the solution ,expressed as TOC can be written as:

$$V \cdot \frac{dTOC(t)}{dt} = r(TOC, I) \cdot W_{Nt} \qquad \text{Eq.2}$$

Where:

TOC(t): TOC at given reaction time, [g/L]

r: reaction rate, [g/(L h)]

W_{Nt}: amount of structured catalyst [g]

The initial condition is:

t=0 $TOC=TOC_0$

The kinetic expression is well described with the classic Langmuir-Hinshelwood (L-H) mechanism terms of mineralization of dyes as in the following:

$$-r = K \cdot \frac{b \cdot TOC}{1 + b \cdot TOC} \cdot \qquad \text{Eq. 3}$$

Where:

K: mineralization constant [mg/(g h)]

b: adsorption equilibrium constant [L/mg]

Eq. 2, coupled with Eq. 3, together with the initial condition, was solved with Euler iterative method to identify the constants K and b by fitting experimental data reported in Figure VIII.30 7 and VIII.31 8 as a function of irradiation time. Also in this case, the fitting procedure was realized by

using the least squares approach obtaining the values of K and b for each catalyst reported in Table VIII.3 and Table VIII.4.

In the case of the system UV+H_2O_2 the constant K has been evaluated following the pseudo first order kinetics obtaining a value of 0.01 and 0.026 h^{-1} for RED and TRZ, respectively.

Table VIII. 3 *: Values of K and b constants for all the structured catalysts in the case of RED dye*

Catalyst	K[mg/(g h)]	b [L/mg]
2.2 La	0.01	0.34
4.5 La	4.89	0.18
10 La	5.31	0.05
17 La	3.41	0.03
0.1 Pt	16.2	0.08
0.16 Pt	4.02	0.06

Table VIII.4*: Values of K and b constants for all the structured catalysts in the case of TRZ dye*

Catalyst	K[mg/(g h)]	b [L/mg]
2.2 La	11.9	0.42
4.5 La	2.57	0.10
10 La	3.27	0.04
17 La	4.13	0.03
0.1 Pt	14.8	0.05
0.16 Pt	26.8	0.08

Figure VIII.32 and Figure VIII.33 show the trend of constant K and CO_2 selectivity (expressed as CO_2/CO ratio) for RED and TRZ dyes in presence of structured catalysts, in comparison with the value obtained for the homogeneous reaction.

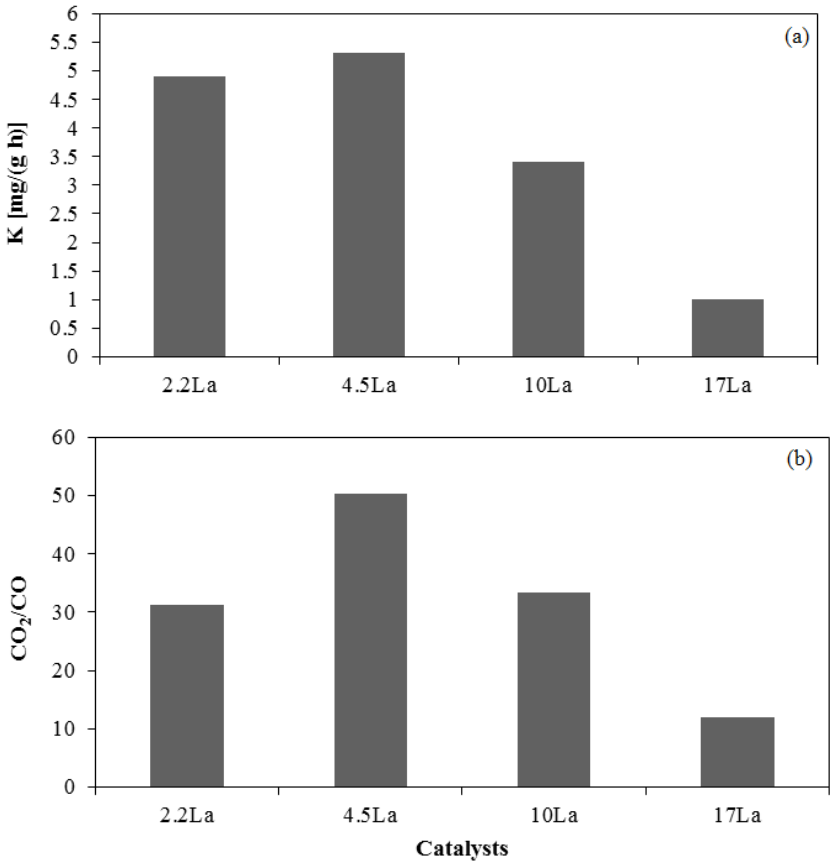

Figure VIII.32*: Trend of the kinetic constant of TOC removal (K) (a) and selectivity to CO2(b) for RED on structured catalysts with different LaFeO3 loading.*

For RED dye, the constant K has reached a maximum value for 4.5La sample (figure VIII.32a), for which also the highest selectivity to CO_2 has been achieved (figure VIII.32b). Therefore it is possible to confirm that for the photo-Fenton treatment of RED dye, the catalyst that allows the best discoloration and TOC removal is the structured catalyst with a $LaFeO_3$ loading of 4.5 wt%. The latter catalyst is able to obtain also the best selectivity to CO_2.

For the dye TRZ the results in terms of kinetic constant K and selectivity to CO_2 are reported in Figure VIII.33.

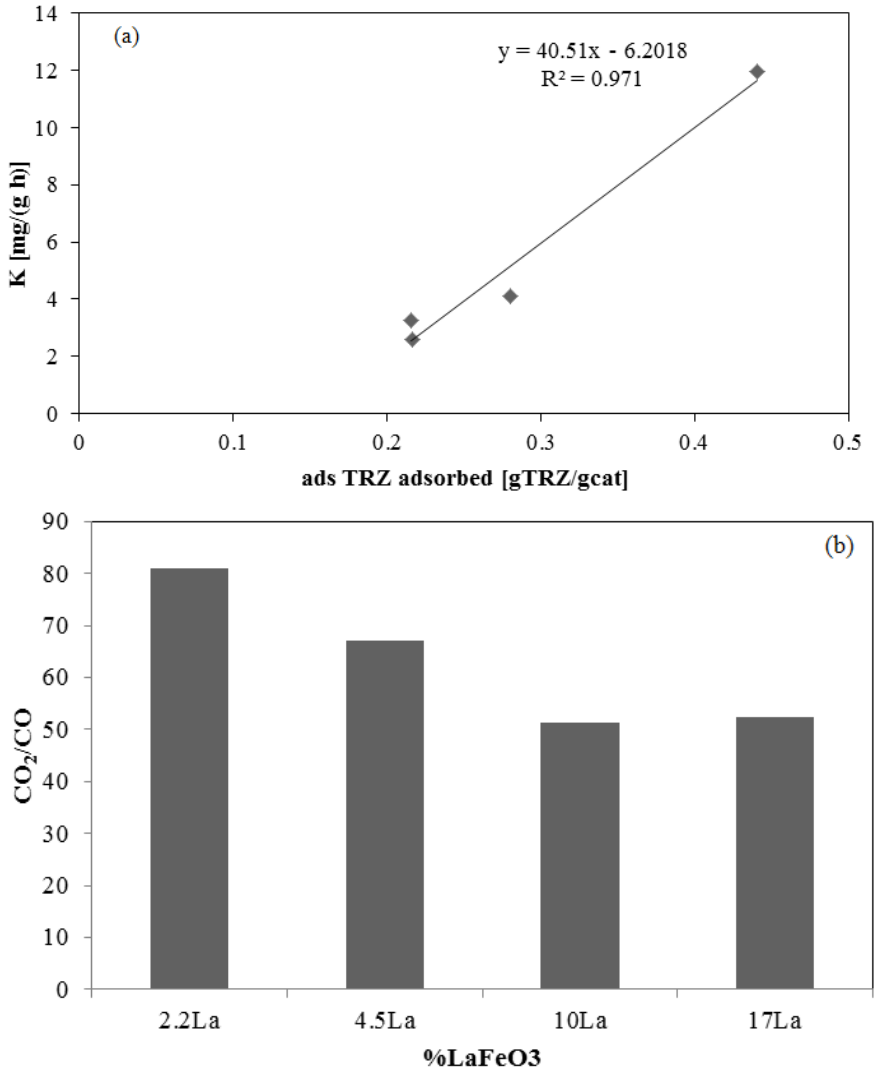

Figure VIII.33: *Trend of the kinetic constant of TOC removal (K) (a) as a function of the amount of TRZ adsorbed on LaFeO3 based catalysts and selectivity to CO2 (b) as a function of LaFeO3 loading.*

In this case, it has been reported the trend of K as a function of the amount of dye adsorbed on $LaFeO_3$ based catalysts (Figure VIII.33a). The constant K increases linearly with the increase of the amount of dye adsorbed on the catalyst surface meaning that the adsorption process enhances the ability in TOC removal under irradiation. In particular the catalyst that ensures the best TRZ adsorption (0.44 g_{TRZ}/g_{cat}) is that one with $LaFeO_3$ content of 2.2 wt%. This catalyst also allows to get the highest CO_2 selectivity (Figure VIII.33b).

Figure VIII.34 reports the trend of the kinetic constant K and CO_2 selectivity for RED (Figure VIII.34a) and TRZ (Figure VIII.34b) in presence of the catalysts containing Pt.

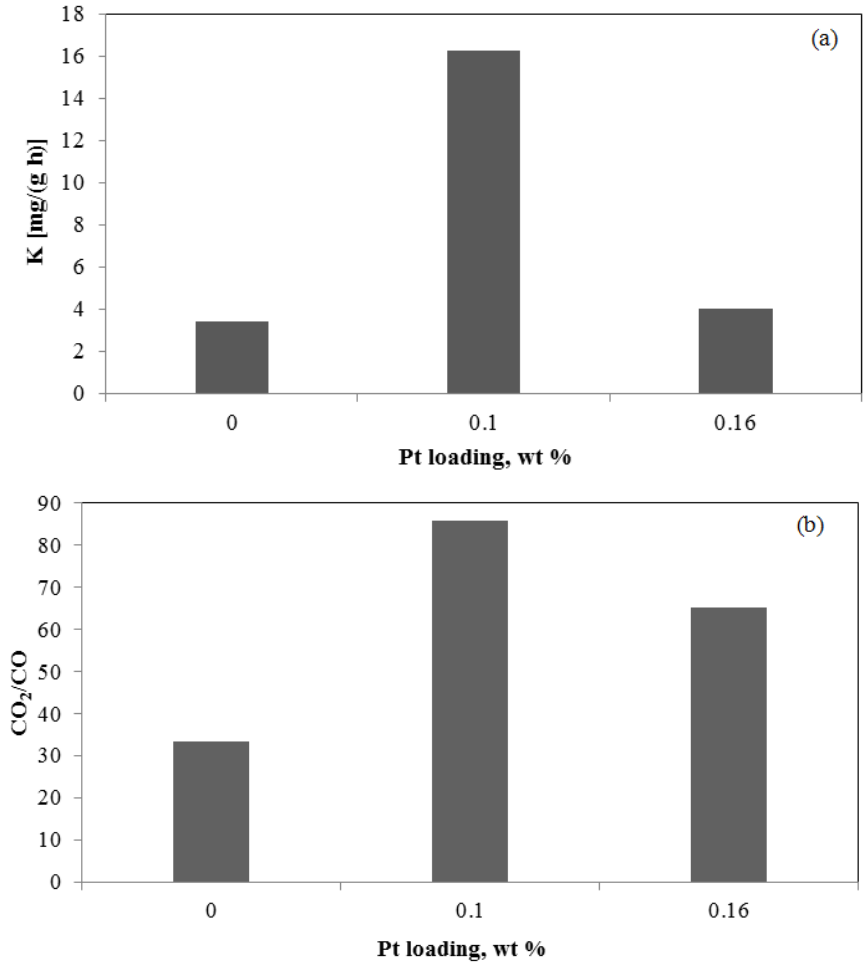

Figure VIII.34: *Trend of the kinetic constant of TOC removal (K) (a) and selectivity to CO2 (b) for RED on structured catalysts with different Pt loading.*

It can be noted that, also in this case, there is an optimal percentage of Pt (0.1wt%) that allows, for RED dye, to reach the highest TOC removal rate with together the highest CO_2 selectivity (Figure VIII.34b).

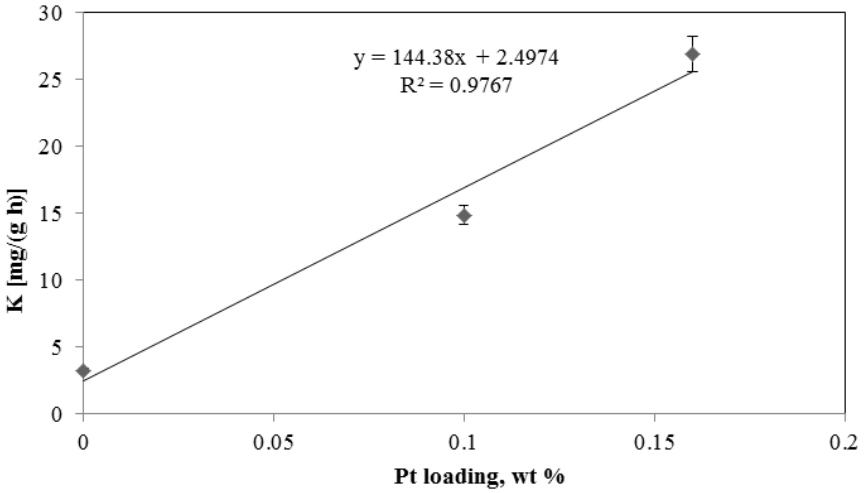

Figure VIII.35 *: Trend of the kinetic constant of TOC removal (K) for tartrazine (TRZ) on structured catalysts with different Pt loading.*

For TRZ (Figure VIII.35), K increases linearly with Pt content. Therefore, higher the content of Pt on the catalyst better is the removal of TOC. Moreover, the CO_2/CO ratio is 50 for the catalyst without platinum, and 97 for that one containing platinum, indicating that the presence of the noble metals influenced strongly the CO_2 selectivity.

From these results it is possible to observe that the efficiency of a heterogeneous photo-Fenton process was evaluated for the removal of food azo-dyes, red allura and tartrazine, from water solutions using structured $LaFeO_3$ catalysts supported on honeycomb monoliths with and without Platinum. The discoloration of RED dye water solution occurs mainly in the homogeneous phase (UV + H_2O_2), while for the TRZ the discoloration depends on the amount of dye adsorbed on the catalyst surface. In the presence of catalysts with platinum**,** 0.1 wt% was the best Pt loading for the discoloration of RED solution. For TRZ, instead, the discoloration process improved as Pt loading was increased.

The presence of the catalyst plays a crucial role in the mineralization (TOC removal) of both azo-dyes. In particular, the best catalysts are 4.5La and 2.2La for RED and TRZ, respectively. The latter catalysts are able to obtain also the best selectivity to CO_2. In presence of Pt, 0.1wt% of Pt loading allowed to reach the highest TOC removal rate for the RED dye water solution, with together the highest CO_2 selectivity. For TRZ, the higher the content of Pt on the catalyst, the better the removal of TOC, and the presence of the noble metals strongly affected the CO_2 selectivity. So it is possible to conclude that the photo-Fenton process proves effective for the treatment of food industry wastewater managing to completely break down non-biodegradable organic substances such as food dyes.

IX Conclusions

The study carried out in this PhD thesis has allowed to obtain interesting results in the valorization of food industry wastewater. In particular, after an overview of the conventional processes nowadays used for the industrial production of hydrogen, the advantages of advanced oxidation processes already used in the water splitting processes for the production of hydrogen (with particular interest to photocatalytic and photoelectrochemical processes) have been highlighted .

In order to evaluate the effectiveness of these processes also for the valorization of food wastewater, aqueous solutions containing known concentrations of glucose were considered. In fact, glucose, typically occurring in some food industry wastewater, looks an interesting source for hydrogen production by photocatalytic treatment because of its high hydrogen/carbon ratio.

It has been found an interesting mechanism resulting from the use of photocatalysts based on titania doped with noble metals (Pd). In particular, Pd deposition onto the sulfated TiO_2 surface throughout the photodeposition time was favorable to the production of H_2 or CH_4 by photocatalysis and it was possible to observe that the value of the H_2/CO_2 molar ratio did not change significantly as irradiation time increased, tending to a value approximately equal to 2 after three hours of irradiation. CO_2 and H_2 are mainly produced from the photocatalytic wet reforming of glucose, and the analysis of liquid phase showed the presence of gluconic acid, a typical product of glucose oxidation. The experimental conditions during photodeposition, such as deposition time, were found to have a strong influence on the final properties of the materials, and consequently on their photocatalytic activity in glucose reforming. A short deposition time (15 min) led to a smaller average particle size and higher dispersion of the palladium on the sulfated TiO_2 surface, as well as a higher fraction of the metal in its metallic state. These features resulted in a good photocatalytic performance in terms of glucose conversion. The best photocatalytic behavior was observed in the sample prepared with 0.5 wt% of palladium and 120 min of photodeposition time. By changing the pH of the solution, it is possible to modulate the performance of the photocatalytic reaction,

producing more methane in alkaline conditions or more hydrogen in acidic conditions.

Also the effect of the surface modification of TiO_2, in particular modified with fluorine ($F–TiO_2$) demonstrated interesting results. In fact, from the photocatalytic results, it was found that this surface modification can inhibit the recombination rate of holes and free electrons, enhancing the photocatalytic activity in the removal of pollutants from aqueous samples. Fluorinated TiO_2 ($F\text{-}TiO_2$) represents an interesting support for noble metals to be used in the photocatalytic process for the hydrogen production from sugars contained in water. In particular, Pt on $F\text{-}TiO_2$ ($Pt\text{-}F\text{-}TiO_2$) significantly enhanced the photocatalytic H_2 production compared to the other investigated catalysts. The increase of photocatalytic activity of $Pt\text{-}F\text{-}TiO_2$, with respect to Pt supported on sulfated TiO_2, is due to the formation of unbounded OH radicals that are more reactive, leading to a higher hydrogen production. In this case the higher hydrogen production was obtained under acidic conditions (pH=2), while the degradation of glucose was higher at pH=6. By HPLC and UV-Vis analyzes performed on the liquid samples, it was also confirmed that, using $Pt\text{-}F\text{-}TiO_2$, it is possible to produce hydrogen by the photocatalytic degradation of glucose obtaining gluconic acid as product.

Another interesting photocatalyst studied for the hydrogen production was $LaFeO_3$. This photocatalysts were successfully synthesized using the solution combustion synthesis method. In order to further improve the performance of the perovskite, the effect of the doping of $LaFeO_3$ with a noble metal very effective and already used in the case of titania was studied. In particular, the effect of different amount of rhodium used for the doping of $LaFeO_3$ prepared through solution combustion synthesis has been investigated. From the characterization results it was possible to observe that the substitutional doping generated by the replacement of Fe^{4+} with Rh^{+4} promotes the separation of charge carriers efficiently, inhibiting the recombination of the photogenerated electron–hole pairs, and consequently enhancing the photocatalytic activity. The total glucose degradation and the highest H_2 production have been achieved with an Rh content equal to 0.7 mol%.

Providing for the application of the photocatalyst to industrial level, the study has been directed to the formulation of a noble metal free photocatalyst. Interesting results were obtained using ruthenium as dopant for $LaFeO_3$.

The introduction of Ru in the crystalline structure of the $LaFeO_3$ caused the enhancement of the photocatalytic activity. For Ru content higher than 0.47 mol%, the photocatalytic activity decreased because of the presence of RuO_2 on the catalyst surface. Therefore 0.47 mol% of Ru loading is considered to be an optimal value for the studied reaction. In particular, after

4 hours of UV irradiation with 0.47%Ru, glucose degradation and hydrogen production were equal to 70% and 3270 mmol/L, respectively.

It is important to underline the effect of the reactor configuration on the hydrogen production and degradation of glucose. The results showed that with the same volume but reducing the diameter of the photocatalytic reactor from 2.5 to 1.25 cm, the photonic transport was enhanced and consequently the activity of the 0.47%Ru increased. In particular, under UV light, the hydrogen production passed from 3270 to 6079 mmol/L and the glucose degradation was complete after 3 hours of irradiation.

The 0.47%Ru photocatalyst was tested on a real wastewater from brewing process. After 4 hours of visible light irradiation, a degradation of maltose equal to 50% was observed and in parallel, photocatalytic hydrogen production reached the value of about 3700 μmol/L.

In order to remove the catalyst after the photocatalytic process with the use of an external magnetic field, the 0.47% Ru was coupled with Fe_2O_3 magnetic particles. With this photocatalyst it was obtained glucose degradation equal to 100% after 4 hours of visible light irradiation and the production of hydrogen equal to 5460 μmol/L. Moreover, this magnetic photocatalyst has proved effective for different cycles of activity. The optimized photocatalyst configuration (67Ru) allows to obtain very interesting results also in the application on a real wastewater from cherry wash containing fructose, glucose, sorbitol and anthocyanins. In fact, the photocatalytic results have confirm the ability of the photocatalytic process in the valorization of a food industry wastewater, obtaining a very high hydrogen production after 4 hours of irradiation time equal to 12340 μmol/L. In order to make the wastewater comply with the limits imposed by the legislation, the organic content has been completely degraded through the photo-Fenton process. In fact, the photocatalytic process used primarily for the valorization of the wastewater through the production of hydrogen and /or methane, was coupled with photo-Fenton system able to mineralize the unconverted organics coming from the photoreactor. In fact, with this process, after 200 min of irradiation the complete TOC removal was obtained.

With the aim to overcome the deadvantages due to the separation of photocatalysts after the treatment, it was also investigated the photoelectrocatalytic process for the hydrogen production, considering the general aspects of the process and in particular the attention has been focused on the electrodeposition process for the synthesis of photoanodes to be used in photoelectrocatalytic reactors .

In fact, using the electrodeposition method, the hematite (Fe_2O_3) film was deposited on transparent FTO and it was used as photoanode. The efficiency of various metal modifiers (Ti, Ni, Sn, Co and Cu) has been tested by monitoring the photoelectrochemical behavior of the modified Fe_2O_3 photoanodes. With Ti-doped hematite photoanode a perfect holes selective

contact without surface states is obtained, determining an increase of the photoelectrocatalytic activity.

In fact, the experimental results showed that the highest photocurrent production has been achieved with the Ti-modified Fe_2O_3 photoanode. The highest hydrogen production (1.43 μmol/min at 0.5 V and 2.30 μmol/min at 0.7 V vs Ag/AgCl) was obtained on a Ti-modified hematite photoanode in the presence of alkaline aqueous electrolyte solution containing 1 g/L glucose as sacrificial agent.

Considering that in the food industry wastewater there is the possibility to try food dyes not biodegradable, in addition to the valorization of the wastewater, the effectiveness of advanced oxidation processes in the removal of these contaminants has been evaluated. The most interesting results were obtained with a heterogeneous photo-Fenton process using structured $LaFeO_3$ catalysts supported on honeycomb monoliths. The presence of the catalyst plays a crucial role in the mineralization (TOC removal) of several food azo-dyes underlining that the photo-Fenton process proves effective for the treatment of food industry wastewater managing to completely break down non-biodegradable organic substances such as food dyes.

References

Acar, C., Dincer, I. & Naterer, G. F. 2016. Review of photocatalytic water-splitting methods for sustainable hydrogen production. *Int. J. Energy Res.,* 40**,** 1449-1473.

Ahmad, H., Kamarudin, S. K., Minggu, L. J. & Kassim, M. 2015. Hydrogen from photo-catalytic water splitting process: A review. *Renewable Sustainable Energy Rev.,* 43**,** 599-610.

Al-Ekabi, H., Safarzadeh-Amiri, A., Sifton, W. & Story, J. 1991. Advanced technology for water purification by heterogeneous photocatalysis. *Int. J. Environ. Pollut.,* 1**,** 125-36.

Aleksić, M., Kušić, H., Koprivanac, N., Leszczynska, D. & Božić, A. L. 2010. Heterogeneous Fenton type processes for the degradation of organic dye pollutant in water - The application of zeolite assisted AOPs. *Desalination,* 257**,** 22-29.

Alexiou, G. E. & Mara, D. D. 2003. Anaerobic waste stabilization ponds: A low-cost contribution to a sustainable wastewater reuse cycle. *Applied Biochemistry and Biotechnology - Part A Enzyme Engineering and Biotechnology,* 109**,** 241-252.

Alfano, O. M., Bahnemann, D., Cassano, A. E., Dillert, R. & Goslich, R. 2000. Photocatalysis in water environments using artificial and solar light. *Catalysis Today,* 58**,** 199-230.

Ambashta, R. D. & Sillanpaeae, M. 2010. Water purification using magnetic assistance: A review. *J. Hazard. Mater.,* 180**,** 38-49.

Anderson, M. A., Gieselmann, M. J. & Xu, Q. 1988. Titania and alumina ceramic membranes. *J. Membr. Sci.,* 39**,** 243-58.

Andreozzi, R., Caprio, V., Insola, A. & Marotta, R. 1999. Advanced oxidation processes (AOP) for water purification and recovery. *Catalysis Today,* 53**,** 51-59.

Antoniadou, M., Daskalaki, V. M., Balis, N., Kondarides, D. I., Kordulis, C. & Lianos, P. 2011. Photocatalysis and photoelectrocatalysis using (CdS-ZnS)/TiO2 combined photocatalysts. *Applied Catalysis B: Environmental,* 107**,** 188-196.

Antoniadou, M., Kondarides, D. I., Labou, D., Neophytides, S. & Lianos, P. 2010. An efficient photoelectrochemical cell functioning in the presence of organic wastes. *Sol. Energy Mater. Sol. Cells,* 94**,** 592-597.

Antoniadou, M., Kondarides, D. I. & Lianos, P. 2009. Photooxidation products of ethanol during photoelectrochemical operation using a

nanocrystalline titania anode and a two compartment chemically biased cell. *Catalysis Letters,* 129**,** 344-349.

Antoniadou, M., Vaiano, V., Sannino, D. & Lianos, P. 2013. Photocatalytic oxidation of ethanol using undoped and Ru-doped titania: Acetaldehyde, hydrogen or electricity generation. *Chemical Engineering Journal,* 224**,** 144-148.

Ao, C. H. & Lee, S. C. 2004. Combination effect of activated carbon with TiO2 for the photodegradation of binary pollutants at typical indoor air level. *J. Photochem. Photobiol., A,* 161**,** 131-140.

Arendt, E., Maione, A., Klisinska, A., Sanz, O., Montes, M., Suarez, S., Blanco, J. & Ruiz, P. 2008. Structuration of LaMnO3 perovskite catalysts on ceramic and metallic monoliths: Physico-chemical characterisation and catalytic activity in methane combustion. *Applied Catalysis A: General,* 339**,** 1-14.

Atabaev, T. S., Ajmal, M., Hong, N. H., Kim, H.-K. & Hwang, Y.-H. 2015. Ti-doped hematite thin films for efficient water splitting. *Appl. Phys. A: Mater. Sci. Process.,* 118**,** 1539-1542.

Bae, S., Kang, J., Shim, E., Yoon, J. & Joo, H. 2008. Correlation of electrical and physical properties of photoanode with hydrogen evolution in enzymatic photo-electrochemical cell. *J. Power Sources,* 179**,** 863-869.

Bak, A., Choi, W. & Park, H. 2011. Enhancing the photoelectrochemical performance of hematite (α-Fe2O3) electrodes by cadmium incorporation. *Appl. Catal., B,* 110**,** 207-215.

Bamwenda, G. R., Tsubota, S., Nakamura, T. & Haruta, M. 1995. Photoassisted hydrogen production from a water ethanol solution a comparison of activities of Au-TiO_2 and Pt-TiO_2. *Journal of Photochemistry and Photobiology A: Chemistry,* 89**,** 177-189.

Banković, P., Milutinović-Nikolić, A., Mojović, Z., Jović-Jovičić, N., Žunić, M., Dondur, V. & Jovanović, D. 2012. Al,Fe-pillared clays in catalytic decolorization of aqueous tartrazine solutions. *Applied Clay Science,* 58**,** 73-78.

Bard, A. J. & Fox, M. A. 1995. Artificial Photosynthesis: Solar Splitting of Water to Hydrogen and Oxygen. *Acc. Chem. Res.,* 28**,** 141-5.

Basavaraja, S., Vijayanand, H., Venkataraman, A., Deshpande, U. P. & Shripathi, T. 2007. Characterization of γ-Fe2O3 nanoparticles synthesized through self-propagating combustion route. *Synth. React. Inorg., Met.-Org., Nano-Met. Chem.,* 37**,** 409-412.

Bell, D. R. & Gochenaur, K. 2006. Direct vasoactive and vasoprotective properties of anthocyanin-rich extracts. *J. Appl. Physiol.,* 100**,** 1164-1170.

Bellardita, M., García-López, E. I., Marcì, G. & Palmisano, L. 2016. Photocatalytic formation of H2 and value-added chemicals in

aqueous glucose (Pt)-TiO2 suspension. *International Journal of Hydrogen Energy,* 41**,** 5934-5947.

Beninca, C., Peralta-Zamora, P., Tavares, C. R. G. & Igarashi-Mafra, L. 2013. Degradation of an Azo Dye (Ponceau 4R) and Treatment of Wastewater from a Food Industry by Ozonation. *Ozone: Sci. Eng.,* 35**,** 295-301.

Benkli, Y. E., Can, M. F., Turan, M. & Çelik, M. S. 2005. Modification of organo-zeolite surface for the removal of reactive azo dyes in fixed-bed reactors. *Water Research,* 39**,** 487-493.

Bertoluzzi, L., Lopez-Varo, P., Jimenez Tejada, J. A. & Bisquert, J. 2016. Charge transfer processes at the semiconductor/electrolyte interface for solar fuel production: insight from impedance spectroscopy. *J. Mater. Chem. A,* 4**,** 2873-2879.

Beydoun, D., Amal, R., Low, G. & McEvoy, S. A preliminary investigation into the synthesis of titania coated magnetite as a novel photocatalyst. 1998. Institution of Chemical Engineers, 4083-4092.

Bolton, J. R. 1996. Solar photoproduction of hydrogen: A review. *Solar Energy,* 57**,** 37-50.

Bora, D. K., Braun, A. & Constable, E. C. 2013. "in rust we trust". Hematite-the prospective inorganic backbone for artificial photosynthesis. *Energy and Environmental Science,* 6**,** 407-425.

Borken, W. & Matzner, E. 2004. Nitrate teaching in forest soils: An analysis of long-term monitoring sites in Germany. *Journal of Plant Nutrition and Soil Science,* 167**,** 277-283.

Borzacconi, L., Lopez, I. & Vinas, M. 1995. Application of anaerobic digestion to the treatment of agroindustrial effluents in Latin America. *Water Science and Technology.*

Bossmann, S. H., Oliveros, E., Göb, S., Siegwart, S., Dahlen, E. P., Payawan Jr, L., Straub, M., Wörner, M. & Braun, A. M. 1998a. New evidence against hydroxyl radicals as reactive intermediates in the thermal and photochemically enhanced fenton reactions. *Journal of Physical Chemistry A,* 102**,** 5542-5550.

Bossmann, S. H., Oliveros, E., Goeb, S., Siegwart, S., Dahlen, E. P., Payawan, L., Jr., Straub, M., Woerner, M. & Braun, A. M. 1998b. New Evidence against Hydroxyl Radicals as Reactive Intermediates in the Thermal and Photochemically Enhanced Fenton Reactions. *J. Phys. Chem. A,* 102**,** 5542-5550.

Bouasla, C., Samar, M. E. & Ismail, F. 2010. Degradation of methyl violet 6B dye by the Fenton process. *Desalination,* 254**,** 35-41.

Bouchy, M. & Zahraa, O. 2003. Photocatalytic reactors. *International Journal of Photoenergy,* 5**,** 191-197.

Brun, M., Berthet, A. & Bertolini, J. C. 1999. XPS, AES and Auger parameter of Pd and PdO. *Journal of Electron Spectroscopy and Related Phenomena,* 104**,** 55-60.

Cao, H., Wang, G., Zhang, L., Liang, Y., Zhang, S. & Zhang, X. 2006. Shape and magnetic properties of single-crystalline hematite (α-Fe2O3) nanocrystals. *ChemPhysChem,* 7**,** 1897-1901.

Cardillo, D., Konstantinov, K. & Devers, T. 2013. The effects of cerium doping on the size, morphology, and optical properties of α-hematite nanoparticles for ultraviolet filtration. *Mater. Res. Bull.,* 48**,** 4521-4525.

Carraro, G., MacCato, C., Gasparotto, A., Montini, T., Turner, S., Lebedev, O. I., Gombac, V., Adami, G., Van Tendeloo, G., Barreca, D. & Fornasiero, P. 2014. Enhanced hydrogen production by photoreforming of renewable oxygenates through nanostructured Fe2O3 polymorphs. *Advanced Functional Materials,* 24**,** 372-378.

Castro, F. D., Bassin, J. P. & Dezotti, M. 2016. Treatment of a simulated textile wastewater containing the Reactive Orange 16 azo dye by a combination of ozonation and moving-bed biofilm reactor: evaluating the performance, toxicity, and oxidation by-products. *Environ. Sci. Pollut. Res.***,** Ahead of Print.

Cesar, I., Kay, A., Gonzalez Martinez, J. A. & Graetzel, M. 2006. Translucent Thin Film Fe2O3 Photoanodes for Efficient Water Splitting by Sunlight: Nanostructure-Directing Effect of Si-Doping. *J. Am. Chem. Soc.,* 128**,** 4582-4583.

Chang, Y. & Zeng, H. C. 2004. Controlled Synthesis and Self-Assembly of Single-Crystalline CuO Nanorods and Nanoribbons. *Cryst. Growth Des.,* 4**,** 397-402.

Chen, Q., Wu, P., Dang, Z., Zhu, N., Li, P., Wu, J. & Wang, X. 2010a. Iron pillared vermiculite as a heterogeneous photo-Fenton catalyst for photocatalytic degradation of azo dye reactive brilliant orange X-GN. *Separation and Purification Technology,* 71**,** 315-323.

Chen, X., Shen, S., Guo, L. & Mao, S. S. 2010b. Semiconductor-based Photocatalytic Hydrogen Generation. *Chem. Rev. (Washington, DC, U. S.),* 110**,** 6503-6570.

Chen, X., Shen, S., Guo, L. & Mao, S. S. 2010c. Semiconductor-based photocatalytic hydrogen generation. *Chemical Reviews,* 110**,** 6503-6570.

Chiarello, G. L., Aguirre, M. H. & Selli, E. 2010. Hydrogen production by photocatalytic steam reforming of methanol on noble metal-modified TiO2. *Journal of Catalysis,* 273**,** 182-190.

Chiarello, G. L., Ferri, D. & Selli, E. 2011. Effect of the CH3OH/H2O ratio on the mechanism of the gas-phase photocatalytic reforming of methanol on noble metal-modified TiO2. *Journal of Catalysis,* 280**,** 168-177.

Chiarello, G. L. & Selli, E. 2014. Photocatalytic production of hydrogen. *Advances in Hydrogen Production, Storage and Distribution.*

Chiovetta, M. G., Romero, R. L. & Cassano, A. E. 2001. Modeling of a fluidized-bed photocatalytic reactor for water pollution abatement. *Chemical Engineering Science,* 56**,** 1631-1638.

Chojnowski, F., Clechet, P., Martin, J. R., Herrmann, J. M. & Pichat, P. 1981. Hydrogen production by water photoelectrolysis with a powder semiconductor anode. *Chem. Phys. Lett.,* 84**,** 555-9.

Chong, R., Li, J., Ma, Y., Zhang, B., Han, H. & Li, C. 2014a. Selective conversion of aqueous glucose to value-added sugar aldose on TiO2-based photocatalysts. *Journal of Catalysis,* 314**,** 101-108.

Chong, R., Li, J., Ma, Y., Zhang, B., Han, H. & Li, C. 2014b. Selective conversion of aqueous glucose to value-added sugar aldose on TiO_2-based photocatalysts. *Journal of Catalysis,* 314**,** 101-108.

Chong, R., Wang, Z., Li, J., Han, H., Shi, J. & Li, C. 2014c. Transition metal (Ni, Fe, and Cu) hydroxides enhanced α-Fe2O3 photoanode-based photofuel cell. *RSC Adv.,* 4**,** 47383-47388.

Ciambelli, P., Sannino, D., Palma, V., Vaiano, V. & Bickley, R. I. 2008. Reaction mechanism of cyclohexane selective photo-oxidation to benzene on molybdena/titania catalysts. *Applied Catalysis A: General,* 349**,** 140-147.

Ciambelli, P., Sannino, D., Palma, V., Vaiano, V. & Mazzei, R. S. 2011a. Intensification of gas-phase photoxidative dehydrogenation of ethanol to acetaldehyde by using phosphors as light carriers. *Photochemical and Photobiological Sciences,* 10**,** 414-418.

Ciambelli, P., Sannino, D., Palma, V., Vaiano, V. & Mazzei, R. S. 2011b. Intensification of gas-phase photoxidative dehydrogenation of ethanol to acetaldehyde by using phosphors as light carriers. *Photochemical & Photobiological Sciences,* 10**,** 414-418.

Colmenares, J. C., Magdziarz, A., Aramendia, M. A., Marinas, A., Marinas, J. M., Urbano, F. J. & Navio, J. A. 2011. Influence of the strong metal support interaction effect (SMSI) of Pt/TiO_2 and Pd/TiO_2 systems in the photocatalytic biohydrogen production from glucose solution. *Catalysis Communications,* 16**,** 1-6.

Colon, G., Hidalgo, M. C. & Navio, J. A. 2003. Photocatalytic behaviour of sulphated TiO2 for phenol degradation. *Appl. Catal., B,* 45**,** 39-50.

Ćurković, L., Ljubas, D., Šegota, S. & Bačić, I. 2014. Photocatalytic degradation of Lissamine Green B dye by using nanostructured sol-gel TiO2 films. *Journal of Alloys and Compounds,* 604**,** 309-316.

Da Silva, J. C. C., Bispo, G. L., Pavanelli, S. P., De Cássia Franco Afonso, R. J. & Augusti, R. 2012. Ozonation of the food dye Brilliant Blue in aqueous medium: Monitoring and characterization of products by direct infusion electrospray ionization coupled to high-resolution mass spectrometry. *Rapid Communications in Mass Spectrometry,* 26**,** 1305-1310.

Da Silva, L. C., Neto, B. D. B. & Da Silva, V. L. 2009. Homogeneous degradation of the Remazol Black B dye by Fenton and photo-Fenton processes in aqueous medium. *Afinidad,* 66**,** 232-237.

Dalbhanjan, R. R., Pande, N. S., Banerjee, B. S., Hinge, S. P., Mohod, A. V. & Gogate, P. R. 2015. Degradation of patent blue V dye using modified photocatalytic reactor based on solar and UV irradiations. *Desalination and Water Treatment*.

Dalmázio, I., Almeida, M. O., Augusti, R. & Alves, T. M. A. 2007. Monitoring the Degradation of Tetracycline by Ozone in Aqueous Medium Via Atmospheric Pressure Ionization Mass Spectrometry. *Journal of the American Society for Mass Spectrometry,* 18**,** 679-687.

Darwent, J. R. & Porter, G. 1981. Photochemical hydrogen production using cadmium sulfide suspensions in aerated water. *J. Chem. Soc., Chem. Commun.***,** 145-6.

Deguchi, S., Takeichi, T., Shimasaki, S., Ogawa, M. & Isu, N. 2011. Photocatalytic hydrogen production from water with nonfood hydrocarbons as oxidizing sacrifice agents. *AIChE J.,* 57**,** 2237-2243.

Dell'Agli, M., Busciala, A. & Bosisio, E. 2004. Vascular effects of wine polyphenols. *Cardiovasc. Res.,* 63**,** 593-602.

Demazeau, G., Baranov, A., Poettgen, R., Kienle, L., Moeller, M. H., Hoffmann, R.-D. & Valldor, M. 2006. An anhydrous high-pressure synthesis route to rutile type RhO2. *Z. Naturforsch., B: Chem. Sci.,* 61**,** 1500-1506.

Desta, M. B. 2013. Batch sorption experiments: Langmuir and freundlich isotherm studies for the adsorption of textile metal ions onto teff straw (eragrostis tef) agricultural waste. *Journal of Thermodynamics,* 1.

Dhanasekaran, P. & Gupta, N. M. 2012. Factors affecting the production of H2 by water splitting over a novel visible-light-driven photocatalyst GaFeO3. *Int. J. Hydrogen Energy,* 37**,** 4897-4907.

Dholam, R., Patel, N., Adami, M. & Miotello, A. 2009. Hydrogen production by photocatalytic water-splitting using Cr- or Fe-doped TiO2 composite thin films photocatalyst. *International Journal of Hydrogen Energy,* 34**,** 5337-5346.

Dinc, E., Baydan, E., Kanbur, M. & Onur, F. 2002. Spectrophotometric multicomponent determination of sunset yellow, tartrazine and allura red in soft drink powder by double divisor-ratio spectra derivative, inverse least-squares and principal component regression methods. *Talanta,* 58**,** 579-594.

Dom, R., Kim, H. G. & Borse, P. H. 2013. Investigation of solar photoelectrochemical hydrogen generation ability of ferrites for energy production. *Mater. Sci. Forum,* 764**,** 97-115, 20 pp.

Dong, S., Zhang, X., He, F., Dong, S., Zhou, D. & Wang, B. 2015. Visible-light photocatalytic degradation of methyl orange over spherical activated carbon-supported and Er3+:YAlO3-doped TiO2 in a fluidized bed. *J. Chem. Technol. Biotechnol.,* 90**,** 880-887.

Dubois, M., Gilles, K. A., Hamilton, J. K., Rebers, P. A. & Smith, F. 1956. Colorimetric method for determination of sugars and related substances. *Analytical Chemistry,* 28**,** 350-356.

Duta, A. & Visa, M. 2015. Simultaneous removal of two industrial dyes by adsorption and photocatalysis on a fly-ash-TiO2 composite. *Journal of Photochemistry and Photobiology A: Chemistry,* 306**,** 21-30.

Edelmann, W., Engeli, H. & Gradenecker, M. 2000. Co-digestion of organic solid waste and sludge from sewage treatment. *Water Science and Technology.*

El Haddad, M. E., Regti, A., Laamari, M. R., Mamouni, R. & Saffaj, N. 2014. Use of fenton reagent as advanced oxidative process for removing textile dyes from aqueous solutions. *Journal of Materials and Environmental Science,* 5**,** 667-674.

Elsalamony, R. A. & Mahmoud, S. A. 2012. Preparation of nanostructured ruthenium doped titania for the photocatalytic degradation of 2-chlorophenol under visible light. *Arabian Journal of Chemistry*.

Epling, G. A. & Lin, C. 2002. Photoassisted bleaching of dyes utilizing TiO2 and visible light. *Chemosphere,* 46**,** 561-570.

Farghali, A. A., Zaki, A. H. & Khedr, M. H. 2016. Control of selectivity in heterogeneous photocatalysis by tuning TiO2 morphology for water treatment applications. *Nanomaterials and Nanotechnology,* 6.

Farhataziz & Ross, A. B. 1977. SELECTED SPECIFIC RATES OF REACTIONS OF TRANSIENTS FROM WATER IN AQUEOUS SOLUTION. III. HYDROXYL RADICAL AND PERHYDROXYL RADICAL AND THEIR RADICAL IONS. *Natl Bur Stand Natl Stand Ref Data Ser*.

Feng, J., Hu, X. & Yue, P. L. 2005. Discoloration and mineralization of Orange II by using a bentonite clay-based Fe nanocomposite film as a heterogeneous photo-Fenton catalyst. *Water Research,* 39**,** 89-96.

Fenton, H. J. H. 1894. Oxidation of tartaric acid in presence of iron. *J. Chem. Soc., Trans.,* 65**,** 899-910.

Fernandez, C., Larrechi, M. S. & Callao, M. P. 2009. Study of the influential factors in the simultaneous photocatalytic degradation process of three textile dyes. *Talanta,* 79**,** 1292-7.

Fernández, C., Larrechi, M. S. & Callao, M. P. 2010. An analytical overview of processes for removing organic dyes from wastewater effluents. *TrAC - Trends in Analytical Chemistry,* 29**,** 1202-1211.

Fox, M. A. & Dulay, M. T. 1993. Heterogeneous photocatalysis. *Chemical Reviews,* 93**,** 341-357.

Frank, S. N. & Bard, A. J. 1977. Heterogeneous photocatalytic oxidation of cyanide ion in aqueous solutions at titanium dioxide powder. *J. Am. Chem. Soc.,* 99**,** 303-4.

Frankin, R. J. 2001. Full-scale experiences with anaerobic treatment of industrial wastewater. *Water Science and Technology.*

Fu, W., Yang, H., Chang, L., Hari, B., Li, M. & Zou, G. 2006. Anatase TiO2 nanolayer coating on strontium ferrite nanoparticles for magnetic photocatalyst. *Colloids Surf., A,* 289**,** 47-52.

Fu, X., Long, J., Wang, X., Leung, D. Y. C., Ding, Z., Wu, L., Zhang, Z., Li, Z. & Fu, X. 2008a. Photocatalytic reforming of biomass: A systematic study of hydrogen evolution from glucose solution. *Int. J. Hydrogen Energy,* 33**,** 6484-6491.

Fu, X., Long, J., Wang, X., Leung, D. Y. C., Ding, Z., Wu, L., Zhang, Z., Li, Z. & Fu, X. 2008b. Photocatalytic reforming of biomass: A systematic study of hydrogen evolution from glucose solution. *International Journal of Hydrogen Energy,* 33**,** 6484-6491.

Fu, X., Wang, X., Leung, D. Y. C., Xue, W., Ding, Z., Huang, H. & Fu, X. 2010. Photocatalytic reforming of glucose over la doped alkali tantalate photocatalysts for H2 production. *Catalysis Communications,* 12**,** 184-187.

Fu, Z., Jiang, T., Liu, Z., Wang, D., Wang, L. & Xie, T. 2014. Highly photoactive Ti-doped α-Fe2O3 nanorod arrays photoanode prepared by a hydrothermal method for photoelectrochemical water splitting. *Electrochim. Acta,* 129**,** 358-363.

Fujishima, A. & Honda, K. 1972a. Electrochemical photolysis of water at a semiconductor electrode. *Nature (London),* 238**,** 37-8.

Fujishima, A. & Honda, K. 1972b. Electrochemical photolysis of water at a semiconductor electrode. *Nature,* 238**,** 37-38.

Fujishima, A. & Zhang, X. 2006. Titanium dioxide photocatalysis: present situation and future approaches. *Comptes Rendus Chimie,* 9**,** 750-760.

Galinska, A. & Walendziewski, J. 2005. Photocatalytic water splitting over Pt-TiO2 in the presence of sacrificial reagents. *Energy Fuels,* 19**,** 1143-1147.

Gernjak, W., Fuerhacker, M., Fernández-Ibañez, P., Blanco, J. & Malato, S. 2006. Solar photo-Fenton treatment - Process parameters and process control. *Applied Catalysis B: Environmental,* 64**,** 121-130.

Ghasemi, Z., Younesi, H. & Zinatizadeh, A. A. 2016. Preparation, characterization and photocatalytic application of TiO2/Fe-ZSM-5 nanocomposite for the treatment of petroleum refinery wastewater: Optimization of process parameters by response surface methodology. *Chemosphere,* 159**,** 552-564.

Ghodbane, H. & Hamdaoui, O. 2009. Intensification of sonochemical decolorization of anthraquinonic dye Acid Blue 25 using carbon tetrachloride. *Ultrasonics Sonochemistry,* 16**,** 455-461.

Gomathisankar, P., Yamamoto, D., Katsumata, H., Suzuki, T. & Kaneco, S. 2013a. Photocatalytic hydrogen production with aid of simultaneous metal deposition using titanium dioxide from aqueous glucose solution. *International Journal of Hydrogen Energy,* 38**,** 5517-5524.

Gomathisankar, P., Yamamoto, D., Katsumata, H., Suzuki, T. & Kaneco, S. 2013b. Photocatalytic hydrogen production with aid of simultaneous metal deposition using titanium dioxide from aqueous glucose solution. *Int. J. Hydrogen Energy,* 38**,** 5517-5524.

Greenlee, W. F., Osborne, R., Dold, K. M., Hudson, L. G. & Toscano Jr, W. A. 1985. Toxicity of chlorinated aromatic compounds in animals and humans: in vitro approaches to toxic mechanisms and risk assessment. *Environmental Health Perspectives,* 60**,** 69-76.

Gregory, P. 1986. Azo dyes: Structure-carcinogenicity relationships. *Dyes and Pigments,* 7**,** 45-56.

Gurav, H. R., Bobade, R., Das, V. L. & Chilukuri, S. 2012. Carbon dioxide reforming of methane over ruthenium substituted strontium titanate perovskite catalysts. *Indian J. Chem., Sect. A: Inorg., Bio-inorg., Phys., Theor. Anal. Chem.,* 51A**,** 1339-1347.

Hajaghazadeh, M., Vaiano, V., Sannino, D., Kakooei, H., Sotudeh-Gharebagh, R. & Ciambelli, P. 2014. Heterogeneous photocatalytic oxidation of methyl ethyl ketone under UV-A light in an LED-fluidized bed reactor. *Catalysis Today,* 230**,** 79-84.

Halas, S. & Durakiewicz, T. 1998a. Work functions of elements expressed in terms of the Fermi energy and the density of free electrons. *Journal of Physics: Condensed Matter,* 10**,** 10815-10826.

Halas, S. & Durakiewicz, T. 1998b. Work functions of elements expressed in terms of the Fermi energy and the density of free electrons. *J. Phys.: Condens. Matter,* 10**,** 10815-10826.

Hambourger, M., Brune, A., Gust, D., Moore, A. L. & Moore, T. A. 2005. Enzyme-assisted reforming of glucose to hydrogen in a photoelectrochemical cell. *Photochemistry and Photobiology,* 81**,** 1015-1020.

Hannum, S. M. 2004. Potential impact of strawberries on human health: a review of the science. *Crit. Rev. Food Sci. Nutr.,* 44**,** 1-17.

Hartmann, H. & Ahring, B. K. 2005. Anaerobic digestion of the organic fraction of municipal solid waste: Influence of co-digestion with manure. *Water Research,* 39**,** 1543-1552.

Hay, A. T. 1873. *IMPROVEMENT IN ELECTRICAL PROTECTION FOR BOILERS*. Copyright (C) 2017 American Chemical Society (ACS). All Rights Reserved.

He, J., Tao, X., Ma, W. & Zhao, J. 2002. Heterogeneous photo-Fenton degradation of an azo dye in aqueous H_2O_2/iron oxide dispersions at neutral pHs. *Chemistry Letters*, 86-87.

He, Q., Mukerjee, S., Shyam, B., Ramaker, D., Parres-Esclapez, S., Illan-Gomez, M. J. & Bueno-Lopez, A. 2009. Promoting effect of CeO2 in the electrocatalytic activity of rhodium for ethanol electro-oxidation. *J. Power Sources,* 193, 408-415.

Hidalgo, M. C., Maicu, M., Navio, J. A. & Colon, G. 2009. Effect of Sulfate Pretreatment on Gold-Modified TiO2 for Photocatalytic Applications. *J. Phys. Chem. C,* 113, 12840-12847.

Hidalgo, M. C., Murcia, J. J., Navío, J. A. & Colón, G. 2011. Photodeposition of gold on titanium dioxide for photocatalytic phenol oxidation. *Applied Catalysis A: General,* 397, 112-120.

Hoffmann, M. R., Martin, S. T., Choi, W. & Bahnemann, D. W. 1995a. Environmental Applications of Semiconductor Photocatalysis. *Chem. Rev. (Washington, D. C.),* 95, 69-96.

Hoffmann, M. R., Martin, S. T., Choi, W. & Bahnemann, D. W. 1995b. Environmental applications of semiconductor photocatalysis. *Chemical Reviews,* 95, 69-96.

Horikoshi, S., Watanabe, N., Onishi, H., Hidaka, H. & Serpone, N. 2002. Photodecomposition of a nonylphenol polyethoxylate surfactant in a cylindrical photoreactor with TiO2 immobilized fiberglass cloth. *Appl. Catal., B,* 37, 117-129.

Hou, D.-X. 2003. Potential mechanisms of cancer chemoprevention by anthocyanins. *Curr. Mol. Med.,* 3, 149-159.

Hou, L., Sun, G., Liu, K., Li, Y. & Gao, F. 2006. Preparation, characterization and investigation of catalytic activity of Li-doped LaFeO3 nanoparticles. *J. Sol-Gel Sci. Technol.,* 40, 9-14.

Huang, C. P., Dong, C. & Tang, Z. 1993. Advanced chemical oxidation: Its present role and potential future in hazardous waste treatment. *Waste Management,* 13, 361-377.

Huang, J., Wang, S., Zhao, Y., Wang, X., Wang, S., Wu, S., Zhang, S. & Huang, W. 2006. Synthesis and characterization of CuO/TiO2 catalysts for low-temperature CO oxidation. *Catal. Commun.,* 7, 1029-1034.

Hudson, J. B. 1998. *Surface Science: An Introduction*, Wiley.

Hwang, Y., Kang, D. S. & Park, M. H. 2010. Solution combustion synthesis and surface properties of LaFeO3 powders. *Journal of Ceramic Processing Research,* 11, 397-400.

Iervolino, G., Vaiano, V., Murcia, J. J., Rizzo, L., Ventre, G., Pepe, G., Campiglia, P., Hidalgo, M. C., Navío, J. A. & Sannino, D. 2016a. Photocatalytic hydrogen production from degradation of glucose over fluorinated and platinized TiO2 catalysts. *Journal of Catalysis,* 339, 47-56.

Iervolino, G., Vaiano, V., Sannino, D., Rizzo, L. & Ciambelli, P. 2016b. Production of hydrogen from glucose by LaFeO3 based photocatalytic process during water treatment. *International Journal of Hydrogen Energy,* 41**,** 959-966.

Ikeue, K., Shinmura, Y. & Machida, M. 2012. Ag-doped Mn-Cd sulfide as a visible-light-driven photocatalyst for H2 evolution. *Appl. Catal., B,* 123-124**,** 84-88.

Ilisz, I., Dombi, A., Mogyorosi, K. & Dekany, I. 2003. Photocatalytic water treatment with different TiO2 nanoparticles and hydrophilic/hydrophobic layer silicate adsorbents. *Colloids Surf., A,* 230**,** 89-97.

Iranpour, R., Stenstrom, M., Tchobanoglous, G., Miller, D., Wright, J. & Vossoughi, M. 1999. Environmental engineering: Energy value of replacing waste disposal with resource recovery. *Science,* 285**,** 706-711.

Isupova, L. A., Alikina, G. M., Tsybulya, S. V., Salanov, A. N., Boldyreva, N. N., Rusina, E. S., Ovsyannikova, I. A., Rogov, V. A., Bunina, R. V. & Sadykov, V. A. 2002. Honeycomb-supported perovskite catalysts for high-temperature processes. *Catalysis Today,* 75**,** 305-315.

Isupova, L. A., Sutormina, E. F., Kulikovskaya, N. A., Plyasova, L. M., Rudina, N. A., Ovsyannikova, I. A., Zolotarskii, I. A. & Sadykov, V. A. 2005. Honeycomb supported perovskite catalysts for ammonia oxidation processes. *Catalysis Today,* 105**,** 429-435.

Jang, J. S., Kim, H. G. & Lee, J. S. 2012. Heterojunction semiconductors: A strategy to develop efficient photocatalytic materials for visible light water splitting. *Catal. Today,* 185**,** 270-277.

Jeong, J. R., Lee, S. J., Kim, J. D. & Shin, S. C. 2004. Magnetic properties of γ-Fe2O3 nanoparticles made by coprecipitation method. *Physica Status Solidi (B) Basic Research,* 241**,** 1593-1596.

Jeppu, G. P. & Clement, T. P. 2012. A modified Langmuir-Freundlich isotherm model for simulating pH-dependent adsorption effects. *Journal of Contaminant Hydrology,* 129-130**,** 46-53.

Ji, P., Takeuchi, M., Cuong, T.-M., Zhang, J., Matsuoka, M. & Anpo, M. 2010. Recent advances in visible light-responsive titanium oxide-based photocatalysts. *Res. Chem. Intermed.,* 36**,** 327-347.

Jiao, H. & Zhao, K. 2016. Hydrothermal Synthesis and Magnetic Property of Monodisperse Plate-Like α-Fe2O3 Nanoparticles. *Synth. React. Inorg., Met.-Org., Nano-Met. Chem.,* 46**,** 1086-1089.

Jin, Z., Zhang, X., Li, Y., Li, S. & Lu, G. 2007. Apparent quantum efficiency for stable hydrogen generation over eosin-sensitized CuO/TiO2 photocatalyst under visible light irradiation. *Catal. Commun.,* 8**,** 1267-1273.

Jing, D., Liu, M., Shi, J., Tang, W. & Guo, L. 2010a. Hydrogen production under visible light by photocatalytic reforming of glucose over an oxide solid solution photocatalyst. *Catal. Commun.,* 12**,** 264-267.

Jing, D., Liu, M., Shi, J., Tang, W. & Guo, L. 2010b. Hydrogen production under visible light by photocatalytic reforming of glucose over an oxide solid solution photocatalyst. *Catalysis Communications,* 12**,** 264-267.

Kalamaras, E., Dracopoulos, V., Sygellou, L. & Lianos, P. 2016. Electrodeposited Ti-doped hematite photoanodes and their employment for photoelectrocatalytic hydrogen production in the presence of ethanol. *Chem. Eng. J. (Amsterdam, Neth.),* 295**,** 288-294.

Kamat, P. V. 2002. Photophysical, photochemical and photocatalytic aspects of metal nanoparticles. *J. Phys. Chem. B,* 106**,** 7729-7744.

Kanhere, P. & Chen, Z. 2014. A review on visible light active perovskite-based photocatalysts. *Molecules,* 19**,** 19995-20022, 28 pp.

Kansal, A., Siddiqui, N. & Gautam, A. 2011. Wastewater treatment of pulp and paper industry: a review. *Journal of environmental science & engineering,* 53**,** 203-218.

Karakitsou, K. E. & Verykios, X. E. 1993. Effects of altervalent cation doping of titania on its performance as a photocatalyst for water cleavage. *J. Phys. Chem.,* 97**,** 1184-9.

Kawai, T. & Sakata, T. 1980. Conversion of carbohydrate into hydrogen fuel by a photocatalytic process. *Nature (London),* 286**,** 474-6.

Kawai, T. & Sakata, T. 1981. Photocatalytic hydrogen production from water by the decomposition of poly(vinyl chloride), protein, algae, dead insects, and excrement. *Chem. Lett.***,** 81-4.

Kenney, J. F., Kutcherov, V. A., Bendeliani, N. A. & Alekseev, V. A. 2002. The evolution of multicomponent systems at high pressures: VI. The thermodynamic stability of the hydrogen–carbon system: The genesis of hydrocarbons and the origin of petroleum. *Proceedings of the National Academy of Sciences,* 99**,** 10976-10981.

Khan, S. U. M., Al-Shahry, M. & Ingler, W. B., Jr. 2002. Efficient photochemical water splitting by a chemically modified n-TiO2. *Science (Washington, DC, U. S.),* 297**,** 2243-2245.

Khetre, S. M., Jadhav, H. V. & Bamane, S. R. 2010. Synthesis and characterization of nanocrystalline Lafeo3 by combustion route. *Rasayan Journal of Chemistry,* 3**,** 82-86.

Kim, J., Hwang, D. W., Kim, H. G., Bae, S. W., Lee, J. S., Li, W. & Oh, S. H. 2005. Highly Efficient Overall Water Splitting Through Optimization of Preparation and Operation Conditions of Layered Perovskite Photocatalysts. *Top. Catal.,* 35**,** 295-303.

Kim, J., Lee, J. & Choi, W. 2008. Synergic effect of simultaneous fluorination and platinization of TiO 2 surface on anoxic

photocatalytic degradation of organic compounds. *Chemical Communications*, 756-758.
Kimling, J., Maier, M., Okenve, B., Kotaidis, V., Ballot, H. & Plech, A. 2006. Turkevich Method for Gold Nanoparticle Synthesis Revisited. *J. Phys. Chem. B,* 110, 15700-15707.
Kisch, H. & Macyk, W. 2002. Visible-light photocatalysis by modified titania. *ChemPhysChem,* 3, 399-400.
Kondarides, D., Daskalaki, V., Patsoura, A. & Verykios, X. 2008a. Hydrogen Production by Photo-Induced Reforming of Biomass Components and Derivatives at Ambient Conditions. *Catalysis Letters,* 122, 26-32.
Kondarides, D. I., Daskalaki, V. M., Patsoura, A. & Verykios, X. E. 2008b. Hydrogen Production by Photo-Induced Reforming of Biomass Components and Derivatives at Ambient Conditions. *Catal. Lett.,* 122, 26-32.
Kordouli, E., Bourikas, K., Lycourghiotis, A. & Kordulis, C. 2015. The mechanism of azo-dyes adsorption on the titanium dioxide surface and their photocatalytic degradation over samples with various anatase/rutile ratios. *Catal. Today,* 252, 128-135.
Kudo, A. 2006. Development of photocatalyst materials for water splitting. *International Journal of Hydrogen Energy,* 31, 197-202.
Kudo, A. & Miseki, Y. 2009. Heterogeneous photocatalyst materials for water splitting. *Chem. Soc. Rev.,* 38, 253-278.
Kumar, P., Sharma, P., Shrivastav, R., Dass, S. & Satsangi, V. R. 2011. Electrodeposited zirconium-doped α-Fe2O3 thin film for photoelectrochemical water splitting. *Int. J. Hydrogen Energy,* 36, 2777-2784.
Kuznetsova, E. V., Savinov, E. N., Vostrikova, L. A. & Parmon, V. N. 2004. Heterogeneous catalysis in the Fenton-type system FeZSM-5/H_2O_2. *Applied Catalysis B: Environmental,* 51, 165-170.
Lachheb, H., Puzenat, E., Houas, A., Ksibi, M., Elaloui, E., Guillard, C. & Herrmann, J.-M. 2002. Photocatalytic degradation of various types of dyes (Alizarin S, Crocein Orange G, Methyl Red, Congo Red, Methylene Blue) in water by UV-irradiated titania. *Appl. Catal., B,* 39, 75-90.
Lalitha, K., Reddy, J. K., Sharma, M. V. P., Kumari, V. D. & Subrahmanyam, M. 2010. Continuous hydrogen production activity over finely dispersed Ag2O/TiO2 catalysts from methanol:water mixtures under solar irradiation: A structure-activity correlation. *Int. J. Hydrogen Energy,* 35, 3991-4001.
Le, T. T., Akhtar, M. S., Park, D. M., Lee, J. C. & Yang, O. B. 2012. Water splitting on Rhodamine-B dye sensitized Co-doped TiO2 catalyst under visible light. *Appl. Catal., B,* 111-112, 397-401.

Lee, J., Park, H. & Choi, W. 2002. Selective Photocatalytic Oxidation of NH3 to N2 on Platinized TiO2 in Water. *Environ. Sci. Technol.,* 36**,** 5462-5468.

Lema, J. M. & Omil, F. 2001. Anaerobic treatment: A key technology for a sustainable management of wastes in Europe. *Water Science and Technology.*

Leong, K. H., Chu, H. Y., Ibrahim, S. & Saravanan, P. 2015. Palladium nanoparticles anchored to anatase TiO2 for enhanced surface plasmon resonance-stimulated, visible-light-driven photocatalytic activity. *Beilstein J. Nanotechnol.,* 6**,** 428-437, 10 pp.

Lettinga, G. ANAEROBIC DIGESTION FOR ENERGY SAVING AND PRODUCTION. Commission of the European Communities, (Report) EUR, 1981. 264-278.

Lettinga, G., Rebac, S., Parshina, S., Nozhevnikova, A., Van Lier, J. B. & Stams, A. J. M. 1999. High-rate anaerobic treatment of wastewater at low temperatures. *Applied and Environmental Microbiology,* 65**,** 1696-1702.

Lexmond, M. J. & Zeeman, G. 1995. Potential of controlled anaerobic wastewater treatment in order to reduce the global emissions of methane and carbon dioxide. *Studies in Environmental Science,* 65**,** 1143-1146.

Li Puma, G. & Brucato, A. 2007. Dimensionless analysis of slurry photocatalytic reactors using two-flux and six-flux radiation absorption-scattering models. *Catal. Today,* 122**,** 78-90.

Li Puma, G. & Yue, P. L. 1998. A laminar falling film slurry photocatalytic reactor. Part I - model development. *Chem. Eng. Sci.,* 53**,** 2993-3006.

Li Puma, G. & Yue, P. L. 2001. A Novel Fountain Photocatalytic Reactor for Water Treatment and Purification: Modeling and Design. *Ind. Eng. Chem. Res.,* 40**,** 5162-5169.

Li, S., Jing, L., Fu, W., Yang, L., Xin, B. & Fu, H. 2007. Photoinduced charge property of nanosized perovskite-type LaFeO3 and its relationships with photocatalytic activity under visible irradiation. *Materials Research Bulletin,* 42**,** 203-212.

Li, Y., Gao, D., Peng, S., Lu, G. & Li, S. 2011. Photocatalytic hydrogen evolution over Pt/Cd0.5Zn0.5S from saltwater using glucose as electron donor: An investigation of the influence of electrolyte NaCl. *Int. J. Hydrogen Energy,* 36**,** 4291-4297.

Li, Y., Wang, J., Peng, S., Lu, G. & Li, S. 2010. Photocatalytic hydrogen generation in the presence of glucose over ZnS-coated ZnIn2S4 under visible light irradiation. *International Journal of Hydrogen Energy,* 35**,** 7116-7126.

Liang, X., Liu, J., Zeng, D., Li, C., Chen, S. & Li, H. 2016. Hydrogen generation promoted by photocatalytic oxidation of ascorbate and

glucose at a cadmium sulfide electrode. *Electrochimica Acta,* 198**,** 40-48.

Lianos, P. 2011. Production of electricity and hydrogen by photocatalytic degradation of organic wastes in a photoelectrochemical cell. The concept of the Photofuelcell: A review of a re-emerging research field. *Journal of Hazardous Materials,* 185**,** 575-590.

Lin, S. H. & Peng, C. F. 1994. Treatment of textile wastewater by electrochemical method. *Water Res.,* 28**,** 277-82.

Link, S. & El-Sayed, M. A. 1999. Size and Temperature Dependence of the Plasmon Absorption of Colloidal Gold Nanoparticles. *J. Phys. Chem. B,* 103**,** 4212-4217.

Linley, S., Liu, Y., Ptacek, C. J., Blowes, D. W. & Gu, F. X. 2014. Recyclable graphene oxide-supported titanium dioxide photocatalysts with tunable properties. *ACS Applied Materials and Interfaces,* 6**,** 4658-4668.

Linsebigler, A. L., Lu, G. & Yates Jr, J. T. 1995. Photocatalysis on TiO2 surfaces: Principles, mechanisms, and selected results. *Chemical Reviews,* 95**,** 735-758.

Liu, B., Li, J., Zhou, B., Zheng, Q., Bai, J., Zhang, J., Liu, Y. & Cai, W. 2010. Kinetics and mechanisms for photoelectrochemical degradation of glucose on highly effective self-organized TiO2 nanotube arrays. *Cuihua Xuebao/Chinese Journal of Catalysis,* 31**,** 163-170.

Liu, Q., Yang, T., Feng, W. & Li, F. 2012a. Blue-Emissive Upconversion Nanoparticles for Low-Power-Excited Bioimaging in Vivo. *J. Am. Chem. Soc.,* 134**,** 5390-5397.

Liu, Y., Guo, L., Yan, W. & Liu, H. 2006. A composite visible-light photocatalyst for hydrogen production. *Journal of Power Sources,* 159**,** 1300-1304.

Liu, Y., Li, J., Qiu, X. & Burda, C. 2007. Bactericidal activity of nitrogen-doped metal oxide nanocatalysts and the influence of bacterial extracellular polymeric substances (EPS). *J. Photochem. Photobiol., A,* 190**,** 94-100.

Liu, Y., Yu, Y.-X. & Zhang, W.-D. 2012b. Photoelectrochemical properties of Ni-doped Fe2O3 thin films prepared by electrodeposition. *Electrochim. Acta,* 59**,** 121-127.

Lofrano, G., Rizzo, L., Grassi, M. & Belgiorno, V. 2009. Advanced oxidation of catechol: A comparison among photocatalysis, Fenton and photo-Fenton processes. *Desalination,* 249**,** 878-883.

Lu, X., Xie, S., Yang, H., Tong, Y. & Ji, H. 2014. Photoelectrochemical hydrogen production from biomass derivatives and water. *Chem. Soc. Rev.,* 43**,** 7581-7593.

Lucas, M. S. & Peres, J. A. 2006. Decolorization of the azo dye Reactive Black 5 by Fenton and photo-Fenton oxidation. *Dyes and Pigments,* 71**,** 236-244.

Mafra, M. R., Igarashi-Mafra, L., Zuim, D. R., Vasques, É. C. & Ferreira, M. A. 2013. Adsorption of remazol brilliant blue on an orange peel adsorbent. *Brazilian Journal of Chemical Engineering,* 30**,** 657-665.

Maicu, M., Hidalgo, M. C., Colón, G. & Navío, J. A. 2011. Comparative study of the photodeposition of Pt, Au and Pd on pre-sulphated TiO_2 for the photocatalytic decomposition of phenol. *Journal of Photochemistry and Photobiology A: Chemistry,* 217**,** 275-283.

Malavasi, L., Mozzati, M. C., Tealdi, C., Azzoni, C. B. & Flor, G. 2005. Influence of Ru Doping on the Structure, Defect Chemistry, Magnetic Interaction, and Carrier Motion of the La1-xNaxMnO3+δ Manganite. *The Journal of Physical Chemistry B,* 109**,** 20707-20713.

Manzini, E., Scaglia, B., Schievano, A. & Adani, F. 2015. Dark fermentation effectiveness as a key step for waste biomass refineries: Influence of organic matter macromolecular composition and bioavailability. *International Journal of Energy Research,* 39**,** 1519-1527.

Martin, C. A., Camera-Roda, G. & Santarelli, F. 1999. Effective design of photocatalytic reactors: influence of radiative transfer on their performance. *Catal. Today,* 48**,** 307-313.

Martínez, B., Roig, A., Obradors, X., Molins, E., Rouanet, A. & Monty, C. 1996. Magnetic properties of γ-Fe2O3 nanoparticles obtained by vaporization condensation in a solar furnace. *Journal of Applied Physics,* 79**,** 2580-2586.

Matsuka, M., Shigedomi, K. & Ishihara, T. 2014. Comparative study of propane steam reforming in vanadium based catalytic membrane reactor with nickel-based catalysts. *International Journal of Hydrogen Energy,* 39**,** 14792-14799.

Matsuoka, M., Kitano, M., Takeuchi, M., Tsujimaru, K., Anpo, M. & Thomas, J. M. 2007. Photocatalysis for new energy production. Recent advances in photocatalytic water splitting reactions for hydrogen production. *Catalysis Today,* 122**,** 51-61.

McCullagh, C., Robertson, J. M. C., Bahnemann, D. W. & Robertson, P. K. J. 2007. The application of TiO2 photocatalysis for disinfection of water contaminated with pathogenic micro-organisms: A review. *Research on Chemical Intermediates,* 33**,** 359-375.

McDonald, K. J. & Choi, K.-S. 2011. Synthesis and Photoelectrochemical Properties of Fe2O3/ZnFe2O4 Composite Photoanodes for Use in Solar Water Oxidation. *Chem. Mater.,* 23**,** 4863-4869.

Meissner, D., Memming, R. & Kastening, B. 1988. Photoelectrochemistry of cadmium sulfide. 1. Reanalysis of photocorrosion and flat-band potential. *J. Phys. Chem.,* 92**,** 3476-83.

Michal, R., Sfaelou, S. & Lianos, P. 2014. Photocatalysis for renewable energy production using photofuelcells. *Molecules,* 19**,** 19732-19750.

Min, B. K., Heo, J. E., Youn, N. K., Joo, O. S., Lee, H., Kim, J. H. & Kim, H. S. 2009. Tuning of the photocatalytic 1,4-dioxane degradation with surface plasmon resonance of gold nanoparticles on titania. *Catal. Commun.,* 10**,** 712-715.

Miranda, A. C., Lepretti, M., Rizzo, L., Caputo, I., Vaiano, V., Sacco, O., Lopes, W. S. & Sannino, D. 2016. Surface water disinfection by chlorination and advanced oxidation processes: Inactivation of an antibiotic resistant E. coli strain and cytotoxicity evaluation. *Science of the Total Environment,* 554-555**,** 1-6.

Mitra, S., Das, S., Mandal, K. & Chaudhuri, S. 2007. Synthesis of a α-Fe2O3 nanocrystal in its different morphological attributes: growth mechanism, optical and magnetic properties. *Nanotechnology,* 18**,** 275608/1-275608/9.

Miyauchi, M., Nakajima, A., Watanabe, T. & Hashimoto, K. 2002. Photocatalysis and photoinduced hydrophilicity of various metal oxide thin films. *Chem. Mater.,* 14**,** 2812-2816.

Muhd Julkapli, N., Bagheri, S. & Bee Abd Hamid, S. 2014. Recent advances in heterogeneous photocatalytic decolorization of synthetic dyes. *Scientific World Journal,* 2014.

Murcia, J. J., Hidalgo, M. C., Navio, J. A., Arana, J. & Dona-Rodriguez, J. M. 2014. Correlation study between photodegradation and surface adsorption properties of phenol and Methyl orange on TiO2 vs platinum-supported TiO2. *Appl. Catal., B,* 150-151**,** 107-115.

Murcia, J. J., Hidalgo, M. C., Navio, J. A., Arana, J. & Dona-Rodriguez, J. M. 2015a. Study of the phenol photocatalytic degradation over TiO2 modified by sulfation, fluorination, and platinum nanoparticles photodeposition. *Appl. Catal., B,* 179**,** 305-312.

Murcia, J. J., Hidalgo, M. C., Navío, J. A., Araña, J. & Doña-Rodríguez, J. M. 2015b. Study of the phenol photocatalytic degradation over TiO<inf>2</inf> modified by sulfation, fluorination, and platinum nanoparticles photodeposition. *Applied Catalysis B: Environmental,* 179**,** 305-312.

Murcia, J. J., Hidalgo, M. C., Navío, J. A., Vaiano, V., Sannino, D. & Ciambelli, P. 2013. Cyclohexane photocatalytic oxidation on Pt/TiO2 catalysts. *Catalysis Today,* 209**,** 164-169.

Nahm, M. H., Herzenberg, L. A., Little, K. & Little, J. R. 1977. A new method of applying the Sips equation. *Journal of Immunology,* 119**,** 301-305.

Nakata, K. & Fujishima, A. 2012. TiO 2 photocatalysis: Design and applications. *Journal of Photochemistry and Photobiology C: Photochemistry Reviews,* 13**,** 169-189.

Navaladian, S., Viswanathan, B., Varadarajan, T. K. & Viswanath, R. P. 2008. A Rapid Synthesis of Oriented Palladium Nanoparticles by UV Irradiation. *Nanoscale research letters,* 4**,** 181-186.

Navarro, R. M., Sanchez-Sanchez, M. C., Alvarez-Galvan, M. C., del Valle, F. & Fierro, J. L. G. 2009. Hydrogen production from renewable sources: biomass and photocatalytic opportunities. *Energy Environ. Sci.,* 2**,** 35-54.

Nguyen-Phan, T. D., Luo, S., Vovchok, D., Llorca, J., Graciani, J., Sanz, J. F., Sallis, S., Xu, W., Bai, J., Piper, L. F. J., Polyansky, D. E., Fujita, E., Senanayake, S. D., Stacchiola, D. J. & Rodriguez, J. A. 2016. Visible Light-Driven H2 Production over Highly Dispersed Ruthenia on Rutile TiO2 Nanorods. *ACS Catalysis,* 6**,** 407-417.

Nomikos, G. N., Panagiotopoulou, P., Kondarides, D. I. & Verykios, X. E. 2014. Kinetic and mechanistic study of the photocatalytic reforming of methanol over Pt/TiO2 catalyst. *Applied Catalysis B: Environmental,* 146**,** 249-257.

Nonomura, K., Komatsu, D., Yoshida, T., Minoura, H. & Schlettwein, D. 2007. Dependence of the photoelectrochemical performance of sensitized ZnO on the crystalline orientation in electrodeposited ZnO thin films. *Phys. Chem. Chem. Phys.,* 9**,** 1843-1849.

Oancea, P. & Meltzer, V. 2013a. Photo-Fenton process for the degradation of Tartrazine (E102) in aqueous medium. *Journal of the Taiwan Institute of Chemical Engineers,* 44**,** 990-994.

Oancea, P. & Meltzer, V. 2013b. Photo-Fenton process for the degradation of Tartrazine (E102) in aqueous medium. *J. Taiwan Inst. Chem. Eng.,* 44**,** 990-994.

Ohno, T., Tsubota, T., Nakamura, Y. & Sayama, K. 2005. Preparation of S, C cation-codoped SrTiO3 and its photocatalytic activity under visible light. *Appl. Catal., A,* 288**,** 74-79.

Okazaki, K., Morikawa, Y., Tanaka, S., Tanaka, K. & Kohyama, M. 2004. Electronic structures of Au on TiO2(110) by first-principles calculations. *Phys. Rev. B: Condens. Matter Mater. Phys.,* 69**,** 235404/1-235404/8.

Ozdemir, O., Dunlop, D. J. & Berquo, T. S. 2008. Morin transition in hematite: size dependence and thermal hysteresis. *Geochem., Geophys., Geosyst.,* 9**,** No pp. given.

Palma, V., Ruocco, C., Meloni, E. & Ricca, A. Oxidative steam reforming of ethanol on mesoporous silica supported Pt-Ni/CeO2 catalysts. Proceedings of the 6th European Fuel Cell - Piero Lunghi Conference, EFC 2015, 2015. 163-164.

Palma, V., Sannino, D., Vaiano, V. & Ciambelli, P. 2010. Fluidized-bed reactor for the intensification of gas-phase photocatalytic oxidative dehydrogenation of cyclohexane. *Industrial and Engineering Chemistry Research,* 49**,** 10279-10286.

Parida, K. M., Reddy, K. H., Martha, S., Das, D. P. & Biswal, N. 2010. Fabrication of nanocrystalline LaFeO3: An efficient sol-gel auto-combustion assisted visible light responsive photocatalyst for water decomposition. *International Journal of Hydrogen Energy,* 35**,** 12161-12168.

Park, C.-d., Walker, J., Tannenbaum, R., Stiegman, A. E., Frydrych, J. & Machala, L. 2009. Sol−Gel-Derived Iron Oxide Thin Films on Silicon: Surface Properties and Interfacial Chemistry. *ACS Applied Materials & Interfaces,* 1**,** 1843-1846.

Park, H., Park, Y., Kim, W. & Choi, W. 2013a. Surface modification of TiO2 photocatalyst for environmental applications. *J. Photochem. Photobiol., C,* 15**,** 1-20.

Park, H., Park, Y., Kim, W. & Choi, W. 2013b. Surface modification of TiO2 photocatalyst for environmental applications. *Journal of Photochemistry and Photobiology C: Photochemistry Reviews,* 15**,** 1-20.

Pascal, C., Pascal, J. L., Favier, F., Moubtassim, M. L. E. & Payen, C. 1999. Electrochemical Synthesis for the Control of γ-Fe2O3 Nanoparticle Size. Morphology, Microstructure, and Magnetic Behavior. *Chem. Mater.,* 11**,** 141-147.

Patsoura, A., Kondarides, D. I. & Verykios, X. E. 2007. Photocatalytic degradation of organic pollutants with simultaneous production of hydrogen. *Catal. Today,* 124**,** 94-102.

Peill, N. J. & Hoffmann, M. R. 1996. Chemical and Physical Characterization of a TiO2-Coated Fiber Optic Cable Reactor. *Environ. Sci. Technol.,* 30**,** 2806-2812.

Phokha, S., Pinitsoontorn, S., Maensiri, S. & Rujirawat, S. 2014. Structure, optical and magnetic properties of LaFeO3 nanoparticles prepared by polymerized complex method. *Journal of Sol-Gel Science and Technology,* 71**,** 333-341.

Pignatello, J. J. & Sun, Y. 1993. Photo-assisted mineralization of herbicide wastes by ferric ion catalyzed hydrogen peroxide. *ACS Symp. Ser.,* 518**,** 77-84.

Pop, L.-C., Dracopoulos, V. & Lianos, P. 2015a. Photoelectrocatalytic hydrogen production using nanoparticulate titania and a novel Pt/carbon electrocatalyst: The concept of the "Photoelectrocatalytic Leaf". *Appl. Surf. Sci.,* 333**,** 147-151.

Pop, L. C., Dracopoulos, V. & Lianos, P. 2015b. Photoelectrocatalytic hydrogen production using nanoparticulate titania and a novel

Pt/carbon electrocatalyst: The concept of the "photoelectrocatalytic Leaf". *Applied Surface Science,* 333**,** 147-151.

Pourreza, N., Rastegarzadeh, S. & Larki, A. 2011. Determination of Allura red in food samples after cloud point extraction using mixed micelles. *Food Chemistry,* 126**,** 1465-1469.

Rahman, G. & Joo, O.-S. 2013. Electrodeposited nanostructured α-Fe2O3 thin films for solar water splitting: Influence of Pt doping on photoelectrochemical performance. *Mater. Chem. Phys.,* 140**,** 316-322.

Rajendran, R., Yaakob, Z., Pudukudy, M., Rahaman, M. S. A. & Sopian, K. 2014. Photoelectrochemical water splitting performance of vertically aligned hematite nanoflakes deposited on FTO by a hydrothermal method. *J. Alloys Compd.,* 608**,** 207-212.

Rajeshwar, K. 2007. Hydrogen generation at irradiated oxide semiconductor-solution interfaces. *J. Appl. Electrochem.,* 37**,** 765-787.

Rajeshwar, K., De Tacconi, N. R. & Chenthamarakshan, C. R. 2001. Semiconductor-based composite materials: Preparation, properties, and performance. *Chemistry of Materials,* 13**,** 2765-2782.

Ramachandran, S., Fontanille, P., Pandey, A. & Larroche, C. 2006. Gluconic acid: Properties, applications and microbial production. *Food Technology and Biotechnology,* 44**,** 185-195.

Ramakrishna, K. R. & Viraraghavan, T. 1997. Dye removal using low cost adsorbents. *Water Sci. Technol.,* 36**,** 189-196.

Rana, S. & Misra, R. D. K. 2005. The anti-microbial activity of titania-nickel ferrite composite nanoparticles. *JOM,* 57**,** 65-69.

Ray, A. K. 2009. Photocatalytic reactor configurations for water purification: experimentation and modeling. *Adv. Chem. Eng.,* 36**,** 145-184.

Reddy, E. P., Davydov, L. & Smirniotis, P. 2003. TiO2-loaded zeolites and mesoporous materials in the sonophotocatalytic decomposition of aqueous organic pollutants: the role of the support. *Appl. Catal., B,* 42**,** 1-11.

Rizzo, L. 2011. Bioassays as a tool for evaluating advanced oxidation processes in water and wastewater treatment. *Water Research,* 45**,** 4311-4340.

Rizzo, L., Sannino, D., Vaiano, V., Sacco, O., Scarpa, A. & Pietrogiacomi, D. 2013. Effect of solar simulated N-doped TiO2 photocatalysis on the inactivation and antibiotic resistance of an E. coli strain in biologically treated urban wastewater. *Applied Catalysis B: Environmental,* 144**,** 369-378.

Robinson, T., McMullan, G., Marchant, R. & Nigam, P. 2001. Remediation of dyes in textile effluent: A critical review on current treatment technologies with a proposed alternative. *Bioresource Technology,* 77**,** 247-255.

Ruppert, G., Bauer, R. & Heisler, G. 1993. The photo-Fenton reaction - an effective photochemical wastewater treatment process. *J. Photochem. Photobiol., A,* 73**,** 75-8.

S.M.Khetre, A. U. C., C.J.Khilare, S.R.Bamane 2011. Synthesis of pure nanoporous LaFeO3 by using organic fuel. *International Journal of Porous Materials,* 1**,** 1-5.

Sabate, J., Anderson, M. A., Kikkawa, H., Xu, Q., Cervera-March, S. & Hill, C. G., Jr. 1992. Nature and properties of pure and niobium-doped titania ceramic membranes affecting the photocatalytic degradation of 3-chlorosalicylic acid as a model of halogenated organic compounds. *J. Catal.,* 134**,** 36-46.

Sacco, O., Stoller, M., Vaiano, V., Ciambelli, P., Chianese, A. & Sannino, D. 2012. Photocatalytic degradation of organic dyes under visible light on n-doped TiO2 photocatalysts. *International Journal of Photoenergy,* 2012.

Sacco, O., Vaiano, V., Han, C., Sannino, D. & Dionysiou, D. D. 2015. Photocatalytic removal of atrazine using N-doped TiO2 supported on phosphors. *Applied Catalysis B: Environmental,* 164**,** 462-474.

Sakata, T. & Kawai, T. 1981. Hydrogen production from biomass and water by photocatalytic processes. *Nouv. J. Chim.,* 5**,** 279-81.

Sakkas, V. A., Islam, M. A., Stalikas, C. & Albanis, T. A. 2010. Photocatalytic degradation using design of experiments: A review and example of the Congo red degradation. *J. Hazard. Mater.,* 175**,** 33-44.

Sannino, D., Vaiano, V., Ciambelli, P., Hidalgo, M. C., Murcia, J. J. & Navío, J. A. 2012a. Oxidative dehydrogenation of ethanol over Au/TiO 2 photocatalysts. *Journal of Advanced Oxidation Technologies,* 15**,** 284-293.

Sannino, D., Vaiano, V., Ciambelli, P. & Isupova, L. A. 2011a. Structured catalysts for photo-Fenton oxidation of acetic acid. *Catalysis Today,* 161**,** 255-259.

Sannino, D., Vaiano, V., Ciambelli, P. & Isupova, L. A. 2013a. Mathematical modelling of the heterogeneous photo-Fenton oxidation Of acetic acid on structured catalysts. *Chemical Engineering Journal,* 224**,** 53-58.

Sannino, D., Vaiano, V., Isupova, L. A. & Ciambelli, P. 2011b. Photo-Fenton oxidation of acetic acid on supported $LaFeO_3$ and $Pt/LaFeO_3$ perovskites. *Pres 2011: 14th International Conference on Process Integration, Modelling and Optimisation for Energy Saving and Pollution Reduction, Pts 1 and 2,* 25**,** 1013-1018.

Sannino, D., Vaiano, V., Isupova, L. A. & Ciambelli, P. 2012b. Heterogeneous photo-Fenton oxidation of organic pollutants on structured catalysts. *Journal of Advanced Oxidation Technologies,* 15**,** 294-300.

Sannino, D., Vaiano, V., Sacco, O. & Ciambelli, P. 2013b. Mathematical modelling of photocatalytic degradation of methylene blue under visible light irradiation. *J. Environ. Chem. Eng.,* 1**,** 56-60.

Saquib, M., Abu Tariq, M., Faisal, M. & Muneer, M. 2008. Photocatalytic degradation of two selected dye derivatives in aqueous suspensions of titanium dioxide. *Desalination,* 219**,** 301-311.

Sasaki, Y., Nemoto, H., Saito, K. & Kudo, A. 2009. Solar water splitting using powdered photocatalysts driven by Z-schematic interparticle electron transfer without an electron mediator. *J. Phys. Chem. C,* 113**,** 17536-17542.

Schrebler, R., Llewelyn, C., Vera, F., Cury, P., Munoz, E., del Rio, R., Gomez Meier, H., Cordova, R. & Dalchiele, E. A. 2007. An Electrochemical Deposition Route for Obtaining α-Fe2O3 Thin Films. *Electrochem. Solid-State Lett.,* 10**,** D95-D99.

Senthilnanthan, M., Ho, D. P., Vigneswaran, S., Ngo, H. H. & Shon, H. K. 2010. Visible light responsive ruthenium-doped titanium dioxide for the removal of metsulfuron-methyl herbicide in aqueous phase. *Sep. Purif. Technol.,* 75**,** 415-419.

Senthilnathan, J. & Philip, L. 2011. Photodegradation of methyl parathion and dichlorvos from drinking water with N-doped TiO2 under solar radiation. *Chem. Eng. J. (Amsterdam, Neth.),* 172**,** 678-688.

Serpone, N., Pelizzetti, E. & Editors 1989. *Photocatalysis. Fundamentals and Applications*, John Wiley & Sons.

Shen, P., Lofaro, J. C., Jr., Woerner, W. R., White, M. G., Su, D. & Orlov, A. 2013a. Photocatalytic activity of hydrogen evolution over Rh doped SrTiO3 prepared by polymerizable complex method. *Chem. Eng. J. (Amsterdam, Neth.),* 223**,** 200-208.

Shen, S., Guo, L., Chen, X., Ren, F., Kronawitter, C. X. & Mao, S. S. 2010a. Effect of Noble Metal in CdS/M/TiO2 for Photocatalytic Degradation of Methylene Blue under Visible Light. *International Journal of Green Nanotechnology: Materials Science & Engineering,* 1**,** M94-M104.

Shen, S., Guo, L., Chen, X., Ren, F., Kronawitter, C. X. & Mao, S. S. 2010b. Effect of Noble Metal in CdS/M/TiO 2 for Photocatalytic Degradation of Methylene Blue under Visible Light. *International Journal of Green Nanotechnology: Materials Science and Engineering,* 1**,** M94-M104.

Shen, S., Kronawitter, C. X., Wheeler, D. A., Guo, P., Lindley, S. A., Jiang, J., Zhang, J. Z., Guo, L. & Mao, S. S. 2013b. Physical and photoelectrochemical characterization of Ti-doped hematite photoanodes prepared by solution growth. *J. Mater. Chem. A,* 1**,** 14498-14506.

Siemon, U., Bahnemann, D., Testa, J. J., Rodríguez, D., Litter, M. I. & Bruno, N. 2002. Heterogeneous photocatalytic reactions comparing

TiO_2 and Pt/TiO_2. *Journal of Photochemistry and Photobiology A: Chemistry,* 148**,** 247-255.

Silva, G. L., Lopes, B. A. & Cardoso, P. E. C. Fenton and photo-Fenton reactions on degradation of food dye. *Dental Materials,* 30**,** e121.

Singh-Rachford, T. N. & Castellano, F. N. 2010. Photon upconversion based on sensitized triplet-triplet annihilation. *Coord. Chem. Rev.,* 254**,** 2560-2573.

Sinha, A. S. K., Sahu, N., Arora, M. K. & Upadhyay, S. N. 2001. Preparation of egg-shell type Al2O3-supported CdS photocatalysts for reduction of H2O to H2. *Catal. Today,* 69**,** 297-305.

Sivula, K., Zboril, R., Le Formal, F., Robert, R., Weidenkaff, A., Tucek, J., Frydrych, J. & Gratzel, M. 2010. Photoelectrochemical Water Splitting with Mesoporous Hematite Prepared by a Solution-Based Colloidal Approach. *J. Am. Chem. Soc.,* 132**,** 7436-7444.

Soares, O. S. G. P., Órfão, J. J. M., Portela, D., Vieira, A. & Pereira, M. F. R. 2006. Ozonation of textile effluents and dye solutions under continuous operation: Influence of operating parameters. *Journal of Hazardous Materials,* 137**,** 1664-1673.

Sohrabi, M. R., Khavaran, A., Shariati, S. & Shariati, S. Removal of Carmoisine edible dye by Fenton and photo Fenton processes using Taguchi orthogonal array design. *Arabian Journal of Chemistry*.

Soon, A. N. & Hameed, B. H. 2011. Heterogeneous catalytic treatment of synthetic dyes in aqueous media using Fenton and photo-assisted Fenton process. *Desalination,* 269**,** 1-16.

Stasinakis, A. S. 2008. Use of selected advanced oxidation processes (AOPs) for wastewater treatment - A mini review. *Global Nest Journal,* 10**,** 376-385.

Strataki, N., Antoniadou, M., Dracopoulos, V. & Lianos, P. 2010. Visible-light photocatalytic hydrogen production from ethanol–water mixtures using a Pt–CdS–TiO2 photocatalyst. *Catalysis Today,* 151**,** 53-57.

Su, H., Jing, L., Shi, K., Yao, C. & Fu, H. 2010. Synthesis of large surface area LaFeO3 nanoparticles by SBA-16 template method as high active visible photocatalysts. *Journal of Nanoparticle Research,* 12**,** 967-974.

Tafdrup, S. 1995. Viable energy production and waste recycling from anaerobic digestion of manure and other biomass materials. *Biomass and Bioenergy,* 9**,** 303-314.

Tahiri Alaoui, O., Herissan, A., Le Quoc, C., Zekri, M. E. M., Sorgues, S., Remita, H. & Colbeau-Justin, C. 2012. Elaboration, charge-carrier lifetimes and activity of Pd-TiO 2 photocatalysts obtained by gamma radiolysis. *Journal of Photochemistry and Photobiology A: Chemistry,* 242**,** 34-43.

Tandon, S. P. & Gupta, J. P. 1970. MEASUREMENT OF FORBIDDEN ENERGY GAP OF SEMICONDUCTORS BY DIFFUSE REFLECTANCE TECHNIQUE. *Phys Status Solidi,* 38**,** 363-367.

Tekbaş, M., Yatmaz, H. C. & Bektaş, N. 2008. Heterogeneous photo-Fenton oxidation of reactive azo dye solutions using iron exchanged zeolite as a catalyst. *Microporous and Mesoporous Materials,* 115**,** 594-602.

Thirumalairajan, S., Girija, K., Ganesh, I., Mangalaraj, D., Viswanathan, C., Balamurugan, A. & Ponpandian, N. 2012. Controlled synthesis of perovskite LaFeO3 microsphere composed of nanoparticles via self-assembly process and their associated photocatalytic activity. *Chemical Engineering Journal,* 209**,** 420-428.

Tijare, S. N., Bakardjieva, S., Subrt, J., Joshi, M. V., Rayalu, S. S., Hishita, S. & Labhsetwar, N. 2014. Synthesis and visible light photocatalytic activity of nanocrystalline PrFeO3 perovskite for hydrogen generation in ethanol-water system. *J. Chem. Sci. (Bangalore, India),* 126**,** 517-525.

Tijare, S. N., Joshi, M. M., Rayalu, S. S. & Labhasetwar, N. K. Photocatalytic hydrogen generation through water splitting on nano-crystalline LaFeO3 perovskite. ACS National Meeting Book of Abstracts, 2010.

Tode, R., Ebrahimi, A., Fukumoto, S., Iyatani, K., Takeuchi, M., Matsuoka, M., Lee, C. H., Jiang, C. S. & Anpo, M. 2010. Photocatalytic decomposition of water on double-layered visible light-responsive TiO2 thin films prepared by a magnetron sputtering deposition method. *Catalysis Letters,* 135**,** 10-15.

Trapalis, C., Todorova, N., Giannakopoulou, T., Romanos, G., Vaimakis, T. & Yu, J. 2008. Preparation of fluorine-doped TiO2 photocatalysts with controlled crystalline structure. *International Journal of Photoenergy,* 2008.

Ueno, H., Nemoto, J., Ohnuki, K., Horikawa, M., Hoshino, M. & Kaneko, M. 2009. Photoelectrochemical reaction of biomass-related compounds in a biophotochemical cell comprising a nanoporous TiO2 film photoanode and an O2-reducing cathode. *J. Appl. Electrochem.,* 39**,** 1897-1905.

Uzun, I. & Güzel, F. 2004. Kinetics and thermodynamics of the adsorption of some dyestuffs and p-nitrophenol by chitosan and MCM-chitosan from aqueous solution. *Journal of Colloid and Interface Science,* 274**,** 398-412.

Vaiano, V., Iervolino, G., Sannino, D., Murcia, J. J., Hidalgo, M. C., Ciambelli, P. & Navío, J. A. 2016a. Photocatalytic removal of patent

blue V dye on Au-TiO2 and Pt-TiO2 catalysts. *Applied Catalysis B: Environmental,* 188**,** 134-146.

Vaiano, V., Iervolino, G., Sannino, D., Rizzo, L., Sarno, G. & Farina, A. 2014a. Enhanced photocatalytic oxidation of arsenite to arsenate in water solutions by a new catalyst based on MoOx supported on TiO2. *Appl. Catal., B,* 160-161**,** 247-253.

Vaiano, V., Iervolino, G., Sannino, D., Rizzo, L., Sarno, G. & Farina, A. 2014b. Enhanced photocatalytic oxidation of arsenite to arsenate in water solutions by a new catalyst based on MoOx supported onTiO_2. *Applied Catalysis B: Environmental,* 160-161**,** 247-253.

Vaiano, V., Iervolino, G., Sarno, G., Sannino, D., Rizzo, L., Murcia Mesa, J. J., Hidalgo, M. C. & Navío, J. A. 2015a. Simultaneous production of CH4 and H2 from photocatalytic reforming of glucose aqueous solution on sulfated Pd-TiO2 catalysts. *Oil and Gas Science and Technology,* 70**,** 891-902.

Vaiano, V., Isupova, L. A., Ciambelli, P. & Sannino, D. 2014c. Photo-Fenton oxidation of t-butyl methyl ether in presence of LaFeO 3 supported on monolithic structure. *Journal of Advanced Oxidation Technologies,* 17**,** 187-192.

Vaiano, V., Sacco, O., Iervolino, G., Sannino, D., Ciambelli, P., Liguori, R., Bezzeccheri, E. & Rubino, A. 2015b. Enhanced visible light photocatalytic activity by up-conversion phosphors modified N-doped TiO2. *Appl. Catal., B,* 176-177**,** 594-600.

Vaiano, V., Sacco, O., Sannino, D. & Ciambelli, P. 2014d. Photocatalytic removal of spiramycin from wastewater under visible light with N-doped TiO2 photocatalysts. *Chemical Engineering Journal*.

Vaiano, V., Sacco, O., Sannino, D. & Ciambelli, P. 2015c. Nanostructured N-doped TiO2 coated on glass spheres for the photocatalytic removal of organic dyes under UV or visible light irradiation. *Appl. Catal., B,* 170-171**,** 153-161.

Vaiano, V., Sacco, O., Sannino, D. & Ciambelli, P. 2015d. Nanostructured N-doped TiO2 coated on glass spheres for the photocatalytic removal of organic dyes under UV or visible light irradiation. *Applied Catalysis B: Environmental,* 170-171**,** 153-161.

Vaiano, V., Sacco, O., Sannino, D. & Ciambelli, P. 2015e. Photocatalytic removal of spiramycin from wastewater under visible light with N-doped TiO2 photocatalysts. *Chemical Engineering Journal,* 261**,** 3-8.

Vaiano, V., Sacco, O., Sannino, D., Ciambelli, P., Longo, S., Venditto, V. & Guerra, G. 2014e. N-doped TiO2/s-PS aerogels for photocatalytic degradation of organic dyes in wastewater under visible light irradiation. *Journal of Chemical Technology and Biotechnology,* 89**,** 1175-1181.

Vaiano, V., Sacco, O., Sannino, D., Stoller, M., Ciambelli, P. & Chianese, A. 2016b. Photocatalytic removal of phenol by ferromagnetic N-TiO2/SiO2/Fe3O4 nanoparticles in presence of visible light irradiation. *Chemical Engineering Transactions.*

Vaiano, V., Sacco, O., Stoller, M., Chianese, A., Ciambelli, P. & Sannino, D. 2014f. Influence of the photoreactor configuration and of different light sources in the photocatalytic treatment of highly polluted wastewater. *International Journal of Chemical Reactor Engineering,* 12**,** 1-13.

van de Krol, R., Liang, Y. & Schoonman, J. 2008. Solar hydrogen production with nanostructured metal oxides. *J. Mater. Chem.,* 18**,** 2311-2320.

Vohra, M. S., Kim, S. & Choi, W. 2003. Effects of surface fluorination of TiO2 on the photocatalytic degradation of tetramethylammonium. *Journal of Photochemistry and Photobiology A: Chemistry,* 160**,** 55-60.

Wang, F. & Liu, X. 2009. Recent advances in the chemistry of lanthanide-doped upconversion nanocrystals. *Chem. Soc. Rev.,* 38**,** 976-989.

Wang, J., Dong, L., Hu, Y., Zheng, G., Hu, Z. & Chen, Y. 2001. Dispersion of NiO supported on γ-Al2O3 and TiO2/γ-Al2O3 supports. *J. Solid State Chem.,* 157**,** 274-282.

Wang, L., Lee, C.-Y. & Schmuki, P. 2013. Ti and Sn co-doped anodic α-Fe2O3 films for efficient water splitting. *Electrochem. Commun.,* 30**,** 21-25.

Wang, W.-Y. & Ku, Y. 2007. Effect of solution pH on the adsorption and photocatalytic reaction behaviors of dyes using TiO2 and Nafion-coated TiO2. *Colloids Surf., A,* 302**,** 261-268.

Wang, W., Tadé, M. O. & Shao, Z. 2015. Research progress of perovskite materials in photocatalysis- and photovoltaics-related energy conversion and environmental treatment. *Chemical Society Reviews,* 44**,** 5371-5408.

Ward, M. D., White, J. R. & Bard, A. J. 1983. Electrochemical investigation of the energetics of particulate titanium dioxide photocatalysts. The methyl viologen-acetate system. *J. Am. Chem. Soc.,* 105**,** 27-31.

Wawrzkiewicz, M. & Hubicki, Z. 2009. Removal of tartrazine from aqueous solutions by strongly basic polystyrene anion exchange resins. *Journal of Hazardous Materials,* 164**,** 502-509.

Whitby, G. E. 1989. The treatment of spa water with ozone produced by UV light. *Ozone: Sci. Eng.,* 11**,** 313-24.

Wu, C.-C., Cho, H.-F., Chang, W.-S. & Lee, T.-C. 2009. A simple and environmentally friendly method of preparing sulfide photocatalyst. *Chem. Eng. Sci.,* 65**,** 141-147.

Wu, J., Doan, H. & Upreti, S. 2008. Decolorization of aqueous textile reactive dye by ozone. *Chemical Engineering Journal,* 142**,** 156-160.

Wu, N.-L. & Lee, M.-S. 2004. Enhanced TiO2 photocatalysis by Cu in hydrogen production from aqueous methanol solution. *Int. J. Hydrogen Energy,* 29**,** 1601-1605.

Wu, X., Yin, S., Dong, Q., Liu, B., Wang, Y., Sekino, T., Lee, S. W. & Sato, T. 2013. UV, visible and near-infrared lights induced NOx destruction activity of (Yb,Er)-NaYF4/C-TiO2 composite. *Sci Rep,* 3**,** 2918.

Wu, X., Yin, S., Dong, Q. & Sato, T. 2014. Blue/green/red colour emitting up-conversion phosphors coupled C-TiO2 composites with UV, visible and NIR responsive photocatalytic performance. *Appl. Catal., B,* 156-157**,** 257-264.

Wu, Z., Zhao, G., Zhang, Y., Liu, J., Zhang, Y. N. & Shi, H. 2015. A solar-driven photocatalytic fuel cell with dual photoelectrode for simultaneous wastewater treatment and hydrogen production. *Journal of Materials Chemistry A,* 3**,** 3416-3424.

Xie, W. 2016. *A dye wastewater treatment tank [Machine Translation]*. Copyright (C) 2017 American Chemical Society (ACS). All Rights Reserved.

Xu, F., Zhang, B. & Lin, Y. 2016. *Advanced treatment for dyeing wastewater and its decolorization method*. Copyright (C) 2017 American Chemical Society (ACS). All Rights Reserved.

Yamabi, S. & Imai, H. 2002. Crystal phase control for titanium dioxide films by direct deposition in aqueous solutions. *Chemistry of Materials,* 14**,** 609-614.

Yamakata, A., Ishibashi, T.-a. & Onishi, H. 2003. Effects of Water Addition on the Methanol Oxidation on Pt/TiO2 Photocatalyst Studied by Time-Resolved Infrared Absorption Spectroscopy. *J. Phys. Chem. B,* 107**,** 9820-9823.

Yan, H., Yang, J., Ma, G., Wu, G., Zong, X., Lei, Z., Shi, J. & Li, C. 2009. Visible-light-driven hydrogen production with extremely high quantum efficiency on Pt-PdS/CdS photocatalyst. *Journal of Catalysis,* 266**,** 165-168.

Yang, S. y., Chen, Y. y., Zheng, J. g. & Cui, Y. j. 2007. Enhanced photocatalytic activity of TiO2 by surface fluorination in degradation of organic cationic compound. *Journal of Environmental Sciences,* 19**,** 86-89.

Yang, W., Li, X., Chi, D., Zhang, H. & Liu, X. 2014. Lanthanide-doped upconversion materials: emerging applications for photovoltaics and photocatalysis. *Nanotechnology,* 25**,** 482001/1-482001/16, 16 pp.

Yavuz, C. T., Prakash, A., Mayo, J. T. & Colvin, V. L. 2009. Magnetic separations: From steel plants to biotechnology. *Chem. Eng. Sci.,* 64**,** 2510-2521.

Yin, J., Bie, L.-J. & Yuan, Z.-H. 2007. Photoelectrochemical property of ZnFe2O4/TiO2 double-layered films. *Mater. Res. Bull.,* 42**,** 1402-1406.

Yu, C., Yu, J. C. & Chan, M. 2009. Sonochemical fabrication of fluorinated mesoporous titanium dioxide microspheres. *Journal of Solid State Chemistry,* 182**,** 1061-1069.

Yu, J., Hai, Y. & Cheng, B. 2011. Enhanced photocatalytic H2-production activity of TiO2 by Ni(OH)2 cluster modification. *J. Phys. Chem. C,* 115**,** 4953-4958.

Yu, J., Xiang, Q., Ran, J. & Mann, S. 2010. One-step hydrothermal fabrication and photocatalytic activity of surface-fluorinated TiO2 hollow microspheres and tabular anatase single micro-crystals with high-energy facets. *CrystEngComm,* 12**,** 872-879.

Yusof, Y. & Johan, M. R. 2014. Concentration-dependent properties of amorphous carbon nanotube/silica composites via the sol-gel technique. *CrystEngComm,* 16**,** 8570-8575.

Zeng, J., Liu, S., Cai, J. & Zhang, L. 2010. TiO2 Immobilized in Cellulose Matrix for Photocatalytic Degradation of Phenol under Weak UV Light Irradiation. *J. Phys. Chem. C,* 114**,** 7806-7811.

Zhang, H., Chen, G., Li, Y. & Teng, Y. 2010. Electronic structure and photocatalytic properties of copper-doped CaTiO3. *Int. J. Hydrogen Energy,* 35**,** 2713-2716.

Zhang, L., Hu, J., Song, P., Qin, H. & Jiang, M. 2006. Electrical properties and ethanol-sensing characteristics of perovskite La1 - XPbxFeO3. *Sensors and Actuators, B: Chemical,* 114**,** 836-840.

Zhang, L., Wang, W., Zhou, L., Shang, M. & Sun, S. 2009. Fe3O4 coupled BiOCl: A highly efficient magnetic photocatalyst. *Appl. Catal., B,* 90**,** 458-462.

Zhang, M., Lin, Y., Mullen, T. J., Lin, W.-f., Sun, L.-D., Yan, C.-H., Patten, T. E., Wang, D. & Liu, G.-y. 2012. Improving hematite's solar water splitting efficiency by incorporating rare-earth upconversion nanomaterials. *J. Phys. Chem. Lett.,* 3**,** 3188-3192.

Zhang, W., Wang, S., Li, J. & Yang, X. 2015a. Photocatalytic hydrogen production from methanol aqueous solution under visible-light using Cu/S–TiO2 prepared by electroless plating method. *Catalysis Communications,* 59**,** 189-194.

Zhang, Y., Tang, B., Wu, Z., Shi, H., Zhang, Y. & Zhao, G. 2016. Glucose oxidation over ultrathin carbon-coated perovskite modified TiO2 nanotube photonic crystals with high-efficiency electron generation and transfer for photoelectrocatalytic hydrogen production. *Green Chemistry,* 18**,** 2424-2434.

Zhang, Y., Zhao, G., Shi, H., Zhang, Y. N., Huang, W., Huang, X. & Wu, Z. 2015b. Photoelectrocatalytic glucose oxidation to promote hydrogen production over periodically ordered TiO<inf>2</inf> nanotube arrays assembled of Pd quantum dots. *Electrochimica Acta,* 174**,** 93-101.

Zhao, J., Chen, C. & Ma, W. 2005. Photocatalytic degradation of organic pollutants under visible light irradiation. *Top. Catal.,* 35**,** 269-278.

Zhao, Y., Swierk, J. R., Megiatto, J. D., Jr., Sherman, B., Youngblood, W. J., Qin, D., Lentz, D. M., Moore, A. L., Moore, T. A., Gust, D. & Mallouk, T. E. 2012. Improving the efficiency of water splitting in dye-sensitized solar cells by using a biomimetic electron transfer mediator. *Proc. Natl. Acad. Sci. U. S. A.,* 109**,** 15612-15616, S15612/1-S15612/8.

Zhe, D., Hu, X., Yue, P. L., Lu, G. Q. & Greenfield, P. F. 2001. Synthesis of anatase TiO2 supported on porous solids by chemical vapor deposition. *Catal. Today,* 68**,** 173-182.

Zheng, J. Y., Son, S. I., Van, T. K. & Kang, Y. S. 2015. Preparation of α-Fe2O3 films by electrodeposition and photodeposition of Co-Pi on them to enhance their photoelectrochemical properties. *RSC Adv.,* 5**,** 36307-36314.

Zhu, J. & Zaech, M. 2009. Nanostructured materials for photocatalytic hydrogen production. *Curr. Opin. Colloid Interface Sci.,* 14**,** 260-269.

Zhu, W., Koziel, J. A., Cai, L., Brehm-Stecher, B. F., Ozsoy, H. D. & Van Leeuwen, J. 2013. Ozonation-based decolorization of food dyes for recovery of fruit leather wastes. *Journal of Agricultural and Food Chemistry,* 61**,** 8198-8206.

Zieliñska, B., Borowiak-Palen, E. & Kalenczuk, R. J. 2008. Photocatalytic hydrogen generation over alkaline-earth titanates in the presence of electron donors. *International Journal of Hydrogen Energy,* 33**,** 1797-1802.

Zysler, R. D., Fiorani, D., Testa, A. M., Suber, L., Agostinelli, E. & Godinho, M. 2003. Size dependence of the spin-flop transition in hematite nanoparticles. *Phys. Rev. B: Condens. Matter Mater. Phys.,* 68**,** 212408/1-212408/4.